Spin-density-wave antiferromagnetism in chromium

Eric Fawcett

Department of Physics, University of Toronto, Toronto, Canada M5S 1A7

A comprehensive account is given of the macroscopic and microscopic physical properties of chromium (and where appropriate those of its dilute alloys) that relate to its antiferromagnetism. Neutron scattering is treated in great detail, first in the historical introduction, then as an experimental probe of both the magnetic structure and the excitations of the incommensurate spin-density-wave state and (with the assistance of x rays) of the concomitant charge-density wave and strain wave. Neutron scattering is considered as a tool to explore not only the disappearance of long-range order with increasing temperature through the growth of excitations as the weak first-order Néel transition is approached, but also the persistence of these spin fluctuations well into the paramagnetic state—processes that are still little understood. The article surveys, without mathematical details, model systems designed to reproduce the magnetic and thermodynamic properties of Cr. The energy-band structure calculations are given a more comprehensive review. Special attention is paid to calculations of the wave-vector-dependent susceptibility that reproduce the observed wave vector of the spin-density wave, and to a recent finite-temperature calculation that gives almost the right Néel temperature. The review of Fermi-surface studies emphasizes those designed to relate the spin-density wave vector (and its pressure dependence) to the nesting vector of the Fermi surface. An account is given of the spectroscopic determination of the energy gap(s), whose theoretical analysis is still unclear, and of experiments aimed at determining physical properties that throw light on the origin of the weak first-order Néel transition. The article describes the use of magnetic anomalies in the elastic moduli to determine the volume dependence of the exchange interaction responsible for antiferromagnetism in Cr. The experimental features of the spin-flip transition are reviewed, although a theory of this phenomenon is wanting. The experimental study of microscopic structure by the use of hyperfine-interaction properties is surveyed. An account is given of both experimental and theoretical studies of the surface of Cr and of Cr films and sandwiches. Finally, "technical antiferromagnetism" is discussed: the effect of severe internal strain in producing a commensurate antiferromagnetic state, wave-vector **Q** domains, polarization **S** domains (for which the experimental evidence is scanty), and ultrasonic attenuation as a tool to study them.

CONTENTS

I. INTRODUCTION

Chromium is the archetypal itinerant antiferromagnet, whose incommensurate spin-density wave (SDW) is characterized by a wave vector **Q** determined by the nesting properties of its Fermi surface. At the same time the persistence of antiferromagnetism in Cr alloys over a wide range of composition, considered in the light of the absence of antiferromagnetism in Mo and W, whose Fermi surfaces are very similar to that of paramagnetic Cr, indicates that the 3*d* character of this metal is of fundamental importance to its being magnetic. Indeed the three elemental antiferromagnets (apart from the rare earths and actinides, in which the localized *f* electrons are responsible for the magnetic nature) are all 3*d* metals: Cr, α-Mn, and γ-Fe. Until very recently (Zhao *et al.*, 1987) this interesting result had not been a feature of any theoretical treatment of antiferromagnetism in transition metals.

The beauty and mystery of Cr do not derive from the fact that it is an antiferromagnet, of which there are many, but from the fact that it is a spin-density-wave antiferromagnet *par excellence*. The richness of the phenomena observed in Cr derives from its itinerant SDW, which is a truly many-body effect.

Previous reviews of antiferromagnetism in Cr include Arrott's (1966) invaluable survey of antiferromagnetism in metals in the light of Overhauser's (1962) theory of SDW's, and Herring's (1966) monograph, which deals comprehensively with theoretical aspects of both ferromagnetism and antiferromagnetism in metals. An excellent recent review by Kulikov and Tugushev (1984) of SDW's and itinerant antiferromagnetism in metals, with particular reference to Cr and its dilute alloys, including a discussion of phase diagrams and electronic properties, provides a comprehensive account and reference list of more recent work, especially theoretical. Steinitz (1986) has recently reviewed experimental data on the physical properties of antiferromagnet (AFM) chromium relating to the thermal activation model of the transverse SDW phase. Landolt-Börnstein (1986) presents a considerable body of data on AFM Cr alloys.

I present here an account of the extensive literature on experimental and theoretical studies of antiferromagnetism in Cr. I shall discuss work on dilute Cr alloys only insofar as is necessary for our understanding of antiferromagnetism in pure Cr.

The first suggestion that Cr might be an antiferromagnet was made by Néel (1936b). He had earlier (1936a) given a list of negative exchange interaction energies between 3*d* atoms, Mn-Mn, Cr-Cr, and Fe-Fe (γ phase) and had estimated (Néel, 1934) the exchange coupling between Cr atoms. This estimate was based on the observation (Néel, 1932) that the paramagnetic susceptibility of a dilute solution of Cr in Au has a Curie-Weiss temperature dependence, so that the temperature independence of the paramagnetism of bulk Cr must be due to negative magnetic interactions between neighboring atoms (Néel, 1986).

The earliest experimental evidence for the existence of a phase transition in Cr, which was only later identified as the Néel transition, was provided by Bridgman (1932), who measured the pressure dependence of the Néel temperature T_N using the anomaly in the electrical resistivity seen at T_N. Many other physical properties of Cr exhibit singular behavior at the phase transition, as reviewed by Sully (1954). The variation with temperature of several physical properties in the neighborhood of the Néel temperature, $T_N \simeq 311$ K, is shown in Fig. 1. Fine *et al.* (1951), using electroformed and annealed pressed powder samples, found at T_N discontinuous changes in the Young's modulus, internal friction, thermal expansivity, electrical resistivity, and thermoelectric power (but not magnetic susceptibility). Their Young's modulus data also disclosed another transition near temperature 121 K, which was later identified as the spin-flip transition, as described in Sec. II.A.

There was a good deal of confusion at first about the origin of the anomaly at T_N, since Cr_2O_3 is also antiferromagnetic with coincidentally almost the same Néel temperature. This confusion was compounded when Shull and Wilkinson (1953) first did neutron diffraction on powdered Cr metal and found a weak (100) magnetic reflection, which disappeared at a temperature of about 475 K. We now know that this anomalously high Néel transition to a commensurate AFM structure is due to internal strain associated with dislocations present in cold-worked Cr. The transition to an incommensurate AFM structure at a temperature close to the correct Néel temperature was first observed in single-crystal Cr and reported almost simultaneously by Bykov *et al.* (1959) and Corliss *et al.* (1959).

I shall develop first in Sec. II a description of the magnetic properties of Cr as determined by neutron scattering. The story in Sec. II.A of how the static magnetic structure was established serves as a historical introduction.

II. NEUTRON SCATTERING

A. Magnetic structure: a historical review

The modern phase of magnetic studies began with the use of neutron diffraction to explore magnetic structures. Thus the first microscopic evidence for antiferromagnetism in Cr was obtained by Shull and Wilkinson (1953) in

the course of a systematic search for antiferromagnets by means of neutron powder diffraction in group-V metals V and Nb, group-VI Cr, Mo, and W, and group-VII α-Mn. Antiferromagnetic reflections were found only in α-Mn and Cr. In Cr the AFM peak at the (100) position corresponded to a moment of $0.40\mu_B$ per atom at temperature 4.2 K. This was about five times larger than that expected for a $\lambda/2$ peak from the nuclear (200) reflection, but the clearest evidence for its magnetic origin was the decrease in intensity with increasing temperature, which when extrapolated to zero, gave a Néel temperature of 475 K.

This commensurate antiferromagnetism persisting up to temperatures considerably higher than the Néel temperature, $T_N \simeq 311$ K, for incommensurate antiferromagnetism in Cr was to be a source of confusion throughout the study of neutron scattering in Cr. Bacon (1961) found that in polycrystalline, as in single-crystal, Cr there is a clear Néel transition at a temperature of about 40 °C, whereas the intensity moves from the incommensurate peaks into the commensurate position and persists up to about 200 °C in a fine-grain polycrystalline sample. Bacon and Cowlam (1969) made a systematic study of this effect in a heavily crushed powder of Cr with various degrees of annealing in order to clarify the relation of commensurate antiferromagnetism to internal strain in the sample. I shall discuss this work as an aspect of technical antiferromagnetism in Sec. VIII.A.

Bykov *et al.* (1959) and Corliss *et al.* (1959) independently first observed the magnetic satellites at $(0,0,1\pm\delta)$ corresponding to a wave vector $\mathbf{Q}=2\pi/a\,(1\pm\delta)$ directed along a cube axis. It was at first thought that the structure was an antiphase domain, with a 180° reversal of the localized spins every 14 unit cells (Corliss *et al.*, 1959). Shirane and Takei (1962) showed, however, that the third-harmonic satellite at $(0,0,1\pm3\delta)$ had an intensity less than 1% of the fundamental $(0,0,1\pm\delta)$, whereas antiphase domains would give about 10%.

Bykov *et al.* (1959) had observed the disappearance of the magnetic satellite at a temperature of about 160 K and had concluded that the AFM phase disappears through a second phase transition back to the paramagnetic phase at this temperature. Hastings (1960) observed the change in intensity of the pairs of satellites along each of the cube axes and concluded that the transition, which he found to be at a temperature of about 110 K, was from a high-temperature transversely polarized phase with spin direction **S** perpendicular to the wave vector **Q** to a low-temperature longitudinally polarized phase with **S** parallel to **Q**.

This spin-flip transition at temperature $T_{SF} \simeq 123$ K was to provide convincing evidence that the structure corresponds to a sinusoidal modulation of the magnetic scattering amplitude at all temperatures, rather than the alternative picture (antiphase domains having been ruled out) of a spiral transversely polarized structure at temperatures above T_{SF} with a sinusoidal modulation of longitudinally polarized spins below T_{SF}. Shirane and Takei (1962) measured the change in intensities of satellites above and below T_{SF} and found that the spiral model would require an increase in amplitude by a factor $\sqrt{2}$ when the temperature decreased through T_N, a most unlikely effect. Brown *et al.* (1965) used a polarized beam diffractometer to show that in the high-temperature phase the spiral model can be ruled out and that the polarization of the spins in the high-temperature phase above T_{SF} is in $\{100\}$ planes.

Shirane and Takei (1962) also found that the wavelength of the modulation changes continuously with temperature from $\simeq 21$ unit cells at temperature 78 K to $\simeq 28$ unit cells near $T_N \simeq 311$ K, thus confirming the earlier observation of Bacon (1961) over a more limited temperature range. The continuous nature of the change in wavelength of the sinusoidal modulation with temperature, as well as with pressure (Umebayashi *et al.*, 1968), provides the best evidence that the magnetic structure of AFM Cr corresponds to a continuous static spin-density wave (SDW) rather than a modulation of localized spins.

Overhauser and Arrott (1960) at first speculated that the localized spins might be oriented by their interaction with a SDW in the conduction-electron gas, as is the case in some rare-earth metals. Overhauser (1962) soon identified AFM Cr as being a manifestation of a static SDW. Lomer (1962) recognized that the large amplitude of the SDW is connected with peculiar geometric features of the Fermi surface of Cr, which permits nesting between electron and hole sheets having similar shape. These are connected by a nesting vector directed along a cube axis, which is roughly constant and equal in magnitude to the measured wave vector of the SDW in Cr. Overhauser (1962) pointed out that the phase transition from the SDW state to the paramagnetic state for a nesting model would have much smaller entropy, as observed in Cr (Beaumont *et al.*, 1960), than the value of the order R ln2 expected for a model of ordered spins. The absence of local moments was also demonstrated by the absence of paramagnetic (diffuse) neutron scattering above the Néel temperature T_N (Wilkinson *et al.*, 1962).

Overhauser and Arrott (1960) had proposed field cooling, i.e., cooling through T_N in a large magnetic field directed along a cube axis, to distinguish between different models for the AFM state of Cr. Shirane and Takei (1962), using a field of 1 T, obtained inconclusive results, and Montalvo and Marcus (1964) first demonstrated with a field of 3 T that field cooling gives a state having tetragonal symmetry in its magnetic susceptibility. They speculated that such a state was a single AFM domain having its wave vector **Q** directed along the field-cooling axis. Arrott *et al.* (1965) confirmed this by neutron diffraction, and Graebner and Marcus (1966) showed that the apparently cubic state of AFM Cr produced by cooling through T_N in the absence of a magnetic field is a polydomain rather than a triple-Q state. They found that, while a non-field-cooled sample exhibited de Haas–van Alphen oscillations at helium temperatures resulting from the superposition of spectra produced by

$\mathbf{Q}_x$, $\mathbf{Q}_y$, and $\mathbf{Q}_z$ states, each having tetragonal symmetry about a different cube axis (Watts, 1964), the de Haas–van Alphen spectrum of a field-cooled sample had full tetragonal symmetry about the field-cooling axis.

Bastow and Street (1966) speculated on the relation of field cooling to the anisotropy of the magnetic susceptibility in the transverse SDW state. The anisotropy of χ in single-Q Cr is consistent with the general rule for antiferromagnets, namely, that $\chi_{\parallel} < \chi_{\perp}$, the subscripts referring to the relative orientations of the polarization direction and the magnetic field. The sign of the anisotropy, which reverses at the spin-flip transition T_{SF} (Montalvo and Marcus, 1964), explains why a magnetic field applied parallel to the wave vector $\mathbf{Q}$ depresses T_{SF} (Street *et al.*, 1968). A large magnetic field, $\mathbf{H}=16$ T, applied in the low-temperature longitudinal SDW phase along the z axis of a largely single-Q sample previously field cooled in a field of 4 T along the z axis, gives a state with domains having wave vectors $\mathbf{Q}_x$ and $\mathbf{Q}_y$ (Werner *et al.*, 1966).

The tetragonality of the crystal structure of single-Q Cr (as we shall refer to a single-domain sample) was first observed independently by Lee and Asgar (1969) and Steinitz *et al.* (1969). The sign of the tetragonality just below the Néel temperature is $c/a > 1$, which explains why uniaxial compressive stress applied along one cube axis while stress cooling through T_N gives rise to a state having domains with wave vectors along the other two cube axes, while tensile stress gives a single-Q state with wave vector $\mathbf{Q}$ along the stress axis (Bastow and Street, 1966). The sign changes to $c/a < 1$ at 230 K (Steinitz *et al.*, 1969).

Figure 1 shows the behavior of several physical quantities at the Néel transition T_N, which suggest that the transition is first order. The earliest clear evidence for the first-order nature of the transition was provided by Arrott *et al.* (1965), who observed in high-quality single crystals of Cr an abrupt drop in the intensity of the AFM peaks at $(0,0,1\pm\delta)$ within a fraction of a degree as the temperature was raised through T_N.

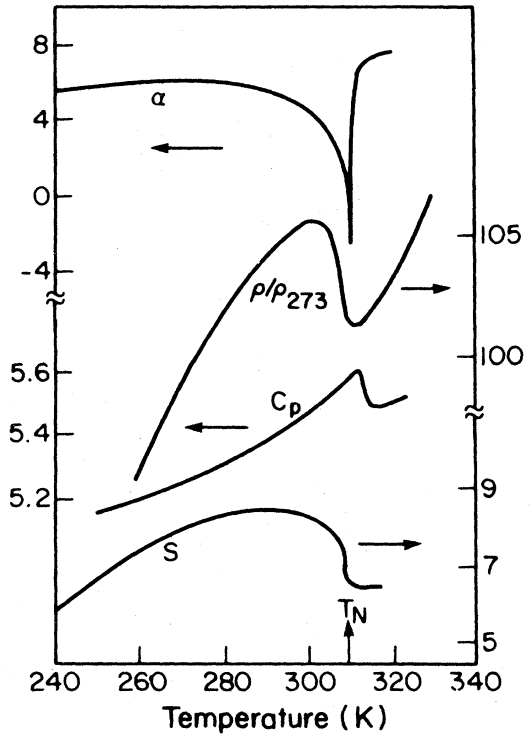

FIG. 1. Physical properties near the Néel transition at temperature $T_N \simeq 311$ K in chromium. The linear thermal expansivity α is in units (10^{-6} K^{-1}); the resistivity ρ is relative to its value at temperature 273 K; the specific heat Cp is in units (cal mol^{-1} K^{-1}); the thermoelectric power S is in units (10^{-6} V K^{-1}) (after Arrott, 1966).

B. Elastic neutron scattering: magnetic structure

1. Dependence of antiferromagnetism in Cr on temperature, pressure, and electron concentration

Neutron scattering has played an essential role in research on magnetism in solids, and in particular in developing our understanding of SDW's in chromium. It is appropriate to show briefly, following Arrott (1966; a more rigorous analysis is given, for example, by Lovesy, 1984), how neutrons, which "see" the magnetic induction field $\mathbf{B}(\mathbf{r})$, may be used to determine the order parameter $\mathbf{M}_{\mathbf{Q}}$ of the SDW, which is the Fourier component of the magnetization $\mathbf{M}(\mathbf{r})$ corresponding to the wave vector $\mathbf{Q}$ of the SDW.

The elastic partial differential neutron scattering cross section into an element $d\Omega$ of solid angle is

$$\frac{d\sigma}{d\Omega} \propto \langle \mathbf{k}' - \mathbf{k} \rangle^2 , \tag{1}$$

where the neutron specified by wave vector $\mathbf{k}$ is scattered into the state with wave vector $\mathbf{k}'$. Thus the scattering process effectively Fourier-analyzes the interaction potential

$$V(\mathbf{r}) = -\boldsymbol{\mu}_n \cdot \mathbf{B}(\mathbf{r}) \tag{2}$$

between the magnetic moment $\boldsymbol{\mu}_n$ of the neutron and the field.

Equations (1) and (2) give

$$\frac{d\sigma}{d\Omega} \propto \mathbf{B}_{\mathbf{q}} \cdot \mathbf{B}_{\mathbf{q}}^* , \tag{3}$$

where $\mathbf{B}_{\mathbf{q}}$ is the Fourier component of $\mathbf{B}(\mathbf{r})$ corresponding to the scattering vector

$$\mathbf{q} = \mathbf{k}' - \mathbf{k} . \tag{4}$$

The magnetization $M(\mathbf{r})$ is the source of $\mathbf{B}(\mathbf{r})$, according to Maxwell's equations,

$$\nabla \times \mathbf{B} = 4\pi \nabla \times \mathbf{M} \quad \text{and} \quad \nabla \cdot \mathbf{B} = 0 , \tag{5}$$

so that with

$$\mathbf{B}(\mathbf{r})=\sum_{\mathbf{q}}\mathbf{B}_{\mathbf{q}}e^{i\mathbf{q}\cdot\mathbf{r}},\quad \mathbf{M}(\mathbf{r})=\sum_{\mathbf{q}}\mathbf{M}_{\mathbf{q}}e^{i\mathbf{q}\cdot\mathbf{r}}\ , \tag{6}$$

we obtain

$$\mathbf{B}_{\mathbf{q}}=4\pi\mathbf{M}_{\mathbf{q}}-4\pi(\mathbf{M}\cdot\hat{\mathbf{q}})\hat{\mathbf{q}}\ , \tag{7}$$

where $\hat{q}$ is a unit vector in the direction of $\mathbf{q}$. Equation (7) is illustrated in Fig. 2, which shows that we can write

$$|\mathbf{B}_{\mathbf{q}}|=|\mathbf{M}_{\mathbf{q}}|\sin\theta_{\mathbf{q}} \tag{8}$$

so that with Eq. (3) we obtain

$$\frac{d\sigma}{d\Omega}=|\mathbf{M}_{\mathbf{q}}|^2\sin^2\theta_{\mathbf{q}}\ , \tag{9}$$

where $\theta_{\mathbf{q}}$ is the angle between $\mathbf{M}_{\mathbf{q}}$ and $\mathbf{q}$. Equation (9) gives the dependence of the intensity, $I=d\sigma/d\Omega$, of a Bragg peak due to a magnetization wave $\mathbf{M}(\mathbf{r})$ [in the case of Cr the SDW having a polarization vector $\mathbf{S}(\mathbf{r})\equiv\mathbf{M}(\mathbf{r})$ which is periodic with a wave vector conventionally denoted by $\mathbf{Q}$].

In the case of a fluctuating field, $\mathbf{B}(\mathbf{r},t)$, like that, for example, associated with spin waves in the ordered state or spin fluctuations in the paramagnetic state of chromium, the scattering is inelastic. The partial differential cross section between states of energy E and E', i.e., in the energy interval $\hbar\omega=E'-E$, which is commonly referred to as the dynamic structure factor $S(\mathbf{q},\hbar\omega)$, may then be written

$$\frac{d^2\sigma}{d\Omega\,d\omega}\propto\mathbf{M}_{\mathbf{q},\omega}\cdot\mathbf{M}^*_{\mathbf{q},\omega}\ , \tag{10}$$

where $\mathbf{M}_{\mathbf{q},\omega}$ is the spatial and temporal Fourier component of $\mathbf{M}(\mathbf{r})$.

The positions in reciprocal space of the satellites around the {100} and {111} points, which characterize the incommensurate magnetic structure of AFM Cr, are shown in Figs. 3(a) and 3(b). The corresponding incommensurate SDW in configuration space is illustrated in Fig. 3(c). The temperature dependence of the intensities of these magnetic satellites is shown in Fig. 4(a). The overall temperature dependence is somewhat sample dependent (Werner *et al.*, 1967a) and has variously been compared with the Brillouin function (Shirane and Takei, 1962) and the BCS function (Overhauser, 1962), i.e., a slow decrease as temperature increases from zero, becom-

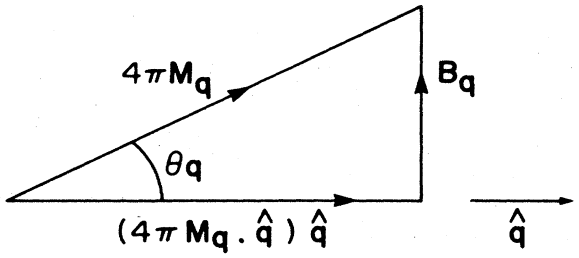

FIG. 2. Vector diagram illustrating Eq. (7).

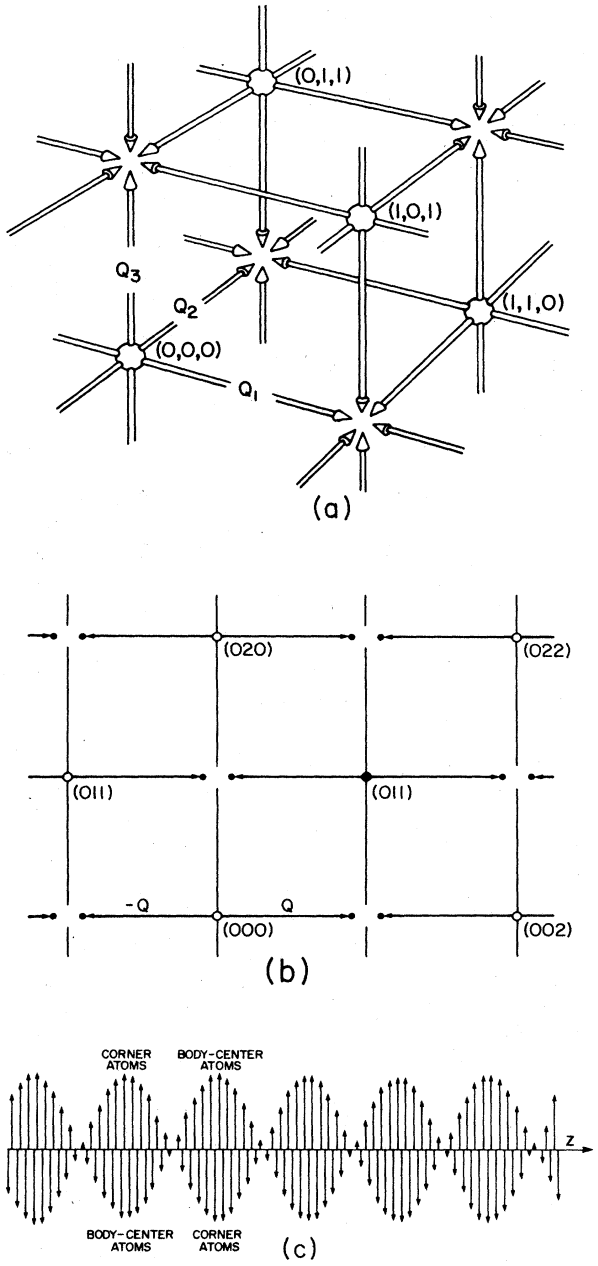

FIG. 3. Magnetic structure of AFM Cr in reciprocal space. (a) The SDW wave vectors $\mathbf{Q}$ are shown along each of the cube axes, corresponding to different single-$\mathbf{Q}$ domains. The open circles show the reciprocal-lattice points with indices (h,k,l) given in units of $a^*=2\pi/a$, which will normally not be specified. The indices (hkl), which have a nonzero structure factor for the body-centered cubic Bravais lattice of Cr, satisfy the condition $(h+k+l)=2n$, where n is an integer (after Arrott, 1966). (b) Section of (a) in the (001) plane for the SDW having wave vector $\mathbf{Q}=(0,0,1\pm\delta)a^*$ directed along the z axis. Two satellites at $(h,k,l\pm\delta)a^*$, with $\delta=1-aQ/2\pi$, are thus associated with each point (hkl) having zero structure factor, i.e., points for which $(h+k+l)=2n+1$ (after Fincher *et al.*, 1979). (c) The SDW corresponding to (b) represented by arrows showing its amplitude at the body-center and corner atoms in the body-centered-cubic lattice (after Fincher *et al.*, 1979).

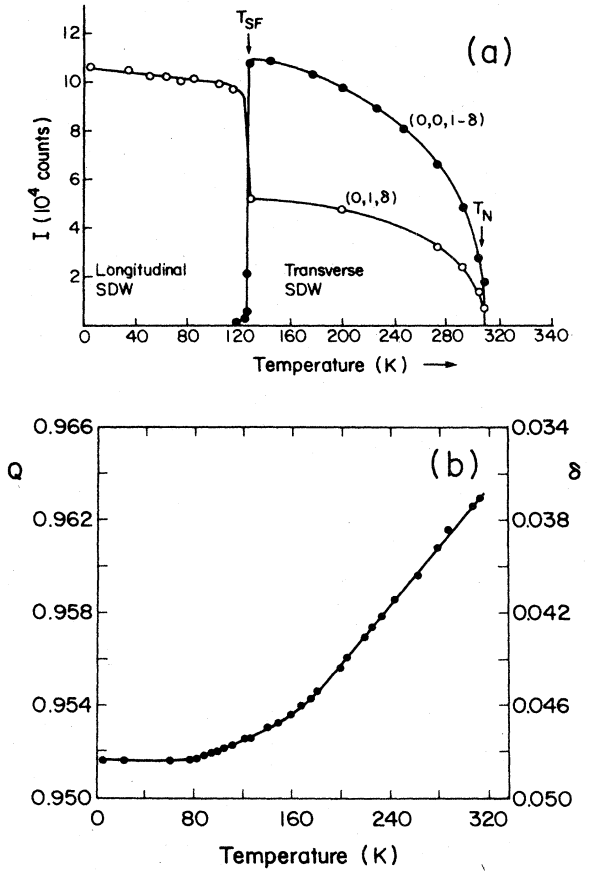

FIG. 4. Temperature dependence of the SDW in chromium. (a) The magnetic satellite reflections in AFM Cr. I is the integrated intensity under the Bragg peaks at the satellite positions shown in Figs. 3 and 14. We follow the arbitrary convention, which we adopt throughout, of taking the wave vector **Q** to be along the z axis. The Néel temperature T_N, spin-flip temperature T_{SF}, and the longitudinal SDW and transverse SDW phases are indicated. The temperature dependence of the first-order transition at T_N is shown in greater detail in Fig. 23 (after Werner *et al.*, 1967a). (b) The SDW wave vector **Q**. Q and $\delta=(1-Q)$ are given in units of $a^*=2\pi/a$ (after Werner *et al.*, 1967a).

ing increasingly rapid as the temperature approaches the Néel transition, with a first-order drop to near zero at T_N (which will be discussed in more detail in Sec. II.C.4).

This behavior is illustrated in Fig. 4(a), where abrupt changes in intensity also occur at the spin-flip transition T_{SF} because of the changes there in the angular term $\sin^2(\mathbf{S}\wedge\mathbf{q})$ in the expression given in Eq. (9) for the neutron scattering intensity. Here **S** is the polarization vector of the SDW, which is equivalent to $\mathbf{M}(\mathbf{r})$ in Eq. (6), and **q** is the neutron scattering vector defined in Eq. (4), so that $(\mathbf{S}\wedge\mathbf{q})\equiv\theta_{\mathbf{q}}$, as shown in Fig. 2.

As the polarization changes at the spin-flip transition T_{SF} from $\mathbf{S}\perp\mathbf{Q}$ in the transverse SDW phase above T_{SF} to $\mathbf{S}\parallel\mathbf{Q}$ in the longitudinal SDW phase below T_{SF}, Eq. (9) shows that reflections of the type $(0,0,1\pm\delta)$ essentially vanish [since $\delta\simeq0.05$, so that $\sin^2(\mathbf{S}\wedge\mathbf{q})\simeq0.0025$] as the intensity is transferred to reflections of the type $(0,1,\pm\delta)$, whose intensity therefore increases. The lack of continuity between the $(0,0,1+\delta)$ curve above T_{SF} and the $(0,1,\delta)$ curve below T_{SF} is discussed by Fawcett, Kaiser, and White (1986).

Figure 4(b) shows the temperature dependence of the magnitude Q of the wave vector **Q** measured in units of $a^*=2\pi/a$, and of the incommensurability parameter, $\delta=1-Q$. Both Q and δ appear to become constant and independent of temperature below a temperature of about 80 K, but recent careful measurements of the temperature dependence of Q by Gibbs *et al.* (1987), who used synchrotron radiation to observe the charge-density wave of wave vector $2Q$, show a continuous decrease with decreasing temperature, with dQ/dT approaching zero below 40 K.

Umebayashi *et al.* (1968) measured, using neutron diffraction, the pressure dependence up to 0.6 GPa of the wave vector **Q** from the Néel temperature to below the spin-flip transition with the results shown in Fig. 71 below. Indirect measurements of the dependence of **Q** on pressure p at low temperature by means of the de Haas–van Alphen effect are also illustrated in Fig. 71 and described in Sec. V.B. The hysteretic behavior of $\mathbf{Q}(p)$, giving rise to two quite different values of $d\mathbf{Q}/dp$ at low temperature, is shown in Fig. 75 and will be discussed in Sec. VIII.E as an aspect of technical antiferromagnetism in Cr.

The variation of the wave vector **Q** and the rms moment $\langle\mu\rangle$, which is a measure of the amplitude of the SDW in dilute alloys of Cr with other transition metals, was first studied systematically by Koehler *et al.* (1966). The dependence of the Néel temperature T_N on impurities was first studied by de Vries (1959), the sensitivity of T_N especially to metals of different groups being an indication of the electronic nature of the transition. The dependence of T_N and **Q** on atomic concentration in various alloys is shown in Figs. 5 and 6.

2. Dependence of antiferromagnetism in Cr on magnetic field

We have seen that field cooling Cr through the Néel transition with a sufficiently large magnetic field $\mathbf{H}_0$ directed along a cube axis produces a single-**Q** sample. For smaller fields the sample remains polydomain but with a preferred orientation along the field direction, the greater part of the sample having a wave vector along this direction. The magnitude of the field required to produce an essentially single-**Q** state depends upon the metallurgical history of the sample.

When an external field **H** is applied along a cube axis perpendicular to the wave vector of a largely single-**Q** sample in the transverse SDW phase, the relative amounts of the different single-**Q** domains remain unchanged. Below the spin-flip transition in the longitudinal SDW phase with $\mathbf{Q}\parallel\mathbf{H}$ there may be **Q** switching to

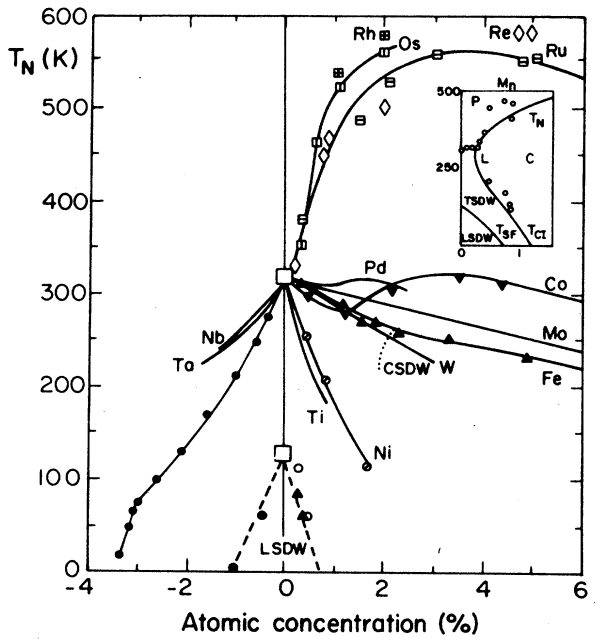

FIG. 5. Dependence of the Néel temperature T_N upon the atomic concentration of various transition-metal impurities in Cr alloys. The spin-flip transition to the longitudinal SDW phase (denoted LSDW) is shown by the dashed lines. The transition to the commensurate phase (denoted CSDW) in Cr*Fe* alloys is shown schematically by the dotted line. Symbols indicating experimental points (reference to the original literature should be made for precise values): ●, V; □, Cr; ○ (inset), Mn; ▲, Fe; ▼, Co; ⊘, Ni; ⊟, Ru; ⊞, Rh; ◇, Re; ◫, Os. The diagram is based on figures of Lebech and Mikke (1972) and Arajs *et al.* (1973), with additional data for Cr*V* (Arajs, 1969), Cr*Fe* (Burke and Rainford, 1978), Cr*Pd* (Moyer *et al.*, 1980), Cr*Ru* (Papoular *et al.*, 1981), Cr*Mn* (Yakhmi *et al.*, 1984), and Cr*Mo* (Cywinski and Hicks, 1986).

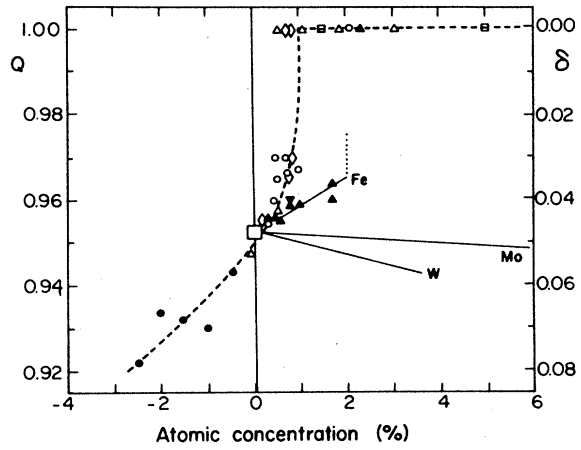

FIG. 6. Dependence of the magnitude Q of the wave vector and $\delta=(1-Q)$ at temperature 100 K upon the atomic concentration of various transition-metal impurities in Cr alloys. The dashed line is a guide for the eye through the experimental points, which are indicated by the same symbols as in Fig. 5. The transition to the commensurate phase ($Q=1.00$ in units of $a^*=2\pi/a$) in Cr*Fe* alloys is shown schematically by the dotted line. The diagram is based on a figure of Lebech and Mikke (1972), with additional data for Cr*Ru* (Papoular *et al.*, 1981) and Cr*Mo* (Cywinski and Hicks, 1986).

the domains having $\mathbf{Q}\perp\mathbf{H}$. These effects have been mentioned by several authors, but have not been studied systematically. We shall return to them in Sec. VIII.B. We shall also discuss later in Sec. VI the effect of a magnetic field on the Néel and spin-flip phase transitions.

For the present we are concerned with the effect of a magnetic field $\mathbf{H}\perp\mathbf{Q}$ on the direction of the polarization vector $\mathbf{S}$ in the transverse SDW phase. Werner *et al.* (1967a, 1968, 1969) showed that $\mathbf{S}$ rotates into the direction perpendicular to $\mathbf{H}$ in the plane perpendicular to $\mathbf{Q}$. The magnetic anisotropy is weak at temperature 298 K, but at 200 K it is much more difficult to rotate $\mathbf{S}$ into the [110] direction with $\mathbf{H}$ along [110] than into the [100] direction with $\mathbf{H}$ along [010] (Werner *et al.*, 1969).

As shown in Fig. 7, the polarization relaxes back with little hysteresis when the field is removed. The intensity is plotted versus the square of the magnetic field in accordance with a thermal activation model developed by Werner *et al.* (1967a) to explain this behavior, which will be discussed in Sec. VIII.C. The characteristic field required to rotate the polarization is both temperature and sample dependent. The sample dependence is an aspect of technical antiferromagnetism, to be discussed in Sec. VIII.

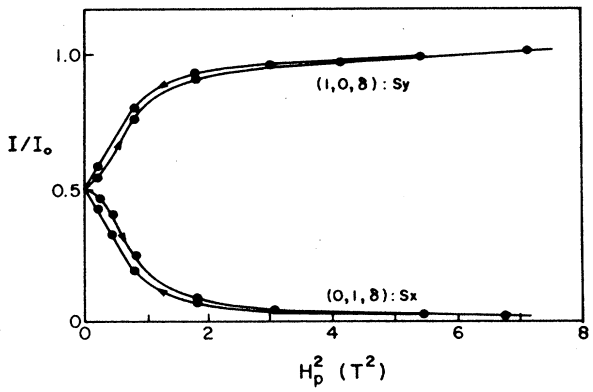

FIG. 7. Magnetic field dependence of the intensity of magnetic satellite reflections in the transverse SDW phase. I/I_0 is the intensity measured relative to its value I_0 in zero field, which is the same at $(1,0,\delta)$, corresponding to polarization direction $\mathbf{S}_y$, as at $(0,1,\delta)$, corresponding to $\mathbf{S}_x$ (see Fig. 14). The polarizing field $\mathbf{H}_p$ is applied along the x axis at temperature 163 K. The arrows show the direction of field sweep, and the data are plotted vs H_p^2 for comparison with the thermal activation model discussed in Sec. VIII.C (after Werner *et al.*, 1968).

3. Magnetic form factors

Moon *et al.* (1966) measured the spatial distribution of spin density in commensurate AFM Cr*Mn* by determining the intensities of six magnetic reflections. Previous work by Corliss *et al.* (1959) and Shirane and Takei (1962) had shown the magnetic form factor in AFM Cr to be similar to the experimental form factor of the 3*d* metal ion Mn^{2+}. Moon *et al.* (1966) believed that the small amount of Mn needed to make Cr a commensurate antiferromagnet would not significantly change the form factor, while the accuracy with which it could be measured was greatly improved: a single magnetic Bragg peak is observed at the magnetic reciprocal lattice position, instead of a group of six satellite peaks, which results in higher peak intensities and a much easier resolution problem, while the rms moment $0.43\mu_B$ (see Sec. II.B.4) is raised to a constant value of about $0.8\mu_B$ per atom (Koehler *et al.*, 1966; see Fig. 6). The Néel temperature is also raised, so that measurements may be made at room temperature without suffering a large loss of intensity.

Moon *et al.* (1966) used three samples containing 1.7, 2.0, and 4.1 at. % Mn, and the consistency of the results justified to some degree their assumption that AFM Cr*Mn* in this respect is equivalent to AFM Cr, though we shall see in Secs. II.C.1 and II.C.2 that this appears not to be so in the case of magnetic excitations. It is interesting to note that in commensurate AFM Cr*Mn* there are three possible magnetic polarization domains with the direction of the polarization vector along each of the three ⟨100⟩ directions, corresponding but not equivalent to the three **Q** domains of AFM Cr. In Cr*Mn* these polarization domains were found to be not equally populated, and so it was necessary to determine the populations for each of the single-crystal samples by measuring three reflections with permuted indices.

The results shown in Fig. 8 are compared with the restricted Hartree-Fock calculations by Freeman and Watson (1961) for atomic Cr rather than the very similar experimental form factor for the Mn^{2+} ion (Corliss *et al.*, 1956). The observed (221) intensity was larger than (300) by about a factor of 6, which corresponds to a 3*d* unpaired spin distribution of $t_{2g}=0.79\pm0.2$ and $e_g=0.21\pm0.2$, and the crosses in Fig. 8 show the values calculated for this configuration. Spherical symmetry would correspond to populations $t_{2g}=0.6$ and $e_g=0.4$.

Stassis *et al.* (1973) used polarized neutrons to measure the form factor of the field-induced magnetic moment in pure Cr. They measured the residual polarization ratio $(R-1)$, defined as the ratio of the coherent diffracted intensities for the two neutron spin states (parallel and antiparallel to the fields on the crystal). The magnetic scattering amplitude $p(\theta)$ is simply related to the residual polarization ratio by the expression

$$R-1\simeq 4p(\theta)/b\ , \tag{11}$$

where θ is the Bragg angle and b is the coherent nuclear scattering amplitude, $b=0.3532\times10^{-14}$ m. The approximation is valid when $p(\theta)\ll b$, a condition fulfilled in these measurements. The magnetic scattering amplitude has paramagnetic, diamagnetic, and spin-orbit scattering components. The correction to the measured polarization ratio introduced by the latter two quantities can be easily calculated and amounts to only 4% for the most severe case of the (110) reflection. The results of this experiment shown in Fig. 9 demonstrate that the spatial distribution of induced magnetic moment is independent of temperature and is essentially the same in AFM Cr as in paramagnetic Cr in the neighborhood of the Néel temperature. Stassis *et al.* found too that the form factor is best fit by a combination of 40% 3*d* spin, which they assume to be given by the experimental form factor of AFM Cr*Mn* and 60% 3*d* orbital given by the Hartree-Fock calculation for the $3d^4 4s^2$ configuration of the free Cr atom.

The large orbital contribution to the induced magnetization in Cr is typical of transition metals that have nearly half-filled *d* bands, and arises from the Van Vleck paramagnetic susceptibility, as first pointed out by Kubo and Obata (1956). Oh *et al.* (1976) have calculated the static susceptibility and the wave-vector-dependent susceptibility $\chi(q)$ for four reciprocal-lattice vectors. They find that in order to fit the experimental field-induced magnetic form factor shown in Fig. 9 it is necessary to assume a large exchange enhancement factor of about 2.5.

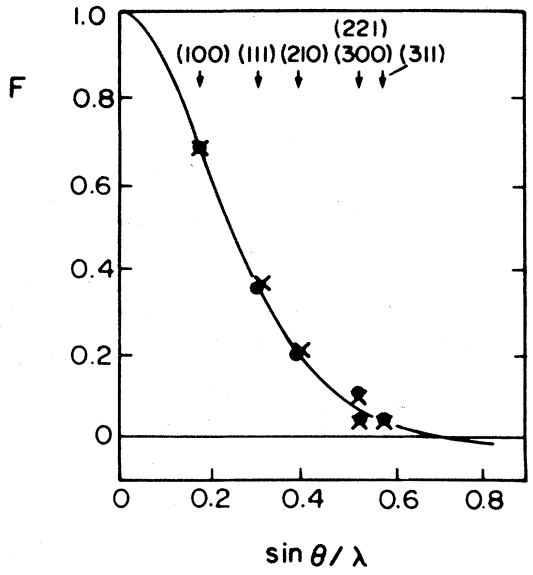

FIG. 8. The magnetic form factor $F(q)$ of Cr*Mn* for scattering vector **q** plotted vs $\sin\theta/\lambda$, θ being the Bragg angle and λ the neutron wavelength. The curve shows the spherical atomic form factor for the $3d^4 4s^2$ configuration (Freeman and Watson, 1961). ●, form factors for each magnetic reflection (identified by indices at the top of the diagram) for the nonspherical atomic configuration given in the text; ×, calculated values as described in the text (after Moon *et al.*, 1966).

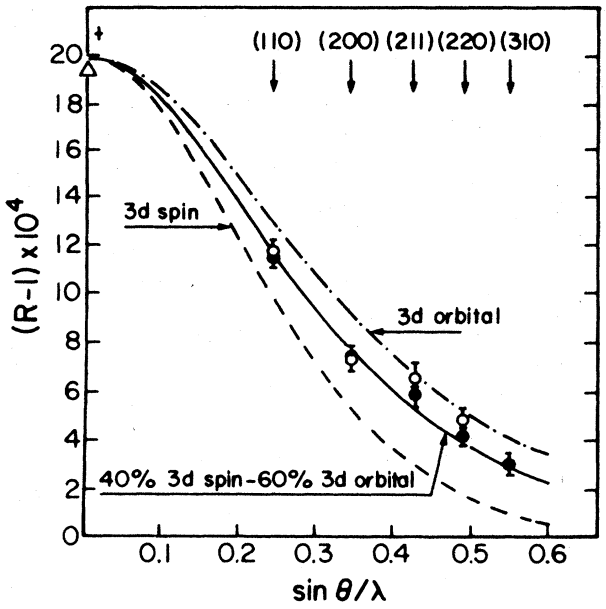

FIG. 9. The form factor of the field-induced magnetism as represented by the residual polarization ratio $R-1$ described in the text: (○, room temperature, 298 K; ●, 373 K). The dashed curve labeled "3*d* spin" shows the experimental magnetic form factor of commensurate AFM Cr*Mn* (Moon *et al.*, 1966) illustrated in Fig. 8. The dot-dashed curve labeled "3*d* orbital" shows the spherical atomic form factor calculated by Freeman and Watson (1961). The solid curve is the best fit to the experimental data with 40% 3*d* spin and 60% 3*d* orbital. The open triangle on the ordinate axis corresponds to the residual polarization ratio for the measured magnetic susceptibility, $\chi=160\times10^{-6}$ emu mol^{-1}, with an applied field $H=2.2$ T (after Stassis *et al.*, 1973).

The magnetic susceptibility obtained by extrapolating the neutron diffraction data back to zero scattering angle is $(163\pm5)\times10^{-6}$ emu mol^{-1}, a value that agrees within experimental error with the magnetic susceptibility 160×10^{-6} emu mol^{-1}, measured on the same samples, as illustrated in Fig. 9. The ratio of 40% 3*d* spin and 60% 3*d* orbital thus gives a value for the gyromagnetic ratio of Cr, $g=1.25\pm0.04$. This is in excellent agreement with the value $g=1.21\pm0.07$, obtained by Huguenin *et al.* (1971), for the gyromagnetic ratio of Cr by direct measurement of the Einstein–de Haas effect.

The worst discrepancy between the calculation of Oh *et al.* (1976) and experiment is for the static susceptibility χ. The low theoretical value, $\chi=140\times10^{-6}$ emu mol^{-1}, suggests that some paramagnetic contributions having relatively uniform spatial contribution have been neglected.

Stassis *et al.* (1973) also measured the residual polarization ratio $(R-1)$ defined in Eq. (11) for the (110) Bragg reflection at several temperatures in the interval 298–373 K and found it to be essentially independent of temperature. This is consistent with the results of paramagnetic (diffuse) scattering experiments, which also fail to reveal the presence of any intrinsic localized moments in the paramagnetic phase of Cr, as we shall describe in more detail in Sec. II.C.5.

4. Magnetic moment at zero temperature

Arrott *et al.* (1967) made a careful measurement of the amplitude of the SDW, expressed as the peak magnetic moment μ_0 per Cr atom at temperature 4.2 K (effectively zero), using a highly perfect single crystal (Werner *et al.*, 1967a). They measured the intensities of all the satellites corresponding to the three possible domains of the longitudinal SDW, and compared the total intensity with the integrated intensity of a nuclear Bragg peak. The average nuclear scattering length and the magnetic form factor for Cr being known, the absolute value of the rms moment, measured in Bohr magnetons μ_B and denoted $\langle\mu(0)\rangle$, is thus obtained. The effects of secondary extinction were checked by measuring at two wavelengths differing by a factor of about 2, the conclusion being that the values for the shorter wavelength, $\lambda=1.07$ Å, are "probably fairly reliable": $\langle\mu(0)\rangle=0.43\mu_B$ and $\mu_0=\sqrt{2}\langle\mu(0)\rangle=0.62\mu_B$. Shirane and Takei (1962) gave a value for the peak moment, $\mu=0.59\mu_B$, at temperature 78 K, which is consistent with this value of μ_0 if the temperature dependence of the intensity, shown in Fig. 3(a), is taken into account.

C. Inelastic neutron scattering: magnetic excitations

1. Spin waves in commensurate antiferromagnetic Cr*Mn*

In a review of neutron scattering experiments of itinerant-electron magnets, Windsor (1977) gave a brief account of the experimental techniques employed and summarized the experimental data for the spin-wave velocity in commensurate AFM Cr*Mn* at a reduced temperature, $T/T_N\simeq0.5$. The only available data for pure Cr (Tsunoda *et al.*, 1972) were for a temperature T above the Néel temperature T_N and, being taken by the time-of-flight technique, were difficult to interpret.

There was a good deal of interest in verifying the prediction of the Overhauser (1962) model of itinerant antiferromagnetism, which for nesting electron and hole spheres, a rough approximation to the actual nesting Fermi surface in Cr (Lomer, 1962), gave a spin-wave velocity (Fedders and Martin, 1966)

$$c=\left[\frac{v_e v_h}{3}\right]^{1/2}, \tag{12}$$

v_e and v_h being the electron and hole Fermi velocities, respectively. Since the resolution problem would be difficult to deal with for such a high spin-wave velocity, it was decided to use a commensurate AFM Cr*Mn* alloy and thereby enhance the intensity of the single commensurate AFM reflection relative to the six satellites shown

in Fig. 3(a) surrounding each magnetic reciprocal-lattice point in incommensurate AFM Cr. It was believed that the spin-wave velocity would be essentially the same in dilute Cr*Mn* alloys as in pure Cr, but, as we shall see in Sec. II.C.2, this assumption is in fact unwarranted.

The dispersion relation for nondispersive spin waves is

$$\omega = cq \ , \tag{13}$$

where ω is the angular frequency and q the magnitude of the wave vector. Thus in $(\mathbf{q},\omega)$ space spin-wave scattering occurs on a four-dimensional cone centered on each magnetic reflection with the ω axis as axis of revolution. The nature of the experimental resolution problem is illustrated in Fig. 10. The optimum fit for both values of the energy transfer,

$$\hbar\omega = \Delta E = |E_f - E_i| \ , \tag{14}$$

E_f and E_i being the final and incident neutron energies, respectively, is obtained for a value of the spin-wave velocity $c = 1.3 \pm 0.15 \times 10^5$ ms^{-1}. Thus the spin-wave dispersion is linear at small wave vectors as expected.

The results of three experimental studies are given in Table I. The measured values of the spin-wave velocity are somewhat smaller than the value, $c = 2.9 \times 10^5$ ms^{-1}, estimated by Gupta and Sinha (1971) from a band-structure calculation.

Liu (1981) has apparently resolved this discrepancy, however. He calculates the long-wavelength part of the magnon dispersion curve by a method analogous to the "frozen phonon" method for calculating lattice vibrational modes. The spin wave is regarded as setting up a static periodic spin deviation, and the increase in total energy of the electron system gives the corresponding spin-wave energy. The resultant spin-wave velocity differs from the expression given in Eq. (12) by a factor $[N(0)U]^{1/2}$, $N(0)$ being the density of states per spin of the nesting part of the Fermi surface and U an effective Coulomb function. Liu estimates this factor to be anywhere between 0.55 and 0.38 for Cr, using Kübler's (1980) calculated value, $U = 0.86$ eV, and estimating $N(0)$ to lie between 0.18 and 0.09 states/eV for each spin. When Gupta and Sinha's (1971) calculated value for the velocity is multiplied by this factor, the resultant values of c ranging from 1.6 to 1.1×10^5 ms^{-1} agree well with the experimental values given in Table I.

Sinha *et al.* (1977) also measured the spin-wave form factor, with the results illustrated in Fig. 11. A comparison with Fig. 8 shows that there is no significant difference from the static magnetic form factor. This provides experimental justification for Liu's (1981) "frozen magnon" method of calculating spin-wave velocities, since it shows that the local moment density on each ion precesses in the external field as a rigid unit. The spin-wave form factor is also essentially the same in the paramagnetic phase as in the AFM phase. The inelastic peaks centered on the magnetic reciprocal-lattice points are still well defined in the paramagnetic phase at $T/T_N = 1.12$, although somewhat broadened.

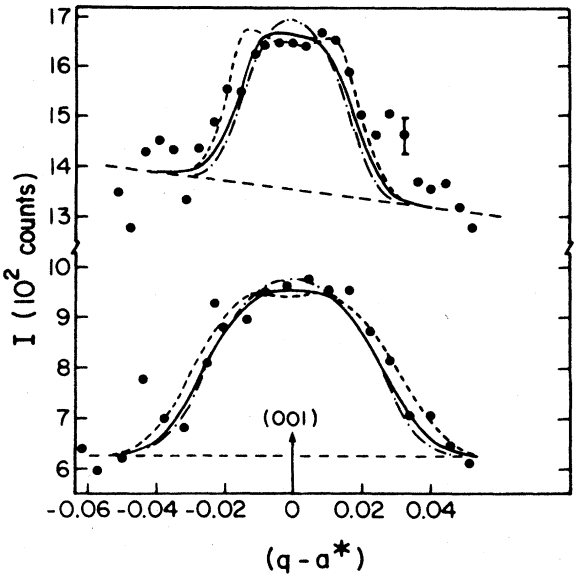

FIG. 10. Inelastic neutron scattering in the commensurate AFM Cr + 5 at. % Mn around the magnetic reciprocal lattice point (001) at reduced temperature, $T/T_N \simeq 0.5$. I is the integrated intensity for constant-ΔE scans for $E_i = 39.3$ meV, $\Delta E = 26.9$ meV (upper diagram), and for $E_i = 79.8$ meV, $\Delta E = 38.5$ meV (lower diagram). The fitted calculated curves are obtained by folding the instrumental resolution function with delta functions on the spin-wave dispersion cone for three values of the spin-wave velocity: dashed curve, $c = 1.15 \times 10^5$ msec^{-1}; solid curve, $c = 1.30 \times 10^5$ msec^{-1}; dot-dashed curve, $c = 1.44 \times 10^5$ msec^{-1} (after Sinha *et al.*, 1977).

2. Spin waves in the longitudinal and transverse spin-density-wave phases of antiferromagnetic Cr

The magnetic excitations of an itinerant SDW system such as that in AFM Cr is clearly of fundamental impor-

TABLE I. Spin-wave velocities in commensurate antiferromagnetic Cr*Mn* at reduced temperature $T/T_N \sim 0.5$.

Reference	Method	at. % Mn	c (10^5 Msec^{-1})[a]
Sinha *et al.* (1969)	Diffraction	1.6	1.3±0.26
Als-Nielsen *et al.* (1971)	Triple-axis	5	1.6±0.16
Sinha *et al.* (1977)	Triple-axis	2	1.3±0.15

[a] 10^5 msec^{-1} = 655 meV Å.

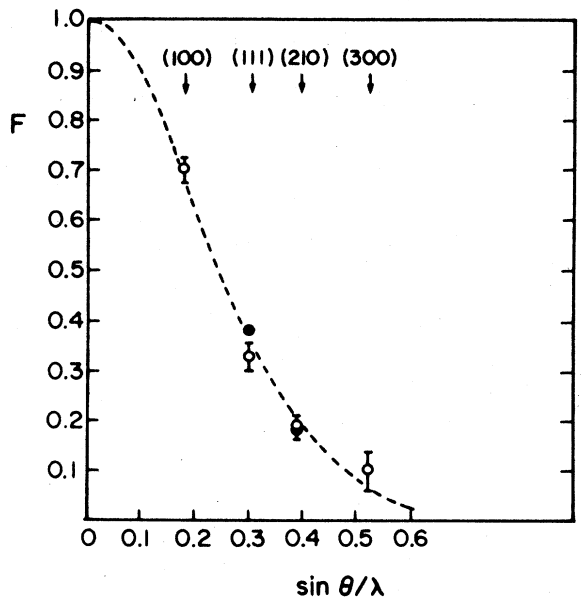

FIG. 11. Spin-wave form factor $F(q)$ in Cr + 2 at. % Mn above and below the Néel temperature. The experimental points are normalized so that the value at (100) is the same as the static magnetic form factor (Moon *et al.*, 1966). The dashed line shows the spherical atomic form factor for the $3d^4 4s^2$ configuration (Freeman and Watson, 1961). ○, reduced temperature, $T/T_N = 0.51$; ●, temperature $T/T_N = 1.12$ in the paramagnetic phase (after Sinha *et al.*, 1977).

tance in the study of magnetism. Nevertheless, only recently in experimental studies at the Brookhaven National Laboratory (Fincher *et al.*, 1979; Grier *et al.*, 1985) and at the Institut Laue-Langevin (Ziebeck *et al.*, 1982; Burke *et al.*, 1983) have we begun to see the main features of the dynamic structure over a wide temperature range, which reveal the nature of these excitations in all their rich variety. We are still far from having a detailed theoretical treatment of these effects, and some aspects of the behavior are most difficult to understand in terms of conventional theories. This should not be surprising, since the magnetic excitation spectrum in a model of commensurate Cr alloys is already quite complex (Walker, 1976), and one might expect the incommensurate system to be even more so.

Particular interest attaches to neutron scattering at the magnetic reciprocal-lattice points produced by commensurate excitations or fluctuations, i.e., by propagating or diffusive modes, respectively. This commensurate scattering was first observed by Windsor (1977) and by Mikke and Jankowska (1979), but it is thought to account for the large amount of scattering at (100) observed in the neighborhood of the Néel temperature in early elastic measurements with poor energy resolution (Wilkinson *et al.*, 1962; Møller *et al.*, 1964). This intrinsic commensurate scattering was observed in the early powder diffraction studies of AFM Cr by the appearance of a commensurate phase with a Néel temperature as high as 475 K (Shull and Wilkinson, 1953) through mechanisms discussed in Sec. VIII.A. Recent inelastic measurements (Grier *et al.*, 1985) show that so-called commensurate diffuse scattering develops in the transverse SDW phase well below the Néel temperature T_N, peaks near T_N, and thereafter decreases, but is still present in the paramagnetic phase up to the highest temperatures measured, of order $2T_N$.

There is some difficulty in the theoretical interpretation of inelastic neutron scattering in AFM Cr. The term "spin waves" is still used, but the excitations involved are clearly not simply precessional modes of localized spins as in the classical picture of transversely polarized spin waves. Critical fluctuations must occur in the neighborhood of the Néel temperature, but their effects may be difficult to disentangle from those of the so-called magnetovibrational modes of excitation, which may also be present (Burke *et al.*, 1983). Furthermore, it is not at all clear to what extent propagating modes of excitation, as opposed to diffusive modes, develop with increasing temperature. For these reasons I present in Table II a guide to the terminology used by Burke *et al.* (1983) and Grier *et al.* (1985). Table II does *not* contain any of the terms "critical fluctuations," "magnetovibrational modes," or "paramagnetic (diffuse) scattering," since while these are well-defined theoretical concepts they cannot at this stage be clearly distinguished in the experimental data.

I shall postpone consideration of commensurate diffuse scattering in the transverse SDW phase of AFM Cr until Sec. II.C.3, neutron scattering near the Néel temperature until Sec. II.C.4 and in the paramagnetic phase until Sec. II.C.5, and consider next spin waves in AFM Cr. There are two interesting features of the inelastic scattering at

TABLE II. Terminology for neutron scattering in antiferromagnetic Cr with Q‖(001).

Position reciprocal space	Magnetic reciprocal lattice points (001)	Satellites of reciprocal lattice points $(0,0,1\pm\delta)$ $(0,1,\pm\delta)$ $(1,0,\pm\delta)$
Elastic scattering	Internal strains	Incommensurate spin-density wave
Inelastic below T_N	Commensurate diffuse	Spin waves
Inelastic above T_N	Commensurate diffuse	Weak (or none)

the magnetic satellites, where spin waves are observed, whose explanation cannot be found in any of the current theories of spin waves. One of these is that with increasing energy the incommensurate peaks move in towards the commensurate positions, as illustrated in Fig. 12. The other is that the spin waves are anisotropic to a degree that depends upon the energy, becoming isotropic at sufficiently high energies in both the transverse and the longitudinal SDW phase, as illustrated for the latter case in Fig. 15 below.

Let us consider first the fact that, instead of the spin-wave dispersion law's being represented as in Fig. 13(a) by a cone centered on each magnetic reciprocal lattice point, as appears to be the case in commensurate Cr*Mn* (see Fig. 10), the spin waves in incommensurate AFM Cr appear to develop only in directions towards the commensurate positions, as illustrated in Fig. 13(b). This behavior is quite unlike that of spin waves in any other magnetic system (Burke, 1985). A spin-wave velocity may be defined by forming the ratio of the energy transfer ΔE to the shift $\Delta\delta$ of the satellite peak from its zero-energy value. This is difficult to estimate, since the intensity of the satellites decreases at higher energies, while the commensurate diffuse scattering becomes relatively stronger. The shift shown in Fig. 12 is $\pm 0.3\delta$, where $\delta = 0.047$ at temperature 130 K (Werner *et al.*, 1967a), which gives for $\Delta E = 30$ meV a value for the velocity $c = 1.5 \times 10^5$ ms^{-1}, equal within the experimental accuracy to that for commensurate Cr*Mn* (see Table I). The lower value $c = 0.7 \times 10^5$ ms^{-1} obtained by Burke *et al.* (1983), who measured the shift $\Delta\delta$ at much lower energies, $\Delta E = 6$ meV, may indicate dispersion, but probably results from experimental error in determining such a small shift.

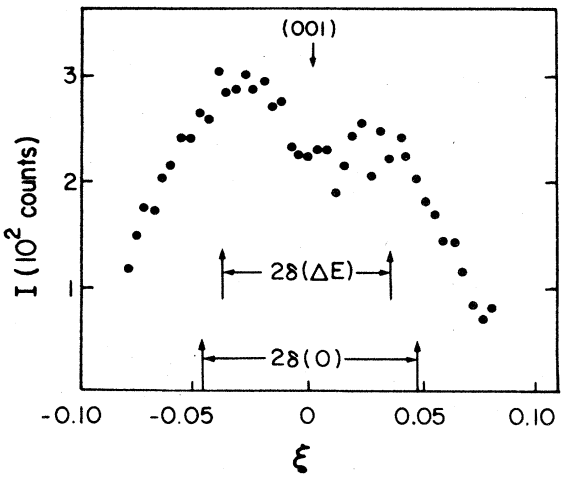

FIG. 12. Constant-ΔE scan for single-Q Cr in the transverse SDW phase at temperature 130 K; $E_i = 70$ meV and $\Delta E = 30$ meV. The wave vector ξ is measured in units of a^* relative to (001) with $\mathbf{Q} = (0,0,1\pm\delta)a^*$. The positions of the elastic peaks, separated by $2\delta(0)$, and of the inelastic peaks, separated by $2\delta(\Delta E)$, are shown (after Fincher, Shirane, and Werner, 1981).

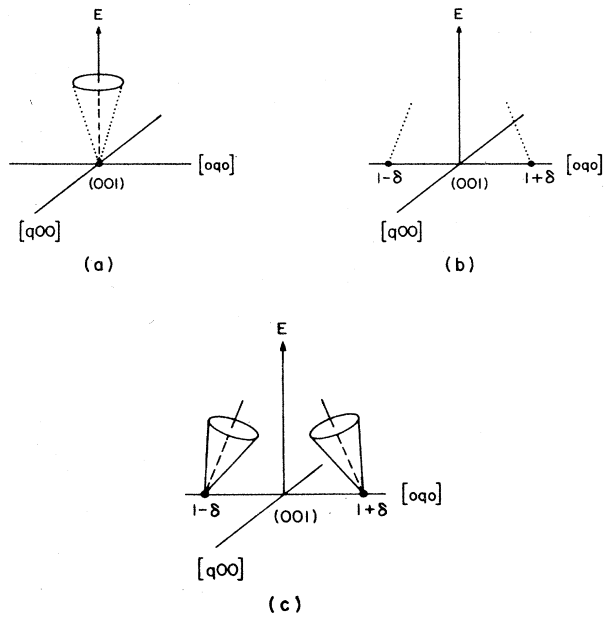

FIG. 13. Schematic diagram of the dispersion surfaces in (a) commensurate AFM Cr*Mn*: a cone emerging from the magnetic reciprocal-lattice point (001); (b) incommensurate single-Q Cr: two lines from the satellites $(0,0,1\pm\delta)$, which move inwards towards (001) (Burke, 1985); (c) an alternative picture for incommensurate single-Q Cr (Werner, 1987).

An alternative interpretation (Werner, 1987) of the data shown in Fig. 12 is illustrated in Fig. 13(c). According to this picture the axes of the cones representing the dispersion law move inwards with increasing energy. The slope of the axis is *not* the spin-wave velocity, which instead is defined by dE/dq for a section with the cone of a plane parallel to the energy axis, and is therefore anisotropic.

I turn now to the energy-dependent anisotropy of the spin waves. We are fortunate in AFM Cr in having the opportunity to measure directly the direction $\tilde{S}$ of the polarization of the spin waves (or of fluctuations of the spin **S**), since we can employ the term $\sin^2(\tilde{S} \wedge \mathbf{q})$ in Eq. (9) for the inelastic neutron scattering intensity to determine $\tilde{S}$ by comparing the intensities for different directions of **q** relative to $\tilde{S}$. Note that **S** is usually referred to as the polarization vector of the SDW, but I shall refer to it here as the spin to make clear the distinction from the unit vector $\tilde{S}$ denoting the direction of fluctuation of **S**.

This method of determining the polarization direction $\tilde{S}$ of the spin waves is illustrated in Fig. 14, in which **S** is shown for both the longitudinal and the transverse phase. In Table III is given the ratio r defined there of the integrated intensities for constant-ΔE scans through different satellites in the directions shown by the dashed lines in Fig. 14. The values of r are those to be expected for the extreme cases of longitudinal polarization of the spin waves on the one hand and transverse polarization on the other and for the intermediate case of isotropic

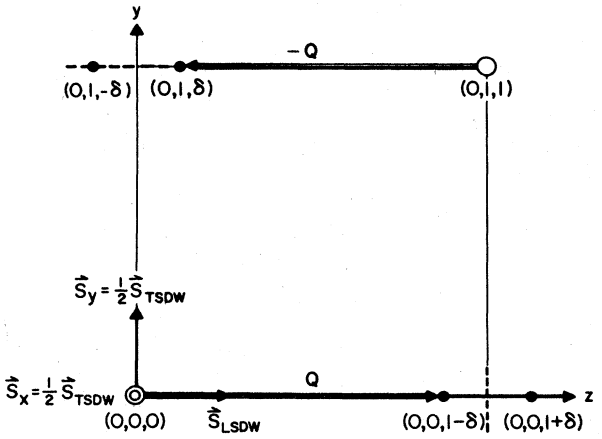

FIG. 14. Magnetic structure of single-**Q** AFM Cr in the (100) scattering plane in reciprocal space. ○, reciprocal-lattice points; ●, satellites for a SDW with wave vector **Q** along the z axis. The dashed lines show the constant-ΔE scans along which the integrated intensity is measured to construct Fig. 16. The dotted line shows the scan corresponding to Fig. 20. The solid line $\mathbf{S}_{LSDW}$ along the z axis indicates the polarization direction in the longitudinal SDW phase, while $\frac{1}{2}\mathbf{S}_{TSDW}$ along the x and y axes indicates the fact that in the transverse SDW phase one-half of the scattering intensity corresponds to polarization along each of these directions.

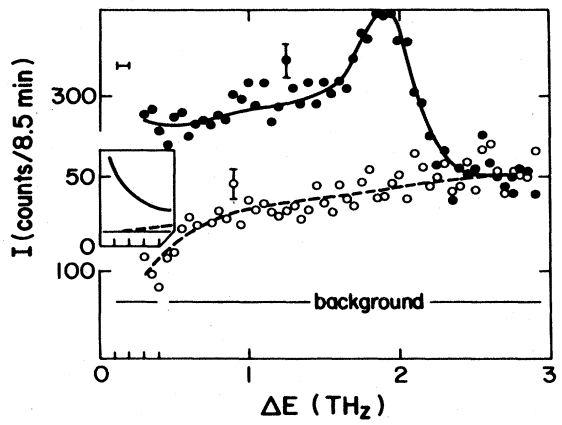

FIG. 15. Constant-**q** scans for single-**Q** Cr in the longitudinal SDW phase at temperature 55 K; $E_f = 11.6$ meV $= 2.66$ THz; ○, $\mathbf{q} = (0,0,1-\delta)$; ●, $\mathbf{q} = (0,1,\delta)$. The inset shows the results at low frequency, taken on a different instrument with $E_i = 34$ meV $= 8.2$ THz, and on the same frequency scale (1 THz $\equiv 4.14$ meV). The curves are a guide to the eye, and the background levels are shown (after Burke *et al.*, 1983).

fluctuations of the spin. The first row, longitudinal $\tilde{S} \| \mathbf{S}$, corresponds also to the intensity ratio for elastic scattering, which agrees with experiment as shown in Fig. 4(a), hence justifying the description given in Sec. II.B.1 of the two SDW phases as being longitudinal below the spin-flip temperature and transverse above.

In the longitudinal SDW phase the satellite peak at $(0,0,1-\delta)$ disappears, as shown in Fig. 4(a). Thus in constant-**q** scans the intensity approaches zero at low ΔE, as shown in Fig. 15 for the scan through this position, while the intensity increases with decreasing ΔE for the scan through $(0,\delta,1)$. At high values of the energy transfer, $\Delta E \geq 2.5$ THz, the intensities are equal, which shows that the fluctuations of the spin **S** giving rise to the inelastic scattering at these high energies are isotropic. The most interesting region is for intermediate values of ΔE, where the ratio r of the intensities is about $\frac{1}{2}$, corresponding to fluctuations that are predominantly longitudinal. The peak in the $(0,1,\delta)$ curve in Fig. 15 is believed by Burke *et al.* (1983) to be associated with magnetovibrational modes of excitation as described in Sec. II.C.4. This means that the longitudinal component $\chi_{zz}(\mathbf{q},\omega)$ of the generalized susceptibility arising from fluctuations of the amplitude, or perhaps the phase, of the longitudinal SDW is larger (by more than a factor of 2) than the transverse component $\chi_{xx}(\mathbf{q},\omega)$ for these energies. This strange behavior, which was observed by both Burke *et al.* (1983) and Grier *et al.* (1985), was said by the former to have been observed in no other well-established cases in the 3*d* metals (Burke, 1985), though longitudinal excitations in the form of propagating crystal-field modes are found in many rare-earth metals and compounds and are well understood.

In the transverse SDW phase the ratio r of intensities shown in Fig. 16 approaches at low energies the value 2 even in elastic scattering [see Fig. 4(a)], which corresponds to longitudinal polarization of the fluctuations (see Table III), while at higher energies, $\Delta E \gtrsim 0.5$ THz (2 meV), the fluctuations are isotropic.

Grier *et al.* (1985) performed very-high-resolution experiments, searching for an energy gap in the spin-wave spectrum. The results, illustrated in Fig. 17, show that there is no gap, with clear indications that the excitations persist down to at least 50 μeV, since constant-ΔE scans through this region show a peak at the magnetic satellite position. Grier *et al.* point out that this observation is surprising if one thinks in terms of a conventional spin wave in a localized-moment antiferromagnet, in which there is a gap δE in the excitation spectrum of magnitude

$$\delta E = (E_A J)^{1/2} . \tag{15}$$

TABLE III. Ratio r of integrated intensity I for constant-ΔE scans. Scans are taken through $(0,0,1\pm\delta)$ and $(0,1,\pm\delta)$ along the dashed lines as shown in Fig. 14 for different polarizations $\tilde{S}$ of spin waves (relative to spin direction **S**) and of **S** (relative to wave vector **Q**). Values are given for $r = I(0,0,1\pm\delta)/I(0,1,\pm\delta)$ for the three cases given in the first column.

Polarization of $\tilde{S}$ relative to spin **S**	Longitudinal SDW **S**∥**Q**	Transverse SDW **S**⊥**Q**
Longitudinal $\tilde{S} \| \mathbf{S}$	0	2
Transverse $\tilde{S} \perp \mathbf{S}$	2	$\frac{2}{3}$
Isotropic	1	1

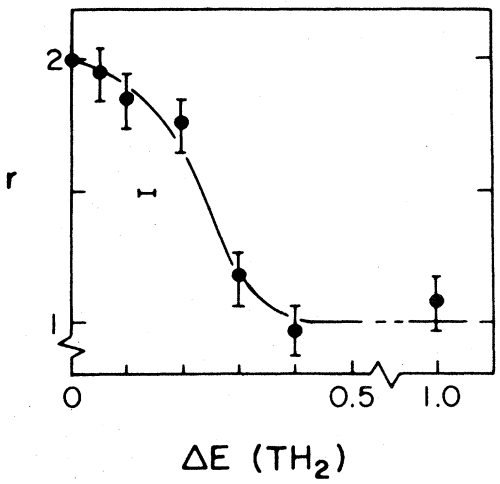

FIG. 16. Ratio r of integrated intensity I as defined in Table III for constant-ΔE scans in the transverse SDW phase at temperature 145 K. $I(0,0,1\pm\delta)$ and $I(0,1,\pm\delta)$ are measured for scans parallel to the y axis and z axis, respectively, as shown by the dashed lines in Fig. 14 (after Burke *et al.*, 1983).

Since the spin-wave velocity is so high, the effective exchange parameter J will be large. We know that the anisotropy energy E_A is large from magnetic torque measurements (Steinitz *et al.*, 1972: see Sec. III.A). However, this model is inappropriate, since in an incommensurate system one expects Goldstone modes to be excited at long wavelengths, giving a continuous excitation spectrum down to zero energy at the elastic scattering position.

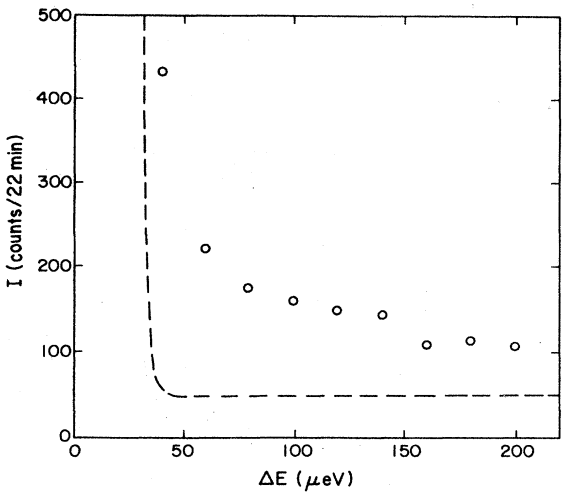

FIG. 17. Lack of evidence for an energy gap in the spin-wave spectrum in the transverse SDW phase: high-resolution (20 μeV) constant-**q** scan for single-**Q** Cr at (0,0,0.958) at temperature 270 K, $E_i=3.8$ meV. The dashed line shows the instrumental background (after Grier *et al.*, 1985).

The excitations in AFM Cr that I have referred to for convenience as "spin waves" have remarkable features, which would seem to need a new theoretical approach for their understanding. Essentially nothing is known, either experimentally or theoretically, about the phase fluctuations of the incommensurate SDW ground state of itinerant-electron systems, though phase fluctuations of charge-density waves leading to elementary excitations called phasons have attracted considerable attention, starting with their theoretical prediction by Overhauser (1971). Grier *et al.* (1985) suggest the following possible modes of excitation of the static SDW in AFM Cr:

(1) *ordinary spin waves,* which can be viewed classically as precessional modes of the 3*d* atomic moments;
(2) *amplitude modes,* for which the amplitude of the SDW fluctuates;
(3) *plason modes,* for which the phase of the SDW as a whole fluctuates, or for which the relative phase of the spin-up and spin-down electron densities fluctuate. This relative phase fluctuation would give rise to dynamic charge-density waves.

The relative importance of these three types of excitations in Cr is not known at all at the present time. There is no reason to suppose that these various modes are independent, or even propagating.

3. Commensurate diffuse scattering in the transverse spin-density-wave phase

The evolution with temperature of commensurate diffuse scattering in the transverse SDW phase is illustrated in Fig. 18. Grier *et al.* (1985) distinguish between the quasielastic background, which increases very rapidly with decreasing energy transfer ΔE (hence the description as "quasielastic") and also with increasing temperature as T approaches the Néel temperature T_N (see Grier *et al.*, 1985, Fig. 5), and the 4-meV excitation, which was first seen by Fincher *et al.* (1979) and which Burke *et al.* (1983) believe to be associated with magnetovibrational modes of excitation. There is also some indication in Fig. 18 at temperature 290 K of an excitation at energy 8 meV, which was seen as well by Burke *et al.* (1983, Fig. 2).

The quasielastic component appears to be diverging at the Néel temperature, and in fact it increases exponentially with temperature over a wide range, as shown in Fig. 19. The intensity of the 4-meV excitation, obtained by subtracting the sloping quasielastic background scattering shown by the dashed lines in Fig. 18, increase gradually with temperature, in rough accord with a Bose thermal factor.

This commensurate diffuse scattering appears to be characteristic of the transverse SDW phase, where it develops with increasing temperature before continuing into the paramagnetic phase as discussed in Sec. II.C.5. Fincher, Shirane, and Werner (1981) emphasize that the

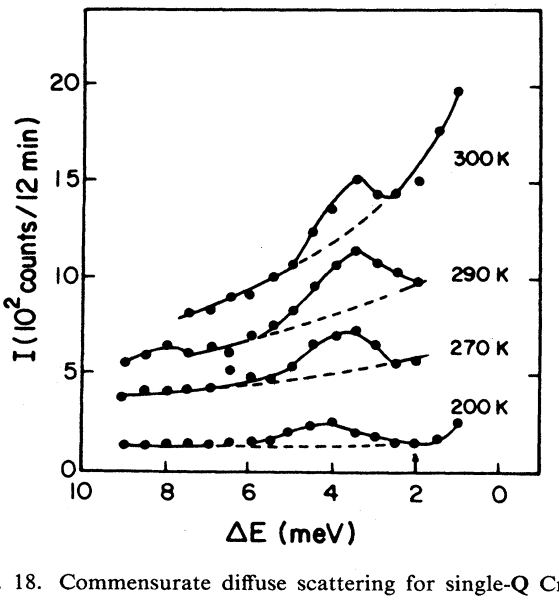

FIG. 18. Commensurate diffuse scattering for single-Q Cr in the transverse SDW phase: constant-q scans at (001) for several temperatures. The dashed lines are a guide to the eye intended to distinguish the "4-meV excitation" from the "quasielastic background" component of the scattering. The arrow shows the energy transfer, $\Delta E = 2$ meV, at which the temperature dependence was measured, as shown in Fig. 19 (after Fincher *et al.*, 1979).

commensurate diffuse peak at (001) disappears between temperature $T = 130$ K, in the transverse SDW phase, and $T = 115$ K in the longitudinal SDW phase, for an energy transfer $\Delta E = 4$ meV (Fincher, Shirane, and Werner, 1981, Fig. 4).

On the other hand, Booth and Ziebeck (1981) found at

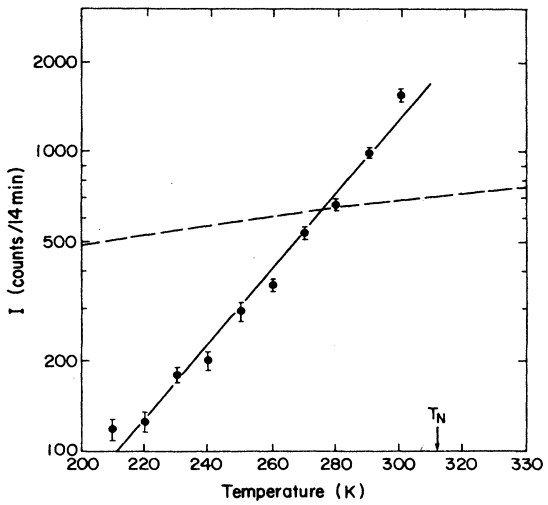

FIG. 19. Temperature dependence of commensurate diffuse scattering at (001) with energy transfer $\Delta E = 2$ meV, as indicated by the arrow in Fig. 18. The dashed line shows the temperature dependence of the Bose thermal factor $[1-\exp(-\Delta E/k_B T)]^{-1}$ for comparison (after Grier *et al.*, 1985).

$T = 4.2$ K a commensurate diffuse peak at (001) and no spin-wave peaks at $(0,0,1\pm\delta)$ for inelastic scans along [001] at $\Delta E = 2$ THz (8 meV). The low-energy behavior in the longitudinal SDW phase at $T = 4.2$ K is indeed difficult to understand. Booth and Ziebeck (1981) used a cylindrical single-crystal sample, which, while being too large to field cool satisfactorily, was found to be almost a single domain with Q along the [001] cylinder axis. They found, as expected in the longitudinal SDW phase, no elastic scattering for a scan along [001] (the dotted line in Fig. 14), but inelastic scattering peaks at the satellite positions in the range $\Delta E = 0.5-1.0$ THz (2–4 meV), and a single commensurate diffuse peak for higher-energy transfers, $\Delta E > 1$ THz (4 meV). The latter result contrasts with the observations of Fincher, Shirane, and Werner (1981, Fig. 6), who found evidence at $T = 115$ K, still in the longitudinal SDW phase, for spin-wave scattering at the satellite positions for energy transfers as large as $\Delta E = 30$ meV.

Grier *et al.* (1985) searched for effects of a magnetic field up to 6 T on the inelastic neutron scattering, but found none. They paid particular attention to the commensurate diffuse scattering, since they expected that this scattering might be related to excitations associated with rotation of the polarization direction **S** of the SDW in the plane transverse to the wave vector **Q**. As described in Sec. II.B.2, a field **H** applied perpendicular to **Q** tends to rotate **S** into a direction perpendicular to both **H** and **Q**. This effect can be monitored by observing the decrease in intensity of the $(0,1,\delta)$ satellite as the field H_x is increased in a Q_z sample, and Grier *et al.* (1985) found that in their sample a field $\mathbf{H} = 2$ T produced a decrease to about 15% of the zero-field value, indicating that **S** is essentially along the y axis in the scattering plane (see Fig. 14). Nevertheless, within the experimental accuracy, there was no apparent effect on the commensurate diffuse scattering at temperature 270 K, the scattering as a function of energy transfer ΔE being essentially the same as the 270-K curve in Fig. 18 both with and without the field. Since the field-induced rotation of the polarization direction is essentially reversible and strongly temperature dependent (see Sec. II.B.2), the lack of a measurable effect is surprising. Grier *et al.* (1985) speculate that only very-low-energy excitations, far below 1.5 meV, might be affected by a magnetic field. This result has significant implications for the thermal activation model of polarization domains, as we shall see in Sec. VIII.C.

Windsor (1977) and Ziebeck and Booth (1979) had found, in experiments up to much higher energy transfers, that scattering at the incommensurate satellites disappears and the scattering cross section evolves with increasing energy into a single diffuse bell-shaped curve centered at (001). Grier *et al.* (1985) noted that this effect was more pronounced at higher temperatures in the transverse SDW phase. It was already noted in Sec. II.C.2 that with increasing energy transfer the spin-wave peaks move inward towards the commensurate (001) position. The surprising feature of this behavior, which is

not at all understood theoretically, is that the commensurate diffuse mode overwhelms the incommensurate ordered structure of AFM Cr as the temperature approaches the Néel transition T_N. One should make further studies of the temperature dependence of these modes at considerably lower energies near T_N.

Burke *et al.* (1983) believe that magnetovibrational modes of excitation are responsible for some aspects of the commensurate diffuse scattering. Their evidence for the existence of these modes is shown in Figs. 20 and 21. The novel feature of Fig. 20 that had not appeared in previous published data (Fincher, Shirane, and Werner, 1981, Fig. 2) is the evolution of the three-peak structure at 1 THz into four peaks in scans at 1.35 and 1.5 THz. The evidence for the outer pair of the five peaks at 1.0 THz, which are plotted in Fig. 21, is not provided in Fig. 20, but Stirling (1985) asserts that these peaks exist in unpublished data.

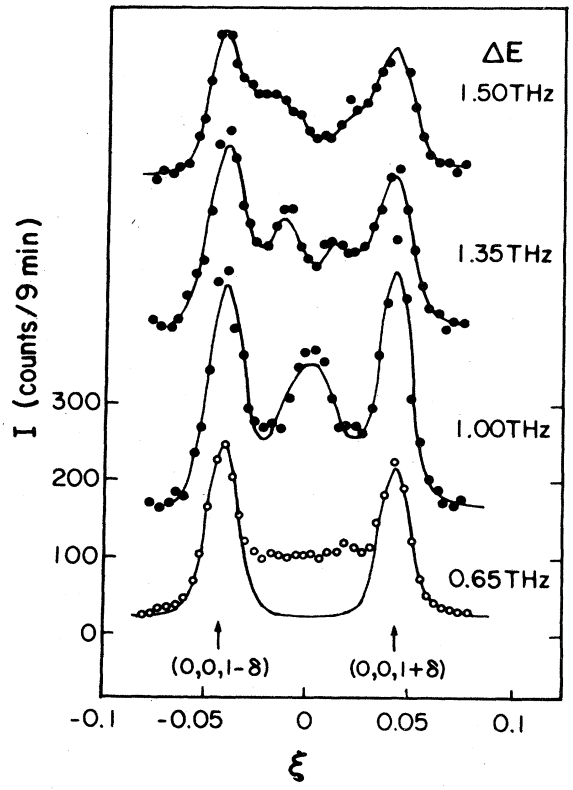

FIG. 20. Constant-ΔE scans along the dotted line in Fig. 14 for single-Q Cr in the transverse SDW phase at temperature 230 K. The positions of the elastic peaks $(0,0,1\pm\delta)$ are shown and the wave vector is measured in units of a^* relative to (001). The solid curves show fits to the data with Gaussian profiles. The intensity I is shown by the ordinate scale, appropriately displaced for each curve, for the energy transfer ΔE (1 THz=4 meV) indicated. All the data were taken with $E_i=2.66$ THz, except the bottom curve, $\Delta E=0.65$ THz, which was measured with $E_F=2.66$ THz. The intensity for this curve has been reduced by a factor of 5 for comparison with the others (after Burke *et al.*, 1983).

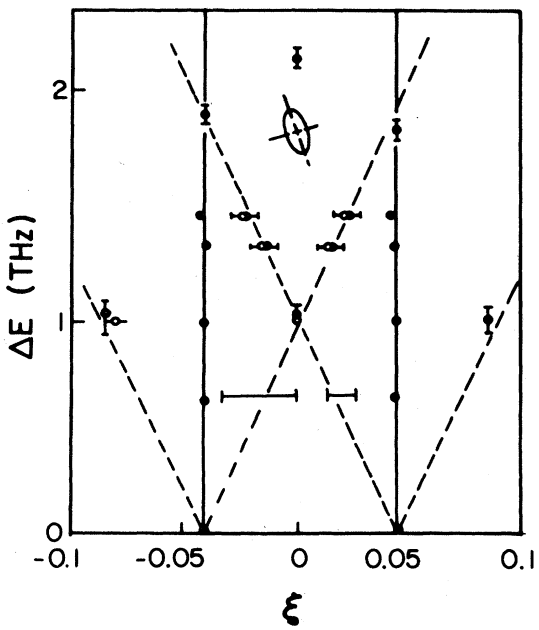

FIG. 21. The dispersion relations corresponding to the scattering peaks seen in Fig. 20. The peaks at $\Delta E=1$ THz (4 meV) outside the interval between the satellites $(0,0,1\pm\delta)$, i.e., outside the range of the constant-ΔE scan of Fig. 20, are very weak (Stirling, 1985). ●, $E_f=2.66$ THz; ○, $E_i=2.66$ THz. The projection of the resolution ellipsoid for $E_f=2.66$ THz is shown (after Burke *et al.*, 1983).

When these peaks are plotted as in Fig. 21, we see not only the usual spin-wave dispersion relation shown by the solid lines (which slowly move inward with increasing energy, giving a spin-wave velocity $c=0.7\times10^5$ ms^{-1}, as discussed above), but also the dashed lines which correspond to a much smaller velocity, $c=6.6\pm0.3\times10^3$ ms^{-1}, the same within experimental accuracy as the longitudinal-acoustic phonons in Cr along [100] (Shaw and Muhlestein, 1971).

Magnetovibrational modes have been proposed by Marshall and Lovesey (1971). They give rise to elastic scattering in the spin system but inelastic in the phonon system, and Burke *et al.* (1983) point out that they represent no more than the longitudinal-acoustic phonon viewed through magnetic interactions with the neutron.

4. Neutron scattering near the Néel temperature

As we shall see in Sec. III, the strong dependence of the Néel temperature T_N of Cr on strain results in smearing of the Néel transition in measurements of physical properties such as specific heat, thermal expansion, electrical resistivity, etc., in samples having inhomogeneous internal stresses. We shall see in Sec. VIII.A that in severely cold-worked samples the defect structures can result in the persistence of antiferromagnetism in the

form of a commensurate AF_0 phase well above T_N.

With this in mind, Grier *et al.* (1985) made careful measurements on two crystals prepared by quite different methods to see by comparison the extent to which sample quality might affect their data. The results appear to be satisfactory, and the elastic scattering data just above T_N shown in Fig. 22, which are plotted in Fig. 23 along with similar data in the vicinity of T_N, are thought to be close to the intrinsic behavior of Cr. From these elastic scattering studies we conclude that some short-range order of the spins persists above T_N, with the elastic peaks broadening and finally disappearing only at about 325 K. The width of the peak in Fig. 22 gives a coherence length of about 1000 Å at 315 K.

The inelastic scattering data near T_N are too fragmentary to give a full description of the critical fluctuations. However, Grier *et al.* (1985) have made constant-energy scans for $\Delta E = 4$ meV from a temperature 311 K just below T_N up to 700 K, with the results shown in Figs. 24 and 25, which we shall discuss further in Sec. II.C.5. For this energy transfer the integrated intensity continues to increase, until it peaks at about 10 K above T_N. For similar constant-ΔE scans, as the energy transfer ΔE increases, the integrated intensity peaks at temperatures still further above T_N.

Two interesting but unconfirmed features of the inelastic neutron scattering in Cr near T_N have been reported. Booth *et al.* (1979, Fig. 1) found an abrupt increase in the intensity of the commensurate diffuse peak at (001) for a constant (unspecified) energy transfer, as temperature T increased through the Néel transition to a value at $T \sim 350$ K more than a factor of 2 greater than that at $T = 300$ K. Ziebeck and Booth (1979, Fig. 2) found at $T = 295$ K a decrease in the integrated intensity of the

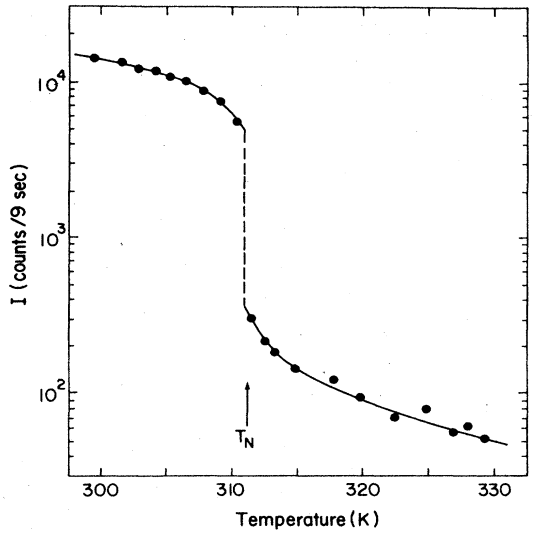

FIG. 23. Temperature dependence of elastic scattering in single-Q Cr at the satellite $(0,0,1-\delta)$ near the Néel temperature T_N (after Grier *et al.*, 1985, from data of Werner *et al.*, 1967a).

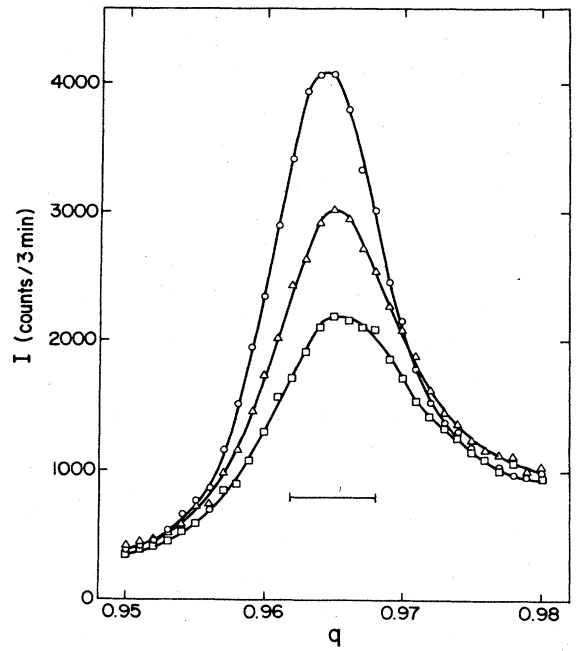

FIG. 22. Elastic scans ($\Delta E = 0$) through the satellite $(0,0,1-\delta)$ in single-Q Cr at three temperatures just above T_N: ○, 313 K; △, 316 K; □, 318 K. The scan direction is shown by the dotted line in Fig. 14. The horizontal bar shows the instrumental resolution (after Grier *et al.*, 1985).

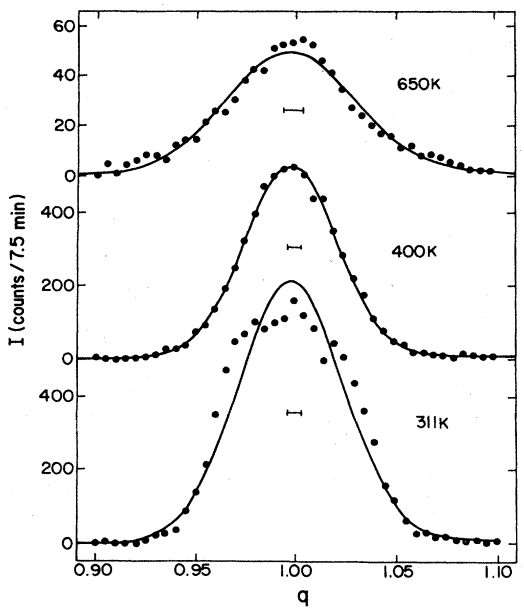

FIG. 24. Inelastic scans ($\Delta E = 4$ meV) through the commensurate position (0,0,1) just below T_N at two temperatures in the paramagnetic phase of a Cr single crystal. The instrumental resolution is shown for each temperature. The scan direction is shown by the dotted line in Fig. 14 (after Grier *et al.*, 1985).

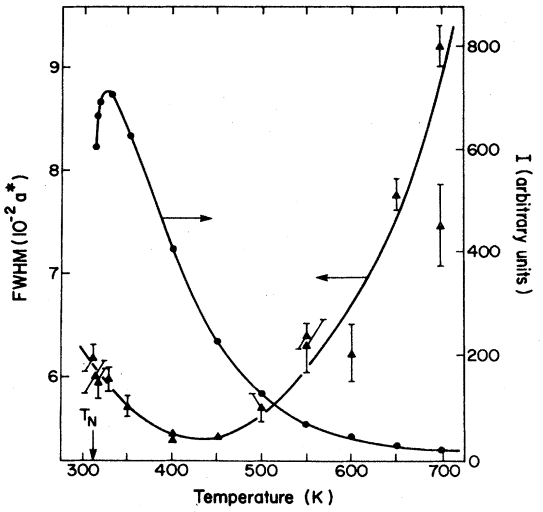

FIG. 25. Temperature dependence of the integrated intensity I and full width at half maximum (FWHM) for inelastic scans ($\Delta E = 4$ meV) similar to those shown in Fig. 24. The FWHM values, which are equal to 2.35σ, were determined by fitting Gaussians to the constant-ΔE scans centered at (001) and convoluting with the instrumental resolution (after Grier *et al.*, 1985).

(001) peak, beginning at energy transfer $\Delta E = 6.5$ THz (27 meV) and continuing up to the highest energies measured, $\Delta E = 18.5$ THz (76 meV), where the intensity is reduced by about an order of magnitude. The integration is made over the wave vector through the commensurate peak, the incommensurate satellite peaks at $T = 295$ K having already disappeared into the central peak for energy transfer, $\Delta E = 1$ THz (4 meV), as reported by Booth and Ziebeck (1981), who point out that the full width at half maximum of the central peak for this value of ΔE is less than the spacing between the satellites for $\Delta E = 0$ (the Bragg peaks).

These authors claim that both features of the inelastic neutron scattering are connected with the energy gap predicted by the nesting model for antiferromagnetism in Cr (see Sec. IV.A.1) and observed in infrared experiments (see Sec. V.C). However, the connection is not clear between this behavior and what one might expect to be associated with an AFM energy gap. Furthermore, these two features were not apparent in the work of Grier *et al.* (1985). It would seem that the inelastic neutron scattering in the neighborhood of the Néel transition in Cr should be explored in much greater detail.

Let us turn now to a consideration of the change in the magnetic moment at the first-order transition at $T_N \simeq 311$ K. The change in the elastic scattering at the transition is shown in Fig. 23. The data were obtained by Werner *et al.* (1967a), who first produced clear evidence that the transition is indeed first order (Arrott *et al.*, 1965). The jump in the Bragg intensity at T_N is 7800 counts, which is to be compared with 107 000 counts at zero temperature, as illustrated in Fig. 4(a). Thus the rms ordered moment per Cr atom $\langle \mu(T_N^-) \rangle$ at a temperature T_N^- just below T_N, if we assume $\langle \mu(T_N^+) \rangle$ to be zero, is $\langle \mu(T_N^-) \rangle = (7.8/107)^{1/2} \langle \mu(0) \rangle = 0.116 \mu_B$ with $\langle \mu(0) \rangle = 0.43 \mu_B$ being the rms ordered moment at zero temperature (see Sec. II.B.4).

The evaluation of the first-order change $\Delta\mu(T_N)$ in the thermal and spatial average moment $\langle\langle \mu^2(T) \rangle\rangle^{1/2}$, which we shall denote simply $\mu(T)$, is much more difficult. Grier *et al.* (1985) call this the effective moment, denoted μ_{eff}, and calculate it from their inelastic neutron scattering data by integration over wave vector and energy as described in the next section. In theoretical terms $\mu(T)$ may be regarded as an ensemble average.

Werner (1987) describes the nature of the problem in determining $\Delta\mu(T_N)$ as follows. At T_N^- an estimate of μ would involve integrating the dynamic structure factor $S(\mathbf{q},E)$ obtained from inelastic neutron scattering data over wave vector $\mathbf{q}$ and energy E, so as to include the spin-wave scattering at the satellite positions and the commensurate diffuse scattering at (001). This has not been done, since there are not sufficient experimental data, and in particular the anisotropy of the fluctuations of the polarization vector is not known. At T_N^+ the estimation of μ is still difficult, because the simple form of the dynamic structure factor given in the next section in Eq. (16) is only an approximation to the true scattering.

5. Neutron scattering in the paramagnetic phase

There is great current interest in the problem of understanding how magnetic metals disorder with increasing temperature and the nature of magnetic fluctuations above the ordering temperature. As we have seen, the disappearance of the long-range incommensurate order at the Néel transition seems to be dominated by the commensurate diffuse mode. In the paramagnetic phase the scattering continues to be confined to the region around the commensurate position (001). It is important to make a clear distinction between this scattering, which as we shall see corresponds to magnetic correlations over a roughly isotropic region of dimensions about 30 Å, and "paramagnetic scattering," which usually refers to scattering by disordered local spins and therefore corresponds to a correlation length of about 3 Å. To avoid confusion I shall refer to the latter as "paramagnetic (diffuse) scattering," since such a short correlation length corresponds to a diffusive mode. I shall continue to refer to the former as "commensurate diffuse scattering," following the usage of Grier *et al.* (1985), although a correlation length as large as 30 Å might be thought enough to sustain propagating modes.

The inelastic scattering illustrated in Fig. 24 for an energy transfer $\Delta E = 4$ meV, already at 311 K, just below the Néel temperature T_N, shows little evidence of incommensurate order. With increasing temperature the scattering evolves into a single Gaussian-shaped peak. The data cannot be fit to a Lorentzian function at any

temperature, but above about 350 K the Gaussian fits are excellent. The linewidth is not monotonic with temperature, but reaches a minimum about 100 K above T_N, as shown in Fig. 25, a result independent of fitting procedure.

Grier *et al.* (1985) have not studied the temperature dependence of the inelastic scattering at other energies in such detail, but conclude on the basis of their available data that, at all temperatures and energy transfers, the scattering remains confined to a region close to (001). The scattering is isotropic about (001), dropping to near zero outside a sphere of radius $0.1a^*$. As the energy transfer is increased, the intensity peaks at temperatures further removed from T_N. The temperature dependence of the spectral distribution of magnetic intensity at $\mathbf{q}=(001)a^*$ is shown in Fig. 26. The scattering extends over a progressively wider energy range as the temperature is raised. These data are consistent with the polarization analysis measurements of Ziebeck *et al.* (1982), from which it was concluded that most of the magnetic scattering fell within their experimental energy window of about 50 meV. The solid lines in Fig. 26 are the result of fitting the data to a resolution-broadened Lorentzian. Corrections for background, the thermal population factor, and energy-dependent beam size effects were made in fitting the data. At temperatures somewhat removed from T_N, in the paramagnetic phase, the magnetic scattering cross section can be adequately described by the product of a Gaussian in momentum space centered at (001)—and equivalent positions—and a Lorentzian in energy. Thus the dynamic structure factor defined in Eq.

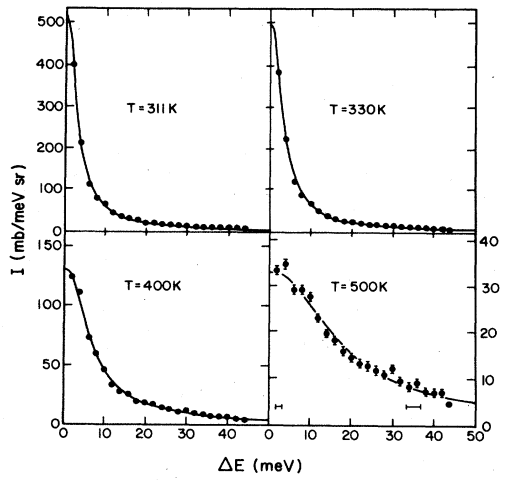

FIG. 26. Intensity as a function of energy transfer ΔE for $E_f=30.5$ meV at $\mathbf{q}=(0,0,1)a^*$ at the Néel temperature, $T_N=311$ K, and three temperatures in the paramagnetic state of Cr. The lines are resolution-broadened Lorentzian fits to the data and correspond to widths Γ given in Table IV with $\Gamma=3.2\pm0.2$ meV at $\Gamma=311$ K (after Grier *et al.*, 1985).

TABLE IV. Lorentzian width Γ and effective moment μ [the ensemble average $\langle\langle\mu^2\rangle\rangle$ denoted μ_{eff} by Grier *et al.* (1985)] at three temperatures in the paramagnetic state of Cr.

T (K)	Γ (meV)	μ (μ_B)
330	3.6(2)	0.28(3)
400	6.7(4)	0.18(2)
500	15.6(9)	0.16(2)

(10) takes on the form

$$S(\mathbf{q},\hbar\omega)=S_0(T)e^{-\xi^2/2\sigma^2}\frac{1}{(\hbar\omega)^2+\Gamma^2}\frac{\hbar\omega/k_BT}{1-e^{-\hbar\omega/k_BT}}\ , \tag{16}$$

where the last factor is the Bose thermal population number. The experimental data in Fig. 25 show that the Gaussian width σ varies only slowly with temperature T, whereas Fig. 26 and Table IV show that the Lorentzian width Γ increases rapidly with T.

Grier *et al.* (1985) put the data of Fig. 26 on an absolute scale, expressing the intensity as a scattering cross section in units of mb/meV sr atom, by normalizing to the integrated intensity of selected phonons with appropriate resolution corrections. They were thus able to evaluate the square of the wave-vector-dependent magnetic moment $|m(\Delta\mathbf{q})|^2$ at $\Delta\mathbf{q}=0$ [with $\Delta\mathbf{q}\equiv\xi=\mathbf{q}-(0,0,1)a^*$], denoted $|m(0)|^2$, by means of the equation

$$f^2(\Delta\mathbf{q})|m(\Delta\mathbf{q})|^2=\int S(\Delta\mathbf{q},\hbar\omega)d(\hbar\omega)\ , \tag{17}$$

where $f(\Delta\mathbf{q})$ is the magnetic form factor, having the value $f(0)\equiv f(100)=0.69$. The effective moment $\mu(T)$ referred to in the preceding section is then obtained by integrating the magnetization surrounding each atom over the atomic volume $a^3/2$, which gives

$$\mu(T)=\frac{1}{\sqrt{2}}\left[\frac{\sigma a}{\sqrt{2\pi}}\right]^{3/2}|m(0)|\ . \tag{18}$$

Grier *et al.* (1985, Table I) found σ to be a slowly varying function of energy transfer, $\Delta E=\hbar\omega$, and used in Eq. (18) the value for $\Delta E=4$ meV obtained by fitting data like those shown in Fig. 24 to the Gaussian form of Eq. (16). The integration over energy, as in Eq. (17), of the data shown in Fig. 26, then gave the values of $\mu(T)$ listed in Table IV.

Grier *et al.* (1985) found no evidence at any temperature for "ordinary paramagnetic scattering resulting from single $3d$ magnetic atoms," i.e., paramagnetic (diffuse) scattering extending over large regions of reciprocal space and having a maximum at the origin. This is consistent with the early results of Wilkinson *et al.* (1962), who performed a very careful experiment, measuring the diffuse scattering from polycrystalline Cr at temperatures of 518 and 706 K and comparing it with scattering at the same angles with the sample in the lon-

gitudinal SDW phase at 86 K. The sample was isotopically enriched so as to eliminate entirely isotopic incoherent and nuclear spin incoherent scattering, and the observed diffuse scattering was corrected for background and thermal diffuse scattering; for the calculated thermal corrections the Debye temperature was established from measurements of the nuclear reflections between 706 and 86 K. The absolute values of the residual diffuse scattering were found to be very small, but by no means negligible. Wilkinson *et al.* performed rough calculations of multiple nuclear Bragg scattering to show that this would account for this residual diffuse scattering. However their conclusion that "localized atomic magnetic moments do not exist above the Néel temperature" was based on the facts that the residual diffuse scattering was the same in the paramagnetic state as in the AFM state and that its angular variation was much less than that for a $3d$ magnetic form factor.

Ziebeck *et al.* (1982) measured the diffuse scattering at three temperatures, 367, 474, and 700 K, in the paramagnetic state using polarized neutrons. Their polarization analysis eliminated essentially all nonmagnetic incoherent scattering, but the energy resolution was very poor. They made a careful study of diffuse scattering at temperature 367 K by making a series of elastic scans at points throughout the Brillouin zone and found significant scattering only in the vicinity of the commensurate position (100). This commensurate diffuse scattering was found to be isotropically distributed about (100). The discrepancy between its absolute value and the results of Grier *et al.* (1985) was discussed above.

I have presented in some detail the available evidence, which seems to support the early conclusion of Wilkinson *et al.* (1962) that there is essentially no paramagnetic (diffuse) scattering in Cr, since the question is of importance in relation to modern theories of metallic magnetism.

It is interesting to compare the commensurate diffuse scattering in Cr with inelastic neutron scattering in the paramagnetic phase of a ferromagnet. The width Γ of the commensurate diffuse scattering is very much greater than that in Ni_3Al, for example, where it is of the form

$$\Gamma(q)=\gamma q(\chi^{-1}+cq^2)\ , \tag{19}$$

approaching zero in the forward scattering direction, i.e., $\mathbf{q}=0$ (Bernhoeft *et al.*, 1986). The reason for this qualitatively different behavior is that in a ferromagnet, unlike an antiferromagnet, the magnetization is a constant of motion.

The form of Eq. (19) corresponds to the relaxation frequency of spin fluctuations in the random-phase approximation, with χ the static magnetic susceptibility. The parameters γ and c feature in the spin-fluctuation model of Lonzarich (1986a), which employs band-structure data and two additional parameters from the magnetic equation of state to determine the Curie temperature T_C and several other characteristic properties of weak itinerant ferromagnets. Typically T_C is much smaller than the Stoner temperature T_0 (e.g., in Ni_3Al, $T_0=300$ K, while $T_C=41$ K), the Curie temperature being depressed by spin fluctuations. It is thought that in Cr, corresponding to the high value of the relaxation frequency Γ, spin fluctuations play a much smaller role, which accounts for the relatively high value of the Néel temperature, in view of the small value of the mean-square moment (Lonzarich, 1986b).

D. Spin-density-wave harmonics, strain wave, and charge-density wave

The strain wave associated with the SDW in chromium was first observed by Tsunoda *et al.* (1974) using x-ray diffraction. Young and Sokoloff (1974) had pointed out that a second-harmonic charge-density wave (CDW) should accompany the incommensurate SDW through electron-phonon interactions, and this in turn should generate a strain wave, i.e., a periodic lattice distortion. Tsunoda *et al.* were motivated, however, to look for the second-harmonic strain wave by a theory of exchange striction in transition-metal alloys (Teraoka and Kanamori, 1978). We note that the strain wave corresponds to atomic displacements and should be seen by both neutrons and x rays, whereas the CDW will give rise to negligibly small neutron-diffraction intensity. It is interesting to note that the strain wave has been seen in electron diffraction (Prekul and Sudareva, 1978).

The Bragg peaks corresponding to elastic scattering by the strain wave and CDW will be seen as even-harmonic satellites of the nuclear (ionic) Bragg peaks. If we suppose their period to correspond to that of the SDW and adopt the usual convention that the wave vector $\mathbf{Q}$ of the SDW is directed along the z axis, the Bragg peaks due to the strain wave and CDW having wave vector $2p\mathbf{Q}$ will occur at positions in reciprocal space

$$(h,k,l\pm 2p\delta)a^* \quad \text{with } h+k+l=2n \qquad (n \text{ integral})\ , \tag{20a}$$

where $2p$ is the even-harmonic number (p integral). On the other hand, as we have seen in Fig. 3, the Bragg peaks due to the SDW and its odd harmonics will be seen as satellites of the points in reciprocal space having zero structure factor for a bcc Bravais lattice, which occur at positions

$$(h,k,l\pm(2p+1)\delta)a^* \quad \text{with } h+k+l=2n+1 \qquad (n \text{ integral})\ , \tag{20b}$$

where $2p+1$ is the odd-harmonic number. Figure 27 shows the structure of AFM Cr in the (100) scattering plane in reciprocal space with those harmonics that have been observed to date, namely, the second-harmonic strain wave and CDW and the third-harmonic SDW (Pynn *et al.*, 1976).

Neutron-diffraction measurements by Pynn *et al.* (1976) on a large single crystal, field cooled in a magnetic field of 12 T to give a 90% single-$\mathbf{Q}$ sample, enabled a

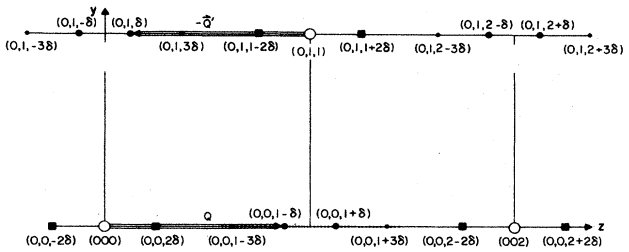

FIG. 27. Structure of single-Q AFM Cr in the (100) scattering plane showing the positions of the Bragg peaks due to ○ nuclear (i.e., ionic) diffraction seen by neutrons and x rays; ●, fundamental SDW and • third-harmonic SDW seen by neutrons; ■ second-harmonic strain wave (SW) seen by x rays and neutrons [and charge density wave (CDW) seen only by x rays]. The strain-wave peaks $(0,0,\pm 2\delta)$ and the third-harmonic peaks $(0,1,2\pm 3\delta)$ have not yet been observed. The dotted line through the satellites around (001) corresponds to the scan of Fig. 33.

comparison to be made between the strain wave of wave vector 2Q having amplitude A_2 and the fundamental and third-harmonic SDW having amplitudes S_1 and S_3, respectively. We note that the dimension of A_2 is length, while S_1 and S_3 are measured in μ_B, but we shall be concerned here only with the amplitude A_2 relative to the lattice spacing a and with the ratio S_3/S_1.

The neutron-diffraction work first established that the period of the strain wave (and indeed that of the third-harmonic SDW) is in fact harmonically related to that of the fundamental SDW to within the experimental accuracy. Furthermore, the direction of the displacement $\mathbf{A}_2$ had previously been shown (Eagen and Werner, 1975) to be along the z axis, parallel to the wave vector Q of the SDW, by the fact that, while strain-wave satellites were seen for (001), (002), and (022), none were discernible for (020). Thus with $2\delta \simeq 0.1$ the scattering vector $(0,2\pm 2\delta,0)$ is almost perpendicular to the displacement $(0,0,A_2)$, giving a very small intensity according to Eq. (29) below. This work had shown also that the spin-flip transition at $T_{SF} \simeq 123$ K had no discernible effect on the amplitude of the strain wave relative to the SDW. The behavior of the third-harmonic SDW satellites as temperature passed through T_{SF} was found to be precisely the same as that of the fundamental SDW, which is illustrated in Fig. 4(a). This showed that the polarization of the third-harmonic SDW changes from being transverse to the wave vector Q above T_{SF} to longitudinal below T_{SF}.

Although in principle both the fundamental SDW and the third-harmonic S_3 can be seen as satellites of any point in reciprocal space satisfying the condition of Eq. (20b), Pynn *et al.* (1976) were able to observe S_3 only around the points {001}. They attributed this to S_3's having the same magnetic form factor as the SDW, i.e., essentially the spherical atomic form factor illustrated in Fig. 11. Since $S_3/S_1 \simeq 10^{-3}$, this makes S_3 too weak to observe for larger values of $(h^2+k^2+l^2)$, i.e., for larger $\sin\theta/\lambda$.

The relative amplitudes S_3/S_1 and A_2/a being, as we shall see shortly, very small justifies the use of Landau theory for a consideration of their relative variation when the amplitude S_1 of the SDW varies with temperature (or alloy concentration). Thus, following Pynn *et al.* (1976), we write the free energy

$$F = F_0 + \alpha_1 S_1^2 + \alpha_2 A_2^2 + \alpha_3 S_3^2 + \alpha_{12} S_1^2 A_2 + \alpha_{13} S_1^3 S_3 + \alpha_{123} S_1 A_2 S_3 + \cdots , \quad (21)$$

neglecting higher harmonics, since $A_{2p+2} \ll A_2$ and $S_{2p+3} \ll S_3$ for $p \geq 1$. While the magnitude of the coefficients α depends upon the particular model chosen to describe the system, Eq. (21) shows that, when F is minimized with respect to the various wave amplitudes, the amplitude for the p harmonic is proportional to S_1^p, the p power of the SDW amplitude S_1.

Pynn *et al.* (1976) measured the intensities of the strain wave and the third harmonic of the SDW between a temperature close to the Néel transition and 80 K, and their results, plotted against the appropriate power of the intensity of the fundamental SDW, are shown in Figs. 28 and 29. The proportionality between $I_2 = A_2^2$ and $I_1^2 = S^4$ seen in Fig. 28 shows that the ratio $A_2(T)/S_1^2(T)$ is constant as expected. Figure 29 shows, however, that, while $S_3(T)/S_1^3(T)$ is constant down to a temperature T of about 200 K, the slope of the curve $I_3(T)$ vs $I_1^3(T)$ approaches zero at lower temperatures.

On the other hand, Iida, Tsunoda, and Nakai (1981) found that the intensity ratio $S_3(e_A)/S_1^3(e_A)$ is by no means constant for varying concentrations x of impurities Mn and V, which correspond in a rigid-band model

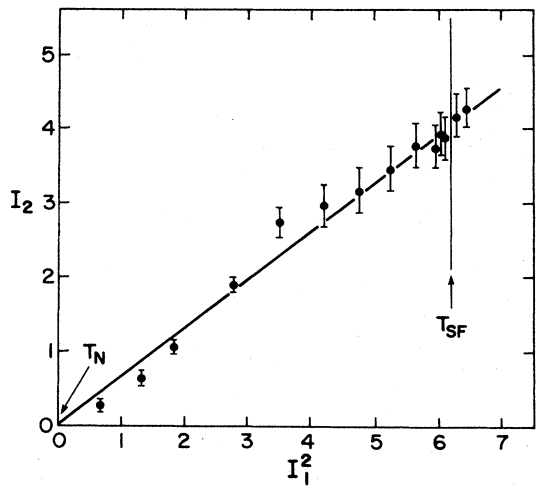

FIG. 28. Intensity I_2 of the strain wave vs the square of the intensity I_1 of the SDW, both being in arbitrary units, between the Néel transition ($I_1 = I_2 \simeq 0$ at the origin) and temperature 80 K. The line shows the proportionality between I_2 and I_1^2 observed over the whole temperature range, with no observable change at the spin-flip transition at $T_{SF} \simeq 123$ K (after Pynn *et al.*, 1976, the data for the temperature dependence of I_1 being taken from the work of Werner *et al.*, 1967a).

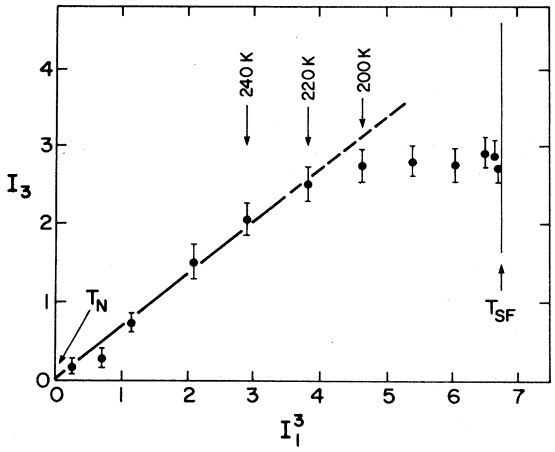

FIG. 29. Intensity I_3 of the third harmonic vs the cube of the intensity I_1 of the SDW, both being in arbitrary units, between the Néel transition ($I_1=I_3\simeq 0$ at the origin) and the spin-flip transition at $T_{SF}\simeq 123$ K. The line shows the proportionality between I_3 and I_1^3 observed at temperatures above about 220 K (after Pynn *et al.*, 1976, the data for the temperature dependence of I_1 being taken from the work of Werner *et al.*, 1967a).

to variation of the electron-to-atom ratio e_A with $e_A=6+x$ for Mn and $e_A=6-x$ for V alloys (see Sec. II.B.1). Figure 30 shows how $S_3(e_A)/S_1(e_A)$ varies with the incommensurability parameter $\delta(e_A)$. Since S_1 at zero temperature decreases by only about 35% between these concentrations [see Koehler *et al.*, 1966, and Hamaguchi *et al.*, 1965, from whom Iida, Tsunoda, and Nakai (1981) took their values of S_1], while S_3 decreases much more rapidly, going to zero in Cr + 0.7 at. % V (see Iida, Tsunoda, and Nakai, 1981, Fig. 4), we conclude that S_3/S_1^3 also decreases rapidly.

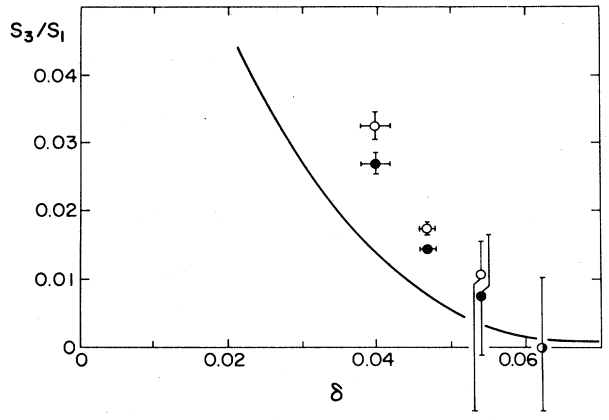

FIG. 30. The ratio S_3/S_1 of the amplitude of the third-harmonic SDW to that of the fundamental SDW plotted vs δ, in units of $a^*=2\pi/a$. The data points from left to right are for Cr + 0.5 at. % Mn at temperature 126 K, pure Cr at 144 K, Cr + 0.3 at. % V, and Cr + 0.7 at. % V. The open and solid circles correspond to the rigid and deformable-spin models, respectively, for different methods of determining S_3/S_1 from the experimental data, as described in the text. The line shows the expected variation of S_3/S_1 for a theoretical model of Kotani (1976, 1978) (after Iida, Tsunoda, and Nakai, 1981).

Tsunoda *et al.* (1975), Iida, Kohno, Tsunoda, and Kunitomi (1981), and Iida, Tsunoda, and Nakai (1981) performed careful measurements of the relative intensities of the various neutron-diffraction satellites in order to determine the phases of the strain wave and the third-harmonic SDW relative to the fundamental SDW. Their measurements also provide an indirect method for measuring the relative amplitudes A_2/a and S_3/S_1. It is instructive to compare their values for the amplitudes with the direct neutron measurements of Eagen and Werner (1975) and Pynn *et al.* (1976), as well as with the x-ray data of Tsunoda *et al.* (1974), which correspond to both strain waves and CDW's.

Figure 31 shows (a) the "triangular" waveform resulting from positive S_3/S_1, which means that the antinodes of S_3 and S_1 have the same sign where they coincide, and (b) the "rectangular" waveform for negative S_3/S_1, where S_3 and S_1 have the opposite sign at the antinodes. We note that in this analysis we assume that the nodes of S_1 coincide with those of S_3 and also of the strain wave (and CDW) A_2, i.e., S_3 and A_2 are either in phase or π out of phase with S_1.

The sign of A_2/S_1 determines the relation between the positions of the antinodes of the SDW and the maximum in the lattice parameter a_j, when we write

$$\mathbf{r}_j=\mathbf{r}_j^0\pm\mathbf{A}_2\sin(2\mathbf{Q}\cdot\mathbf{r}_j^0) \tag{22}$$

and

$$\mathbf{S}_j=\mathbf{S}_1\cos(\mathbf{Q}\cdot\mathbf{r}_j^0) \tag{23}$$

with Q being in units of $a^*=2\pi/a$. When the displaced

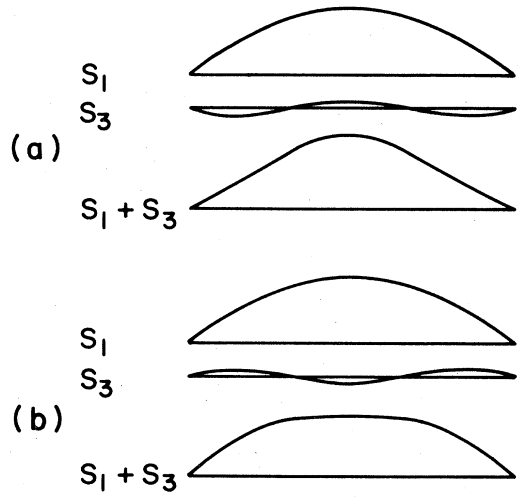

FIG. 31. The two possible phase relations of the third-harmonic SDW S_3 to the fundamental SDW S_1 illustrated schematically for (a) positive S_3/S_1 giving "triangular" waveform and (b) negative S_3/S_1 giving a "rectangular" waveform which corresponds to that seen in Cr (after Iida, Tsunoda, and Nakai, 1981).

atomic positions, given by Eq. (22), and the magnetic moments, given by Eq. (23), are substituted in the expression for the magnetic structure factor, the relative intensities of the two SDW satellites about a point **G** in reciprocal space, after correcting for the relative values of the squares of the magnetic form factor, Lorentz factor, and Debye-Waller factor, is

$$R_{\parallel}=\frac{I(\mathbf{G}-\delta)}{I(\mathbf{G}+\delta)}\simeq 1\mp 2\mathbf{G}\cdot\mathbf{A}_2\ , \tag{24}$$

where **G** and $\delta=1-\mathbf{Q}$ are all in units of $a^*=2\pi/a$ and $\mathbf{A}_2$ is in units of a. We have employed here for generality a vector amplitude $\mathbf{A}_2$, but in the usual case with **Q** along the z axis and considering the SDW satellites of (001) we obtain

$$R_{\parallel}=\frac{I(1-\delta)}{I(1+\delta)}\simeq 1\mp\frac{4\pi A_2}{a}\ . \tag{25}$$

These equations correspond to the rigid-spin model employed by Tsunoda *et al.* (1975), in which each atom keeps the same magnitude (and of course direction) of magnetic moment when it is displaced. Iida, Tsunoda, and Nakai (1981) considered also the deformable-spin (flexible-spin) model, writing

$$\mathbf{S}_j=\mathbf{S}_1\cos(\mathbf{Q}\cdot\mathbf{r}_j) \tag{26}$$

instead of Eq. (23), so that the magnitude of the moment varies so as to keep the waveform of the SDW unchanged, i.e., the fundamental and third-harmonic SDW remain purely sinusoidal. In this case we obtain in place of Eq. (24)

$$R_{\parallel}=\frac{I(\mathbf{G}-\delta)}{I(\mathbf{G}+\delta)}\simeq\left[\frac{1\mp(\mathbf{G}+\mathbf{Q})\cdot\mathbf{A}_2/2}{1\pm(\mathbf{G}-\mathbf{Q})\cdot\mathbf{A}_2/2}\right] \tag{27}$$

which gives, with $\mathbf{G}=(001)a^*$ and $\mathbf{A}_2\|\mathbf{Q}$,

$$R_{\parallel}=\frac{I(1-\delta)}{I(1+\delta)}\simeq\left[\frac{1\mp(2-\delta)\pi A_2/a}{1\pm\delta\pi A_2/a}\right]^2\simeq 1\mp\frac{4\pi A_2}{a} \tag{28}$$

in the approximation $\delta\pi A_2/a\ll 1$. Thus, in this good approximation, the two models give identical expressions for the intensity ratio $R_{\parallel}$ of the SDW satellites associated with the strain wave.

Tsunoda *et al.* (1975) found that the value of the ratio to be substituted in Eq. (25) or (28) was 1.044 for measurements of the intensities of the SDW satellites at temperature 293 K. This shows that the positive sign is to be chosen in these equations, corresponding to the negative sign in Eq. (22), with the displacement and lattice parameter varying relative to the SDW as shown in Fig. 32(b). The amplitude of the strain wave corresponding to this

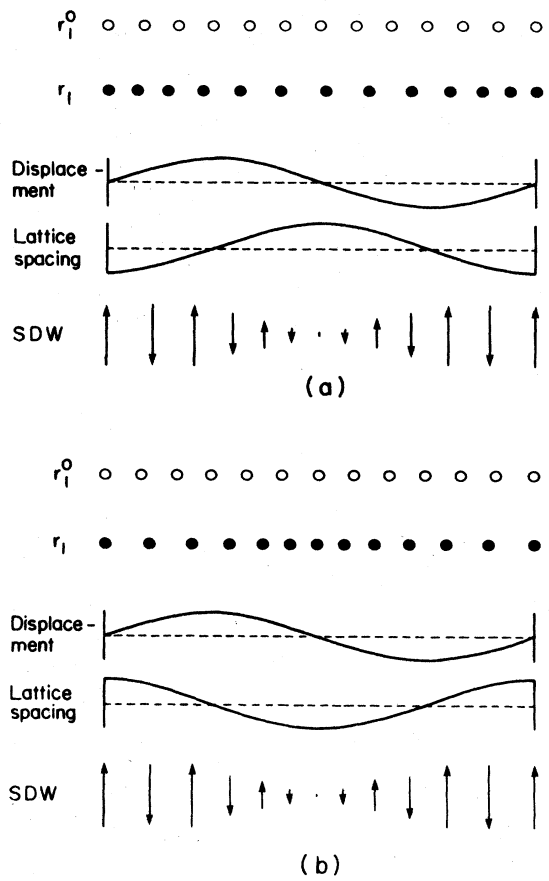

FIG. 32. The two possible phase relations of the strain wave (SW) A_2 and the SDW S_1 illustrated schematically for (a) positive A_2/S_1, for which the displacement of the atomic position due to the SW is in phase with the SDW, so that the minimum lattice spacing coincides with the antinode of the SDW [+ sign in Eq. (12) and − sign in Eqs. (15) or (18)] and (b) conversely for negative A_2/S_1, which corresponds to the behavior observed in Cr (after Tsunoda *et al.*, 1975).

magnitude of the intensity ratio is $A_2/a=3.5\pm10^{-3}$, which is somewhat larger than the value $A_2/a=1.7\pm0.2\times10^{-3}$ at temperature 130 K obtained by Eagen and Werner (1975). These authors used direct methods to determine the amplitude of the strain wave, which are clearly more accurate than the indirect method employed by Tsunoda *et al.* (1975). They normalized the strain-wave Bragg peak both to the fundamental SDW peaks, whose absolute intensities had been measured previously [see Sec. II.B.4 and Fig. 4(a)] and to the nuclear Bragg peaks, whose intensity can be calculated from the known coherent nuclear scattering length per atom, $b=3.635\times10^{-15}$ m.

Tsunoda *et al.* (1974) had previously used x-ray diffraction to determine A_2/a at temperature 153 K. This is a direct method which compares the intensity of the second-harmonic satellite peak with that of the Bragg peak at the reciprocal-lattice point. The ratio of intensities is

$$R_{20}=\frac{I(\mathbf{G}-2\delta)}{I(\mathbf{G})}=\frac{1}{3}\left[\frac{\mathbf{G}\cdot\mathbf{A}_2}{2}\right]^2 =\tfrac{4}{3}\pi^2\left[\frac{A_2}{a}\right]^2 \tag{29}$$

in the case of $\mathbf{G}=(220)a^*$, with the assumption that in the non-field-cooled sample one-third of the volume consists of domains having wave vector $\mathbf{Q}$ oriented along each of the cube axes.

Equation (29) follows from substituting the displaced atomic positions given by Eq. (22) in the expression for the lattice structure factor, which gives

$$\begin{aligned}F(\mathbf{q},\mathbf{A}_\omega)&=\sum_j\exp(i\mathbf{q}\cdot\mathbf{r}_j)\\&=\sum_j\exp(i\mathbf{q}\cdot\mathbf{r}_j^0)\exp[\pm i\mathbf{q}\cdot\mathbf{A}_2\sin(2\mathbf{Q}\cdot\mathbf{r}_j^0)]\\&\simeq\sum_j\delta(\mathbf{q}-\mathbf{G}_j)+\frac{\mathbf{q}\cdot\mathbf{A}_2}{2}\delta(\mathbf{q}-\mathbf{G}_j\mp2\delta)\ ,\end{aligned} \tag{30}$$

$\delta(\mathbf{x})$ being the Kronecker delta and $\mathbf{G}_i$ reciprocal-lattice vectors. The approximation in Eq. (30) is valid provided the summation over $\mathbf{G}_j$ is restricted to small enough values of $|\mathbf{G}_j|$ that $\mathbf{G}_j\cdot\mathbf{A}_2\ll1$, and Tsunoda *et al.* (1974) found this to be the case for $\mathbf{G}=(220)a^*$. The observed value of the intensity ratio is $R_{20}=8.64\times10^{-5}$, and substitution in Eq. (29) gives a value $A_2/a=2.5\pm0.5\times10^{-3}$.

Pynn *et al.* (1976) applied the direct neutron-diffraction method of normalizing the strain-wave Bragg peaks to the fundamental SDW peaks and to the nuclear Bragg peaks and obtained the value $A_2/a=1.3\pm0.3\times10^{-3}$ at temperature 200 K. By the use of Fig. 4(a), which shows the form of the temperature dependence of S_1^2 and the linear relation between S_1^2 and A_2 illustrated in Fig. 28, we obtain the value $A_2/a=1.45\pm0.4\times10^{-3}$ at temperature 153 K (not 1.6×10^{-3} as given by Pynn *et al.*, 1976). This value is somewhat smaller than that of Tsunoda *et al.* (1974) for the same temperature, but the latter depends on an assumption about the relative volumes of different domains, and Tsunoda (1985) recommends adoption of the former.

Mori *et al.* (1975) demonstrated the existence of a CDW in chromium of amplitude of the same order of magnitude as the strain wave by measuring the ratio R_{22} of the x-ray diffraction intensities of the $(2\pm2\delta,0,0)$ peaks. If the relative amplitude of the CDW is $\pm\sigma$, which in terms of charge density means that

$$\rho_j(\mathbf{r}-\mathbf{r}_j)=\rho^0(\mathbf{r}-\mathbf{r}_j)[1\pm\sigma\cos(2\delta\cdot\mathbf{r}_j^0)]\ , \tag{31}$$

where $\rho^0(\mathbf{r}-\mathbf{r}_j^0)$ is the electron density around lattice site $\mathbf{r}_j^0$ without the CDW, then one obtains

$$R_{22}=\frac{I(2+2\delta,0,0)}{I(2-2\delta,0,0)}=\left|\frac{\frac{K_+A_2}{2}\mp\frac{\sigma}{2}}{\frac{K_-A_2}{2}\mp\frac{\sigma}{2}}\right| \tag{32}$$

with $K_\pm=(2\pm2\delta)2\pi/a$.

The measurements at temperature 150 K gave an intensity ratio $R_{22}=0.908$, and with $A_2/a=2\times10^{-3}$ the calculated ratio for $\sigma=0$ was estimated by Mori *et al.* (1975) to be $R_{22}=0.933$, taking into account the atomic form factor, Lorentz factor, polarization, and Debye-Waller factor. This gives $\sigma\simeq8\times10^{-3}$ with a positive sign, which means that the electron density is large at the antinode of the SDW. This value is to be compared with theoretical estimates of $\sigma\gtrsim10^{-2}$ by Young and Sokoloff (1974), $\sigma\sim5\pm2\times10^{-3}$ by Kotani (1975), and $\sigma\simeq1.4\times10^{-3}$ by Nakajima and Kurihara (1975).

It should be noted that the contribution of the CDW to the intensity ratio R_{20} in Eq. (29), which was used by Tsunoda *et al.* (1974) to determine A_2/a, is very small (Tsunoda, 1985). Thus Pynn *et al.* (1976) were mistaken to attribute the apparent discrepancy between the neutron and x-ray diffraction values of A_2/a to a CDW.

Let us consider now the determination by Iida, Tsunoda, and Nakai (1981) of the phase of the third harmonic of the SDW relative to that of the fundamental SDW, the two possibilities being illustrated in Fig. 32. Iida *et al.* obtained rather different expressions for the ratio of the intensities of the satellites of (100) for the two spin models, which presumably accounts for the difference between the positions of the open and solid symbols in Fig. 30. In the approximations $\pi A_2/a\ll|S_3/S_1|$ and $\delta\ll1$ [Tsunoda, 1985, points out that in fact $(\pi A_2/a)/(|S_3/S_1|)\simeq0.3$, so that the former approximation is not too good], both reduce to the same expression

$$R_{33}=\frac{I(1-3\delta)}{I(1+3\delta)}\simeq1\pm\frac{4\pi A_2/a}{S_3/S_1}\ , \tag{33}$$

which corresponds to either of the equations that may be used to describe the third-harmonic SDW,

$$\mathbf{S}_{j3}=\pm\mathbf{S}_3\cos(3\mathbf{Q}\cdot\mathbf{r}_j^0) \tag{34}$$

for the rigid-spin model or

$$\mathbf{S}_{j3}=\pm\mathbf{S}_3\cos(3\mathbf{Q}\cdot\mathbf{r}_j) \tag{35}$$

for the deformable-spin model.

The neutron-diffraction peaks for the third-harmonic SDW and the fundamental SDW around (100) are shown in Fig. 33. The third-harmonic peaks are roughly of the same intensity, but when they corrected their ratio for the relative values of the squares of the magnetic form factor, Lorentz factor, and Debye-Waller factor, Iida, Tsunoda, and Nakai (1981) obtained the value $R_{33}=0.50\pm0.06$. Equation (33) shows, therefore, that the minus sign must be chosen, and Eqs. (34) and (35) show that this means that S_3/S_1 is negative. Thus the phases of S_3 and S_1 differ by π, corresponding to the "rectangular" waveform shown in Fig. 32(b).

Kotani (1975, 1976, 1978) developed a theory of higher harmonics of SDW in Cr in the framework of the nesting model which reproduces this observed behavior. As the electron-to-atom ratio increases and the commensurabili-

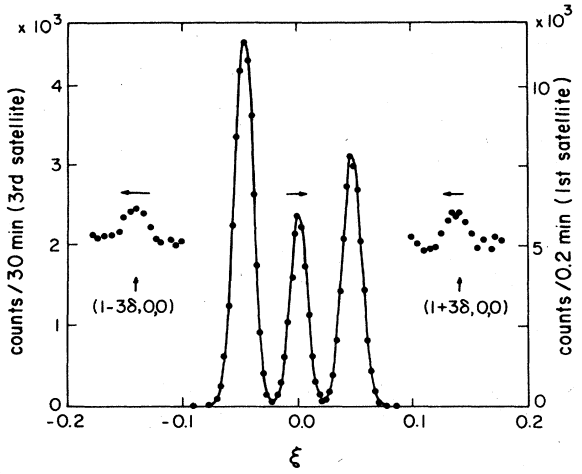

FIG. 33. Elastic scans at temperature 144 K in a non-field-cooled single crystal of Cr through the fundamental and third-harmonic satellites around (001), i.e., along the dotted line in Fig. 27. The scales for $I(I\pm\delta)$ and $I(I\pm3\delta)$ are shown on the right- and left-hand vertical axes, respectively (after Iida, Tsunoda, and Nakai, 1981).

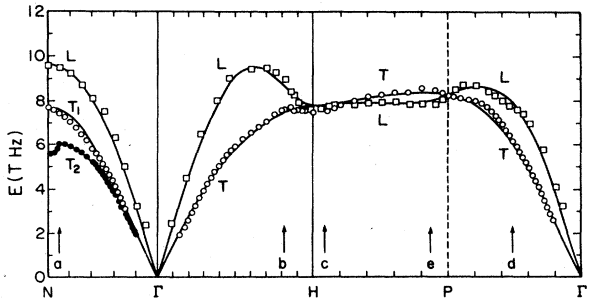

FIG. 34. Phonon dispersion relations of chromium at room temperature. L and T denote longitudinal and transverse modes, respectively. The curves represent a fourth-neighbor Born–von Kármán analysis of the experimental data (after Shaw and Muhlestein, 1971; the arrows *a*, *b*, *c*, and *d* indicating Kohn anomalies have been shifted slightly and the arrow *e* is added to their Fig. 1 in accordance with Muhlestein *et al.* (1972a, 1972b) and Table II in Laurent *et al* (1981).

ty parameter $\delta=1-Q$ approaches zero, the harmonic content increases, and the waveform approaches the truly rectangular shape corresponding to antiphase domains of a commensurate structure.

Pynn *et al.* (1976) found by directly comparing the intensity I_3 of the third-harmonic satellite with I_1 for the fundamental SDW that, at temperature 200 K, $|S_3/S_1|=(I_3/I_1)^{1/2}=1.65\pm0.05\times10^{-2}$. Since S_3/S_1^3 is approximately constant below 200 K from Fig. 29, we can estimate the value of $|S_3/S_1|$ at 144 K for comparison with the ratio of the amplitudes estimated by the indirect method by Iida, Tsunoda, and Nakai (1981), using as well the change in intensity of the SDW between these two temperatures obtained from Fig. 4(a). The value thus obtained, $|S_3/S_1|=1.8\times10^{-2}$, is only about half the value obtained by substituting $R_{33}=0.5$ and $A_2/a=1.45\times10^{-3}$ in Eq. (33) (with the negative sign), which gives $S_3/S_1=-3.6\times10^{-2}$. This discrepancy, however, can be attributed to the oversimplified form of Eq. (23); a more exact analysis gives $S_3/S_1=2.1\times10^{-2}$, in reasonably good agreement with the neutron-diffraction value (Tsunoda, 1985).

E. Lattice vibrations

Kohn (1959) first showed that the interaction between the conduction electrons and the lattice vibrations in a metal may give rise to an observable anomaly in the phonon dispersion relations. This anomalous behavior is expected to occur when the phonon wave vector is equal to an extremal dimension of the Fermi surface. These Kohn anomalies have been seen in several metals and are useful as a caliper of the Fermi surface in alloys where impurity scattering precludes the use of the more accurate de Haas–van Alphen technique. In the case of Cr, Kohn anomalies have been used to caliper the Fermi surface of paramagnetic Cr, as we shall see in Sec. IV.B.1, since the de Haas–van Alphen technique can be used only at low temperatures where, of course, Cr is AFM.

The lattice vibrations of Cr were first measured by Møller and Mackintosh (1965) using inelastic neutron scattering. They found no change in the phonon spectrum between temperature $T=100$ K, well below the Néel temperature, $T_N\simeq311$ K, and $T=400$ K, above T_N. The phonon linewidths progressively increased with increasing temperature, but the phonon energies were unchanged.

Shaw and Muhlestein (1971) made a more thorough study of inelastic neutron scattering at room temperature, since the measurements of Møller and Mackintosh were too sparse to identify any but the most striking of the Kohn anomalies, that indicated by the arrow labeled *a* in Fig. 34. The relation of these Kohn anomalies to nesting properties of the Fermi surface of chromium will be discussed in Sec. IV.B.1. Comparison of the experimental phonon dispersion curves with theory will be made in Sec. IV.C.

III. BULK PHYSICAL PROPERTIES

We have seen in Sec. II.C.5 that magnetism manifests itself in the neutron scattering in Cr in the paramagnetic phase up to at least twice the Néel temperature. One should accordingly pay some attention to the bulk physical properties of Cr in the paramagnetic as well as in the AFM phase. I shall present here some of the experimental data for the behavior near the Néel transition to the transverse SDW phase and near the spin-flip transition to the longitudinal SDW phase, but I shall defer until Sec. VI a systematic consideration of the behavior at the phase transitions in the light of theoretical discussions.

I consider here the magnetic susceptibility, specific heat, thermal expansion, elastic moduli, and transport properties (electrical resistivity and thermoelectric power). I shall defer until Sec. VIII a consideration of ultrasonic attenuation and internal friction, which provide information about domain effects.

A. Magnetic susceptibility χ

The magnetic susceptibility χ drops as the temperature decreases below the Néel temperature $T_N \simeq 311$ K, as one expects for an AFM system, with a singularity also at $T_{SF} \simeq 123$ K, as illustrated in Fig. 35. The minimum in χ at a temperature below 100 K, seen also by Moyer *et al.* (1976) and Köbler and Dubiel (1985), is unlikely to be related to antiferromagnetism in Cr, since the amplitude of the SDW changes little below T_{SF}.

It should be remembered that the spin paramagnetism, which for a nesting model is the only term in χ affected by the formation of a SDW, is in fact smaller than the orbital paramagnetism (Huguenin *et al.*, 1971). This accounts for the relatively small decrease in χ associated with antiferromagnetism in Cr, together with the fact that the nesting model predicts that the component $\chi_\perp$ of the susceptibility tensor for magnetic field perpendicular to the polarization direction will be unchanged by the SDW. Shimizu (1970) has suggested, however, that the orbital paramagnetism might also be affected by the energy gaps associated with the SDW.

The twofold symmetry of the magnetic torque measured about a cube axis, for a Cr sample that had been cooled through the Néel temperature T_N in a large magnetic field $\mathbf{H}_c$ along that axis, led Montalvo and Marcus (1964) to the discovery of the field-cooling technique to produce a single-**Q** sample. When $\mathbf{H}_c$ is removed at some temperature well below T_N but above the spin-flip temperature T_{SF}, the components of the magnetic-susceptibility tensor may be determined by applying the field along any one of the cube axes. Alternatively, the difference between two components may be determined by measuring the magnetic torque about a third cube axis. One should note that the term "cube axis" refers to paramagnetic Cr, the symmetry in the longitudinal SDW phase being tetragonal, while in the transverse SDW phase with a polarizing field along a "cubic axis" perpendicular to **Q** the symmetry is orthorhombic.

The components of the magnetic-susceptibility tensor in the two AFM phases are defined in Fig. 36 and their values near the spin-flip transition are given in Table V.

B. Specific heat

Most experimental studies of the specific heat of AFM Cr have been in the neighborhood of the Néel transition and, in particular, have attempted to determine the latent heat of the first-order transition. This work will be discussed in Sec. VI.A.1. The specific heat over a wide temperature range, together with the thermal expansivity, is shown in Fig. 39 below.

The low-temperature specific heat, in which the electronic term linear in temperature becomes prominent, shows most clearly the effect of antiferromagnetism in Cr. The Sommerfeld coefficient Γ of this term is a measure of the density of states at the Fermi surface. The nesting model of antiferromagnetism in Cr, which we shall discuss in Sec. IV.A.1, predicts that Γ will be reduced, since at low temperatures thermal excitation will not occur across the energy gap produced at the Fermi surface by electron-hole pairing.

The results shown in Fig. 37 strongly support this picture. In the range of composition where the alloys are AFM the value of Γ is reduced below the interpolated nonmagnetic value. Heiniger (1966) pointed out that this reduction roughly parallels the variation of the Néel temperature of the alloy as the alloy composition is varied.

Muheim and Müller (1964) had previously found that the specific heat at low temperature and the anomaly in the electrical resistivity at the Néel transition in the Cr*Re* system could be accounted for by Overhauser's SDW theory.

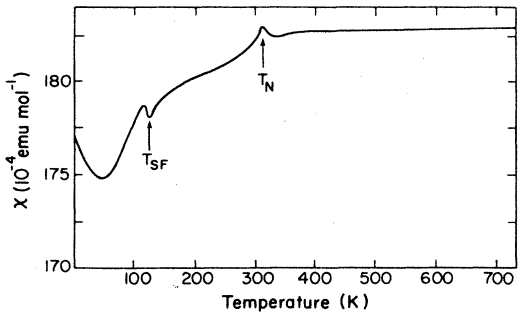

FIG. 35. Temperature dependence of the magnetic susceptibility χ of polycrystalline Cr, showing anomalies at the Néel temperature T_N and the spin-flip temperature T_{SF}. The room-temperature value, $\chi = 160 \times 10^{-6}$ emu mol^{-1}, given by Stassis *et al.* (1973) is preferred (after Bender and Müller, 1970).

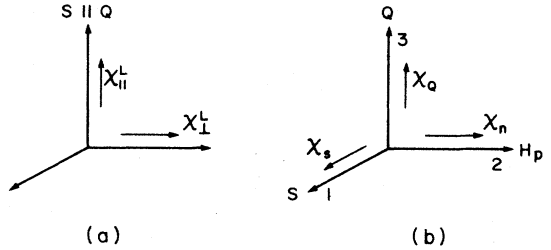

FIG. 36. Components of the magnetic-susceptibility tensor for single-**S** single-**Q** Cr: (a) longitudinal SDW phase with polarization **S** parallel to SDW wave vector **Q** for temperature $T < T_{SF}$; (b) transverse SDW state with **S**⊥**Q** for $T_{SF} < T < T_N$ with a polarizing magnetic field $\mathbf{H}_p$ in the direction shown, resulting in a single-**S** state with **S**⊥**H**.

TABLE V. The magnetic-susceptibility tensor of single-S single-Q Cr near the spin-flip temperature $T_{SF} \simeq 123$ K. The components are given in units of 10^{-6} emu mol^{-1}.

Longitudinal SDW phase temperature $T \lesssim T_{SF}$			Transverse SDW phase temperature $T \gtrsim T_{SF}$	
	a		a	b
$\chi_{\parallel}^{L}$	151.4	χ_Q	161.4	
$\chi_{\perp}^{L}$	159.8	χ_n	159.0	
		χ_S		
		$\chi_Q - \chi_n$	2.5	3.2
		$\chi_n - \chi_S$		5.7

[a] Pepper and Street (1966).
[b] Steinitz *et al.* (1972).

C. Thermal expansion

As for the specific heat, most interest in the thermal expansion of AFM Cr has attached to the behavior near the Néel temperature. This work and the thermal expansion anomaly at the spin-flip transition will be discussed in Sec. VI.B. Lee and Asgar (1969) and Steinitz *et al.* (1969) first measured the anisotropy of the thermal expansion in single-S single-Q Cr. Steinitz *et al.* (1970) extended their measurements to low temperatures, and the results are illustrated in Fig. 38.

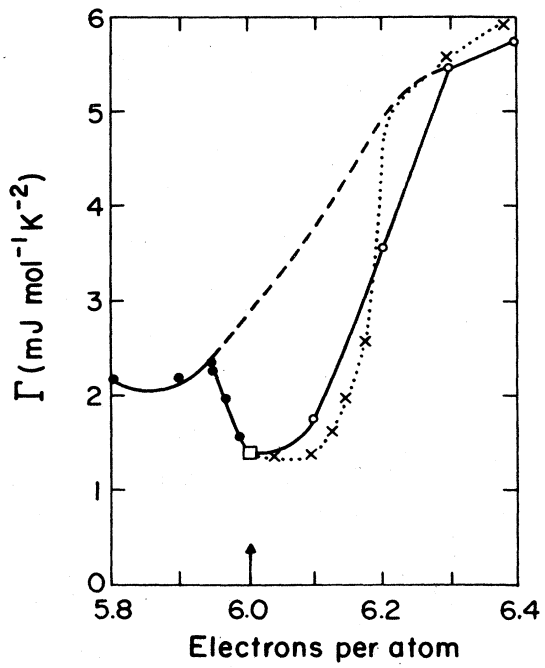

FIG. 37. Sommerfeld coefficient Γ at low temperatures of the specific-heat term linear in temperature for pure Cr (□), Cr*V* (●), Cr*Re* (×), and Cr*Os* (○) alloys. Γ is plotted vs electron-per-atom ratio determined from the alloy composition. The interpolation indicated by a dashed line for nonmagnetic alloys with Cr is estimated from the variation of Γ with composition in the homologous alloy systems Mo*Nb* /*Re* and W*Ta* /*Re* (after Heiniger, 1966).

It is interesting to note that the strain ε_Q along **Q**, measured relative to the strain along both the directions transverse to **Q**, is positive in the transverse SDW phase below the Néel temperature T_N. This result is consistent with the observation of Bastow and Street (1966) that stress-cooling a single crystal of Cr through T_N with a tensile stress along a cubic axis produces a single-**Q** state with **Q** along that axis.

At low temperatures the thermal expansivity α $(=d\varepsilon/dT)$ of Cr is negative, as first reported by White (1961). This indicates that the electronic term linear in temperature in the thermal expansion is strongly affected by antiferromagnetism in Cr, just like the corresponding linear term in the specific heat discussed in Sec. III.B. When the ratio of these terms is combined with the bulk modulus in the usual expression for the electronic Grüneisen parameter, a large negative value is obtained, $\gamma_e \simeq -10$. Kaiser *et al.* (1985) found that γ_e is roughly constant in dilute Cr*V* alloys, while the Néel temperature changes by an order of magnitude, and that the negative thermal expansivity is only weakly anisotropic.

The fact that magnetic neutron scattering is still observed in Cr at high temperatures in the paramagnetic phase (see Sec. II.C.5) has directed interest towards the

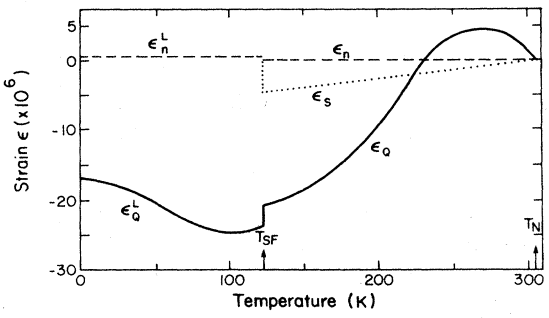

FIG. 38. Thermal expansion of single-S single-Q Cr. The strain ε_Q along **Q** and ε_s along **S** in the longitudinal SDW phase is measured relative to the strain in the field direction **H** in Fig. 36(b), which is denoted by the subscript n. In the longitudinal phase, ε_Q^L along **Q** is measured relative to ε_n^L perpendicular to **Q** (after Steinitz *et al.*, 1969, 1970).

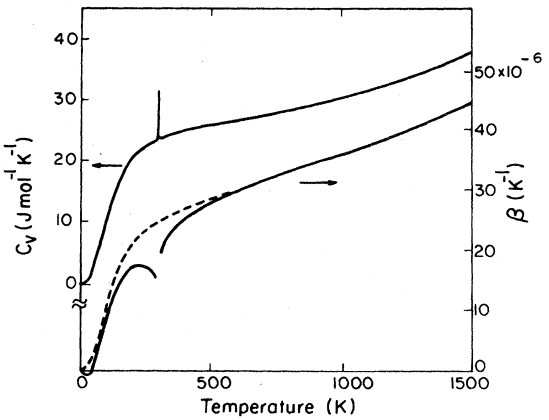

FIG. 39. Thermal expansion and specific heat of Cr over a wide temperature range. The specific heat at constant volume C_v (left-hand scale) and the volume thermal expansivity β (right-hand scale) are shown for pure Cr, while β_P (dashed line) is shown also for a paramagnetic alloy $Cr_{95}V_5$ (after White *et al.*, 1986).

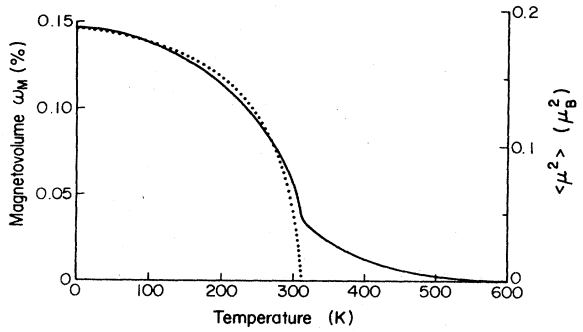

FIG. 40. Temperature dependence of the magnetovolume ω_M (solid curve) and, in the AFM phase, the mean-square magnetic moment $\langle\mu^2\rangle$ (dotted curve) in Cr (after Fawcett, Kaiser, and White, 1986).

thermal expansion and specific heat at high temperatures (Fawcett, Kaiser, and White, 1986a). Their temperature dependences up to about $5T_N$ are shown in Fig. 39.

The paramagnetic alloy $Cr_{95}V_5$ provides a reference with which to determine the temperature dependence of the magnetovolume

$$\omega_M(T)=\int_T^{T_0}[\beta(T)-\beta_P(T)]dT \ , \tag{36}$$

where $\beta\simeq\beta_P$ for temperatures higher than T_0, with $T_0\simeq 600$ K, from Fig. 39. The resultant temperature dependence of the magnetovolume shown in Fig. 40 is found to parallel, in the AFM phase, the temperature dependence of the mean-square magnetic moment $\langle\mu^2(T)\rangle$ obtained from the neutron-diffraction data shown in Fig. 4(a). Fawcett, Kaiser, and White (1986) have obtained from the comparison a value $C/B=2.4\%$ μ_B^{-2} for the ratio of the magnetoelastic coupling constant C to the bulk modulus B, using the expression

$$\omega_M=\frac{C}{B}\langle\mu^2\rangle \ . \tag{37}$$

D. Elastic moduli

The transition to the transverse SDW phase produces changes in some of the elastic moduli of Cr even more dramatic than that seen in the thermal expansion. The first observation of the effect of antiferromagnetism on the Young's modulus, $E=d\sigma/d\varepsilon$, σ and ε being the uniaxial stress and strain, respectively, was made in polycrystalline Cr by Fine *et al.* (1951), who found at a frequency of 70 kHz a reduction of E, i.e., the ΔE effect corresponding to softening of the crystal. The softening began well above T_N (see Fig. 40 below), with a pronounced sharp minimum at T_N (see Figs. 41 and 43 below) and a jump at T_{SF}.

Munday and Street (1971) made a systematic study throughout the transverse SDW phase of the temperature dependence of E, as well as of the internal friction characterized by the logarithmic decrement of elastic vibrations in a single crystal of Cr. They field-cooled the [110] sample, this being the direction of the 120-kHz vibrations, in a magnetic field $\mathbf{H}_c=3.45$ T, applied either along [110], giving roughly equal amounts of $\mathbf{Q}_x$ and $\mathbf{Q}_y$ domains (see Sec. VIII.B) or along [001], giving a single-**Q** sample with wave vector **Q** along [001]. In the latter case a polarizing field $\mathbf{H}_p=3.45$ T was applied along

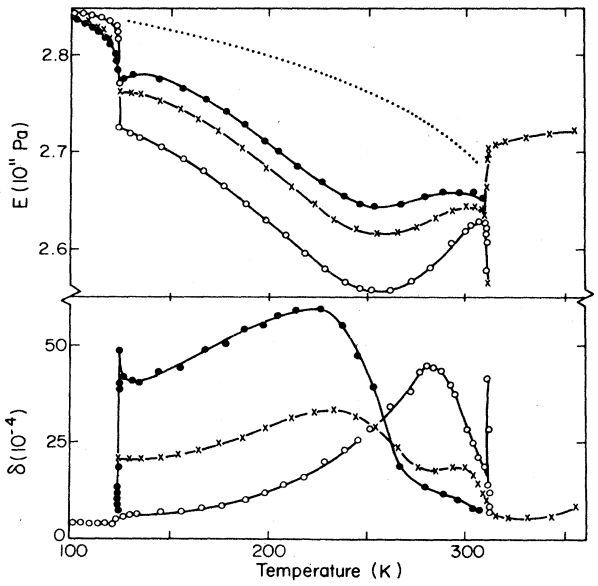

FIG. 41. Young's modulus E and logarithmic decrement δ of Cr measured along [110]. ×, poly-**Q**; ●, field-cooled along [1$\bar{1}$0]; ○, field-cooled along [001] (single **Q**); dotted curve, single-**S** single-**Q** curve obtained by extrapolating field-dependence curves to high fields (after Munday and Street, 1971).

[110] to give a single-**S** state with polarization **S** along [110]. The results, illustrated in Fig. 41, show that in the single-**S** single-**Q** state antiferromagnetism produces only a relatively small change in the [110] Young's modulus in the transverse SDW phase, as compared with the neighboring paramagnetic and longitudinal SDW phases. The effect of antiferromagnetism on the internal friction (not shown in Fig. 41) is also small in the single-**S** single-**Q** state, except at the Néel and spin-flip transitions. The strong effects of antiferromagnetism in the transverse SDW phase, seen in both E and the logarithmic decrement δ in the absence of a large polarizing field $\mathbf{H}_p$ in the single-**Q**, the two-domain, and the polydomain states, are associated with rotation of the polarization direction of the SDW because of magnetoelastic coupling with the elastic vibrations. These effects will be discussed in Sec. VIII.D as an aspect of technical antiferromagnetism.

Ultrasonic measurements of the elastic moduli likewise should be performed on a single-**S** single-**Q** sample if they are to characterize the intrinsic properties of the SDW state without complications associated with rotation of the polarization direction **S** under the influence of the acoustic wave. Palmer and Lee (1971) first applied a measuring field to suppress rotation of **S**, but did not field-cool their sample. Muir *et al.* (1987a; Muir, Perz, and Fawcett, 1987) performed all the measurements needed to determine the nine coefficients of the elastic-modulus tensor corresponding to the orthorhombic symmetry of the single-**S** single-**Q** state, as illustrated in Fig. 42. Their results, shown in Figs. 43–45, will be discussed in Secs. VI.A.3 and VI.B.

Katahara *et al.* (1979) measured the elastic moduli of single-crystal Cr under pressure up to 0.5 GPa over a temperature range from 80 to 700 K. In the paramagnetic phase the shear moduli increase linearly with pressure and decrease linearly with temperature. On the other hand, the longitudinal modulus C_{11} increases with temperature up to a maximum at 475 K and then decreases and becomes a linear function of temperature above 550 K, as shown in Fig. 46.

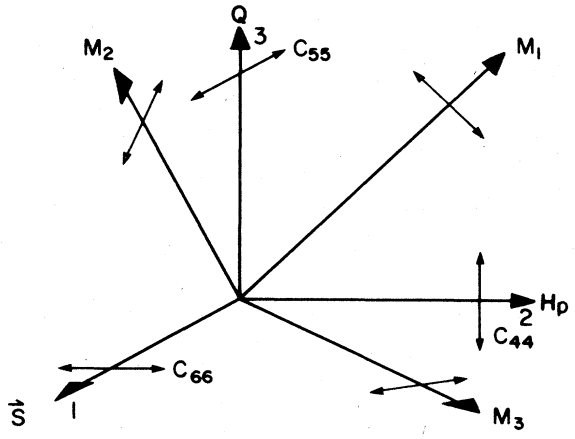

FIG. 42. The configurations of wave propagation and polarization needed to determine the nine elastic moduli of orthorhombic single-**S** single-**Q** Cr in the transverse SDW phase. Longitudinal waves propagating along the three axes determine C_{11}, C_{22}, and C_{33}, while transverse waves propagating along one axis with polarization ($\leftrightarrow$) along another determine C_{44}, C_{55}, and C_{66}. Propagation of shear waves along the three $\langle 110 \rangle$ directions of polarization as shown and labeled M_1, M_2, and M_3 give velocities corresponding to expressions like Eq. (82) from which C_{12}, C_{13}, and C_{23} can be extracted.

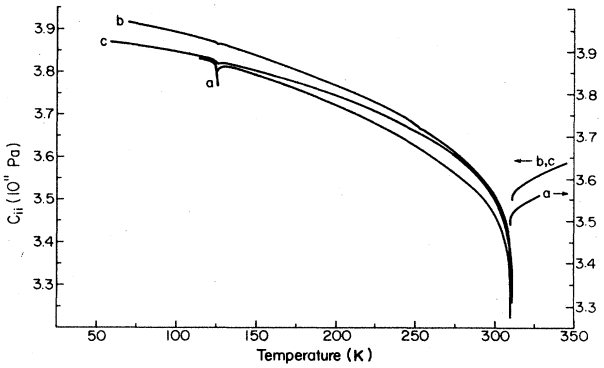

FIG. 43. Temperature dependence of the longitudinal elastic moduli (a) C_{11}, (b) C_{22}, and (c) C_{33} throughout the transverse SDW phase of single-**S** single-**Q** Cr (after Muir *et al.*, 1987b).

E. Transport properties

The electrical resistivity ρ of Cr increases as temperature decreases through the Néel temperature T_N, with a singularity in ρ at the first-order transition at T_N. This increase in ρ, as the amplitude of the SDW increases with decreasing temperature, was recognized by Trego and Mackintosh (1968) as being due to the formation of energy gaps on the nesting parts of the Fermi surface. They showed also that in a single-**Q** sample the increase in ρ as temperature T decreases below T_N,

$$\Delta\rho(T)=\rho_{\mathrm{AFM}}(T)-\rho_{\mathrm{P}}(T)\ , \tag{38}$$

is anisotropic. In Eq. (38) ρ_{P} is the resistivity in the

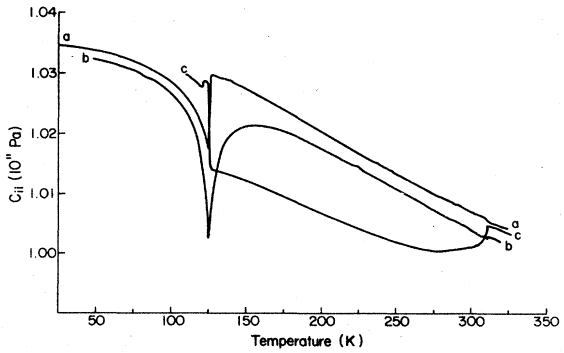

FIG. 44. Temperature dependence of the shear elastic moduli (a) C_{44}, (b) C_{55}, and (c) C_{66} throughout the transverse SDW phase of single-**S** single-**Q** Cr (after Muir *et al.*, 1987b).

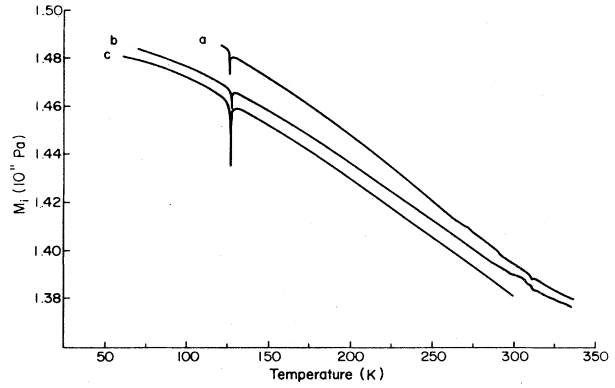

FIG. 45. Temperature dependence of the combination of elastic moduli corresponding to quasishear waves along the three ⟨110⟩ directions and polarized as shown in Fig. 42: (a) M_3; (b) M_2; and (c) M_1 (after Muir *et al.*, 1987).

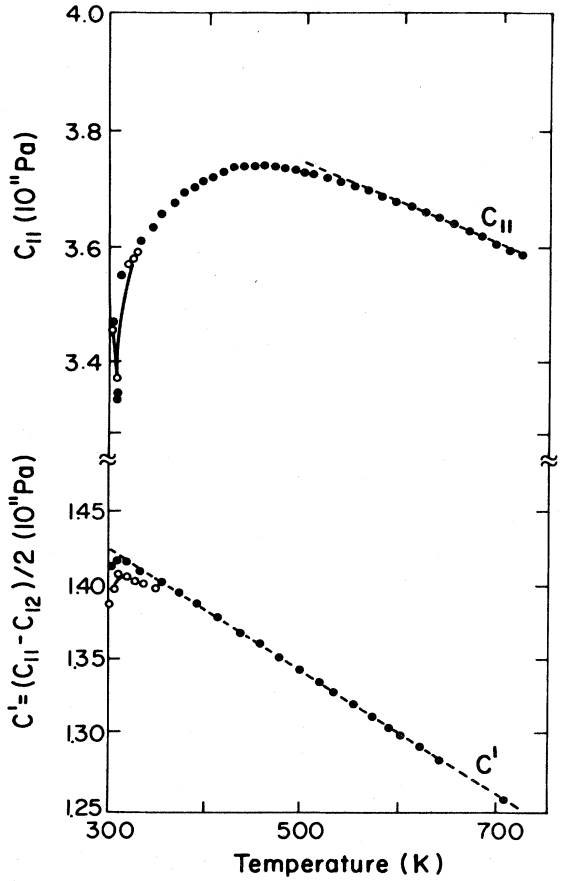

FIG. 46. Temperature dependence (●) of the elastic moduli C_{11} and $C' = (C_{11} - C_{12})/2$ of Cr from just below the Néel temperature to high temperatures in the paramagnetic phase, showing for comparison the data (○) of Palmer and Lee (1971). The dashed curves show the approximately linear temperature dependence which the moduli approach at high temperatures (after Katahara *et al.*, 1979).

paramagnetic phase extrapolated into the AFM phase, and $\Delta\rho(T)$ is about a factor of 2 greater for current **J** parallel to **Q** than for **J** perpendicular to **Q**, as illustrated in Fig. 47. This anisotropy is to be expected, since nesting of the Fermi surface with **Q** along a particular cubic axis will create energy gaps preferentially over regions where the Fermi velocity is close to that axis rather than to the other cubic axes.

No quantitative estimate of the anisotropy of ρ has been made for comparison with experiment since, as discussed in Sec. IV.B, the detailed nature of the Fermi surface of AFM Cr is understood only partially. The temperature dependence $\Delta\rho(T)$ is, however, instructive, since it follows quite well the BCS function. This was demonstrated by McWhan and Rice (1967), who estimated $\rho_P(T)$ below the Néel temperature by suppressing the antiferromagnetism with pressure. We might expect the change in the resistivity to parallel the BCS temperature dependence of the amplitude of the SDW, which may be obtained from Fig. 4(a), if the increase in ρ is mainly due to the decrease in the effective number of conduction electrons, with little effect from the change in the relaxation time.

Trego and Mackintosh (1968) also used the anomaly in $\rho(T)$ at the Néel transition in AFM Cr alloys as a marker for the Néel temperature T_N and thus determined the concentration dependence of T_N in alloys with V, Mn, Mo, W, and Re. Most of the data in Fig. 5 were acquired by this quick and convenient method, which many researchers have used.

As in the case of other physical properties, the behavior of the transport properties close to T_N has been the subject of careful study. Work on the critical behavior near T_N of the thermoelectric power (Fote *et al.*, 1973) and the electrical resistivity (Muir and Ström-Olsen, 1971; Akiba and Mitsui, 1972) will be described in Sec. VI.A.4.

The thermoelectric power S, conductivity σ, and

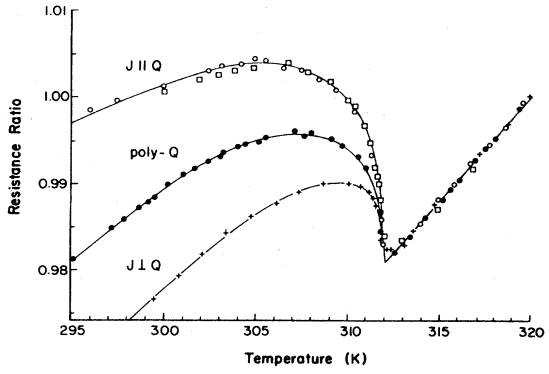

FIG. 47. Temperature dependence of the resistance of single-**Q** and poly-**Q** Cr near the Néel transition. The ordinate is the resistance ratio referred to the value of the resistance at temperature 320 K. The scatter of the different experimental points for the **J**||**Q** curve indicates the variation in resistance depending upon sample history (after Muir and Ström-Olsen, 1971).

thermal conductivity κ between temperatures $T=300$ and 1300 K were measured by Moore *et al.* (1976), who give extensive references to work on the transport properties of paramagnetic Cr. The temperature dependence of the Lorenz number, $L=\kappa/\sigma T$, near the Néel transition is interesting, but is not understood. Goff (1970) measured σ and κ in Cr from 1.5 to 330 K in order to determine $L(T)$, which at all temperatures T above 90 K is greater than the Sommerfeld value, $L_0=2.445\times10^{-8}$ V^2K^{-2}.

IV. THEORY

A. Model systems

1. Microscopic models

The study of SDW formation in idealized models of the electronic structure of metals allows a simple understanding of most of the properties of antiferromagnetism in chromium. In the first place one can show that the SDW wave vector **Q** should connect two pieces of the Fermi surface (Overhauser, 1962), and that the stability of the SDW state is enhanced if the Fermi surface has the so-called nesting property (Lomer, 1962), i.e., electron and hole surfaces can be superposed by translation through the nesting vector $\tilde{Q}$. The magnitude of $\tilde{Q}$ turns out, as we shall see in Sec. IV.B, to be essentially the same as that of **Q** in the real metal.

Overhauser (1962) showed that a linearly polarized SDW should have a lower energy than a helical SDW. This is particularly remarkable in view of the result that the ground state of the isotropic Heisenberg model, often used to describe localized spin (as opposed to itinerant-electron) systems, has a helical ground state (Yoshimori, 1959). Furthermore, one can examine the stability of a multi-Q state relative to that of a single-Q state and show that the single-Q state is favored for a Fermi surface like that of Cr (Fenton, 1976a).

The simplest of all models is Overhauser's (1960) one-dimensional gas of electrons, having three-dimensional spins interacting via a repulsive delta-function potential. In this model, if one looks for a self-consistent solution in the form of a helical SDW of positive helicity, one finds a self-consistent Hartree-Fock potential of the form

$$U(z)=g[\sigma_x\cos(Qz)+\sigma_y\sin(Qz)]\ , \tag{39}$$

where g and Q are parameters to be determined and σ_x and σ_y are Pauli matrices. This potential has the property that its only nonzero matrix elements are between free-electron states $(k,\uparrow)$ and $(k+Q,\downarrow)$, thus producing energy gaps in the original free-electron spectrum as shown in Fig. 48(a). Note that, in order to obtain the lowest overall energy, the wave vector Q of the SDW must be such that the energy gaps occur at the Fermi energy; in this case, the electron states that are raised in energy are not occupied, whereas those states lowered in energy are occupied, thus allowing the SDW to produce an overall reduction in energy. A detailed calculation produces the same result as this naive and oversimplified argument (Overhauser, 1960).

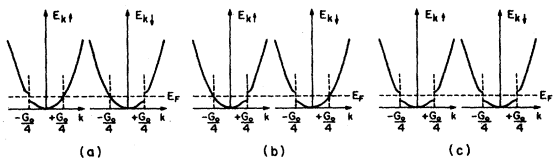

FIG. 48. In the absence of a SDW the electron dispersion relation consists of two parabolas, one for spin up and one for spin down. The figure shows the energy gaps introduced by a commensurate SDW into these two parabolas at $\pm G_0/4$, G_0 being the reciprocal-lattice spacing corresponding to the lattice parameter, in the case when the ground state contains (a) a positive helicity SDW, (b) a negative helicity SDW, and (c) a linearly polarized sinusoidal SDW. E_F is the Fermi energy.

The Hartree-Fock potential for a helical SDW of negative helicity is given by Eq. (39) with Q replaced by $-Q$, and has matrix elements between free-electron states $(k,\uparrow)$ and $(k-Q,\downarrow)$, and produces energy gaps as shown in Fig. 48(b). The positive and negative helicity states have the same energy.

Now note that a superposition of helical waves with positive and negative helicity gives a linearly polarized sinusoidal wave and that such a wave produces, as shown in Fig. 48(c), all of the energy gaps resulting from the two helical components shown in Figs. 48(a) and 48(b). If the magnitudes of the energy gaps are not too large, the positive and negative helicity components of the sinusoidal wave will not interfere, and the gain in energy expected from a linearly polarized wave should be approximately twice that for a single helical wave. Similar arguments apply in the three-dimensional case and account for the observed linear polarization of the SDW in Cr.

In three dimensions the question arises whether the structure of the SDW is single **Q**, let us say $\mathbf{Q}_3$, with $\mathbf{Q}_1$ and $\mathbf{Q}_2$ equally possible, so that one might expect a real single crystal to be multidomain with domains corresponding to $\mathbf{Q}_1$, $\mathbf{Q}_2$, and $\mathbf{Q}_3$ regions, which we shall call poly-Q; or multi-Q with the three SDW's interpenetrating each other. The stability of the single-Q SDW in the case of Cr can be seen by reference to Fig. 49. Let us suppose that a helical SDW of wave vector $\mathbf{Q}_3$ and positive helicity produces energy gaps on the shaded portions of the Fermi surface, so that a helical SDW of negative helicity and the same wave vector will produce gaps on the remaining portions of the Fermi surface. The linearly polarized sinusoidal wave results from a superposition of these two helical states taken alone. Here the wave vector $\mathbf{Q}_3$ was chosen to be along $\mathbf{k}_z$, but an equivalent picture would be obtained by taking a SDW of wave vector $\mathbf{Q}_2$ lying along $\mathbf{k}_y$. The important point is that all of the Fermi surface is involved in forming a linearly polarized SDW of either wave vector $\mathbf{Q}_3$ or $\mathbf{Q}_2$, except for the corners of the hole surface in the case when the electron

surface is smaller, as in Fig. 49. Almost all the electrons on the Fermi surface are paired by the SDW Q_3, and it is these same electrons that would be paired by the SDW Q_2, with the choice of partners being different in the two cases. The interference that occurs when the two types of pairing are simultaneously present causes the double-Q state (Fenton, 1976a; Buker, 1982). Thus a single-Q state is to be expected for the two-dimensional Fermi surface shown in Fig. 49, and a similar argument holds for Cr with the electron and hole squares of Fig. 49 being replaced by electron and hole octahedra, as illustrated in Figs. 57 and 58 below. The fact that the single-Q SDW is favored in Cr is due to the Fermi-surface geometry—the formation of a SDW in a metal having an almost spherical Fermi surface could give rise to a triple-Q structure (Overhauser, 1962).

Other features of antiferromagnetism in Cr to be explained by means of microscopic models include the following: the variation with temperature of the energy gap Δ, the amplitude μ_0 of the SDW, and its wave vector **Q**; the effect of changing the electron-to-atom ratio (by alloying Cr with nonmagnetic transition metals) upon the Néel temperature T_N, the rms moment $\langle\mu\rangle$, the wave vector **Q**, and in particular the phase diagram showing the regions of incommensurate SDW (ISDW, sometimes referred to as sinusoidal SDW with the acronym SSDW) and commensurate SDW (CSDW, sometimes referred to as an antiferromagnetic SDW with the acronym ASDW); the occurrence of the harmonic component of the SDW and the second (and higher even) harmonics corresponding to the concomitant charge-density wave and the temperature dependence of their amplitude relative to the amplitude μ_0 of the fundamental SDW; the spin-wave spectrum both above and below the Néel temperature.

A comprehensive set of references to the literature on microscopic models of itinerant-electron antiferromagnetism can be found in a recent paper by Machida and Fujita (1984, Refs. 3–21). These authors use the two-band imperfect nesting model first introduced by Shibatani *et al.* (1969). Machida and Fujita formulated the problem within the mean-field approximation with an infinite number of odd harmonics of the fundamental SDW, and obtained an exact solution by means of mathematical techniques developed recently to solve formally analogous problems in one-dimensional Peierls systems.

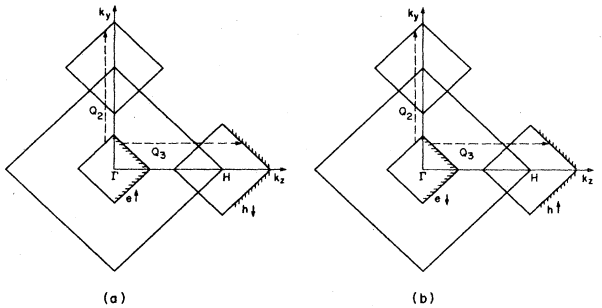

FIG. 49. Fermi surface for a schematic two-dimensional model of Cr [cf. Fig. 59, which shows a (100) section of the calculated Fermi surface of Cr]. The first Brillouin zone is duplicated so as to allow both spin up (↑) and spin down (↓) for electrons (e) and holes (h) to be shown separately: (a) $e\uparrow$ and $h\downarrow$, (b) $e\downarrow$ and $h\uparrow$. The electron surface is centered on the center Γ of the Brillouin zone, whereas the hole surface is centered on the corner H of the zone. A helical SDW of wave vector Q_3 and positive helicity produces energy gaps on the shaded portions of the Fermi surface.

Fenton (1986) has criticized the formulation of Machida and Fujita (1984) on the grounds that nonlinear effects are much less important for a SDW than for a CDW. For the same transition temperature, a SDW is much more rigid than a CDW, and thus harmonic effects are much weaker for a SDW. Thus in Cr the amplitude of the third harmonic of the SDW relative to that of the fundamental is very small, $S_3/S_1=0.0165$, while the amplitude of the strain wave relative to the lattice parameter is only $A_2=0.0013$, at temperature 200 K (Pynn *et al.*, 1976). Fenton (1984, 1986) maintains that the harmonic structure in Cr is dominated by the fact that the CDW of wave vector 2**Q** distorts the lattice, whereas the fundamental SDW does not.

Machida and Fujita (1984) present nevertheless a consistent set of results describing many of the properties of Cr and its dilute alloys, which it is convenient to quote, while crediting, where appropriate, authors who had previously obtained similar results. It should be noted that Buzdin and Tugushev (1983a, 1983b) independently obtained the exact phase diagram for the octahedra model, as illustrated in Fig. 51 below, using the same method as Machida and Fujita (1984).

Fedders and Martin (1966) considered the simplest two-band model, namely, electron and hole spheres having the same radius but different Fermi velocities v_e and v_h. Muheim and Müller (1964) had employed a more general model to analyze their data for the low-temperature specific heat and electrical resistivity through the Néel transition in the Cr*Re* system. The spheres in the Fedders-Martin model nest perfectly, giving rise to an insulating commensurate AFM state. The theory is formally similar to the BCS theory for a superconductor, with triplet pairing of electron and hole instead of singlet pairing of electrons of opposite spin as in a Cooper pair. Thus the energy gap, as first pointed out by Overhauser (1962), varies with temperature like that of a superconductor. The anisotropy of the magnetic susceptibility is the same as that of an antiferromagnet of localized spins, as observed in Cr (see Sec. III.A), namely, $\chi_\perp > \chi_\parallel$ for $T < T_N$, $\chi_\perp$ and $\chi_\parallel$ being measured with magnetic field perpendicular and parallel, respectively, to the polarization direction of the SDW.

The Fedders-Martin model gives a linear dispersion relation for spin waves at zero temperature, the velocity $v_F/\sqrt{3}$ [Eq. (13) of Sec. II.C.1] being the same as the Fermi velocity v_F apart from a numerical factor. This will in general be considerably larger than the spin-wave velocity of a localized-spin antiferromagnet or a typical pho-

non velocity. The spin waves in an itinerant model are therefore difficult to resolve in neutron inelastic scattering experiments. It is believed, however, that these high-velocity spin waves have been seen in the commensurate AFM Cr*Mn* (see Sec. II.C.1).

Shibatani *et al.* (1969) introduced the two-band imperfect nesting model used most extensively to describe antiferromagnetism in Cr and its dilute AFM alloys, namely, nesting octahedra of different sizes corresponding to the electron and hole surfaces centered at the Γ and H points, respectively, of the Brillouin zone in paramagnetic Cr (Fig. 57 below). They also included the reservoir of electrons corresponding to the rest of the Fermi surface (the electron balls at X and the hole ellipsoids at N in Figs. 57 and 58) which was first introduced by Penn (1966).

The Rice model (1970), which has spherical electron and hole surfaces of different radii and a reservoir, is a variant of the Shibatani model. When electron-phonon coupling is introduced, the parameters of the Rice model can be chosen to give a first-order Néel transition (Nakanishi and Maki, 1972; Nakajima and Kurihara, 1975). A sufficiently strong electron-phonon coupling gives a similar result for the Shibatani model (Kotani, 1975).

The model is essentially one dimensional, corresponding to the single-Q nature of the SDW, as illustrated in Fig. 50. We show the distance $G_0/2$ between the centers of the octahedra as the distance from the center Γ to the corner H of the Brillouin zone, so as to keep in mind the application of the model to AFM Cr. The Fermi velocities v_F of the electrons and holes are equal, and there are two parameters available to vary the properties of the model. The first is the energy misfit,

$$h=\tfrac{1}{2}\hbar v_F(k_e-k_h)\ , \tag{40}$$

which is normalized by writing

$$h=H/\delta_0\ , \tag{41}$$

where δ_0 is the energy parameter corresponding to the energy gap (and therefore proportional to the Néel temperature T_{N0}) for zero H, i.e., equal octahedra and therefore perfect nesting (δ_0 must not be confused with the incommensurability parameter). The second is the reservoir density of states ρ_r, which is measured relative to the sum of the electron ρ_e and hole ρ_h densities of states by writing it in the form

$$\rho=\frac{\rho_r}{\rho_e+\rho_h}\ . \tag{42}$$

Temperature T is expressed as a reduced temperature t relative to the Néel temperature T_{N0} for perfect nesting

$$t=T/T_{N0}\ . \tag{43}$$

Figure 51 shows the boundaries between the various phases for this model. The fit with the experimental data for the Néel temperature is quite good, as Sato and Maki (1974) had previously found. Machida and Fujita (1984) suggest that the deviation for large values of x, between the observed value of T_N which goes to zero, corresponding to the disappearance of antiferromagnetism in CrV for $x\simeq 4$ at. %, and the theoretical curve, may be due to the three-dimensional nature of the electron-hole system, for which the model is not valid. The closed circles with bar in Fig. 51 show the commensurate-incommensurate transition for Cr*Mn* alloys. This transition is first order with hysteresis (see, for example, Geerken *et al.*, 1982), while different choices of the parameters for variants of the model (Rice, 1970; Shibatani, 1970) can give either a

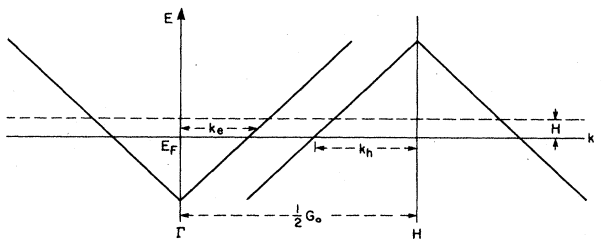

FIG. 50. Schematic energy-band structure for the two-band imperfect nesting model. The dashed line corresponds to equal-sized electron and hole octahedra and lies at energy H above the Fermi level E_F. The electron reservoir is not shown.

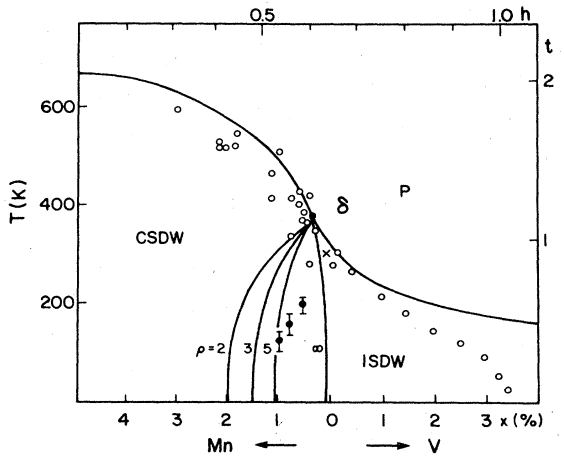

FIG. 51. Phase diagram for the two-band imperfect nesting model showing the reduced Néel temperature (the boundaries between the paramagnetic P phase and the SDW phases) as a function of the misfit parameter h [Eqs. (40) and (41)]. The phase boundary between the commensurate (CSDW) and incommensurate (ISDW) phases is shown for several values of the density of states ρ of the reservoir relative to the electron and hole octahedra [Eq. (42)]. The experimental points for the Néel temperature of Cr*Mn* ($x=e_A-6$) and CrV ($x=6-e_A$) alloys having electron concentration e_A (electrons per atom) are shown with the choice $T_{N0}=677$ K and arbitrary scaling between h and x to optimize the fit with experiment (the same scaling is used to compare experimental data with the model in Figs. 52 and 53). ⧳, experimental data for the CSDW-ISDW phase transition of Cr*Mn* alloys, which is first order and exhibits hysteresis; ×, pure Cr; ●, the triple point (after Machida and Fujita, 1984).

first-order or a continuous transition. The value for ρ chosen by Machida and Fujita in analyzing other properties of the system is $\rho=3$, a compromise, since $\rho=5$ seems to fit better the data in Fig. 51. The fit to the variation of the wave vector **Q** shown in Fig. 52 is quite satisfactory, as is the variation of the amplitude of the SDW for the model in comparison with the rms magnetic moment shown in Fig. 53.

Kotani (1976, 1978) applied the two-band imperfect nesting model to explain the observed behavior, when temperature and electron concentration are varied, of the harmonics of the SDW and of the CDW, as described in Sec. II.D (see Figs. 29 and 30), and Machida and Fujita (1984) obtained similar results. The distinctly novel feature of their work is the prediction of two energy gaps; comparison with the observed optical reflectivity will be discussed in Sec. V.C.

Fenton (1976b) and Sonin (1978) have discussed the significance of the free phase angle for the incommensurate SDW in Cr. According to Fenton, the spin supercurrent, which comprises two counterflows of electron-hole pairs with spins up and down, will occur in the plane perpendicular to the wave vector **Q**. Coherent interference effects at a weak-link Cr-Cr tunnel junction, analogous to the Josephson effect in a superconductor, would involve a spin current and magnetic field gradient, instead of the charge current and voltage difference for weakly coupled superconductors. These effects are not likely to be measurable, however, since after leaving the junction the spin current, which is not a conserved quantity, decays rapidly to zero (Fenton, 1986).

Sonin (1978) speculates, on the other hand, that electrical current in the bulk will induce an excitonic superflow of electron-hole pairs moving in the same direction independent of the sign of the spin, which will decrease the energy gap, and predicts that hysteresis of the measured gap (see Sec. V.C) will occur if the current is cycled. Sonin points out that the spin supercurrent is analogous to superflow in superfluid ^{3}He and should be observable in a planar antiferromagnetic like the transverse SDW phase of Cr.

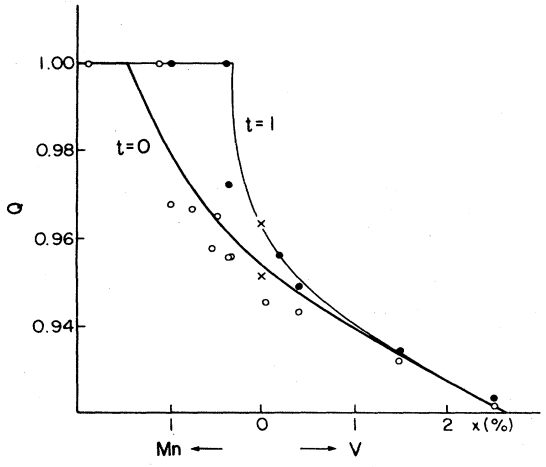

FIG. 52. Dependence of the wave vector Q in units of a^* upon the electron concentration x for the two-band imperfect nesting model compared with data for Cr*Mn* and Cr*V* alloys. Experimental values of Q: ○, at low temperature; ●, at temperature $T \lesssim T_N$, i.e., reduced temperature $t \lesssim 1$; ×, for pure Cr. The ordinate scale is adjusted by choosing the energy parameter $\delta_0=0.044$; the reservoir density-of-states parameter defined in Eq. (32) is $\rho=3$ both here and in Fig. 53 (after Machida and Fujita, 1984).

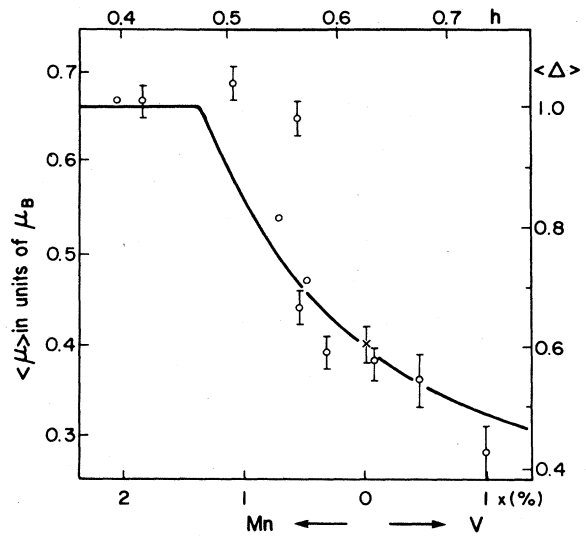

FIG. 53. Dependence of the rms magnetic moment, $\langle\mu\rangle\equiv\langle\mu(0)\rangle=\mu_0/\sqrt{2}$, μ_0 being the SDW amplitude at zero temperature upon the electron concentration x for the two-band imperfect nesting model compared with data for Cr*Mn* and Cr*V* alloys. The cross corresponds to pure Cr. The left ordinate scale is adjusted to give the experimental value in the commensurate state. The right ordinate scale shows the average amplitude $\langle\Delta\rangle$ of the SDW as a function of the energy parameter h relative to its constant value in the commensurate state (after Machida and Fujita, 1984).

Although the nesting of the Fermi surface of Cr undoubtedly determines the wave vector of the SDW, Teraoka and Kanamori (1978) point out that the states near the Fermi surface contribute only a small fraction of the relatively large energy of the SDW, as we shall see in Sec. IV.B.3 (Windsor, 1972). Teraoka and Kanamori purpose an interacting virtual-state model, based on the Alexander-Anderson-Moriya theory of the exchange interaction between two transition-metal magnetic atoms (Moriya, 1965), and thus unify the concept of a localized moment with that of itinerant electrons.

In the theory of Teraoka and Kanamori, the mechanism that lowers the energy of the incommensurate SDW state (or rather, the long-period commensurate SDW state) relative to that of the commensurate SDW state (i.e., ASDW state) is a compromise between the two AFM couplings of nearest and next-nearest neighbors, which is achieved with the help of a charge-density wave. The period of the SDW is, however, arbitrarily taken to

be an integral number, $p=20$, of lattice constants, close to the observed incommensurate period.

The model shows why the magnetic moment in the commensurate SDW state in Cr*Mn* alloys is almost the same near the commensurate-incommensurate transition as in the incommensurate SDW state (Hamaguchi *et al.*, 1965), which the nesting model fails to explain (Shibatani *et al.*, 1969). It also gives a value, $S_3/S_1=0.021$, for the ratio of the amplitudes of the third-harmonic and the fundamental SDW, which compares well with the observed value $S_3/S_1=0.0165\pm0.005$ (Pynn *et al.*, 1976). Moreover, the amplitudes of the CDW and the strain wave agree with the observed values (Tsunoda *et al.*, 1974; Pynn *et al.*, 1976; see Sec. II.D).

2. Dynamical magnetism

Spin waves in the commensurate SDW system were predicted by Fedders and Martin (1966; see also Rajagopal, 1965) to have a linear dispersion relation with a velocity essentially the same as the Fermi velocity [Eq. (12)]. The experimental data for commensurate AFM Cr*Mn*, illustrated in Fig. 10 and tabulated in Table I, are consistent with this idea. Liu (1970) used the Fedders-Martin model of equal electron and hole spheres and, taking into account depairing due to impurity and phonon scattering, determined the magnon (spin-wave) line shape up to high energies. At low temperatures with increasing energy the magnon line remains well defined until the gap energy, and thereafter broadens rapidly due to the magnon's decaying by electron-hole pair production. With increasing temperature at low energy the magnon line broadens as the Néel temperature T_N is approached and becomes peaked at zero wave vector. This corresponds to diffusive (rather than propagating) modes, which are referred to as a paramagnons (i.e., magnons in the paramagnetic phase) or spin fluctuations.

Sato and Maki (1974) obtained the very different result that the spin wave remains well defined as the temperature approaches T_N, but the velocity decreases as $(T_N-T)^{1/2}$. They attribute this discrepancy to an error in Liu's (1970) formulation of the problem. Sato and Maki used a two-band model of unequal nesting octahedra similar to that of Shibatani *et al.* (1969), but without the electron reservoir. They found that near T_N the velocity of the spin wave also approached zero as they varied the electron-to-atom ratio so as to approach the incommensurate-commensurate (*I-C*) transition by changing the energy parameter H in Fig. 50. Walker (1976) used Rice's (1970) model of two unequal spheres with an electron reservoir and found that at low temperatures the velocity is independent of electron-to-atom ratio in the commensurate phase. This zero-temperature result is in striking contrast with the finding of Sato and Maki that near T_N the spin-wave velocity goes to zero at the *I-C* transition. Walker did not calculate the velocity in the incommensurate phase, but he found that in the metastable phase, which coexists with the incommensurate phase, the spin-wave velocity decreases as the energy parameter H in Fig. 50 continues to increase beyond the critical value for the *I-C* transition.

The polarization direction $\tilde{S}$ of the spin waves relative to the spin direction $\mathbf{S}$ of the spins was transverse in Walker's (1970) calculation for the commensurate AFM. Sato and Maki (1974) found that spin waves, which above the Néel temperature T_N correspond to an isotropic diffusive mode, decompose below T_N into longitudinal and transverse components, i.e., fluctuations in the amplitude and the direction, respectively, of the polarization of the SDW. Comparison should be made with the neutron scattering results given in Sec. II.C.2 (see Figs. 15 and 16 and Table III).

These various treatments of the spin-wave problem for different models of the SDW system (see also Akhiezer and Barannik, 1982) concur in giving a spin-wave velocity, at low temperature in an itinerant antiferromagnet, that is essentially equal to the Fermi velocity. One should note, however, Fisher's (1972) result

$$c=\left[\frac{J_e a}{3K}v_F\right]^{1/2}=(\tfrac{1}{3}v_e v_F)^{1/2} \tag{44a}$$

with

$$v_e=\frac{J_e a}{3h},\quad J_e=\tfrac{1}{5}(I+4J)\ , \tag{44b}$$

where I and J are the Coulomb and exchange energies, respectively. Thus v_e is an effective velocity determined by the interaction potential.

Zhu and Walker (1986) have studied the spin-wave excitations of a linearly polarized SDW like that in Cr, using the phenomenological model to be discussed in the next section (IV.A.3). They find that the spin waves have an anisotropic velocity

$$c_z=2S\left[A(0)\frac{\partial^2 A(\mathbf{q})}{\partial q_z^2}\right]\ , \tag{45a}$$

$$c_\perp=2S\left[A(0)\frac{\partial^2 A(\mathbf{q})}{\partial q_\perp^2}\right]\ , \tag{45b}$$

where $\mathbf{S}$ is the polarization vector of the SDW and $A(\mathbf{q})$ is the coefficient of the term $\mathbf{S}\cdot\mathbf{S}^*$ in the Landau-type free energy of Eq. (54), the derivatives being taken at $\mathbf{q}=Q\hat{z}$.

Expressions for the spin-wave velocity equivalent to Eq. (45) are obtained for all even-commensurate SDW's (i.e., $2n\mathbf{Q}=\mathbf{G}$, a reciprocal-lattice vector, with n an integer) and also for an incommensurate SDW. The spin-wave modes for an odd-commensurate SDW are qualitatively different, but are not relevant to the case of Cr. The anisotropic velocity in Eq. (45) is proportional to the amplitude of the SDW and therefore in a mean-field theory varies with temperature T as $(T_N-T)^{1/2}$, T_N being the Néel temperature. Zhu and Walker note that Sato and Maki (1974) obtained the same result using a microscopic model, but to our knowledge this interesting prediction has not been tested experimentally.

Let us consider next the energy gap associated with itinerant antiferromagnetism, which may manifest itself as an AFM resonance. Sokoloff (1969a, 1969b, 1969c) showed that at zero temperature one should observe a peak at the energy gap Δ in the inelastic neutron scattering at the magnetic reciprocal-lattice point, or at the magnetic satellite in the case of an incommensurate SDW. This peak is due to an overdamped collective mode, which may be pictured as a weakly bound electron-hole pair having the same spin, which travels together through the lattice as an exciton. There is no evidence for this behavior in the neutron scattering (see Fig. 17). The optical absorption, however, which has the same form as the neutron scattering cross section for longitudinal spin fluctuations, does indicate an energy gap decreasing with temperature in the expected way as the Néel transition is approached (see Sec. V.C).

Fenton (1978) has discussed the possibility of antiferromagnetic resonance in chromium by analogy with the "internal Josephson effect" predicted for the superfluid phases of ^{3}He. The expressions for the resonant frequencies for a small time-dependent field $\mathbf{H}(t)$ applied parallel or perpendicular to the static field $\mathbf{H}_0$ involve the static susceptibility χ, the gyromagnetic ratio γ, and anisotropy energies K_1 and K_2 defined by Werner *et al.* (1967b) by the equation

$$E(\mathbf{S})=K_1\cos^2\theta+K_2\sin^2 2\phi \ , \tag{46a}$$

where

$$\theta=\mathbf{S}\wedge\mathbf{Q} \ \text{ and } \ \varphi=\mathbf{S}\wedge\mathbf{x} \ . \tag{46b}$$

Thus the K_1 term expresses the spin-flip anisotropy energy, which changes sign at T_{SF} (see Sec. VI.B), while the K_2 term corresponds to fourfold spin anisotropy energy in the plane perpendicular to $\mathbf{Q}$ (see Sec. II.B.2). The predicted frequencies ω_z for the longitudinal configuration, $\mathbf{H}(t)\|\mathbf{H}_0$, and ω_t for transverse, $\mathbf{H}(t)\perp\mathbf{H}_0$, in the transverse (TSDW) and longitudinal (LSDW) phases are given in Table VI in terms of the characteristic frequencies

$$\Omega_1^2=\frac{2\gamma^2|K_1|}{\chi} \ \text{ and } \ \Omega_2^2=\frac{8\gamma^2K_2}{\chi} \ . \tag{47}$$

Fenton estimates that these frequencies are in the far-infrared range.

3. Phenomenological models

The simple microscopic models described in Sec. IV.A.1 are successful in relating the fundamental properties of the SDW in chromium and its dilute AFM alloys to the Fermi-surface properties, namely, the single-$\mathbf{Q}$ nature and linear polarization of the SDW and the magnitude and direction of the wave vector $\mathbf{Q}$. When additional experimental information concerning the magnetic anisotropy (see Secs. II.B.2 and III.A) is employed to determine the full symmetry of the Landau-type free energy, a phenomenological model may be constructed that provides a framework for the discussion and correlation of many other properties, especially around the Néel temperature T_N and the spin-flip temperature T_{SF} (Shimizu, 1970; Walker, 1980a, 1980b). Some progress has been made towards calculating from microscopic models some of the terms in the phenomenological models, and references to this work are given by Walker (1980b) and Buker (1982).

In developing a phenomenological model to describe the behavior of Cr close to T_N, I follow Walker (1980b), who begins by writing the spin density

$$\mathbf{S}(\mathbf{r})=\mathbf{S}\exp(i\mathbf{Q}\cdot\mathbf{r})+\mathbf{S}^*\exp(-i\mathbf{Q}\cdot\mathbf{r}) \ , \tag{48}$$

where $\mathbf{S}$ is the complex polarization vector. Different choices for $\mathbf{S}$ describe different types of SDW, and in particular

$$\mathbf{S}=\tfrac{1}{2}S_0\hat{x},\mathbf{Q}=Q\hat{z} \tag{49}$$

gives a transverse linearly polarized SDW

$$\mathbf{S}(\mathbf{r})=\hat{x}S_0\cos(Qz) \ , \tag{50}$$

while the choice

$$\mathbf{S}=\tfrac{1}{2}S_0(\hat{x}-i\hat{y}), \quad \mathbf{Q}=Q\hat{z} \tag{51}$$

gives a helical SDW of positive helicity,

$$\mathbf{S}(\mathbf{r})=S_0[\hat{x}\cos(Qz)+\hat{y}\sin(Qz)] \ . \tag{52}$$

The state of the system and hence its free energy are expressed in terms of $\mathbf{S}$ and the wave vector $\mathbf{Q}$, which is written as a function,

$$\delta=\tfrac{1}{2}\mathbf{G}_0-\mathbf{Q} \ , \tag{53}$$

TABLE VI. Antiferromagnetic resonance frequencies predicted by Fenton (1978) for an itinerant-electron antiferromagnet.

Configuration		(Frequency)^2 ω_z^2	(Frequency)^2 ω_t^2
TSDW	$\mathbf{H}_0\|\mathbf{Q}$	Ω_2^2	$(\gamma H_0)^2+\Omega_1^2$
	$\mathbf{H}_0\perp\mathbf{Q},\mathbf{H}_0\perp\mathbf{S}$	Ω_1^2	$(\gamma H_0)^2+\Omega_2^2$
LSDW	$\mathbf{H}_0\|\mathbf{Q}$	0	$\frac{1}{2}\{\gamma^2H_0^2+\Omega_1^2\pm[\gamma^2H_0^2+\Omega_1^2)^2-\Omega_1^4]^{1/2}\}$
	$\mathbf{H}_0\|\mathbf{Q}$	Ω_1^2	$(\gamma H_0)^2+\Omega_1^2$

where $\frac{1}{2}\mathbf{G}_0 = 2\pi/a$ is the vector ΓH along the cube axis of the Brillouin zone (See Fig. 61 below). Since $\boldsymbol{\delta}$ is small and $\mathbf{S}$ also is small close to T_N, the free energy expanded in ascending powers of these quantities may be terminated at relatively low order,

$$F = F_0 + A(\boldsymbol{\delta})\mathbf{S}\cdot\mathbf{S}^* + B'(\mathbf{S}\cdot\mathbf{S}^*)^2 + B''\,|\,\mathbf{S}\cdot\mathbf{S}\,|^2 + C\sum_i \delta_i^2\,|\,S_i\,|^2 + E\sum_i |\,S_i\,|^4 . \quad (54)$$

F_0 is the free energy in the paramagnetic state, and i is summed over x, y, and z. The coefficients A, B', and B'' are functions of $\boldsymbol{\delta}$, but only A need be considered by expanding in powers of the components of δ,

$$A(\boldsymbol{\delta}) = A_0 + A_2\delta^2 + A_4'\delta^4 + A_4''(\delta_x^4 + \delta_y^4 + \delta_2^4) . \quad (55)$$

The terms in A, B', and B'' might be considered as exchange terms, since they are invariant with respect to arbitrary rotations of $\mathbf{S}$, whereas the terms in C and E, which couple the direction of $\mathbf{S}$ to the orientation of the lattice, are magnetic anisotropy terms. The assumption appears to work well in Cr that these magnetic anisotropy terms, which correspond to relativistic effects, are much smaller than the exchange terms,

$$|\,E\,| \ll |\,B\,|, |\,B'\,| \quad \text{and} \quad |\,C\,| \ll |\,A_z\,| . \quad (56)$$

If we neglect magnetic anisotropy as a first approximation and write $C = E = 0$, we see by minimizing $A(\boldsymbol{\delta})$ with respect to $\boldsymbol{\delta}$ that $A_2 < 0$ gives a nonzero value of $\boldsymbol{\delta}$, corresponding to an incommensurate SDW. If $A_4'' < 0$, $\boldsymbol{\delta}$ is in a $\langle 100 \rangle$ direction as observed in Cr, whereas $A_4'' > 0$ gives $\boldsymbol{\delta}$ in a $\langle 111 \rangle$ direction. If $B'' > 0$, a helical SDW has lowest energy, so we must choose $B'' < 0$, corresponding to the observed linearly polarized SDW. An early attempt by Shimizu (1970) to formulate a phenomenological theory of the SDW state in Cr had the defect that it could not account for the linearly polarized nature of the actual SDW (Walker, 1980a).

The polarization $\mathbf{S}$ of the SDW relative to $\boldsymbol{\delta}$ and to the lattice is determined by introducing the magnetic anisotropy terms, with $C > 0$ close to T_N giving the observed transverse SDW state. The spin-flip transition to the longitudinal SDW state is obtained by assuming C to be temperature dependent, with a change of sign at T_{SF}. The parameter E must be negative so as to give $\mathbf{S}$ in the transverse phase preferentially along $\langle 100 \rangle$ rather than along $\langle 110 \rangle$.

An interesting magnetic phase diagram (Barak *et al.*, 1981; Barak and Walker, 1981) is obtained by applying a magnetic field $\mathbf{H}$ to chromium in the vicinity of the spin-flip temperature T_{SF}, where there is a relatively small energy difference between the longitudinal and transverse SDW states so that $\mathbf{H}$ can change T_{SF} appreciably. With $\mathbf{H}$ in a direction close to a cube axis, an additional phase is obtained, which is associated with rotation of $\mathbf{S}$ away from the cube axis, since the magnetic energy term is a minimum for $\mathbf{S} \perp \mathbf{H}$. We shall discuss the magnetic phase diagram near T_{SF} in Sec. VI.B, Fig. 84.

The addition of terms involving crystal strains to Eq. (54) allows the study and correlation of a wide variety of effects involving magnetostrictive interactions, such as anomalies in the thermal expansion and elastic constants at both the Néel temperature T_N and the spin-flip temperature, stress cooling, and stress dependence of T_N (Barak and Walker, 1982). Here the identification of the various terms in the free energy as exchange terms (and thus relatively large) or as magnetic anisotropy terms (and thus relatively small) allows one successfully to classify the relative orders of magnitude of these magnetostrictive effects. Thus this mean-field analysis can explain why certain elastic constants undergo relatively large changes at T_N, but it does not give a quantitative description.

Specific predictions, which will be compared with experiment in Sec. VI.A.2, include the following.

(1) Changes $\Delta\alpha_i = \alpha_i^+ - \alpha_i^-$ of the three components of the thermal expansivity tensor are all positive and satisfy the inequalities

$$|\,\Delta\alpha_3 - \Delta\alpha_1\,|, |\,\Delta\alpha_2 - \Delta\alpha_1\,| \ll \Delta\alpha_1, \Delta\alpha_2, \Delta\alpha_3 , \quad (57)$$

where the subscript notation follows the convention of Fig. 36(b).

(2) Changes $\Delta\alpha_i$ in the thermal expansivity are related to changes ΔS_{ij} in components of the compliance tensor S_{ij} by the relations

$$\Delta\alpha_i \frac{dT_N}{d\sigma_j} = -\Delta S_{ij} , \quad (58)$$

where σ_i is a component of the stress tensor.

(3) Changes ΔC_{ii} $(i = 1,2,3)$ in the diagonal components of the stiffness tensor (i.e., the three Young's moduli), corresponding to the propagation of longitudinal sound waves along the three axes, are all positive and equal when higher-order magnetoelastic terms are neglected.

(4) Changes ΔC_{ii} $(i = 4,5,6)$ in the diagonal components of the stiffness tensor, corresponding to the propagation of shear sound waves along the three axes, are all zero.

(5) Changes ΔM_i $(i = 1,2,3)$ in the elastic moduli, corresponding to propagation of shear sound waves in the three $\{110\}$ directions as illustrated in Fig. 42, are much smaller than the changes ΔC_{ii} $(i = 1,2,3)$ in the elastic moduli along the axes.

The challenge to the microscopic theory is to obtain the correct signs for the parameters in Eq. (54). The microscopic origin of linear polarization of the transverse SDW corresponding to $B'' < 0$ is well understood as resulting from the nesting octahedral Fermi surface (Fenton, 1976a). A microscopic understanding of the change in sign of C, corresponding to the spin-flip transition, remains an outstanding problem (see Sec. VI.B).

B. Energy-band structure

1. Band structure of paramagnetic Cr

Asdente and Friedel (1961) calculated the d-band structure and Fermi surface of chromium using a crude form of the tight-binding method. They made drastic approximations concerning the crystal potential, the wave functions, and the matrix elements, but the feature of their calculation that resulted in their Fermi surface's being quite different from that of paramagnetic Cr (and the other group-VI metals Mo and W) was the neglect of hybridization with the s band.

The essential features of the Fermi surface of Cr illustrated in Figs. 57–59 below, which are based on a later band-structure calculation, were first inferred by Lomer (1962) from the results of a calculation of the band structure of iron (Wood, 1962). The portions of particular interest are the closed electron and hole surfaces centered on Γ and H, respectively, whose nesting was suggested by Lomer (1962) to be responsible for the incommensurate nature of the SDW in Cr. Other features of interest are the hole pocket around N and the electron lens along the ΓH axis. Similar surfaces were inferred for Cr by Mattheiss (1965) on the basis of his band-structure calculation for W.

The first band-structure calculation to demonstrate the existence of these features of the Fermi surface specifically in Cr was an augmented-plane-wave computation by Loucks (1965). He included the effects of exchange and correlation by using the approximation first introduced by Slater (1951), who proposed that such effects might be taken into account by means of a potential depending only on the local charge density $\rho(\mathbf{r})$. This $\rho^{1/3}$ potential has been extensively used in band-structure calculations, frequently multiplied by a parameter $\alpha \leq 1$ to yield the so-called $X\alpha$ potential (see Table XI below). Loucks's calculation was not carried to self-consistency, but this Fermi surface confirmed the essential features of Lomer's model, except that no hole pockets were obtained at N.

Loucks's value for the nesting vector was $\tilde{Q}=0.90a^*$, while the experimental value at low temperatures is $\mathbf{Q}=0.95a^*$. A better test of the calculation, however, is a comparison of the variations of $\tilde{Q}$ and $\mathbf{Q}$ with alloying. The addition of Mn to Cr increases the electron concentration and hence causes the electron surface to expand and the hole surface to contract. This should cause $\mathbf{Q}$ to increase, while the addition of V, on the other hand, should cause it to decrease. These qualitative predictions are in accord with the experimental results, as illustrated in Fig. 5. Koehler *et al.* (1966) estimated quantitatively the change in $\tilde{Q}$ from the work of Loucks, since he calculated the shape and volume of energy surfaces near the Fermi surface. Application of the rigid-band model to his results suggests that $\tilde{Q}$ should change by approximately 1% for each 1 at.% V or Mn added. The experimental results show roughly twice this rate of change of $\mathbf{Q}$. Again this discrepancy is probably within the calculational error, particularly as $\tilde{Q}$ is not calculated quite correctly for pure Cr. Indeed, if one takes as the Fermi surface for Cr the set of energy surfaces that give the correct $\tilde{Q}$, its rate of change with alloying is almost correctly predicted. Since the volume compensation of electrons and holes is then lost, however, this calculation is not particularly meaningful.

Asano and Yamashita (1967) used the Korringa-Kohn-Rostoker (KKR) method to calculate the band structures of both paramagnetic and AFM Cr and carried their calculations to approximate self-consistency. They include exchange by using the $X\alpha$ potential with $\alpha=1$ ($\alpha=0.5$ was used for the AFM calculation—see Table IX below) and also imposed a correlation correction.

The most extensive calculations of the band structure of Cr was performed by Rath and Callaway (1973) and Laurent *et al.* (1981), who employed the linear combination of Gaussian orbitals (LCGO) method. This method was developed over a period of years by these authors and others and applied to a number of metals (see Laurent *et al.*, 1981 for references). The important considerations were self-consistency, accurate treatment of crystal potentials, an appropriate choice of exchange potential, and a calculational procedure that provides wave functions in a convenient form for further applications—in particular for the eventual calculation of the wave-vector-dependent susceptibility $\chi(\mathbf{q})$ (see Sec. IV.B.3). The later calculation improved on the earlier by the addition of f orbitals to the basis, improved convergence procedures for lattice sums, and a more accurate calculation of the Fourier transform of the exchange potential, and should be regarded as the definitive band-structure calculation for paramagnetic Cr. It was the basis of the calculation described in Sec. IV.B.3 of Zhao *et al.* (1987) of the wave-vector-dependent susceptibility $\chi(q)$ including many-body effects, which without adjustable parameters gave a singularity in $\chi(q)$ indicating antiferromagnetism with SDW wave vector equal to the observed value.

Figure 54 shows the results of Rath and Callaway (1973) for the nesting vector $\tilde{Q}$, since similar data were not reported for the later calculation. The quantity $\tilde{\delta}$, defined in Eq. (1), ranges from 0.024 to 0.055 in the (001) plane through the origin Γ in Fig. 59, with $\tilde{Q}$ taken to be along [001], and from 0.026 to 0.037 in a plane displaced along $\tilde{Q}$ by $a^*/24$. The value of the wave vector $\mathbf{Q}$ of the SDW corresponds to $\delta=0.037$ near the Néel temperature and $\delta=0.048$ at low temperatures, as illustrated in Fig. 5.

Laurent *et al.* (1981) employed two different exchange potentials which resulted in quite similar band structures (see Table VII), one of which is illustrated in Fig. 55. The corresponding density of states $N(E)$ as a function of energy E is shown in Fig. 56, E_F indicating the Fermi energy. Computer-generated sections of the Fermi surface are shown in Fig. 57 and should be compared with the well-known picture shown in Fig. 58. The (100) and

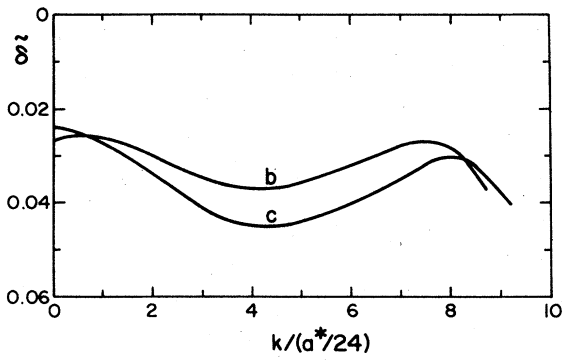

FIG. 54. Variation of the nesting vector $\tilde{Q}=(0,0,1-\tilde{\delta})$ between the electron and hole surfaces centered on Γ and H, respectively (see Fig. 59). The origin of $\tilde{Q}$ is on the line of intersection of the (001) plane through the origin, giving curve b, and in a plane displaced along $\tilde{Q}$ by $a^*/24$, giving curve c (after Rath and Callaway, 1973).

(110) cross sections through the origin in an extended zone scheme are shown in Figs. 59 and 60, respectively. Figure 57(a) shows clearly the electron balls along ΓH which, together with the roughly octahedral electron surface centered on Γ, form the electron "jack." The electron lens along ΓH, shown shaded in Fig. 59, touches the electron jack. Spin-orbit interaction will resolve the degeneracy at the point of contact and also the degeneracy at the point of contact between the electron jack and the hole surface centered on H, shown shaded in Fig. 58. The spin-orbit splitting is very small in Cr, but it has been observed in Mo, and in W it is so large that the electron lens is completely eliminated (see the review by Mackintosh and Andersen, 1980). The body of the electron jack centered on F and the hole surface centered on H are approximately octahedral, with almost plane faces, which are separated by the nesting vector $\tilde{Q}$ having approximately the same value as the wave vector $\mathbf{Q}$ of the SDW in Rath and Callaway's (1973) calculation (see Fig. 54). The nesting octahedra models discussed in Sec. IV.A.1 are based on this feature of the Fermi surface of Cr.

We shall see in Sec. V.B how a good deal of information about the Fermi surface of paramagnetic Cr can be obtained from measurements of the de Haas–van Alphen effect, which are necessarily made at liquid-helium temperatures where Cr is AFM. It is appropriate, however, to compare here the theoretical Fermi surface of paramagnetic Cr with experimental calipers provided by Kohn anomalies observed in the dispersion relations.

The experimental data of Shaw and Muhlestein (1971) shown in Fig. 34 were measured by inelastic neutron scattering at room temperature, where Cr is AFM. Møller and Mackintosh (1965) had shown, however, that the dispersion relations were essentially unchanged between temperatures 100 and 400 K, well below and above, respectively, the Néel temperature $T_N \simeq 311$ K. Thus the Kohn anomalies shown in Fig. 34 may be related to the nesting properties of the Fermi surface of paramagnetic Cr, as shown in Fig. 60.

The values listed in Table VII show reasonably good agreement between experiment and theory, though in some cases the identification of the Kohn anomaly with a nesting vector is rather tentative. In particular, the Kohn anomaly indicated by the arrow labeled b in Fig. 34 was identified by Shaw and Muhlestein (1971) with the nesting vector between the electron and hole octahedra, but its position at about $0.85\Gamma H$ gives a nesting vector $\tilde{Q}=0.85a^*$, somewhat smaller than the wave vector of the spin-density wave, $Q=0.95a^*$. Laurent *et al.* (1981) identify this anomaly with the ΓH extremum of the electron jack, but this seems unlikely. They suggest that a magnon-phonon interaction is involved which obscures the Kohn anomaly corresponding to the wave vector Q.

Laurent *et al.* (1981) also compare their Fermi surface with de Haas–van Alphen data, but a discussion of this comparison is deferred until Sec. V.B. They use their

TABLE VII. Dimensions of the Fermi surface of chromium. The direction and position of the Kohn anomalies are shown in Fig. 34. The theoretical values of the Fermi-surface nesting vectors a, b, c, d, and e correspond to calculations performed by Laurent *et al.* (1981) using the KSG potential (Kohn and Sham, 1965; Gaspar, 1954) and the VBH potential (von Barth and Hedin, 1972). The experimental values are obtained from the work of Shaw and Muhlestein (1971) and Muhlestein *et al.* (1972a, 1972b) as quoted by Laurent *et al.* (1981, Table II). The Fermi-surface nesting vectors are shown in Fig. 60 and are identified in the table with the Kohn anomalies similarly identified in Fig. 34.

Fermi-surface nesting vector	Experiment Kohn anomaly	Theory KSG	Theory VBH
[111] extremum of ball on electron jack $---d$	0.50 ΓP	0.54	0.52
[001] see text	0.85 ΓH	0.82	0.83
[011] nesting of electron jack body and hole at $N---a$	0.90 ΓN	0.84	0.84
[111] nesting of electron jack ball and hole $N------e$	0.54 ΓH	0.54	0.54
[111] nesting of electron jack body and hole at $H---c$	0.94 ΓH	0.98	0.99

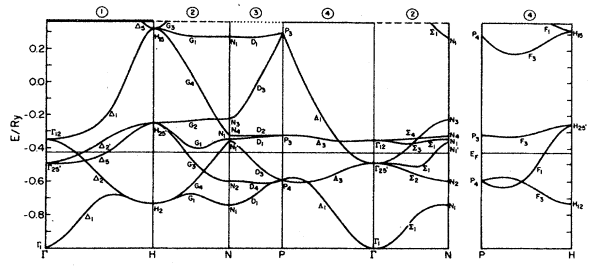

FIG. 55. Energy bands of chromium (KSG potential—see Table VII) along lines of high symmetry. The panels are coded for comparison with Figs. 62 and 63 in accordance with Fig. 61 (after Laurent *et al.*, 1981).

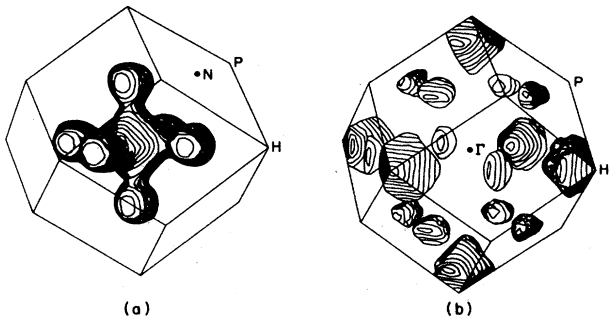

FIG. 57. Fermi surface of chromium: (a) electron "jack"; (b) hole surfaces around H and N (after Laurent *et al.*, 1981).

calculated wave functions to determine the x-ray form factor, the Compton profile, and the optical conductivity of Cr. The agreement with experiment is quite good, as, for example, in a comparison of the spherically averaged Compton profile with the experimental data of Paakari *et al.* (1975); Ohara *et al.* (1974) also measured the anisotropy of the Compton profile. I shall not discuss these features of the electronic structure, however, since they are remote from our particular concern with the properties of AFM Cr.

Pattnaik *et al.* (1983) determined the volume dependence of the Fermi surface of Cr by choosing a set of Slater-Koster parameters to make an optimal fit to the band structure calculated by Laurent *et al.* (1981) at the experimental lattice constant a_{0e}; they then used the parameters to generate a band structure for a_{0e} and for $0.99a_{0e}$. I shall discuss their results in Sec. V.B.

2. Band structure of commensurate antiferromagnetic Cr

The first calculation of the energy-band structure of commensurate AFM Cr was performed by Switendick (1966), who used full Slater exchange, the $X\alpha$ potential with $\alpha=1$, and obtained a large magnetic moment, $\mu_0 > 3\mu_\beta$, as self-consistency was approached. It has since become clear that the reason for this failure to obtain a value in agreement with the much smaller experimental moment is the fact that the use of full Slater exchange in fact neglects correlation, and therefore gives too strong a tendency towards magnetism (Gunnarsson, 1976). Asano and Yamashita (1967) considered, like Switendick, a hypothetical AFM state with wave vector $\mathbf{Q}=\frac{1}{2}a^*$ and obtained a Fermi surface consistent with Lomer's model. They obtained a moment $\mu_0=0.6\mu_B$, equal to the observed peak value $\mu_0=0.62\mu_B$, for the SDW in chromium for a rather low value of the parameter $\alpha=0.5$, in the $X\alpha$ potential. Their Fermi surface for commensurate AFM Cr was supported by later de Haas–van Alphen

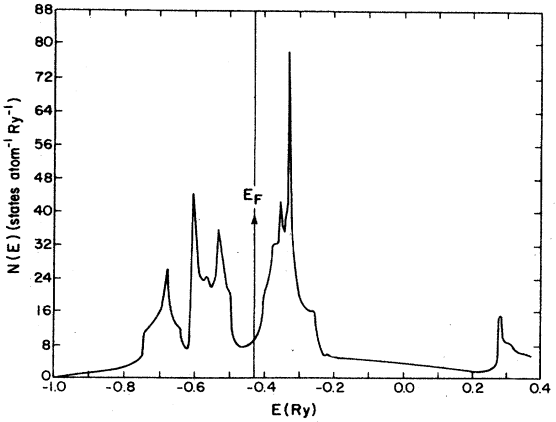

FIG. 56. Density of states of chromium (after Laurent *et al.*, 1981).

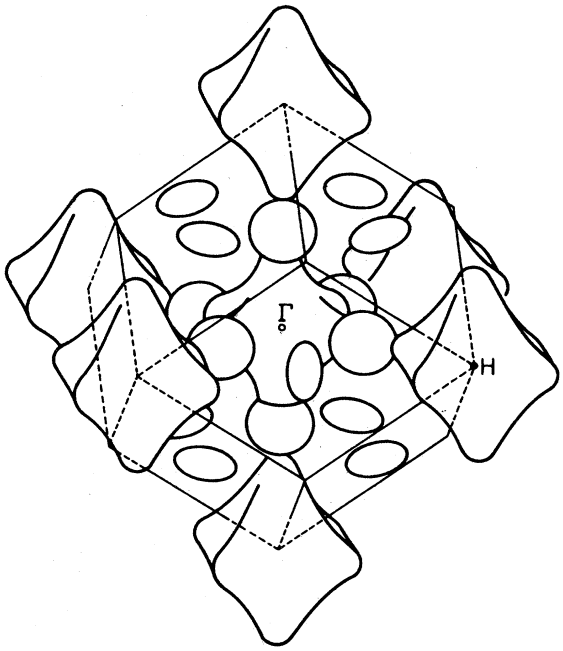

FIG. 58. Fermi-surface sketch for Cr, Mo, and W (after Mattheiss, 1965).

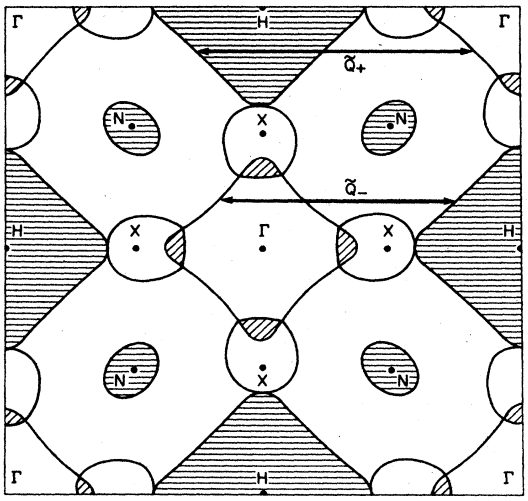

FIG. 59. Fermi-surface cross section: (100) plane (after Laurent *et al.*, 1981). Typical nesting vectors, $\tilde{Q}_\pm=(0,0,1\pm\tilde{\delta})$, between the Γ and *H* surfaces are shown.

measurements of Graebner (1971) on the commensurate AFM alloy Cr + 1.76 at. % Mn.

Three calculations (Kübler, 1980; Skriver, 1981; Kulikov and Kulatov, 1982) have been performed in the local spin-density approximation (LSDA) to the density functional theory of Kohn and Sham (1965). This formalism contains no adjustable parameters and is therefore more satisfying than a calculation using an adjustable exchange potential. The input to the calculations is simply the atomic numbers of Cr and its crystal structure. The lattice constant a_0 is obtained from the minimum of the total energy, or equivalently from the equation of state with pressure set equal to zero. The values of a_0 and the bulk modulus B_0 in the ground state are compared with experiment, as well as the magnetic moment μ_0, to provide criteria for the success of the calculations.

Kübler (1980) did three sets of calculations in which the ground state is assumed to be (a) nonmagnetic (called paramagnetic, *P*-Cr) with a bcc unit cell and the Brillouin zone shown in Fig. 61. (b) ferromagnetic (*F*-Cr) with the same unit cell, and (c) commensurate antiferromagnetic (AFM-Cr) with a simple cubic unit cell giving a simple cubic Brillouin zone, as shown by the dashed lines in Fig. 61. For the calculation of *F*-Cr the converged potential calculated for *P*-Cr is used to generate two potentials $V_\uparrow$ and $V_\downarrow$ by applying a magnetic field, the spin-up and spin-down electrons, respectively, being treated independently in these potentials. The magnetic field is removed, and in the subsequent iterations the system is found to relax to equilibrium at the paramagnetic state *P*-Cr.

This result is to be expected, since the density of states at the Fermi surface is so low, as shown in Fig. 56. Skriver (1981) points out that this means that ferromagnetism does not occur, despite the fact that the effective Stoner exchange interaction in Cr given in Table X is comparable in magnitude with that in the ferromagnetic metals Fe, Co, and Ni (Gunnarsson, 1976). It is interesting to note that a calculation by Pindor *et al.* (1983), using a Korringa-Kohn-Rostoker coherent-potential approximation, similarly gave no self-consistent disordered-local-moment state for Cr, whereas Fe, Co, and Ni did develop local magnetic moments.

In the AFM-Cr calculation the spin is either up (↑) or down (↓) at the body-center and body-corner atomic sites, labeled α and β. Thus quantities $n(r)$ and $m(r)$

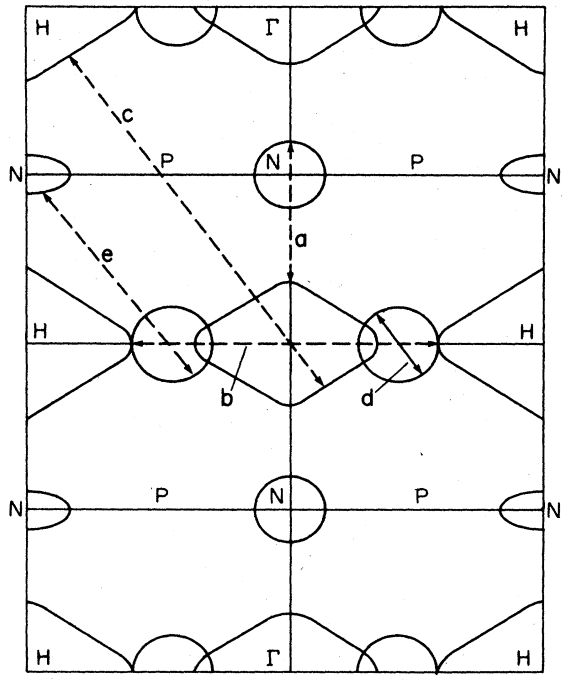

FIG. 60. Fermi-surface cross section: (110) plane (after Laurent *et al.*, 1981). Nesting vectors identified in Fig. 34 and in Table VII are shown.

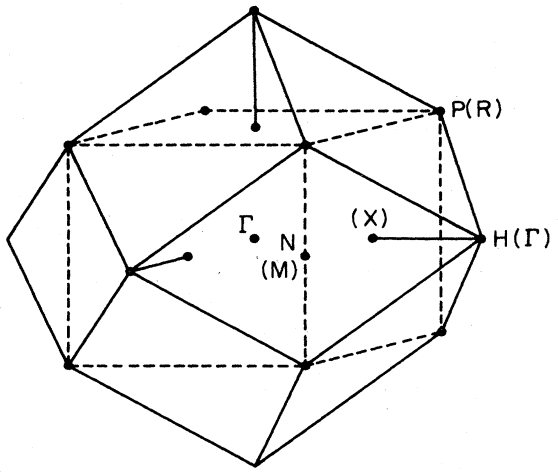

FIG. 61. Simple cubic Brillouin zone of commensurate AFM-Cr (dashed lines) inscribed inside the bcc Brillouin zone of nonmagnetic *P*-Cr.

proportional to the charge density and magnetic moment, respectively, at the two atomic sites may be written

$$n_\alpha(r)=n_{\uparrow\alpha}+n_{\downarrow\alpha}=n_{\uparrow\beta}+n_{\downarrow\beta}=n_\beta(r)\ , \tag{59a}$$

$$m_\alpha(r)=n_{\uparrow\alpha}-n_{\downarrow\alpha}=-n_{\uparrow\beta}+n_{\downarrow\beta}=-m_\beta(r)\ . \tag{59b}$$

This leads to the relations

$$n_{\uparrow\alpha}=n_{\downarrow\beta} \quad \text{and} \quad n_{\downarrow\alpha}=n_{\uparrow\beta}\ , \tag{60}$$

which in conjunction with the LSDA formalism give rise to similar relations among the one-electron potentials

$$V_{\uparrow\alpha}=V_{\downarrow\beta} \quad \text{and} \quad V_{\downarrow\alpha}=V_{\uparrow\beta}\ . \tag{61}$$

This implies that the two spin bands are degenerate, while the sublattice magnetic moment defined by

$$m=\int_{\text{sphere }\alpha} m_\alpha(r)4\pi r^2 dr \tag{62}$$

is determined by the properties of the site-decomposed density of states, as shown in Fig. 64 below. Thus it is necessary to calculate only the spin-up bands, say, and then use the relations

$$n_\alpha(r)=n_{\uparrow\alpha}+n_{\uparrow\beta}\ , \tag{63a}$$

$$m_\alpha(r)=n_{\uparrow\alpha}-n_{\uparrow\beta}\ . \tag{63b}$$

The resultant energy bands of AFM-Cr are shown in Fig. 62 and are to be compared with energy bands of *P*-Cr folded back into the simple cubic Brillouin zone (see Fig. 61). To assist in this comparison the various panels of Figs. 62 and 63 are coded. Figure 63 should also be compared with the energy-band structure of paramagnet-

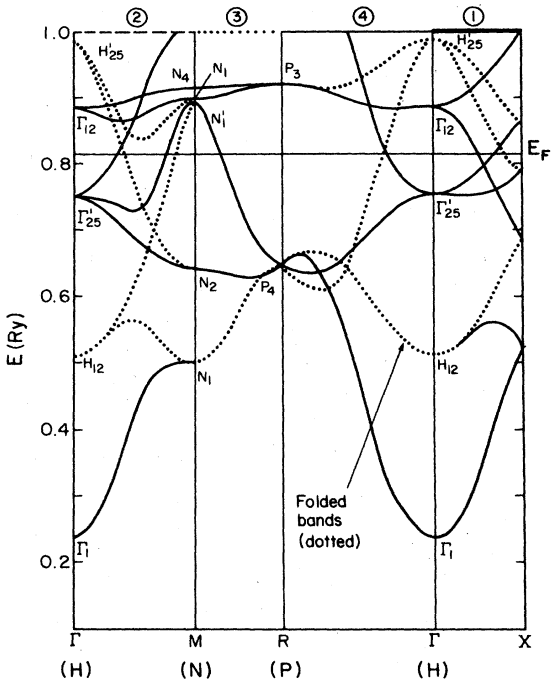

FIG. 63. Energy-band structure of nonmagnetic *P*-Cr folded back into the simple cubic Brillouin zone (after Kübler, 1980).

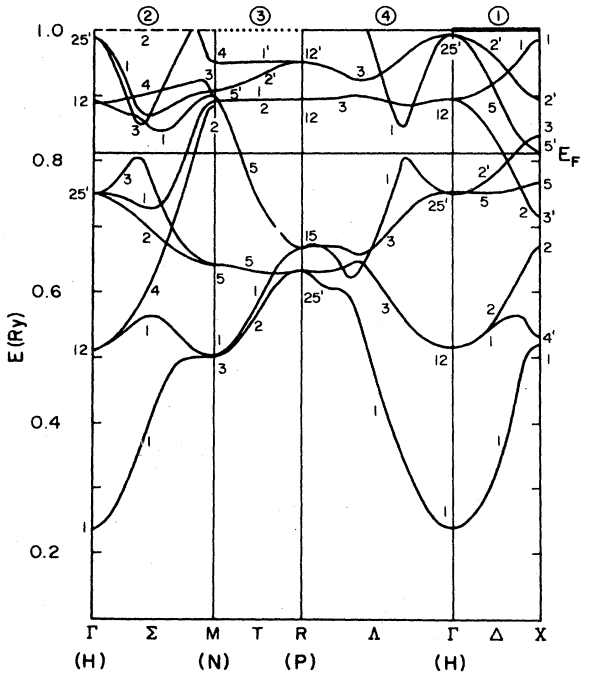

FIG. 62. Energy-band structure of commensurate AFM-Cr at the experimental lattice constant (after Kübler, 1980).

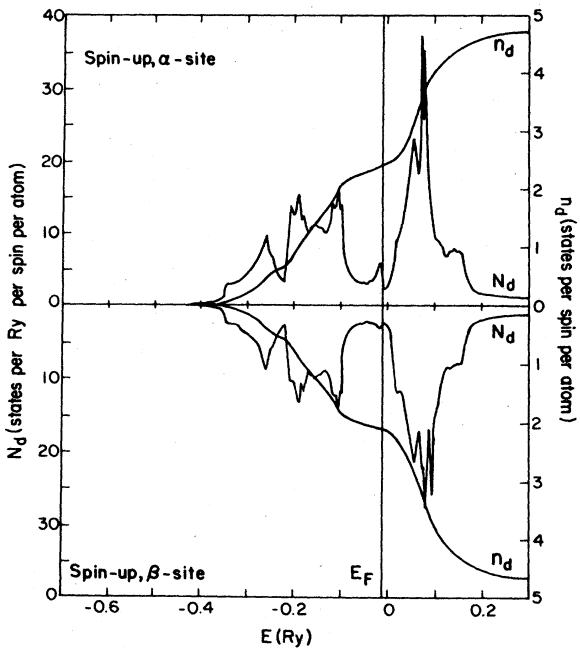

FIG. 64. Site-decomposed *d*-band density of states $N_d(E)$ and number of states $n_d(E)$ below energy E for commensurate AFM-Cr at the experimental lattice constant (after Skriver, 1981).

ic Cr shown in the bcc Brillouin zone in Fig. 55, which is similarly coded.

Skriver (1981) obtained a very similar energy-band structure for AFM-Cr, and we show in Fig. 64 his results for the site-decomposed (or equivalently spin-decomposed) density of states $N_d(E)$ for the d electrons. Table VIII shows that in fact the magnetism is almost entirely associated with the d electrons.

Kübler (1980) repeated the calculations for nonmagnetic P-Cr and commensurate AFM-Cr at three different lattice constants, and thus minimized the total energy so as to determine the equilibrium lattice constant a_0, the cohesive energy E_{co}, and bulk modulus B, as well as the magnetic moment m defined in Eq. (52) and its volume derivative. The results are given in Table IX, together with the nesting vector $\tilde{Q}$, which is seen to deviate slightly from the commensurate value $a^*=2\pi/a$ by the fact that in the ΓM panel of Fig. 63 the two electron bands intersect at a point slightly above the Fermi energy, forming a small triangle with the E_F line, whose base is $\tilde{\delta}=\hat{1}-\tilde{Q}$. Figure 62 shows that in AFM-Cr an energy gap E_g is formed at this point, whose magnitude and volume derivative are given in Table IX. A similar energy gap is formed along $\Gamma R(HP)$, and the depression of the occupied states below these gaps leads to AFM-Cr's being energetically favorable, relative to P-Cr, as the ground state for chromium. These gaps are responsible for the rapid variation of the density of states in the neighborhood of the Fermi energy seen in Fig. 64.

Let us now turn again to the work of Skriver (1981), who followed a somewhat different procedure from Kübler (1980) and calculated the equation of state. He thus obtained the pressure P and bulk modulus B as well as the moment m, all as functions of volume, or equivalently of the radius S of the Wigner-Seitz spheres $S=\frac{1}{2}(\pi/3)^{1/3}a$, a being the lattice constant.

Figure 65 shows that, while the equation of state is in reasonably good agreement with experiment, the calculated value of the lattice constant corresponding to zero pressure is about 2% less than the experimental value. A discrepancy in the same sense and of about the same magnitude is also found in calculations in the LSDA for ferromagnetic metals (Pettifor, 1980). In the case of AFM-Cr, however, the most disturbing feature of this discrepancy is that, at the calculated lattice constant a_0, the value of the sublattice magnetic moment is not only considerably less than its experimental value, but the calculation is not fully converged (Skriver, 1985). It should be noted that Kübler's (1980) calculated value of a_0 for AFM-Cr also is about 1% less than the experimental value. Skriver (1985) suggests that these discrepancies may mean that commensurate AFM-Cr is in fact not an equilibrium state: the additional energy gained from the energy gaps associated with the incommensurate SDW may be required to stabilize antiferromagnetism in Cr.

Skriver (1981) developed a Stoner picture for AFM-Cr analogous to the ferromagnetic picture, in which the two spin bands are exchange split by an amount $\Delta=mI$, where m is the magnetic moment and I an effective Stoner interaction parameter in the LSDA. In the AFM case the Stoner I may be defined through the relation

$$mI=C_{\downarrow\alpha}-C_{\uparrow\alpha}=C_{\uparrow\beta}-C_{\uparrow\alpha}\ , \tag{64}$$

where m is the sublattice magnetic moment defined in Eq. (62) and $C_{\sigma t}$ is the center of the d band of spin σ for atom t.

Skriver (1981) points out that the low value $N(E_F)=8.2$ states Ry^{-1} of the density of states at the Fermi surface gives a value $IN(E_F)=0.50$, well below the condition for the onset of ferromagnetism,

$$IN(E_F)=1\ , \tag{65}$$

for the value $I=60.3$ mRy thus obtained; but that the similar condition for antiferromagnetism is

$$I\chi_0(Q)=1\ , \tag{66}$$

where $\chi_0(Q)$ is the maximum value of the wave-vector-dependent susceptibility $\chi_0(q)$, so that the exchange-enhanced susceptibility in the random-phase approximation given in Eq. (74) becomes infinite. Skriver (1981) presents a simplified version of condition (66) valid for

TABLE VIII. The l-projected and site-decomposed number of states n_l below the Fermi energy E_F and density of states $N_l(E_F)$ at the Fermi level at the experimental lattice constant a in nonmagnetic P-Cr and commensurate AFM-Cr (after Skriver, 1981). The experimental lattice constant at room temperature, $a=2.884$ Å $=5.451$ Au, is hardly significantly different from the value $a_{0e}=2.881$ at low temperature (White *et al.*, 1986). Skriver (1981) quotes a Wigner-Seitz radius, $S=2.684$ Au, as the experimental value, which corresponds to the room-temperature lattice constant 2.884 Å also used by Kübler (1980), while Kulikov and Kulatov (1982) use a somewhat smaller value, 2.880 Å.

			AFM-Cr	
	Orbital	P-Cr	Spin-up ↑	Spin-down ↓
n_l (states per atom spin)	s	0.31	0.31	0.31
	p	0.41	0.41	0.41
	d	2.28	2.42	2.13
$N_l(E_F)$ (states per Ry atom spin)	s	0.03	0.03	0.02
	p	0.48	0.47	0.46
	d	3.62	2.55	2.28

TABLE IX. Ground-state properties of nonmagnetic *P*-Cr and commensurate AFM-Cr at the calculated equilibrium lattice constant a_0 (after Kübler, 1980).

	a_0	a_{0e}	E_{c0} (Ry)		B (GPa)		m (μ_B)		$d\ln m/d\omega$		E_g (Ry)		$\tilde{Q}a^*$		$d\ln\tilde{Q}/d\omega$	
	Calc.	Expt.	Calc.	Expt.	Calc.	Expt.	Calc.	Expt.	Calc.	Expt.	Calc.	Expt.	Calc.	Expt.	Calc.	Expt.
P-Cr	2.854		−0.335		255								0.950		0.03	
AFM-Cr	2.855	2.882	−0.339	−0.301	213	190	0.59	0.62[a]	11[b]	32[c]	0.037			0.952		d

[a] This is the amplitude μ_0 of the SDW in chromium at low temperature (see Sec. II.B.4), but perhaps the rms value $0.43\mu_\beta$ is more appropriate.
[b] Kübler (1980) gives $d\ln m/dp = 50\ \text{GPa}^{-1}$, which we have converted to a volume dependence by using his calculated value for the bulk modulus, $B = 213$ GPa, but note that here and in Fig. 11 we give the correct low-temperature value, $B = 190$ GPa (Palmer and Lee, 1971).
[c] Here we use the experimental value $B = 162$ GPa, close to the Néel temperature (Bolef and de Klerk, 1963).
[d] See Sec. V.B.

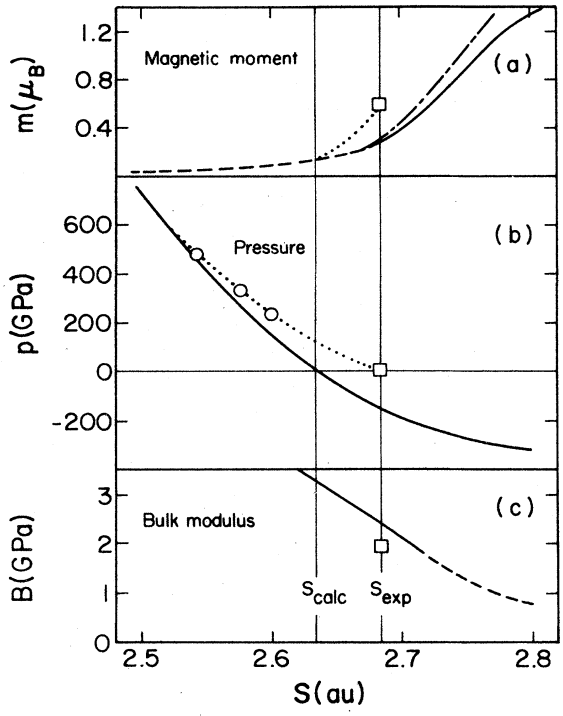

FIG. 65. Comparison between calculated and experimental sublattice magnetic moment m, pressure p, and bulk modulus B. □, experimental values, $\mu_0 = 0.62\mu_B$ (a more appropriate value might be the rms moment $0.43\mu_B$ in Cr) and $B = 190$ GPa, at the room-temperature experimental Wigner-Seitz radius, $S_{\text{exp}} = 2.684$ Au corresponding to the lattice parameter $a = 2.881$ Å; ○, results of shock measurements. Dotted curves show the experimental variation of p and of m, as explained in the text. Solid curves represent results of fully self-consistent calculations, while dashed curves represent estimates that are not fully converged. The dot-dashed curve shows the result of a Stoner theory (after Skriver, 1981). The vertical line at the calculated $S_{\text{calc}} = 2.633$ Au, corresponding to zero pressure, is also shown.

commensurate AFM-Cr, i.e., for $\mathbf{q} = (001)a^*$, and the resultant hybridized Stoner theory gives results shown by the dot-dashed curve in Fig. 65.

The Stoner theory is useful for testing the accuracy of the LSDA calculations. Thus it is found that the sublattice magnetic moment m is very sensitive to the value of the effective Stoner interaction parameter I, an increase of I from 60.3 to 64 mRy, increasing m from $0.29\mu_\beta$ to $0.6\mu_B$ at the experimental lattice constant in Fig. 65. This might suggest that the difficulty mentioned above in obtaining the correct moment in calculations for AFM-Cr might be due simply to the manner in which exchange and correlation are included in the LSDA. Various calculations, including several with different varieties of the LSDA, seem, however, to favor a somewhat lower value of I, as indicated in Table X.

It should be noted that the general energy scale of the band structure of Cr, like the Stoner parameter in the LSDA, varies rather little for the many band-structure

TABLE X. Effective Stoner interaction parameter I and the susceptibility $\chi(\mathbf{Q})$ at the commensurate wave vector $\mathbf{Q}=(001)a^*$ for AFM-Cr (after Skriver, 1981).

	a	b	c	d	e	f	g	h
I (mRy)	60.3	56	62	51	55	68		
$\chi(\mathbf{Q})$ (states mRy^{-1})	>0.017	~ 0.020					~ 0.014	~ 0.010

[a] Skriver (1981).
[b] Asano and Yamashita (1967, 1971).
[c] Janak (1977)—"exact" value.
[d] Glötzel *et al.* (1981).
[e] Kulikov and Kulatov (1982).
[f] Kulikov *et al.* (1987).
[g] Gupta and Sinha (1971) at an incommensurate **Q**.
[h] Windsor (1972)—see Fig. 67.

calculations that have been performed, as seen in Table XI. The values obtained for the density of states at the Fermi surface, also given in Table XI, vary over a wider range.

Electronic structure calculations for metastable fcc Cr performed by Xu *et al.* (1984) show that, unlike bcc Cr, whose Fermi energy is near a minimum in the density of states (see Fig. 56), fcc Cr has one of the highest densities of states of fcc metals. However, the Stoner factor, $IN(E_F)=0.82$, is too low for ferromagnetic order, according to the condition (65).

Ukai and Mori (1982) and Nakao *et al.* (1986) have obtained, by means of a tight-binding calculation, remarkably good agreement with the observed properties of Cr, in particular the value of the incommensurability parameter δ and its dependence on electron concentration in dilute alloys and on pressure, and the concentration dependence of the spin-flip temperature T_{SF}. They evaluate the energy corresponding to long-period commensurate SDW and find that a periodicity of 21 lattice spacings, i.e., the closest commensurate period corresponding to the observed low-temperature value $\delta=0.047$ (Werner *et al.*, 1967a), has a lower energy E_{21} than neighboring periods of 12 and 23 lattice spacings. They evaluate the free energy at finite temperatures by including an entropy term, following an unspecified procedure, and discriminate between the energies of the longitudinal SDW and transverse SDW states by including a spin-orbit interaction.

Ukai and Mori (1982) find that the spin-flip transition in Cr is at temperature $100<T_{SF}<150$ K, and that the depression of T_{SF} in dilute CrV and CrMn alloys is reproduced, as well as the increase of δ in CrV and decrease in CrMn, with an incommensurate-commensurate

TABLE XI. The principal characteristics of the energy-band structure and of the density of states $N(E_F)$ at the Fermi surface of chromium from various calculations (after Kulikov and Kulatov, 1982). Note abbreviations: KKR, Korringa-Kohn-Rostoker; LCGO, linear-combination Gaussian orbitals; LSDA, local spin-density approximation.

Method and authors	Occupied d band E_F-H_{12} (Ry)	Total d band H'_{25}-H_{12} (Ry)	Fermi energy E_F-Γ_1 (Ry)	$N(E_F)$ (states Ry^{-1}) P-Cr	AFM-Cr
KKR, $X\alpha$, $\alpha=0.5$ (AFM-Cr) Asano and Yamashita (1967)	0.323	0.485	0.518	12.1	8.6
Model Hamiltonian, $X\alpha$, $\alpha=0.75$ (AFM-Cr) Yasui *et al.* (1970)	0.245	0.467	0.500	17.8	
LCGO, $X\alpha$, $\alpha=\frac{2}{3}$ Rath *et al.* (1973)	0.299	0.481	0.536	9.6	
KKR, von Barth–Hedin (1972) exchange Moruzzi *et al.* (1978)	0.353		0.568	9.5	
KKR, $X\alpha$, $\alpha=1$ Kulikov (1979)	0.305	0.451	0.508		
LSDA, Hedin-Lundquist exch. (AFM-Cr) Kübler (1980)	0.31	0.48	0.58	10.1	8.7
LSDA, von Barth–Hedin exch. (AFM-Cr) Skriver (1981)	0.33	0.50	0.62	8.2	5.8
KKR, Hedin-Lundquist exch. (AFM-Cr) Kulikov and Kulatov (1982)	0.336	0.519	0.611	7.5	3.8
LMTO, von Barth–Hedin exchange with self-energy correction (AFM-Cr) Kulikov *et al.* (1987)	0.31		0.57		9.2

transition with increasing temperature in the latter, as observed experimentally. Nakao *et al.* (1986) reproduce the observed temperature and pressure dependence of δ.

I am skeptical of these results of Mori and his collaborators, since the energy differences are incredibly small, e.g., Nakao *et al.* (1986) find that $E_{19}-E_{21}=0.3$ μRy/atom and $E_{23}-E_{21}=2.1$ μRy/atom, with $E\simeq 0.45$ Ry/atom. In any case, the physical origin of the results is obscure in these calculations.

3. Wave-vector-dependent susceptibilities $\chi_0(\mathbf{q})$ and $\chi(\mathbf{q})$

We saw in Sec. IV.B.2 how important the nesting of the Fermi surface in Cr is in producing a maximum in $\chi_0(\mathbf{q})$, and hence satisfying in the random-phase approximation the condition (66) for antiferromagnetism at some incommensurate wave vector $\mathbf{Q}$. The wave-vector-dependent susceptibility in this section will be denoted $\chi_0(\mathbf{q})$, and $\chi(\mathbf{q})$ will be used for the exchange-enhanced susceptibility. The homologous metal Mo (and presumably also W) has a similar maximum in $\chi_0(\mathbf{q})$, since the Fermi surfaces of these metals are similar to that of paramagnetic Cr (Mackintosh and Andersen, 1980). The Stoner exchange interaction parameter I is smaller, however, in the 4*d* and 5*d* metals than in the 3*d* metals, where the densities of states, and hence exchange and correlation effects, are stronger (Moruzzi *et al.*, 1978; Glötzel *et al.*, 1981).

Zhao *et al.* (1987) have used a tight-binding formulation to compute, following the theory of Callaway *et al.* (1983), the many-body exchange-correlation-enhanced wave-vector-dependent susceptibility $\chi(\mathbf{q})$ of Cr and the transition metals around Cr in the periodic table. They find that Cr is AFM, while V and Mo are clearly paramagnetic. The other 3*d* metal calculated was Mn, which appears also to be AFM for both bcc and fcc structures. The complexity of these formidable calculations is so great as to obscure the physics. I shall therefore first describe the much simpler calculation of Windsor (1972), which is physically transparent and has considerable heuristic value.

Windsor considered perturbation of the system by a staggered magnetic field

$$\mathbf{H}(\mathbf{r})=\mathbf{H}_{\mathbf{q}}e^{i\mathbf{q}\cdot\mathbf{r}}\ , \tag{67}$$

which produces a magnetization in a linear-response theory

$$\mathbf{M}(\mathbf{r})=\mathbf{M}_{\mathbf{q}}e^{i\mathbf{q}\cdot\mathbf{r}}\ . \tag{68}$$

The wave-vector-dependent susceptibility in general is a tensor relating the vectors $\mathbf{H}_{\mathbf{q}}$ and $\mathbf{M}_{\mathbf{q}}$, but we can simplify the problem by considering $\mathbf{H}_{\mathbf{q}}$ to be along a symmetry axis, such that $\mathbf{M}_{\mathbf{q}}\|\mathbf{H}_{\mathbf{q}}$, and write $\chi_0(\mathbf{q})$ as a scalar,

$$\chi_0(\mathbf{q})=\frac{1}{(\frac{1}{2}g\mu_B)^2}\frac{M_{\mathbf{q}}}{H_{\mathbf{q}}}\ , \tag{69}$$

where $g=2$, since we are considering in this case spin susceptibility. Windsor (1972) used a Lindhard summation over points $\mathbf{k}$ within the Brillouin zone to evaluate $\chi_0(\mathbf{q})$ numerically,

$$\chi(\mathbf{q})=\sum_{\mathbf{k}}\sum_{\mu\nu}\frac{n^{\nu}_{\mathbf{k}+\mathbf{q}}-n^{\mu}_{\mathbf{k}}}{E_{\mathbf{k}+\mathbf{q}}-E_{\mathbf{k}}}\,|\,M^{\mu\nu}_{\mathbf{k},\mathbf{k}+\mathbf{q}}\,|^2\ , \tag{70}$$

where μ and ν are band indices; $E^{\mu}_{\mathbf{k}}$ and $E^{\nu}_{\mathbf{k}+\mathbf{q}}$ are band-structure energies at points separated by the vector $\mathbf{q}$; $n^{\mu}_{\mathbf{k}}$ and $n^{\nu}_{\mathbf{k}+\mathbf{q}}$ are occupation functions at zero temperature, having the values 1 or 0 according to whether the state is occupied or not, which may be taken as Fermi functions

$$f^{\mu}_{\mathbf{k}}=\{1+\exp[(E_F-E_{\mathbf{k}})/k_BT]\}^{-1} \tag{71}$$

if a finite-temperature T calculation is to be performed; and M is a matrix element

$$M^{\mu\nu}_{\mathbf{k},\mathbf{k}+\mathbf{q}}=\langle\,\psi^{\nu}_{\mathbf{k}+\mathbf{q}}\,|\,e^{i\mathbf{q}\cdot\mathbf{r}}\,|\,\psi^{\mu}_{\mathbf{k}}\,\rangle\ . \tag{72}$$

The susceptibility $\chi_0(0)$ for $\mathbf{q}=0$, corresponding to a uniform magnetic field, will according to Eqs. (70) and (72) take the value

$$\chi_0(0)=N(E_F)\ , \tag{73}$$

where $N(E_F)$ is the density of states at the Fermi surface, because of the orthogonality between different bands if the wave functions $\psi^{\mu}_{\mathbf{k}}$ form a complete set. This is the case in Windsor's calculation, the energies $E_{\mathbf{k}}$ used in the computation being derived, in a tight-binding approximation based on the bands of Asano and Yamashita (1967), with five 3*d* and one 4*s* orbital.

Windor (1972) notes that, in the single-band case treated by Izuyama *et al.* (1963) in deriving the expression for the exchange-enhanced susceptibility in the random-phase approximation

$$\chi(\mathbf{q})=\frac{\chi_0(\mathbf{q})}{1-I\chi_0(\mathbf{q})}\ , \tag{74}$$

I being the exchange interaction parameter, the matrix element in $\chi_0(\mathbf{q})$ is the form factor $f(\mathbf{q})$, so that condition (66) is satisfied. In the first estimate of $\chi_0(\mathbf{q})$ in Cr, however, by Evenson *et al.* (1969), the matrix element was simply taken as unity in the multiband calculation and the fact that $\chi_0(\mathbf{q})$ was overestimated by an order of magnitude was shown by the fact that the limiting value as $\mathbf{q}$ goes to zero exceeded $(\frac{1}{2}g\mu_\beta)^2N(E_F)$ by a large factor.

Although the tight-binding band structure is necessarily less accurate than calculations such as that of Loucks (1965) based directly on the potential, it has the merit that the wave functions may be rigorously defined at each value of $\mathbf{k}$, and for each of the six bands μ, by only six coefficients $C^{\mu}_{i}(\mathbf{k})$, giving the components of the $i=xy$, yz, zx, x^2-y^2, $3z^2-r^2$, and *s*-like parts of the wave function. The energies and wave functions were calculated at

650 points in the bcc Brillouin zone, corresponding to a mesh with 22 points between Γ and H. The Fermi surface in an extended zone scheme and the energy bands close to the Fermi level E_F are shown in Fig. 66(a) and 66(b).

The matrix elements (72) and hence $\chi_0(\mathbf{q})$ are calculated for $\mathbf{q}$ along the ΓH line, and the wave-function coefficients, such as those in Fig. 66(c), enable the contributions to $\chi_0(\mathbf{q})$ from pairs of states $\mathbf{k}$ and $\mathbf{k}+\mathbf{q}$ to be classified, so long as the energy levels are within ± 0.5 eV of E_F. Figure 67 shows the resultant breakdown of $\chi_0(\mathbf{q})$ into "outer" contributions from outside this range, intraband contributions N-N, H-H, Γ-Γ, and α-α, and interband contributions among which only the Γ-H contribution is distinguished. We see that, while $\chi_0(\mathbf{q})$ has a maximum close to the wave vector $Q=0.95a^*$ of the SDW in Cr, the maximum value, $\chi_0(\mathbf{Q})=0.77$ $\mathrm{eV}^{-1}\,\mathrm{atom}^{-1} \equiv 0.010$ states mRy^{-1}, is too small to satisfy the condition (66) for antiferromagnetism, i.e., the exchange-enhanced susceptibility $\chi(\mathbf{q})$ in Eq. (64) does not diverge as $\mathbf{q}$ tends to $\mathbf{Q}$. This is not important, however, since the calculation was not intended to be numerically accurate.

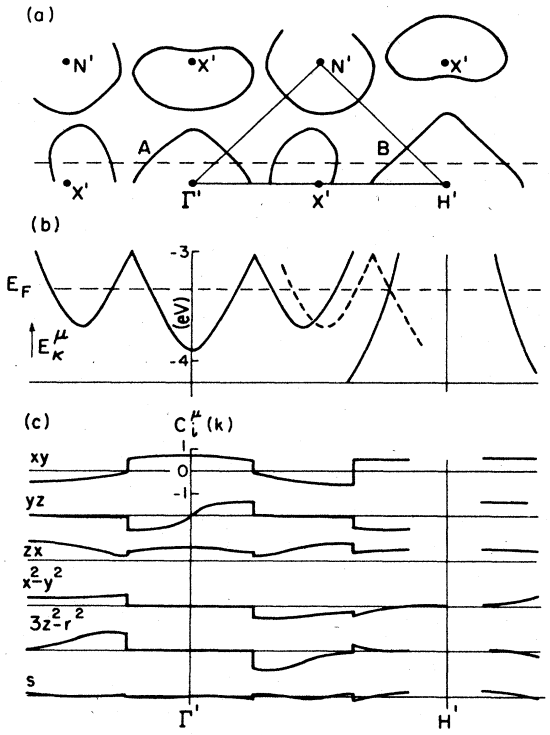

FIG. 66. Calculation of the wave-vector-dependent susceptibility of chromium: (a) Fermi surface in the $(0,0,\frac{3}{22})$ plane; (b) energies E_k^μ near the Fermi level E_F; (c) wave-function coefficients $C_l^\mu(\mathbf{k})$ along the $(\zeta,\frac{21}{22},\frac{3}{22})$ line, shown broken in the $(0,0,\frac{3}{22})$ plane Fermi-surface section. A and B denote nesting surfaces and the dashed curves in (b) show $E_{\mathbf{k}+\mathbf{q}}^\mu$ with $\mathbf{q}=\langle\frac{21}{22},0,0\rangle$, i.e., with the energy bands on the left remapped so that A intersects B at the Fermi level. The labels Γ', H', N', and X' mark the positions above the corresponding points in the symmetry plane (after Windsor, 1972).

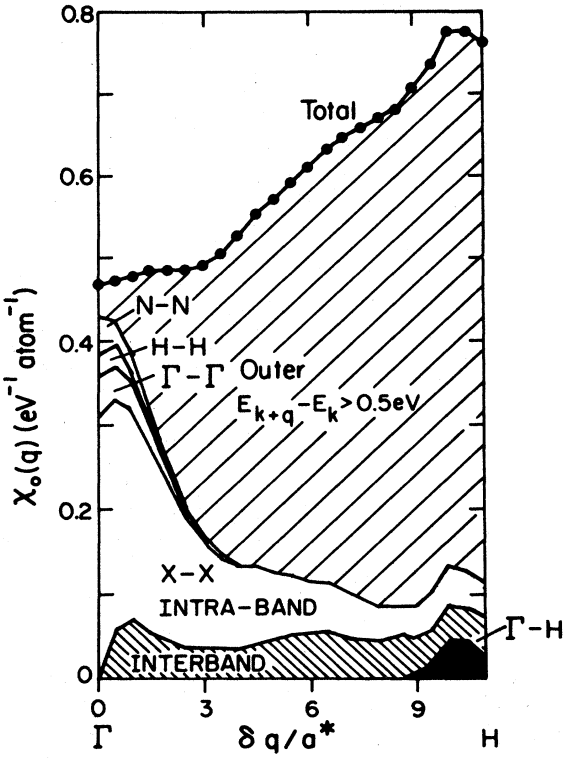

FIG. 67. The wave-vector-dependent susceptibility $\chi_0(\mathbf{q})$ for wave vector $\mathbf{q}$ along ΓH in Cr calculated at its Néel temperature, $T \simeq 311$ K (after Windsor, 1972).

The striking feature of Fig. 67 is rather that the contribution to the maximum in $\chi_0(\mathbf{q})$ near $Q=0.95a^*$, from the nesting octrahedra centered on Γ and H, is only a small peak on top of a much larger broad maximum originating in the outer contributions from regions remote from the Fermi level. The significance of this result is that nesting of the Fermi surface, which has played such an important role in the theory of antiferromagnetism in Cr, in fact constitutes only a very small (but still critical) factor in determining the incommensurate nature of the antiferromagnetism. Windsor (1972) explores in more detail the various contributions to $\chi_0(\mathbf{q})$ and finds that the Γ-H terms, though small, are the largest individual terms. The density of states near the Fermi level or the X balls is about four times larger than for the Γ or H octahedra, but the X-X contribution to $\chi_0(\mathbf{q})$ is attenuated at large $\mathbf{q}$ by small matrix elements. For example, the wave functions have xy (and zx) coefficients with the same sign near the two X' points and x^2-y^2 (and $3z^2-r^2$) coefficients of opposite sign, so that the overlap is small.

The calculation of Zhao *et al.* (1987) are based upon the band-structure calculations of Papaconstantopoulos (1986) for V, Mn, and Mo and of Laurent *et al.* (1981) and Pattnaik *et al.* (1983) for Cr. Approximations are

necessary in calculating the many-body effects, but no adjustable parameters are used. The results, shown in Fig. 68, demonstrate singularities in $\chi(q)$ corresponding to antiferromagnetism for Cr and for both bcc and fcc Mn.

The peak in $\chi_0(q)$ for Cr at $Q=0.96a^*$ is seen also in the calculations of Gupta and Sinha (1971) and Windsor (1972; see Fig. 67). The peak is considerably reduced in Mo because of the 4*d* character of the wave function. Zhao *et al.* (1986) also report changes in Fermi-surface nesting with the Fermi energy, which successfully explain the concentration dependence of the wave vector of the SDW in Cr*V* and Cr*Mn* alloys illustrated in Fig. 6.

The values $\chi_0(0)=8.40\mu_B^2\ \mathrm{Ry}^{-1}$ and $\chi_0(0)=11.0\mu_B^2\ \mathrm{Ry}^{-1}$, calculated by Zhao *et al.* (1987), give an enhancement factor 1.30 for the paramagnetic susceptibility of Cr, which compares favorably with the value obtained by Janak (1977).

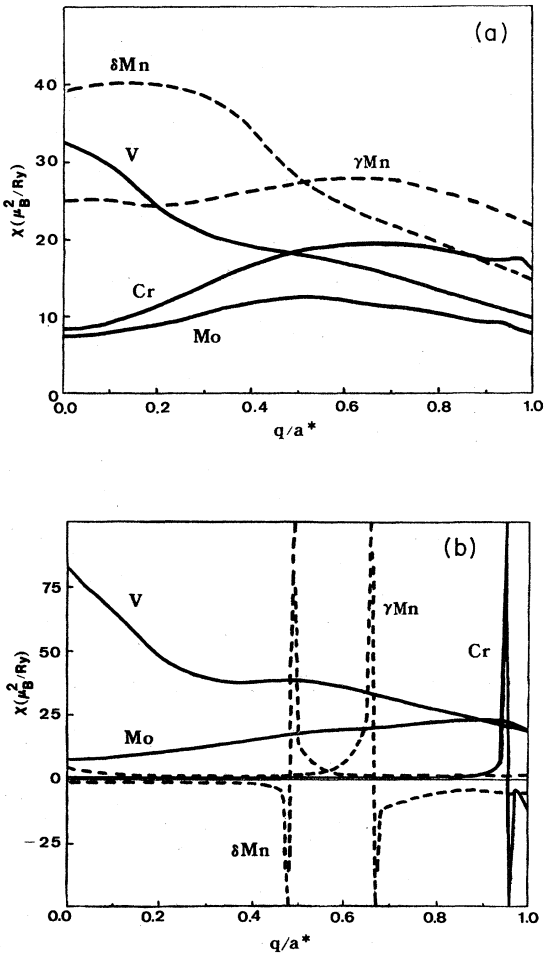

FIG. 68. (a) Wave-vector-dependent susceptibility $\chi_0(q)$; (b) exchange-correlation-enhanced susceptibility $\chi(q)$, along the cube axis for V, Cr, bcc δMn, fcc γMn, and Mo. The data for Cr and Mn in (b) are divided by a factor of 10 so as to plot on the same scale as V and Mo (after Zhao *et al.*, 1987).

4. Finite-temperature calculations

The bulk magnetism as well as the magnetic moment in the surface layers has been calculated recently by Hasegawa (1986), employing a spin-fluctuation theory based on a tight-binding model. At zero temperature the results are similar to previous calculations described in Sec. IV.B.2. The average peak moment μ decreases from $0.60\mu_B$ at zero temperature to zero at the calculated Néel temperature, $T_N=370$ K, where a second-order phase transition is predicted to occur. The rms moment, which we have previously in Sec. II.B.4 denoted $\langle\mu(0)\rangle$ at zero temperature, is here denoted $\langle M^2\rangle^{1/2}$, following Hasegawa, who denotes the peak moment $\langle M\rangle$. He finds that the ratio $\langle M^2\rangle^{1/2}/\langle M(0)^2\rangle^{1/2}$ is still 0.6 at T_N and increases linearly with temperature in the paramagnetic phase to 0.9 at $2T_N$. The latter result is in qualitative agreement with previous spin-fluctuation calculations by Evangelou *et al.* (1982) and Shimizu *et al.* (1983), which were, however, limited to the paramagnetic phase.

This linear increase of the rms moment in the paramagnetic phase is characteristic of spin-fluctuation theory (Moriya and Kawabata, 1973) and should be compared with the high-temperature neutron scattering results described in Sec. II.C.5 and thermal expansion results described in Sec. III.B.

C. Lattice vibrations

The experimental data of Shaw and Muhlestein (1971) for the phonon dispersion relations of Cr determined from inelastic neutron scattering are shown in Fig. 34, and identification of several features with Kohn anomalies is illustrated in Fig. 60 and Table VII (see Sec. IV.B.2). Feldman's (1970) calculation of the phonon dispersion relations, using a tensor-force model including up to four nearest-neighbor interactions, was published just before the work of Shaw and Muhlestein (1971), and Feldman fitted his model to the earlier data of Møller and Mackintosh (1965) and the elastic constants at room temperature (Bolef and de Klerk, 1963). Neither Feldman's calculation nor that of Cavalheiro and Shukla (1978), who used a de Launay model, is intended to accommodate the delicate features of the phonon dispersion curves corresponding to Kohn anomalies, but the broad features of the lattice vibration spectrum can be explained within a framework that includes the elastic constants, specific heat, and Debye-Waller factor (Feldman, 1970).

V. EXPERIMENTAL DETERMINATION OF THE ELECTRON STRUCTURE

A. Early Fermi-surface studies

The earliest measurement of a Fermi-surface property of chromium was a determination of its area S by Fawcett and Griffiths (1962), using the anomalous skin

TABLE XII. Estimates of the contributions to the Fermi-surface area S and the relative contributions to the density of states $N(E_F)$ at the Fermi surface from the various pieces according to the calculations of Laurent *et al.* (1981).

Piece of Fermi surface	Area S (Au^2)	% contribution to $N(E_F)$
6 electron balls at X	1.32	52
6 hole pockets at N	1.01	18
Electron octahedron at Γ	0.67	16
Hole octahedron at H	1.05	14
Total	4.05	100

effect. The resultant value, $S_{\mathrm{AFM}}=2.54\pm0.25$ Au^2, is little more than half the value for paramagnetic Cr, which may be estimated from the Fermi surface calculated by Laurent *et al.* (1981) and shown in Fig. 57. The contributions to S from the various pieces of Fermi surface are listed in Table XII, together with the relative contributions to the density of states $N(E_F)$ at the Fermi surface, which are obtained by weighting the areas according to their inverse velocities estimated from the slopes of $E(\mathbf{k})$ curves at E_F obtained from the energy-band structure shown in Fig. 55.

This latter estimate may be related to the observation by Heiniger (1966) that the electronic specific heat in AFM Cr is only about half the value of that for paramagnetic Cr, obtained by interpolation between the results for paramagnetic alloys of Cr with neighboring transition metals. Thus, according to Table XII, gapping the Fermi surface of half the electron octahedron at Γ and the corresponding area of the hole octahedron at H would reduce the $N(E_F)$ by only about 30%, and Heiniger's result suggests that some appreciable fraction of the surface of the electron balls at X and hole pockets at N must also be gapped.

This would explain the reduction of Fermi-surface area in AFM Cr obtained by measurements of the surface conductance under conditions of the anomalous skin effect observed by Fawcett and Griffiths (1962). It should be pointed out, however, that the Fermi-surface areas of Mo and W, also measured by Fawcett and Griffiths, are only about half the values estimated from band-structure calculations, and these metals are not AFM. In the case of these metals, the apparent low values of S are thought to be due to the difficulty in preparing satisfactory electropolished samples, which gives rise to an erroneously low surface conductance.

B. de Haas–van Alphen effects

The determination of the Fermi surface of AFM Cr by means of the de Haas–van Alphen (dHvA) effect was a *tour de force* in that the complex spectra with up to 20 or so branches demanded excellent experimental technique, including the first systematic use of Fourier analysis of dHvA data; and the interpretation of these spectra was perhaps the most difficult problem to be tackled by any graduate student in experimental study of the Fermi surface. It is remarkable that independently John Graebner (Graebner and Marcus, 1966, 1968) and Rod Day (1968) performed this difficult experiment and developed essentially the same picture of the Fermi surface of AFM Cr.

Watts (1964) had already established, using pulsed magnetic fields of $\mathbf{H}\sim10$ T to measure the dHvA effect in Cr, that a sample field-cooled in a field $\mathbf{H}_c=6.5$ T, along a cube axis, has a dHvA spectrum with tetragonal symmetry about that axis, which he deduced was the direction of the wave vector $\mathbf{Q}$ of the SDW. Graebner and Marcus (1966), working at lower fields below 3.3 T with carefully selected samples of Cr grown by the iodide-vapor process, having residual resistance ratios between room temperature and liquid-helium temperatures of about 1000, and measuring at fields $\mathbf{H}<\mathbf{H}_c$ so that there was no appreciable change in the state of the sample, confirmed the tetragonal symmetry.

The top panel of Fig. 69 shows the dHvA spectrum of a single-$\mathbf{Q}$ sample of Cr. Graebner and Marcus (1968) showed that most branches of this spectrum correspond to cyclotron orbits involving magnetic breakdown across the AFM energy gaps at the Fermi surface associated

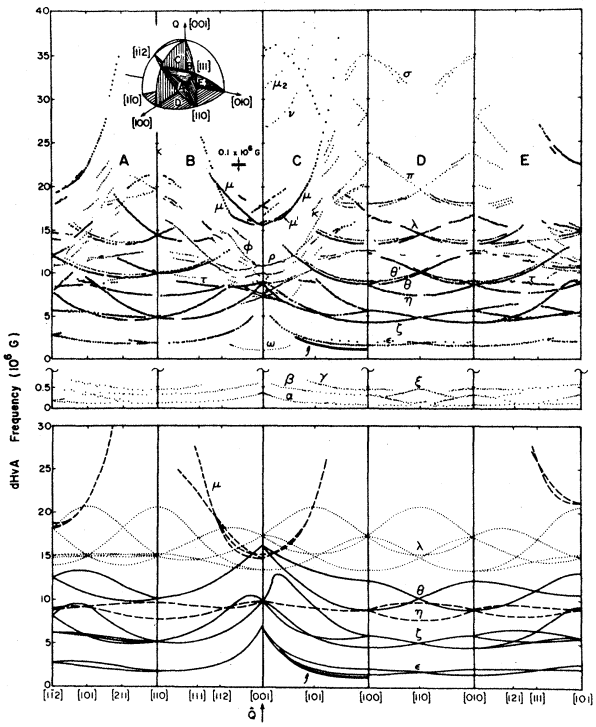

FIG. 69. Top: dHvA frequency vs magnetic field direction in the major symmetry planes of AFM Cr (after Graebner and Marcus, 1968), with frequency branches identified with orbits on the hole ellipsoid chain indicated by using heavier dots for the data points. Bottom: calculated dHvA frequencies for various orbits on the hole ellipsoid chains: solid curves, at N_1 (and N_2); dashed curves, at N_3; dotted curves, on the entire hole ellipsoids at N (after Reifenberger *et al.*, 1980).

with the incommensurate SDW. Lomer (1965) pointed out that such gaps should occur at planes in reciprocal space

$$\mathbf{K}=\tfrac{1}{2}(m\mathbf{G}+n\mathbf{Q}) , \tag{75}$$

where m and n are integers and $\mathbf{G}$ is a reciprocal-lattice vector. Lomer (1965) developed a classification scheme that regarded the SDW as a perturbation giving rise to a hierarchy of energy gaps. This scheme is somewhat misleading (Reifenberger *et al.*, 1980), since it led to incorrect estimates by Graebner and Marcus (1968) based on Falicov and Zuckermann's (1967) analysis that only second- and higher-order gaps ($n \geq 2$) would break down at their moderate fields. In fact, all the cyclotron orbits shown in Fig. 70 have been seen, including the extremal cross section of the entire ellipsoid at N, which corresponds to branch λ of the dHvA spectrum of Fig. 69 (Fawcett *et al.*, 1976).

In the construction shown in Fig. 70, the chains are generated by translating the hole ellipsoids at N (see Figs. 58 and 61) through wave vectors given by Eq. (67). The calculated dHvA spectrum for the chain model shown in the bottom panel of Fig. 69 was computed by Reifenberger *et al.* (1980), using the dimensions of the hole ellipsoids determined by Graebner and Marcus (1968), as listed in Table XIII. The agreement with experiment is quite remarkable: the chain model reproduces the symmetry of many of the dHvA data, and agreement with measured dHvA frequencies is obtained to within an accuracy of better than $\pm 10\%$.

Most of the remaining dHvA branches, ρ, ν, π, μ, and χ (the latter not shown in Fig. 69), have since been identified as also being associated with the ellipsoid chains at N, as illustrated in Fig. 70 (Venema *et al.*, 1980; Ruesink and Templeton, 1984). None has been identified with the electron ball chain at X, as was first suggested by Graebner and Marcus (1968). Likewise no branches have been identified as originating on either the electron octahedron at Γ or the hole octahedron at H, presumably because the gapping of these surfaces precludes the formation of complete cyclotron orbitals, even with magnetic breakdown.

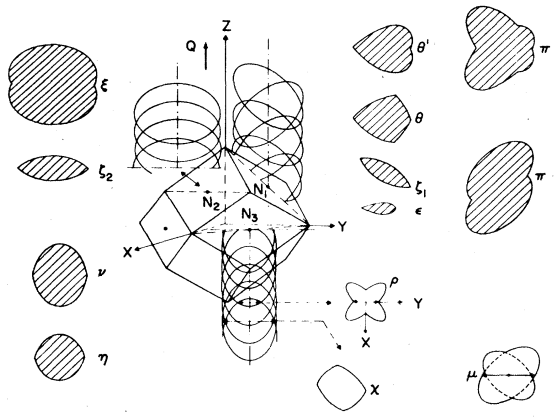

FIG. 70. Some extremal cross sections, all of which have been seen in the dHvA spectrum, of the chainlike Fermi-surface sheets associated with the hole ellipsoids at points N of the Brillouin zone. The wave vector $\mathbf{Q}$ of the SDW is along [001], the shaded cross sections are in the (100) plane, and the unshaded in the (001) plane. The notation corresponds to the branches of the dHvA spectrum of Fig. 69, but the indices of the points N follow a convention different from that of Graebner and Marcus (1968) (after Venema *et al.*, 1980).

TABLE XIII. Comparison of dimensions of the Fermi surface of AFM chromium measured by Graebner and Marcus (1968) using the dHvA effect and calculated by Laurent *et al.* (1981) using the KSG and VBH potentials (see Table VII). The experimental dimensions of the N ellipsoids are much more secure than those of the X balls, since no cyclotron orbits have been clearly established for the latter.

		Theory	
Semiaxes	Expt. (Å^{-1})	KSG (Å^{-1})	VPH (Å^{-1})
Hole ellipsoids at N			
NH	0.173	0.186	0.185
$N\Gamma$	0.234	0.304	0.310
NP	0.268	0.316	0.324
Electron balls at X			
ΓH	0.26	0.30	0.30
$\perp\Gamma H$	0.25	0.30	0.30

The occurrence of doublet and triplet frequency branches in the dHvA spectrum of Cr was first remarked by Graebner and Marcus (1968), and more extensive data showing this feature were obtained in ultrasonic attenuation studies by Wallace and Bohm (1968) and Snider and Thomas (1971). The effect remains unexplained in detail, but in principle it may be understood as originating in magnetic breakdown between a higher-frequency orbit, θ, λ, or π in Fig. 69, for example, and one of the very-low-frequency orbits α, β, γ, or ξ, none of which has been identified but whose frequencies in some cases are roughly equal to the difference frequency. Fawcett *et al.* (1976) have shown that in some cases the fact that the stress dependence of the frequency is very similar for the two members of a doublet (e.g., θ and θ') shows this explanation to be incorrect. An alternative explanation, whereby a sector of the ellipsoid chain is added to the basic orbit through magnetic breakdown, is illustrated in Fig. 70 for θ and θ', and may also explain the λ and λ' doublet. Reifenberger *et al.* (1980) point out, however, that in each case the area of the added sector is considerably smaller than the difference frequency between the members of the doublet.

Graebner and Marcus (1968) determined the effective mass and Dingle temperature of various cyclotron orbits by measuring the temperature dependence of the dHvA amplitude, with the results given in Table XIV. A striking feature of the oscillatory magnetoresistance (which we shall refer to as Shubnikov–de Haas or ShdH oscillations), first noted by Arko *et al.* (1969), is that the temperature dependence of the amplitude is much weaker

TABLE XIV. Effective mass m^*/m_0 and Dingle temperature T_D of various cyclotron orbits in AFM chromium. The ranges of values measured for the various branches of the dHvA spectrum in plane C of Fig. 69 are given (after Graebner and Marcus, 1968).

dHvA branch	m^*/m_0	T_D (K)
ε	0.18	0.47
Γ	0.34–0.43	0.5–1.5
θ,θ'	0.34–0.41	0.9
μ	0.49	

than that of a typical dHvA amplitude. They also found that only one of the seven frequency branches of the ShdH spectrum coincides with a branch of the dHvA spectrum. To explain these two features, Reifenberger *et al.* (1980) suggested that ShdH oscillations in Cr are largely due to quantum interference, which accounts for similar characteristics of the ShdH oscillations in Mg (Stark and Freidberg, 1974).

Arko *et al.* (1968) had previously found that the transverse magnetoresistance of Cr saturates at high magnetic fields when both the field and current directions are perpendicular to the wave vector **Q** of the SDW, while for other field directions it has a quadratic field dependence. This behavior is characteristic of a compensated metal, whose Fermi surface supports open orbits along **Q**. Quantum interference occurs between electron waves pursuing different trajectories in the direction of **Q** along the network of intersecting orbits on the chains at N, as illustrated in Fig. 70, the phase difference being periodic in reciprocal magnetic field. The fact that these open orbits dominate the high-field magnetoconductivity tensor explains why quantum interference occurring on only a small part of the Fermi surface can determine the major features of the ShdH spectrum.

Fletcher (1985) has taken advantage of the high sensitivity of thermopower measurements to investigate the ShdH oscillations with higher resolution than the magnetoresistance measurements. This allows more detailed information to be obtained, which reveals new branches of the ShdH spectrum. Fourier analysis of the peaks in fields up to $\mathbf{H}=8$ T provides rough estimates of the breakdown fields for the various orbits. The values range from 0 to 40 T, with most being about 30 T.

An important application of the dHvA effect in AFM Cr has been to determine the pressure dependence of the wave vector **Q** of the SDW. This was first measured directly by neutron diffraction between the Néel temperature and temperature $T=100$ K by Umebayashi *et al.* (1968), and later down to $T\sim 20$ K by Fawcett *et al.* (1978). The results, illustrated in Fig. 71, show that the pressure dependence extrapolated to low temperature is in reasonably good agreement with the value obtained by Venema *et al.* (1980) in dHvA work done at pressures of about 0.4 GPa. There is a major discrepancy, however, with the low-temperature value, obtained by Fawcett

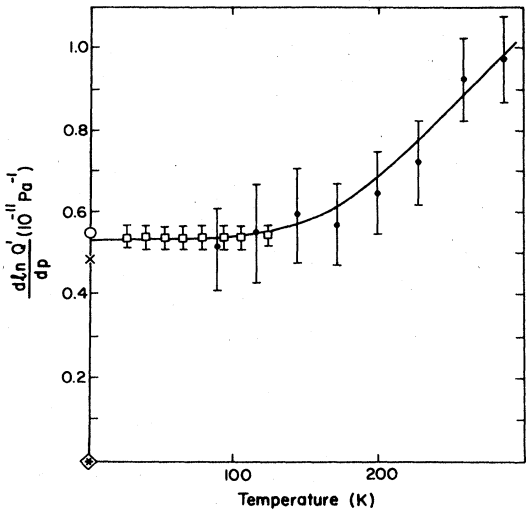

FIG. 71. The pressure dependence of the wave vector **Q** of the SDW in AFM chromium expressed in units of a^* [see Eq. (79)] vs temperature, measured under various experimental conditions: ●, neutron diffraction (Umebayashi *et al.*, 1968, as analyzed by Venema *et al.*, 1980); □, neutron diffraction (Fawcett *et al.*, 1978); *, oscillatory magnetostriction at zero pressure (Fawcett *et al.*, 1976); ×, high-pressure dHvA (Venema *et al.*, 1980); ○, low-pressure dHvA in soft mode; ◇, low-pressure dHvA in hard mode (see text: Ruesink and Templeton, 1984).

et al. (1976) using the technique of oscillatory magnetostriction combined with dHvA torque to determine the uniaxial stress dependence of the Fermi surface (Fawcett *et al.*, 1980), which corresponds to a zero pressure value, since the measured strain results from internal stress. This discrepancy was resolved by Ruesink *et al.* (1980) and Ruesink and Templeton (1984), who used fluid helium at relatively low pressures up to 14 MPa and studied hysteresis effects.

Ruesink and Templeton (1980) used a method introduced by Griessen *et al.* (1976) and developed by Venema *et al.* (1980) to separate the two factors contributing to stress dependence of the frequency of a breakdown orbit on the ellipsoid chain. As illustrated in Fig. 72 the area A of such an orbit may be written as a function of A_0 and δ/a,

$$A = A(A_0, \delta/a) , \tag{76}$$

and partial derivatives $\partial \ln A/\partial \ln A_0$ and $\partial \ln A/\partial \ln(\delta/a)$ may be computed in terms of the parameters of the ellipsoid chain model. Thus the measured stress dependence of the orbit $\partial \ln A/\partial\delta$, δ being either uniaxial stress (Griessen *et al.*, 1976) or pressure p (Venema *et al.*, 1980, and Ruesink and Templeton, 1984), may be used to define two coordinates,

$$X = \frac{\partial \ln A}{\partial \ln(\delta/a)} \Big/ \frac{\partial \ln A}{\partial \ln A_0} \tag{77}$$

and

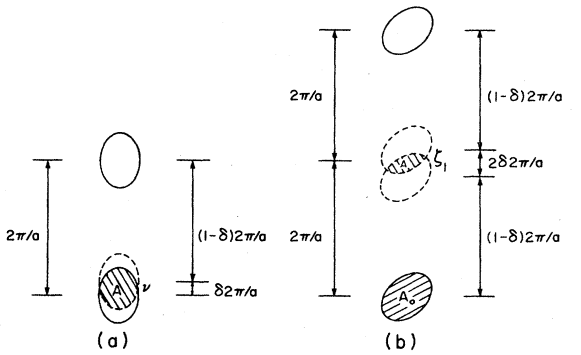

FIG. 72. The origin of two breakdown orbits on the ellipsoid chain at N_1 (orbit ξ_1) and N_3 (orbit ν) as illustrated in Fig. 70, showing how the area A of each will depend separately on the area A_0 of the whole ellipse and on the incommensurability parameter δ/a (after Ruesink and Templeton, 1984).

$$Y=\frac{\partial \ln A}{\partial \sigma}\Big/\frac{\partial \ln A}{\partial \ln A_0}\ . \tag{78}$$

The coordinate X is calculated for each orbit from the model, while the coordinate Y represents the observed response of the orbit to change of stress, normalized by the rate of change of the orbit area A with A_0, the latter also being calculated from the model.

If it is assumed that the shape of the ellipsoids is not affected by stress, an assumption justified by the success of this method of analysis, then the X and Y coordinates for the various orbits should all lie on the same straight line, whose slope is $\partial \ln(\delta/a)/\partial\sigma$ and whose intercept with the Y axis is $\partial \ln A_0/\partial\sigma$. Exactly the same analysis may be used for any other parameter that changes δ and A_0 according to the same scaling laws, in particular the electron concentration μ, which may be varied by introducing impurities into Cr.

Thus in Fig. 73 we show in the top panel the X-Y plot for Cr-rich alloys measured by Gutman and Stanford (1971). The slope of the line gives $\partial \ln(\delta/a)/\partial\mu=-0.43(3)$ (at. %)$^{-1}$ in good agreement with the value obtained from neutron-diffraction measurements at liquid-nitrogen temperature (Komura *et al.*, 1967).

The bottom panel of Fig. 73 shows, however, that the stress dependence of δ/a is essentially zero for stress both parallel and perpendicular to **Q**. The resultant pressure dependence of δ/a is therefore zero, a result which, as mentioned earlier, was found to be in contradiction with the direct measurement of the wave vector by neutron diffraction under pressure. The different results are listed in Table XV, and for comparison with Fig. 71 we list also $\partial \ln Q'/\partial p$, where

$$Q'=Q/a^*=Qa/2\pi\ , \tag{79}$$

so that $\delta=1-Q'$, and with the isothermal compressibility $K=-3\partial \ln a/\partial p$ we obtain

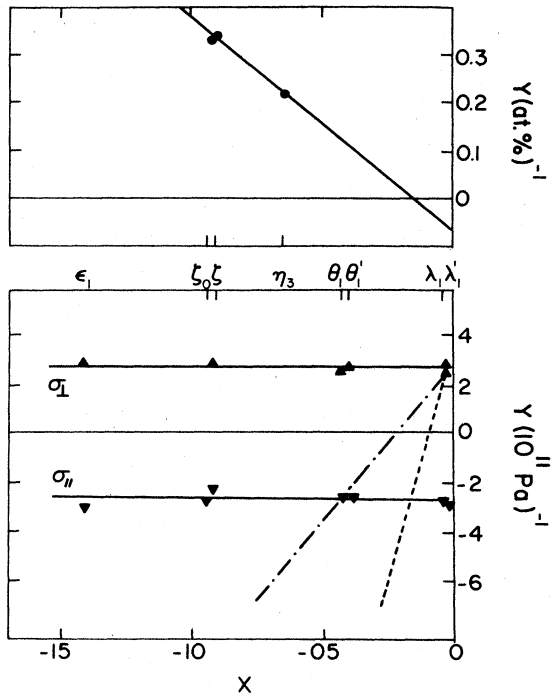

FIG. 73. X-Y experimental plots [see Eqs. (77) and (78)]. Top: electron concentration dependence. Bottom: stress dependence for σ_{11} and σ_1 parallel and perpendicular, respectively, to the wave vector **Q** [the dot-dashed line and dashed line correspond to the predicted X-Y plots for the hydrostatic pressure dependence of δ/a at 93 and 311 K, respectively, given by Umebayashi *et al.* (1968)] (after Griessen *et al.*, 1976).

$$\frac{\partial \ln Q'}{\delta p}=\frac{\delta}{1-\delta}\left[\frac{K}{3}-\frac{\partial \ln(\delta/a)}{\partial p}\right] \tag{80}$$

with $\delta=0.048\,66$ (Werner *et al.*, 1967a) and $K=5.25\times10^{-12}$ Pa^{-1} (Palmer and Lee, 1971) at low temperatures.

It is evident that the pressure dependence of Q' (or δ/a) and of A_0 is quite different for the oscillatory magnetostriction results than for the results of dHvA measurements under high pressure, the latter giving a value of $\partial \ln Q'/\partial p$ essentially in agreement with the neutron-diffraction result, as seen in Fig. 71 and Table XV. Ruesink and Templeton (1984) were able to reproduce either value of $\partial \ln Q'/\partial p$ (and the corresponding different values of $\partial \ln A\sigma/\partial p$) under different experimental conditions, as illustrated in Fig. 74. They used fluid helium to apply pressures up to 14 MPa and found two modes corresponding to hysteretic pressure dependence. When the pressure is first applied, the relative phase follows curve (1) of Fig. 74, the so-called soft mode, having large pressure dependence of Q' in agreement with the neutron-diffraction result, as shown in Table XV. When the pressure is removed [curve (2)] or reapplied up to the same pressure p_h [curve (3)], the hard mode is observed, having a small value of $\partial \ln Q'/\partial p$ in agreement with the oscillatory magnetostriction result. When p increases beyond

TABLE XV. Pressure derivatives of the area A_0 of the cross section of the hole ellipsoid and of the incommensurability parameter δ.

Experimental method		$\frac{\partial \ln A_0}{\partial p}$ (10^{-11} Pa^{-1})	$\frac{\partial \ln(\delta/a)}{\partial p}$ (10^{-11} Pa^{-1})	$\frac{\partial \ln Q'}{\partial p}$ (10^{-11} Pa^{-1})
Neutron diffraction under pressure (Fawcett *et al.*, 1978)			10.5(10)	−0.54(5)
Oscillatory magnetostriction (Griessen *et al.*, 1976, Fawcett *et al.*, 1976)		2.6(3)	0.0(3)	0.01(1)
dHvA under high pressure (Ruesink and Templeton, 1984)	hard mode	1.85(15)	0.0(3)	0.01(1)
	soft mode	−0.1(5)	10.7(6)	−0.55(3)

p_h, the behavior reverts to the soft mode, but the hysteretic behavior occurs again on reducing pressure from a new higher-value p_h. In this case there is also strong hysteresis between curves (5) and (6), both, however, following the hard mode for most of the pressure interval up to the higher p_h. The X-Y plot for the two modes is shown in Fig. 75.

I shall postpone until later a discussion of the explanation of this interesting hysteretic behavior of the wave vector under pressure. It is believed to be connected with pinning of the SDW by lattice defects, and therefore will be discussed in Sec. VIII.E as an aspect of technical antiferromagnetism in the longitudinal SDW phase.

One might ask which of the two values in Table XV for the pressure dependence of the wave vector **Q** is the "correct" intrinsic value. As we shall see in Sec. VIII.E, the answer might be neither, since the observed dependence of **Q** on pressure, being hysteretic, nowhere corresponds to the thermodynamic equilibrium behavior. The high value for the pressure dependence of **Q** in the soft mode (and at high pressures) seems to be inconsistent with the small pressure dependence of the nest vector $\vec{Q}$ in the homologous paramagnetic metal Mo (Venema *et al.*, 1980).

Fletcher and Osborne (1973) attempted to explain this apparent discrepancy by postulating a strong anisotropy in the elastic constants of single-**Q** Cr, resulting in a shear deformation under hydrostatic pressure, but such anisotropy is not in fact observed (Muir *et al.*, 1987c). Fenton (1979) claims that a correct treatment of the two-band imperfect nesting model can give the observed

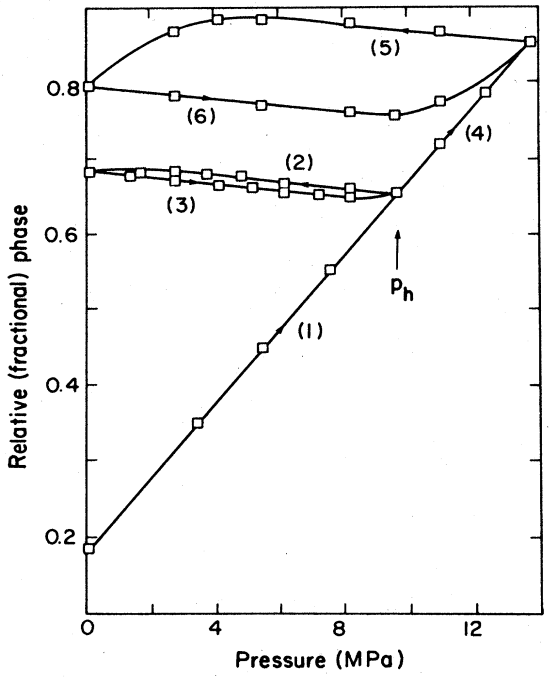

FIG. 74. Pressure dependence of the area of the ν orbit relative to the ζ_1 orbit (see Fig. 72) shown here as a change in the relative phase of the two dHvA frequency branches. The arrow on each curve shows the direction of the pressure change (after Ruesink and Templeton, 1984).

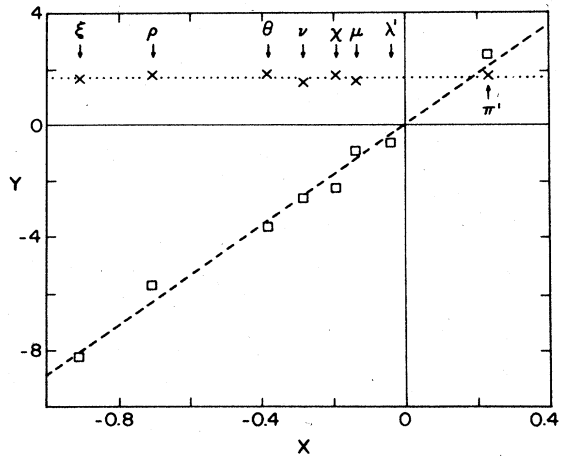

FIG. 75. X-Y experimental plots for the soft mode (□ and dashed curve) and the hard mode (× and dotted curve) (after Ruesink and Templeton, 1984).

difference between the pressure dependence of $\tilde{Q}$ and that of **Q**. He also explains the decrease of **Q** with decreasing temperature, though $\tilde{Q}$ of course is unchanged in a cubic metal.

We note that the logarithmic volume dependence of the wave vector corresponding to the low-temperature neutron diffraction data shown in Fig. 71 (i.e., in the soft mode) is very large: $dl(\delta/a)/d\omega \simeq -20$ (Venema *et al.*, 1980). This may be regarded as a Grüneisen parameter and is comparable in magnitude with the Grüneisen parameters obtained from the pressure dependence of the Néel temperature (McWhan and Rice, 1967), $\gamma_{TN} = -28$, and from the magnetic anomalies in the elastic moduli and the thermal expansion (Muir, Fawcett, and Perz, 1987a; see Sec. VI.A.3), $\gamma_{TN\_} = -37$.

This strong volume dependence of the strain-density-wave and its associated thermophysical properties is due to the effect of volume strain on the kinetic energy associated with magnetic ordering (Fawcett *et al.*, 1986b). It should be a feature of any successful microscopic model of antiferromagnetism in chromium.

C. Antiferromagnetic energy gap

We have seen in Sec. IV.A.1 that nesting models for antiferromagnetism in an itinerant-electron system predict the occurrence of an energy gap Δ at the Fermi surface, whose temperature dependence should resemble that of the BCS function, with Δ disappearing at the Néel temperature. The temperature dependence of the resistivity is consistent with this picture, as we have seen in Sec. III.E. The temperature dependence of the intensity of the elastic neutron scattering peaks shown in Fig. 4(a) gives the temperature dependence of $|M_Q|^2$ according to Eq. (9) [note that I normally denote the magnetization $\mathbf{M}(\mathbf{r})$ by $\mathbf{S}(\mathbf{r})$, the polarization vector], which is proportional to Δ^2 (Overhauser, 1962).

In order to determine the magnitude of the gap, as well as its relative temperature dependence, we must turn to spectroscopic methods of investigation. We should keep in mind here the possibility that the temperature dependence of the amplitude of the SDW may differ in principle from that of the energy gap determined by spectroscopic methods, since these two quantities correspond to experimental probes having different energies. The time scale of the neutron probe is much longer than that of the photon probe, which is of order $\hbar/\Delta$ (Werner, 1987).

Barker *et al.* (1968) first observed the energy gap in AFM Cr in infrared reflectivity. At low temperatures the reflectivity showed a minimum at $\Delta \simeq 0.1$ eV, which disappeared in the paramagnetic phase. Lind and Stanford (1972) first observed two more reflectivity minima in AFM Cr at higher energies. Machida *et al.* (1984) showed that the two lower-energy minima, corresponding at low temperatures to energy gaps $\Delta_1 \simeq 0.12$ eV and $\Delta_2 \simeq 0.45$ eV, are associated with antiferromagnetism. As illustrated in Figs. 76 and 77, they progressively decrease in magnitude and shift to lower energies as the amplitude of the SDW decreases with increasing temperature. By contrast, the minimum at 0.9 eV in Fig. 76 remains relatively unchanged, and presumably corresponds to some feature of the energy-band structure of Cr that is little affected by the onset of antiferromagnetism.

Machida *et al.* (1984) believe that the occurrence of two energy gaps is characteristic of the incommensurate SDW. Fenton and Leavens (1980) have offered alternative explanations for the two energy gaps, which have also been discussed by Young and Sokoloff (1974). Measurements on Cr*Mn* alloys having commensurate AFM structure, by Barker and Ditzenberger (1970) and Bos and Lynch (1970), appear to confirm that the commensurate SDW shows only one energy gap. Measurements of the energy-gap structure by other experimental methods would be useful to check these infrared results.

Cook (1987) has determined the temperature dependence of the energy gap, using surface electromagnetic waves (SEW). The SEW method is a much more sensitive probe at the Néel transition than reflectivity methods, because of the relatively large distance, $\simeq 1$ cm, over which it may be made to interact with the surface. The SEW data are consistent with the reflectivity work and offer the hope, by the use of various laser frequencies, of studying in detail the temperature dependence of the gap close to T_N.

In Fig. 78 the absorption coefficient α of a SEW induced by a CO_2 laser operating at 940 cm^{-1} shows an increase with temperature above the Néel temperature, $T_N \simeq 311$ K, as one would expect for a Drude metal. The most interesting feature of Cook's results appears just below T_N, as the gap opens up and α increases with *decreasing* temperature until a low-temperature plateau is reached. The calculated curve is based on estimates of the plasma frequencies obtained from the experimental temperature dependence of the electrical resistivity ρ by use of Drude theory. The magnitude and temperature

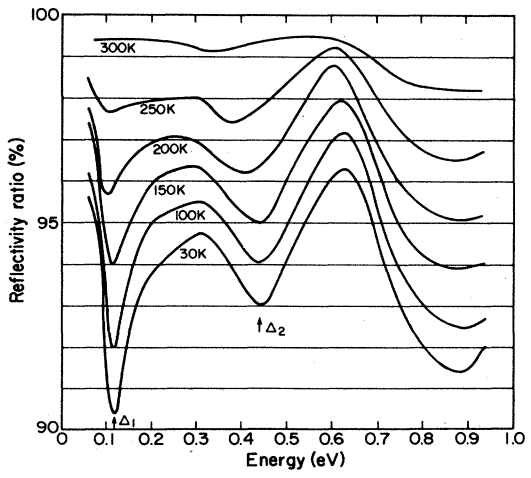

FIG. 76. The temperature dependence of the reflectivity of chromium on photon energy, normalized to temperature, $T = 400$ K (after Machida *et al.*, 1984).

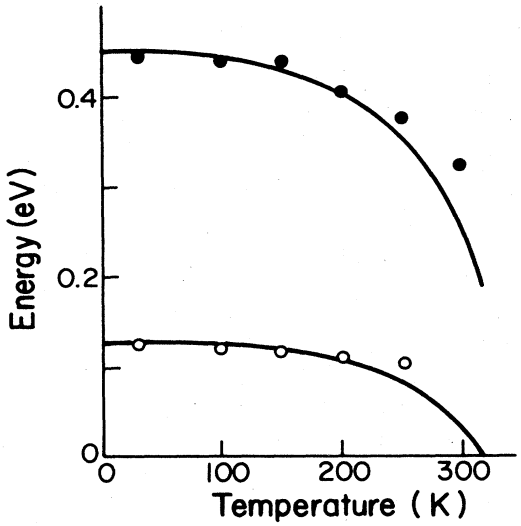

FIG. 77. Comparison of reflectivity data for chromium with the theoretical curves of Machida and Fujita (1984): ○, minimum Δ_1; ●, minimum Δ_2 in Fig. 76 (after Machida *et al.*, 1984).

dependence of the gap is estimated from the parameters of Barker and Ditzenberger (1970), whose data extend up to 200 K and are extrapolated up to T_N. The calculated α shows an abrupt step at T_N, similar to that in ρ. Cook did not observe such a step in α, perhaps due to surface strain in his samples.

Other spectroscopic probes that have been used to investigate AFM Cr in comparison with paramagnetic Cr include angle-resolved photoemission (Johansson *et al.*, 1980) and thermoreflectance (Colavita *et al.*, 1983). The photoemission data show some small changes between AFM and paramagnetic Cr, but the contrast is quite dramatic in the thermoreflectance, as illustrated in Fig. 79. Here a minimum in the thermoreflectance curve for

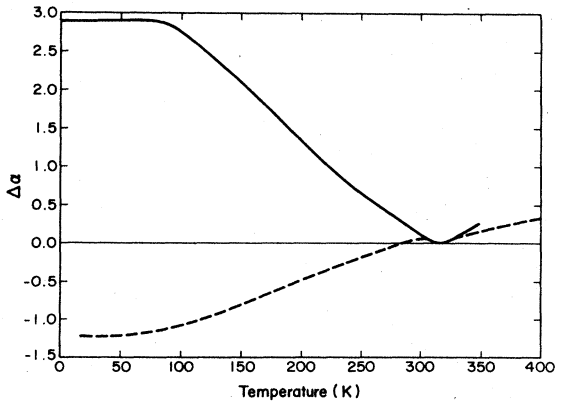

FIG. 78. Temperature dependence of the relative surface-electromagnetic-wave (SEW) absorption coefficient, $\Delta\alpha = \alpha(T) - \alpha(312\text{ K})$, as measured (solid curve) and as calculated (dashed curve) from the electrical resistivity (after Cook, 1987).

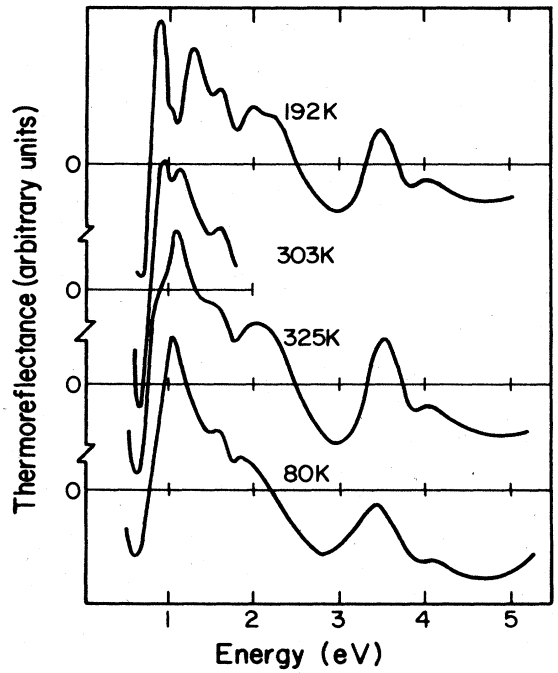

FIG. 79. Thermoreflectance of chromium vs photon energy at various temperatures, as indicated. The bottom curve was measured on a Cr film (after Colavita *et al.*, 1983).

AFM Cr at energy about 1.0 eV has almost disappeared at a temperature 10 K below $T_N \simeq 311$ K, and becomes a peak in the curve for paramagnetic Cr. The cause of this behavior is not known.

VI. MAGNETIC TRANSITIONS

A. Néel transition

The existence of a first-order transition at the Néel temperature in AFM Cr is observed quite clearly in elastic neutron scattering (Fig. 23) and in thermal expansion, as illustrated in Fig. 81 below. This first-order transition is weak and intervenes in what appears to be the approach to a continuous transition, as the order parameter decreases with increasing temperature.

A renormalization-group analysis by Bak and Mukamel (1976) showed that the Ginzburg-Landau-Wilson Hamiltonian has no stable fixed points, which suggests that fluctuations occur as the transition is closely approached, making the transition first order. When one seeks a microscopic model that might exhibit the behavior suggested by this analysis, the various attempts (Kimball and Falicov, 1968; Kimball, 1969; Rice, 1970; Malaspinas and Rice, 1972; Young and Sokoloff, 1974; and Kotani, 1975) must be deemed unsuccessful. In particular, it is difficult to adapt satisfactorily the nesting model described in Sec. IV.A.1, which has been so successful in describing many other properties of AFM Cr,

so as to produce a weak first-order transition.

Several researchers have attempted to determine critical exponents for the Néel transition in AFM Cr by fitting to power laws the changes in physical properties that approach singularity at the Néel temperature T_N. This procedure strictly is inadmissible for a first-order transition, but since the transition is so weak in Cr, the amplitude of the SDW is still small just below T_N, and the exponents of the power laws may then have some physical significance. I shall not, however, quote results for critical exponents since, apart from this difficulty in principle, the practical difficulties of determining unambiguous values have proved formidable. This is due in part to the great sensitivity to strain of the SDW near T_N.

The phenomenological model of Walker (1980b) described in Sec. IV.A.3, being a mean-field theory, gives a continuous transition with the usual mean-field critical exponents. This theory will be employed in the discussion of the change in the elastic constants at the Néel transition.

It is convenient to discuss in Sec. VI.A.3 the close relation observed (Muir *et al.*, 1987a) between the temperature dependence of the magnetic contributions to the bulk modulus and the thermal expansivity. These physical quantities are proportional over a very wide temperature range both below and above T_N, though with a different constant of proportionality. Muir *et al.* explain this behavior in the antiferromagnetic phase close to the Néel transition using a model in which the free energy is a function of reduced temperature relative to a volume-dependent Néel temperature.

1. Specific heat

The latent heat at the Néel transition is extraordinarily difficult to determine because of the strong stress dependence of the Néel temperature, which results in smearing of the transition in a sample having internal strain due to lattice defects. Careful attention to sample preparation has resulted in an estimate 1.2 ± 0.2 J mol^{-1}, based on a consideration of the data given in Table XVI.

The total magnetic entropy is even more difficult to estimate, because of the absence of a base line for paramagnetic Cr to which the specific heat of AFM Cr can be referred. Figure 80 illustrates how this problem was solved by using a dilute CrV alloy, in which the Néel temperature seen was depressed about 50 K below its value in pure Cr. As shown in Table XVI, this gives for the magnetic entropy a value 35 mJ mol^{-1} K^{-1}, which is the preferred estimate. The corresponding magnetic enthalpy is 10.5 J mol^{-1}.

2. Thermal expansion

The thermal expansion at the Néel transition is illustrated in Fig. 81. The region of negative thermal expansivity may be taken as a rough measure of the broadening

TABLE XVI. The latent heat at the Néel transition and the total magnetic entropy for Cr.

Reference	Latent heat (J mol^{-1})	Total energy (mJ mol^{-1} K^{-1})
Beaumont *et al.* (1960)		18
Salamon *et al.* (1969)		29
Garnier and Salamon (1971)	0.8±0.2	
Weber and Street (1972)	0.8±0.2	70
Polovov (1974)	1.1±0.1	121
Benediktsson *et al.* (1975)	1.0±0.1	
Williams *et al.* (1979)	1.4	35

of the transition by inhomogeneous internal stress, which is thus about 10 MPa, the pressure dependence of T_N being about -0.5 K/GPa (Mitsui and Tomizuka, 1965). This weak first-order transition is superimposed on a continuous transition of width about 3 K, this being roughly the interval over which deviations occur from the idealized first-order transition, represented by the dashed lines in Fig. 81. The corresponding discontinuity in the strain, $\Delta\varepsilon \simeq 11\times10^{-6}$, includes, however, some length change associated with the continuous transition, so that it represents an upper limit for the first-order strain. The Clausius-Clapeyron relation thus gives on an upper limit, 1.4 J mol^{-1}, for the latent heat, which is consistent with the data given in Table XVI.

The discontinuity in strain at T_N appears to be isotropic to an accuracy of about 5% (Lee and Asgar, 1969), though it is not clear to what extent anisotropy can be determined experimentally with a polarizing field, which may affect the single-Q domain nature of the sample as one approaches close to T_N (Muir, 1987).

The anisotropy of the discontinuity in the linear thermal expansivity at T_N is small but significant, as we

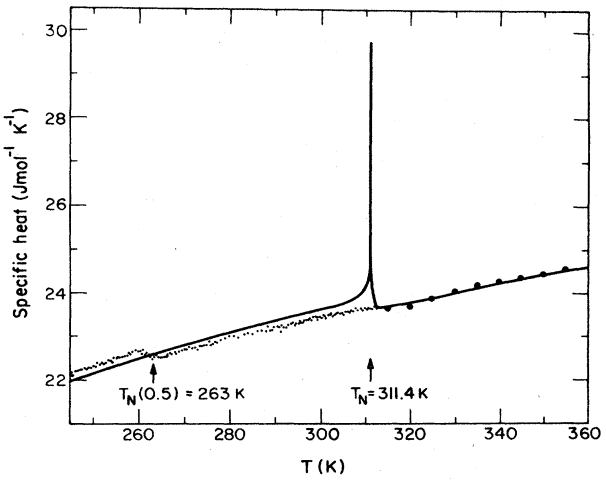

FIG. 80. Temperature dependence of the specific heat of Cr (solid curve) and the alloy $Cr_{99.5}V_{0.5}$ (experimental points) in the neighborhood of the Néel transitions (after Williams *et al.*, 1979, and Fawcett, Kaiser, and White, 1986).

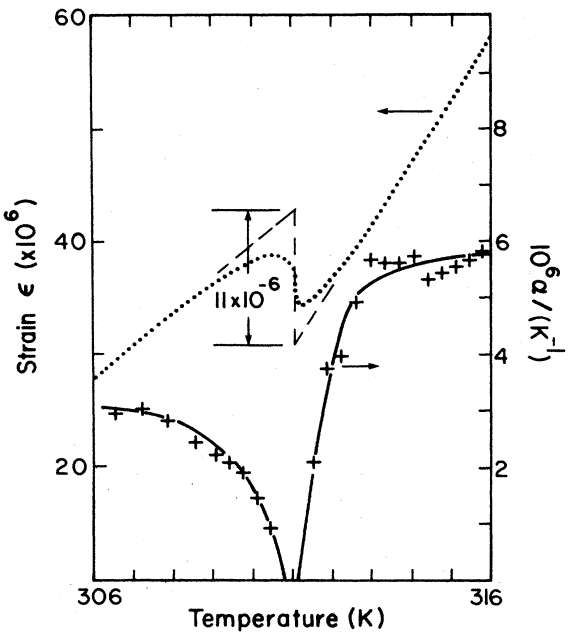

FIG. 81. Temperature dependence of the linear strain, $\varepsilon=(L_{293}-L_T)/L_{293}$, and its derivative with respect to temperature T, and the thermal expansivity α near the Néel transition in Cr. Strain ε: experimental points ● (most omitted for clarity) and ideal first-order transition (long-dashed curve). Expansivity α: calculated points + and smoothed solid curve (after Fawcett, Roberts, Day, and White, 1986).

have seen in Sec. IV.A.3. Thus Lee and Asgar (1969) give an average value of $\Delta\alpha_i$ $(i=1,2,3)$ $\simeq 4.0\times10^{-6}$ K^{-1}, while Steinitz *et al.* (1969) obtain $\Delta\alpha_3-\Delta\alpha_1 \simeq 0.25\times10^{-6}$ K^{-1} and $\Delta\alpha_2-\Delta\alpha_1\simeq 0.02\times10^{-6}$ K^{-1}, with the convention for labeling axes as given in Fig. 36.

The effect of magnetic field on the Néel temperature T_N was determined by Barak *et al.* (1981), who employed a capacitance dilatometer to measure the discontinuous length change parallel to the field to signal the Néel transition. T_N was found to be independent of field up to 16 T, to an accuracy between +10 and −20 mK. Melcher and Wallace (1970) had previously found no change in T_N with a precision ±10 mK in a field of 10 T.

3. Elastic moduli

Inspection of Figs. 43–45 in Sec. III.D shows that the predictions of Walker's (1980b) phenomenological mean-field theory, described in Sec. IV.A.3, for the relative magnitudes of the anomalies at the Néel transition in the different elastic moduli are qualitatively correct. Thus

$$\Delta C_{ii} \gg \Delta C_{Mi} \simeq \Delta C_{\alpha\alpha} \quad (i=1,2,3;\alpha=4,5,6) \ . \tag{81}$$

The fact that the shear moduli ($\alpha=4,5,6$) have small but finite anomalies at the Néel transition, in apparent disagreement with the prediction of the theory, can readily be explained as being due either to the sample's not being perfectly single-S single-Q (Muir *et al.*, 1987) or to the actual Néel transition's being weakly first order rather than continuous as in Walker's theory.

In an orthorhombic system, the quasishear moduli C_{Mi} (see Fig. 42) are of the form

$$C_{Mi}=\tfrac{1}{4}(C_{22}+C_{33}+2C_{44}) -\tfrac{1}{2}[(C_{23}+C_{44})^2+\tfrac{1}{4}(C_{22}-C_{33})^2]^{1/2} \ . \tag{82}$$

Figures 43–45 show, however, that in single-S single-Q chromium the deviation of C_{ij} from being a cubic tensor is small throughout most of the transverse SDW phase, i.e.,

$$C_{ii}\simeq C_{11} \quad (i=1,2,3), \quad C_{\alpha\alpha}\simeq C_{44} \quad (\alpha=4,5,6), \qquad C_{Mi}\simeq C_{M1} \quad (i=1,2,3) \ , \tag{83}$$

so that Eq. (82) gives

$$C_{Mi}\simeq \tfrac{1}{2}(C_{11}-C_{12}) \ . \tag{84}$$

The only exception to Eqs. (83) is the modulus C_{66}, which Fig. 44(c) shows to have a fairly strong magnetic anomaly below T_N. This modulus corresponds to both propagation and displacement directions being in the plane perpendicular to **Q**. Walker has shown that, without a polarizing field $\mathbf{H}_p$, Cr is unstable to a spontaneous deformation corresponding to this configuration. The observed softening of C_{66} below T_N is attributed by Muir *et al.* (1987) to persistence of the instability, even for the large polarizing field $\mathbf{H}_p=5$ T, used in their measurements.

Muir *et al.* (1987a) relate Eqs. (82)–(84) to a thermodynamic analysis of the temperature dependence of the elastic moduli and the bulk thermal expansivity in the transverse SDW phase. They express the magnetic free energy $-\Delta F(t)$ in the form

$$\Delta F(t)=\phi f(t,\varepsilon_i) \ , \tag{85}$$

where ϕ is a positive constant and t is the reduced temperature

$$t=T/T_N(\varepsilon_i) \ , \tag{86}$$

ε_i being components of the strain tensor, T the temperature, and $T_N(\varepsilon_i)$ the strain-dependent Néel temperature.

The observed temperature dependence of the elastic moduli of Cr, as expressed in Eqs. (83) and (84), then leads (Muir *et al.*, 1987a) directly to the following results. (1) The shear strain dependence of T_N is much weaker than the longitudinal strain dependence,

$$\frac{\partial \ln T_N}{\partial \varepsilon_\alpha} \ll \frac{\partial \ln T_N}{\partial \varepsilon_i} \quad (i=1,2,3;\alpha=4,5,6) \ . \tag{87}$$

(2) The longitudinal strain dependence is almost isotropic and mainly a volume dependence, i.e., the dependence on tetragonal strain, $\gamma=\frac{1}{2}(\varepsilon_1-\varepsilon_2)$, is much weaker than the dependence on volume strain ω,

$$\frac{\partial \ln T_N}{\partial \varepsilon_i} \simeq \frac{\partial \ln T_N}{\partial \omega}, \quad \frac{\partial \ln T_N}{\partial \gamma} \ll \frac{\partial \ln T_N}{\partial \omega} . \tag{88}$$

(3) $T_N(\varepsilon_i)$ is an approximately linear function of ε_i for small strain,

$$\frac{1}{T_N}\frac{\partial^2 T_N}{\partial \varepsilon_i \partial \varepsilon_i} \ll \frac{\partial \ln T_N}{\partial \varepsilon_i} . \tag{89}$$

Walker's (1980b) results for the stress dependence of T_N are similar to these assumptions, which accordingly are consistent with the symmetry properties of the transverse SDW and the observed near-isotropy of the thermal expansivity (Lee and Asgar, 1969; Steinitz *et al.*, 1969) as described in Secs. IV.A.3 and VI.A.2.

The validity of this single-parameter theory, according to which the magnitude of magnetic contributions to the elastic moduli and to the thermal expansivity depends only on $\partial \ln T_N/\partial\omega$, may be tested by comparing the magnetic contribution $\Delta B(t)$ to the bulk modulus with the magnetic contribution $\Delta\beta(t)$ to the volume thermal expansivity for $t \lesssim 1$. According to Eq. (85) and in the approximations (87)–(89), the ratio of these two quantities may be used to define a temperature-dependent Grüneisen parameter (Muir *et al.*, 1987a),

$$\gamma(t) = -\frac{1}{T_N B(t)}\frac{\Delta B(t)}{\Delta\beta(t)}$$

$$= -\frac{\partial \ln T_N}{\partial \omega}\frac{t[2f'(t)+tf''(t)]}{[f'(t)+tf''(t)]} . \tag{90}$$

Near T_N one might expect $f'(t)$ to be small compared with $f''(t)$, and with the variation in $B(t)$ much smaller than that in $\Delta\beta(t)$, Eq. (90) predicts the ratio $\Delta B(t)/\Delta\beta(t)$ to be approximately constant.

Figure 82 shows that in fact $\Delta B(t)$ and $\Delta\beta(t)$ give a linear plot over a very wide temperature range both below and *above* T_N. The constant of proportionality for $T < T_N$ gives a constant value for the Grüneisen parameter, $\gamma_{TN-} = -37$, when substituted in Eq. (90), with the average value for $Cr_{95}V_5$, $\bar{B} = 2.07 \times 10^{11}$ Nm^{-2}, substituted for $B(t)$. Alberts and Lourens (1985) find that for $Cr_{95}V_5$, $B(t)$, varies by less than 1% between 130 K and T_N and less than 3% between T_N and 500 K. A similar procedure for the paramagnetic phase for $T > T_N$ gives a somewhat larger value, $\gamma_{TN+} = -144$. It appears from this result that the short-range magnetic order and magnetic fluctuations in the disordered phase of Cr (Grier *et al.*, 1985) are even more volume dependent than is the SDW in the AFM phase.

Katahara *et al.* (1979) measured the elastic moduli of single-crystal Cr up to a pressure of 5 kbar, and it is interesting to note that the behavior of the Néel transition pressure p_N as a function of pressure at constant temperature $T < T_N \simeq 311$ K, is analogous to that observed as a function of temperature at ambient pressure. Thus the longitudinal modulus C_{11} shows a strong magnetic anomaly at p_N, whereas the shear modulus C_{44} and quasishear

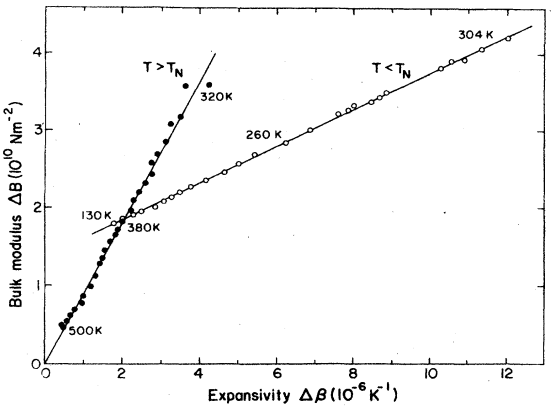

FIG. 82. Comparison of the magnetic anomalies of the bulk modulus $\Delta B(t)$ and the volume thermal expansivity $\Delta\beta(t)$ in chromium: ○, below the Néel transition in the temperature range 130–304 K; ●, above the Néel transition in the temperature range 320–500 K. Both $\Delta B(t)$ and $\Delta\beta(t)$ are obtained by comparing chromium with the paramagnetic alloy $Cr_{95}V_5$, whose thermal expansivity was measured by White *et al.* (1986) and bulk modulus by Alberts and Lourens (1985). The data of Katahara *et al.* (1979) for the elastic constants of Cr up to 700 K were used for $T > T_N$.

modulus C_M show no discontinuity but a change in the pressure dependence dC/dp.

4. Transport properties

Akiba and Mitsui (1972) have performed a critical-exponent analysis of their data for the temperature dependence of the resistivity ρ above and below the Néel transition. Fote *et al.* (1973) have similarly analyzed the thermoelectric power below the Néel temperature T_N, while recognizing that the first-order transition at T_N masks a continuous transition at a higher temperature, which would be the appropriate temperature for a proper analysis of the effect of critical fluctuations. The expected correspondence between the critical exponent of the derivative $d\rho/dT$ of the resistivity with respect to temperature and the critical exponent of the specific heat (Fisher and Langer, 1968) has been investigated in Cr by Salamon *et al.* (1969), and Fote *et al.* (1973) have explored the possibility of correspondence also for the thermopower.

None of this work seems, however, to have shed much light on the critical behavior of AFM Cr at the Néel transition. A more rewarding line of research, employing nuclear relaxation time measured by means of nuclear magnetic resonance, will be discussed in Sec. VII.A.

5. Effect of stress, magnetic field, and impurities

There is a strong pressure dependence of the Néel temperature T_N, as first measured by Mitsui and Tomizuka (1965). Their value, $dT_N/dp = -0.51$ K GPa^{-1}, was

confirmed by McWhan and Rice (1967) as being the limiting low-pressure value, but they found that at high pressure up to 820 GPa, where the Néel transition is depressed to below 100 K, T_N varies exponentially with volume if the bulk modulus B is assumed constant. With $B=162$ GPa the logarithmic volume dependence is thus constant over this pressure range, $d\ln T_N/d\ln V=+26.5$.

There has been some interest in the possibility of reducing the dimensionality of the order parameter by reducing the symmetry of the transverse SDW phase by applying external fields so as to reduce spin fluctuations and induce a continuous Néel transition. Vettier (see Fawcett *et al.*, 1984) found that a 7-T magnetic field applied at 30° to the wave vector **Q** of the SDW, so as to make it single-polarization as well as single-**Q** right up to the Néel transition, did not change the first-order nature of the transition. In fact, T_N is remarkably insensitive to magnetic field, as remarked in Sec. VI.A.2.

Barak and Walker (1982) investigated the effect of uniaxial stress on the Néel transition in Cr, using renormalization-group methods. They predicted that a compressive [110] stress would lead to a tricritical point where the Néel transition becomes continuous, but unfortunately attempts by Fawcett *et al.* (1984) to observe such an effect resulted only in irreversible broadening of the transition.

It seems, however, that dilute impurities produce a clear change in the nature of the transition, as illustrated in Fig. 83. The first-order transition seen in the thermal expansion of pure Cr, illustrated in Fig. 81, has changed with the introduction of only 0.5 at. % V into an apparently continuous transition, which is not appreciably broadened by inhomogeneity of composition. Fawcett, Roberts, Day, and White (1986a) found that Mo as a solute in Cr produces a similar effect on the transition. Camargo and Brotzen (1982) and Castro *et al.* (1986) found that 0.67 at. % V in Cr dramatically suppresses the ultrasonic attenuation, which is very large at T_N in pure Cr (>40 dB cm^{-1}, according to Fawcett *et al.*, 1975).

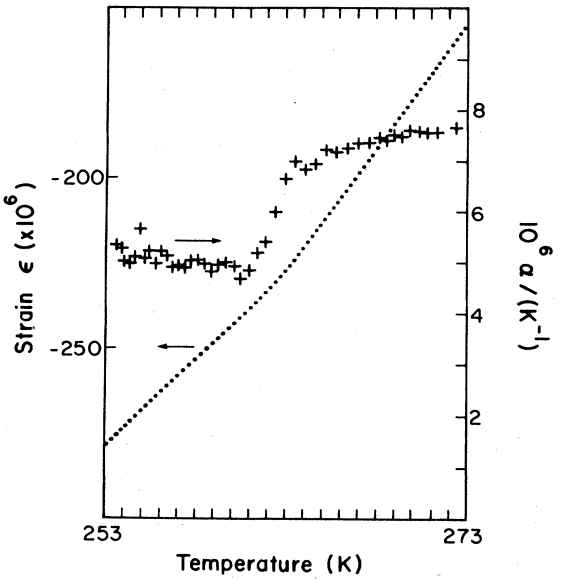

FIG. 83. Temperature dependence of the linear strain, $\varepsilon=(L_{293}-L_T)/L_{293}$, and its derivative with respect to temperature T, the thermal expansivity α, near the Néel transition in Cr + 0.5 at. % V. Strain ε: experimental points ●. Expansivity α: calculated points + (after Fawcett, Roberts, Day, and White, 1986).

B. Spin-flip transition

The spin-flip transition at temperature $T_{SF}\simeq 123$ K can readily be described within the framework of a Landau-type model, for example, by introducing temperature dependence with a change of sign at T_{SF} in the leading term A_0 in Eq. (45) for the anisotropy coefficient of the quadratic term in the amplitude S of the SDW in the free energy of Eq. (44) (Allen and Young, 1975). When one attempts to develop a microscopic theory to explain this change of sign, however, one finds that the two mechanisms responsible for uniaxial anisotropy in ferromagnets, magnetic dipole interaction and spin-orbit coupling, both have the same temperature dependence, namely that of the AFM energy gap squared. Thus a zero crossing of the anisotropy coefficient does not occur (Allen and Young, 1977). Cowan (1978) has provided a phenomenological theory in which the SDW drives the spontaneous strain through a magnetostrictive coupling between the strain field and the magnetic field, as well as through a spin-independent coupling between the strain and the electrons. The spontaneous strain and the spin-flip transition are thus obtained.

The magnetic phase diagram near T_{SF} has been mapped out by observing the peaks in the ultrasonic attenuation, which occur at the phase boundaries (Barak *et al.*, 1981). Analysis of the phenomenological free energy constructed by the use of symmetry arguments (Walker, 1980b) gives the phase diagram shown in Fig. 84. When the magnetic field **H** is close to the direction of **Q** and the temperature somewhat below T_{SF}, a new phase l_2 intervenes between the low-field longitudinal SDW phase l_1 and the high-field transverse SDW phase t. At the phase boundaries the angle between the polarization vector **S** and **Q** changes discontinuously in first-order transitions. Below a critical temperature, which increases as the angle θ between **H** and **Q** increases, the discontinuous change in the angle at the phase transition from l_1 to l_2 disappears. There is a line of triple points at which l_1, l_2, and t are coexistent, but the l_2 phase disappears for $\theta\geq \tan^{-1}\frac{1}{2}=26.7°$.

Measurements of the magnetic torque (Griessen and Fawcett, 1977) near T_{SF} were explained by Barak and Walker (1981) by use of this model and estimates for the anisotropy in the discontinuities in the magnetic susceptibility at T_{SF} based on the work of Pepper and Street (1966). Alternatively the thermal activation model of polarization domains (Sec. VIII.C) may be used to describe

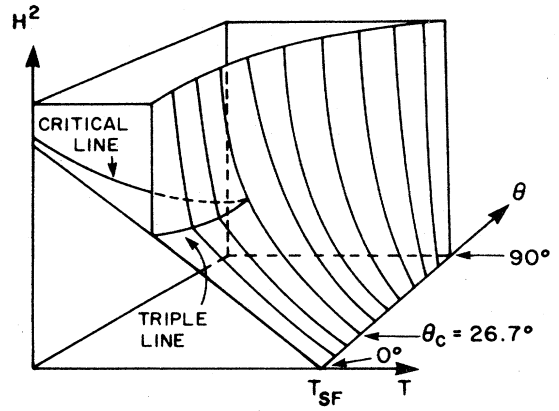

FIG. 84. Magnetic phase diagram for the model free energy of chromium described in the text near the spin-flip temperature T_{SF}, θ being the angle between the magnetic field **H** and the wave vector **Q** of the SDW, θ_c is the critical temperature where the l_2 phase disappears (after Barak *et al.*, 1981).

the essential features of the phase diagram shown in Fig. 84 (Steinitz and Pink, 1980), as well as the torque data (Steinitz *et al.*, 1972).

Dubiel (1984) has observed the spin-flip transition by means of the Mössbauer effect in ^{119}Sn dissolved in Cr. He found the transition to be clearly first order, with hysteresis in some features of the Mössbauer spectrum. Both the Mössbauer effect and the time-differential perturbed angular correlation (TDPAC) technique, described in Sec. VII.A, show a precursor to the spin-flip transition starting about 10 K below T_{SF}. The TDPAC results show this clearly in Fig. 85, as do the shear-wave data shown in Fig. 44. These results may provide some evidence for the mixed state of longitudinal and transverse SDW phases that Griessen and Fawcett (1977) invoke to explain the broad spin-flip transition seen in the magnetic torque as the magnetic field direction moves away from the **Q** vector.

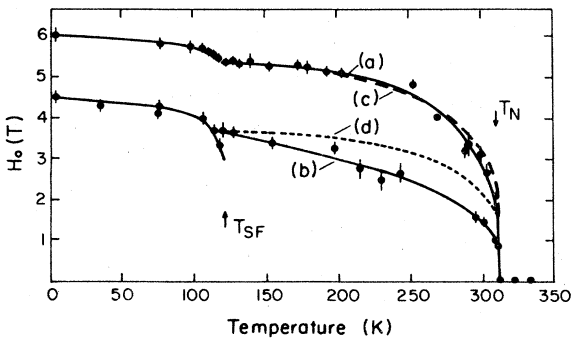

FIG. 85. Temperature dependence of the maximum hyperfine field H_0 produced by the SDW in Cr: (a) Cd probe; (b) Ta probe. Temperature dependence of the amplitude of the SDW [(c) and (d); from the data in Fig. 4(a)] normalized to the hyperfine fields at temperature 128 K (after Venegas *et al.*, 1980).

The pressure dependence of the spin-flip transition measured by Alberts and Fisher (1980) is $dT_{SF}/dp = 0.59 \pm 0.05$ K GPa^{-1}. When combined in a Clausius-Clapeyron relation with the volume change $\Delta V/V = 1.14 \times 10^{-6}$, measured by Steinitz *et al.* (1969), this gives a latent heat 0.03 J mol^{-1}, which agrees well with the measured value 0.04 ± 0.02 J mol^{-1} of Benediktsson and Åström (1982) but less well with the value 0.07 J mol^{-1} of Polovov (1974).

The components of the magnetic-susceptibility tensors in the transverse SDW and longitudinal SDW phases just above and below, respectively, the spin-flip temperature are given in Table V.

The behavior of the elastic moduli at the spin-flip transition is most interesting (Fawcett *et al.*, 1988). The longitudinal elastic moduli C_{ii} $(i = 1,2,3)$ show only small anomalies at T_{SF} (Fig. 43), while the anomalies in the quasishear moduli C_{Mi} (Fig. 45) are somewhat larger in magnitude but still occur over a narrow temperature interval around T_{SF}.

The magnetic anomalies in the shear moduli $C_{\alpha\alpha}$ $(\alpha = 4,5,6)$, on the other hand, occur over a wide temperature range about T_{SF} and show remarkable differences that have not been explained. Thus C_{44} (curve *a* in Fig. 44) shows a precursor to the spin-flip transition, with softening beginning almost immediately as temperature increases from zero, whereas C_{55} (curve *b* in Fig. 44) shows softening both above T_{SF}, beginning at about 175 K, and below like C_{44}. The third shear modulus C_{66} (curve *b* in Fig. 44) abruptly softens as the temperature increases through T_{SF}, which is consistent with the explanation offered in Sec. VI.A.3 for the softening close to the Néel transition.

VII. MICROSCOPIC PROPERTIES AND SURFACE ANTIFERROMAGNETISM

A. Hyperfine-interaction properties

Hyperfine interactions provide information about the microscopic structure of the hyperfine field either at the Cr nucleus, ^{53}Cr having a spin $\frac{3}{2}$ and a natural abundance of almost 10%, or at an impurity atom that probes the field of the SDW. They also provide information about the nuclear relaxation time or the motional narrowing at either the ^{53}Cr nucleus or that of the probe atom. The spin-lattice relaxation time becomes very short close to the Néel temperature because of spin fluctuations. Motional narrowing could in principle provide information about phasons or other excitations, but thus far has not been observed. Polycrystalline samples or powders have been used to avoid texture effects and thus simplify the interpretation, but in principle hyperfine interactions may be used to explore the SDW in single-**Q** Cr.

The influence of the probe atom on the SDW must be a matter of concern if one wishes to explore the SDW of pure Cr. On the other hand, the properties of the impur-

ity atom itself on the Cr matrix may be of great interest: does it have a magnetic moment, for example, and if so how does it couple to the SDW?

The SDW in Cr has been investigated by use of nuclear magnetic resonance (NMR; Barnes and Graham, 1962), Mössbauer effect (Street and Window, 1966), time-differential perturbed angular correlation (TDPAC; Benski *et al.*, 1975), and muon-spin resonance (μSR; West *et al.*, 1981), where in each case I have given the reference to the earliest significant reported work.

The first convincing experiments were performed by Street and Window (1966) using the Mössbauer effect with ^{119}Sn as the probe. They showed that the hyperfine field distribution was consistent with an incommensurate linear SDW, which disappeared in a clear first-order transition at the Néel temperature. The Mössbauer effect was used by Window (1970) to determine the effect of cold work on the AFM structure of Cr, as I shall describe in Sec. VIII.A. Dubiel (1984) has found remarkable precursor and hysteretic effects at the spin-flip transition using the Mössbauer effect as described in Sec. VI.B. Dubiel and Le Caër (1987) have measured the Mössbauer effect of ^{119}Sn at a (110) face of Cr and find that it can be described in terms of a snoidal SDW equivalent to a third-harmonic SDW having about two percent of the amplitude of the fundamental SDW.

TDPAC has the great advantage over the Mössbauer effect of high sensitivity, so that the concentration of the probe atom can be kept well below 1 ppm. The difficulty in general with the Mössbauer-effect method is the poor field resolution and the small amplitude of the hyperfine field components of the spectrum. This leads to the use of a relatively high concentration of the probe atom, typically above 0.1 at. % (> 1000 ppm), with the attendant difficulty that the SDW may be severely perturbed.

Teisseron *et al.* (1978) used a ^{181}Ta probe (^{181}Hf being the parent nucleus) while Venegas *et al.* (1980) used ^{111}Cd (^{111}In being the parent nucleus), the latter being a superior probe because of its large anisotropy and its lifetime being in the correct range. The results, illustrated in Fig. 85, show that the Néel transition is clearly first order and that the spin-flip transition is also first order, but with a precursor starting about 20 K below the transition temperature, $T_{SF} \simeq 123$ K, which suggests a region of mixed longitudinal SDW and transverse SDW phases. The fact that the hyperfine field appears to be different above and below the spin-flip transition is difficult to reconcile with the very small volume change, which implies that amplitude of the SDW changes very little at the transition (Fawcett, Kaiser, and White, 1986).

The hyperfine field distribution indicates that neither probe atom perturbs the SDW, i.e., they neither clamp its phase nor distort its shape. The temperature dependence of the hyperfine field at the Ta atom, however, deviates from that of the amplitude of the SDW as determined by neutron diffraction.

The other important application of hyperfine interactions to the study of AFM Cr is the measurement of the

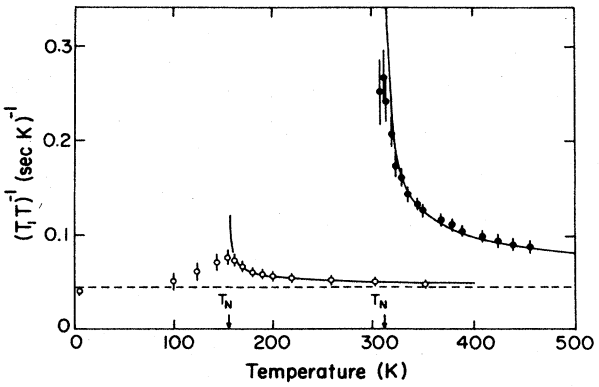

FIG. 86. Temperature dependence of the nuclear spin relaxation rate $(T_1T)^{-1}$ of ^{53}Cr: ●, Cr; ○, $Cr_{98}V_{02}$. The dashed curve shows the Korringa rate $(T_{10}T)^{-1}$ for ^{53}Cr. The solid curves show the functions of the form of Eq. (84) which best fit the data: $0.044+0.5(T-T_N)^{-1/2}$ for Cr and $0.044+0.075(T-T_N)^{-1/2}$ for $Cr_{98}V_{02}$ (after Kontani and Masuda, 1983).

spin-lattice relaxation time T_1 of the ^{53}Cr isotope having spin $\frac{3}{2}$ to determine the temperature dependence of the spin fluctuations near the Néel temperature. In Fig. 86 the temperature dependence of the reciprocal product $(T_1T)^{-1}$ of T_1 with temperature T is found to agree well with the expression

$$\frac{1}{T_1T} = A_1 + \frac{A_2}{(T-T_N)^{1/2}} , \tag{91}$$

as shown by the fitted curves. Here $(T_{10}T)^{-1}$ is obtained from the spin-lattice relaxation time T_{10} of ^{53}Cr in nonmagnetic $Cr_{95}V_5$, which varies inversely with temperature T according to the Korringa theory. The second term of Eq. (91) is of the form predicted by a theory of spin fluctuations as formulated by Hasegawa (1978a, 1978b) for a nesting model and by Moriya and Kawabata (1973) for a self-consistent renormalization theory of an itinerant antiferromagnet.

B. Surfaces of Cr and epitaxial Cr/Au(100)

I discuss the surface of Cr under the rubric of microscopic properties, since microscopic probes such as low-energy electron diffraction (LEED), Auger electron spectroscopy (AES), electron energy-loss spectroscopy (EELS), ultraviolet photoelectron spectroscopy (UPS), angle-resolved photoelectron spectroscopy (ARPES), etc., are experimental tools used to study them.

Apart from two-dimensional ferromagnetism, which is thought to occur in the surface layer of Cr(100), and superconductivity, which some experiments indicate to be associated with the epitaxial interface Cr/Au(100) and perhaps other interfaces, the structure of Cr(100) is itself of interest. Apparently, unlike Mo(100) and W(100), it

does not reconstruct (Foord and Lambert, 1982).

Two early experimental results suggested that the AFM state of bulk Cr may be profoundly modified in fine particles or thin films. Schmidt *et al.* (1972) found that ion-beam sputtered Cr thin films of thickness 1–3 μm were superconducting, with transition temperatures up to 1.5 K, depending upon the preparation procedure. Matsuo and Nishida (1980) found that fine particles of diameter 0.04–0.08 μm showed a strong magnetic susceptibility, which peaked at a temperature of 300 K and thereafter decreased to reach the small paramagnetic value at an apparent ferromagnetic transition temperature $T_C \simeq 800$ K. The magnetization exhibited hysteresis at temperatures $\lesssim 300$ K. Exposure to air eliminated the hysteresis and reduced the saturation magnetization by about a factor of 3, which indicates that the anomalous behavior is associated with the surface of the particles.

1. Surface of Cr(100) and Cr(110)

Teraoka and Kanamori (1978) had suggested that surface-induced antiferromagnetism would persist above the bulk Néel temperature, because of enhancement of the local density of states at the Fermi energy due to the decrease in the number of neighboring atoms. Allan (1978, 1979, 1981) also predicted that the reduced coordination number 4 at the Cr(001) surface would result in surface magnetic order, and indeed his first tight-binding calculation (Allan, 1978) had indicated a ferromagnetic surface phase characterized by an exchange-split surface spin density of states with large localized surface magnetic moments of about 2.8 μ_B. Grempel (1981) extended the theory to finite temperature using a spin-fluctuation formalism, and predicted the persistence of Cr(001) surface ferromagnetism for temperatures up to $T_S = 850$ K. The saturation magnetization shows a peak at the bulk Néel temperature and then decreases in a mean-field fashion to disappear continuously at T_S. This behavior is similar to that observed by Matsuo and Nishida (1980) in fine particles of Cr having a Curie temperature of about 800 K.

The surface ferromagnetism may be understood intuitively with reference to Fig. 87, since commensurate single-**Q** antiferromagnetism in a bcc structure corresponds to the polarization in alternate (001) planes being antiparallel, so that the surface (001) plane contains atoms having the same spin direction.

The moments of the first six layers of atoms given in the caption of Fig. 87 were calculated by Victora and Falicov (1985) using the Slater-Koster tight-binding scheme with one- and two-center integrals treated as parameters, which are chosen to fit the bulk band structure of Moruzzi *et al.* (1978). The calculations included *s*, *p*, and *d* orbitals with interactions up to second nearest neighbors. The near-surface layers are AFM, layers 5 and 6 having essentially the same equal and opposite moments, but the moment per atom is still somewhat enhanced relative to the maximum value $0.62\mu_B$ of the SDW observed in bulk Cr.

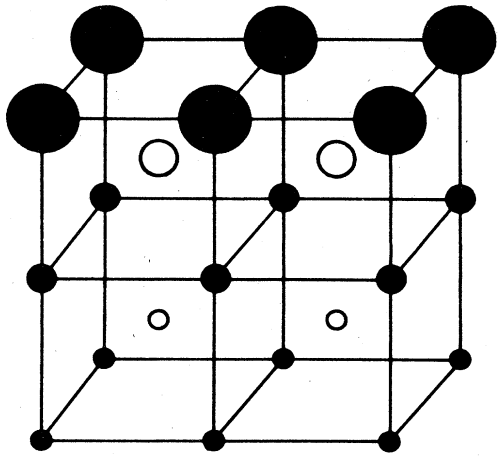

FIG. 87. Magnetic moments of surface and near-surface atoms at the Cr(001) surface. The diameter of the circles represents the magnitude of the moment μ: surface layer, $\mu_1 = 3.00\mu_B$; second layer, $\mu_2 = -1.56\mu_B$, $\mu_3 = 1.00\mu_B$, $\mu_4 = -0.93\mu_B$, $\mu_5 = -0.86\mu_B$, $\mu_6 = 0.85\mu_B$. Solid (open) circles indicate polarization parallel (antiparallel) to ⟨100⟩ (or ⟨010⟩) (after Victora and Falicov, 1985; Klebanoff and Shirley, 1986).

In the most recent calculation by Hasegawa (1986) the moment per atom in the surface layer is somewhat smaller than in other calculations, but still much larger than the bulk moment per atom, which is not reached until the eighth layer. Hasegawa did finite-temperature calculations for the different layers, with most interesting results, e.g., that a moment remains on every layer up to the eleventh up to $3.0T_N$, while all magnetism disappears at the Curie temperature of the surface layer, $3.25T_N$, where $T_N = 370$ K is the calculated Néel temperature.

The first experimental evidence for ferromagnetic order in the Cr(100) surface was provided by Rau and Eichner (1981) using electron-capture spectroscopy, though their sample displayed a 2×2 structure indicative of impurities, which may have affected their results.

Angle-resolved photoelectron spectroscopy (ARPES) has been employed by Klebanoff *et al.* (1984; Klebanoff, Victora *et al.*, 1985; Klebanoff, Robey *et al.*, 1985, 1986) to probe the surface and near-surface regions of Cr(001). This technique provides a wealth of information about the local density of states for different points in the Brillouin zone, and at higher energies can also probe the valence electron spin (Klebanoff and Shirley, 1986). We shall refer the reader to the review paper by Klebanoff, Robey *et al.* (1986) for experimental details explaining how the angle of emission and the different polarization geometries are used to determine the symmetries of the various features of the ARPES spectrum. As illustrated in Fig. 88, exposure to a contaminating gas severely reduces their intensity and hence shows that the two salient features of the spectrum, labeled 1 and 2, are associated with surface states.

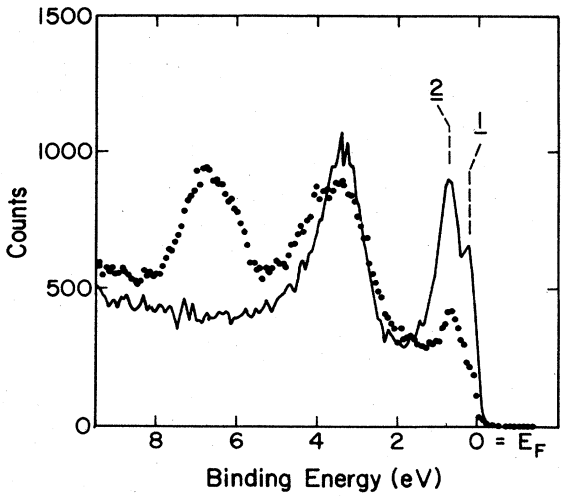

FIG. 88. Normal emission *P*-polarization ARPES spectra for photon energy 23.0 eV of the Cr(001) surface before (line) and after (dots) covering by five layers of CO. The binding energy E is measured relative to the Fermi level E_F (after Klebanoff *et al.*, 1986).

Figure 89 shows how the binding energies corresponding to features 1 and 2 of the spectrum converge with increasing temperature to a single feature at about 800 K, which is tentatively attributed to the disappearance of surface ferromagnetism, being in good agreement with the surface ordering temperature, $T_S = 850$ K, calculated by Grempel (1981).

The labels associated with features of the theoretical electronic structure indicated in Fig. 90 correspond to the assignment by Klebanoff, Robey *et al.* (1986) of feature 2 in Fig. 88 to nearly degenerate, Δ_5-symmetry, up- and down-spin surface states, corresponding to d_{xz} and d_{yz} orbital character, and the assignment of feature 1 in Fig. 88 to a Δ_1-symmetry up-spin surface state, corresponding to d_{z^2} orbital character.

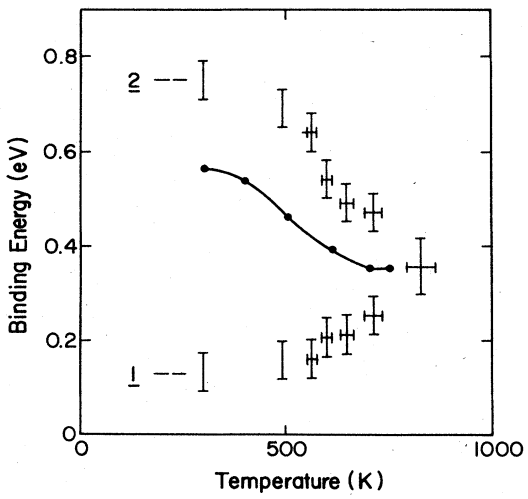

FIG. 89. Binding energies of the features labeled 1 and 2 in Fig. 88 as a function of temperature. The solid circles and line show, for comparison with feature 2, the temperature dependence of the exchanging splitting in Ni suitably scaled in energy (Klebanoff *et al.*, 1986).

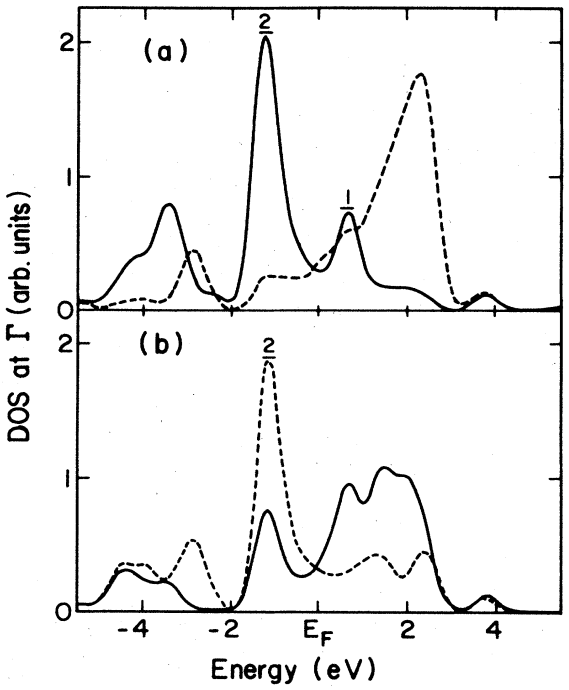

FIG. 90. The *d*-orbital component of the projected surface: (a) surface layer and (b) second layer. For both (a) and (b) the solid curve corresponds to polarization parallel to the magnetization of the surface layer (solid circles in Fig. 87) and the dashed curve to polarization antiparallel (open circles in Fig. 87). The relation of features 1 and 2 of the ARPES spectrum of Fig. 88 to the theoretical electronic structure as suggested by the labels is discussed in the text (after Victora and Falicov, 1985).

The overall agreement of the ARPES data with theory indicates that the Cr(001) surface is ferromagnetic. This interpretation and the resemblance of the temperature dependence of feature 2 to that of the exchange splitting in Ni, as illustrated in Fig. 89, suggests that the decrease of binding energy of feature 2 corresponds to the progressive decrease of surface ferromagnetism with increasing temperature.

Other features of the ARPES spectra, as described by Klebanoff *et al.* (1986) show that the near-surface electrons feel, and self-consistently establish, antiferromagnetism in the near-surface layers of Cr(001), in accordance with the theoretical predictions of Allan (1978, 1979, 1981) and Grempel (1981). Victora and Falicov (1985) find that the moment on alternate layers alternates between up and down and progressively decreases until it is essentially AFM by layer 5, as indicated in Fig. 87.

Klebanoff, Robey *et al.* (1985) measured the ARPES spectra at various temperatures up to ~1100 K, and found evidence that near-surface antiferromagnetism persists up to these high temperatures. This stability may

derive from that of the Cr(100) ferromagnetic surface phase, which Matsuo and Nishida (1980) apparently saw in fine particles of Cr up to about 800 K.

For the Cr(110) surface Victora and Falicov (1985) obtain an AFM configuration, as one expects intuitively, since the (110) plane includes both the body-center and corner atoms of the cubic unit cell. The moment of the surface atoms is considerably enhanced, $\mu_1 = 2.31\mu_B$. Persson and Johansson (1986), on the other hand, measured an ARPES spectrum with a feature at about 0.6 eV binding energy, which disappeared with a half-layer of oxygen contamination. This is similar to the feature 2 in Fig. 88, which Klebanoff *et al.* (1986) associated with a ferromagnetic surface layer.

Persson and Johansson (1986) performed a band-structure calculation for paramagnetic Cr and used it to calculate theoretical spectra for different emission angles, which matched fairly well their observed ARPES spectra for Cr(110). They concluded from this comparison that the 0.6-eV feature is due to a *d*-band surface state. The ferromagnetic or AFM nature of this state is not specified.

2. Epitaxial Cr/Au(100) monolayer, sandwiches, and superlattices

Superconductivity with transition temperatures up to 3 K in 2.5-nm multilayers of Cr sandwiched between thicker Au(100) films was reported by Brodsky *et al.* (1982). The question immediately arose whether the Cr(100) ferromagnetic surface states persisted at the Cr-Au interface, and if so why the ferromagnetism did not suppress the superconductivity. Brodsky *et al.* advanced a hypothesis to circumvent this problem. They attributed the superconductivity to a new fcc phase of Cr having the Au lattice constant, which corresponds to a 41% increase in volume and thus an increased density of states $N(E_F)$ at the Fermi surface.

One would expect, however, strain-free epitaxy of bcc Cr(100) on fcc Au(100), due to fortuitous matching of the primitive two-dimensional square nets. Zajac *et al.* (1985) employed the several techniques listed at the beginning of Sec. VII.B to explore the epitaxy and electronic structure of the Cr-Au(100) interface. Their results were all compatible with bcc structure, and their UPS spectra were similar to the ARPES spectra, which Klebanoff *et al.* (1986) had interpreted as indicating a ferromagnetic surface layer. Zajac *et al.* estimated the surface moment to be $2.4\mu_B$ per atom.

Hanf *et al.* (1987), on the other hand, find large surface moments $\sim 5\mu_B$ per atom for up to three layers of Cr on Au(100). They attribute this to the formation of substitutional fcc Ru-Cr alloy having large local moments. Upon further Cr deposition they suggest that bcc Cr forms on top of the interface alloy.

Table XVII shows the results of the theory and experiment for the ferromagnetic Cr layer, or in some cases AFM double layer, for epitaxial Cr/Au(100); the Cr(100) results are also summarized here. Oguchi and Freeman (1986) used a spin-polarized linearized muffin-tin-orbital method within a local spin-density functional formalism to calculate various configurations. Magnetic interactions between Cr layers in the superlattices always result in AFM coupling, which doubles the unit cell as indicated in Table XVII for the monolayer superlattice. The moment of the Cr atom in this case is slightly larger than in the ferromagnetic case, the latter being energetically unfavorable by 0.14 eV (11 mRy) per formula unit. This enhancement of the moment can be understood by the fact that the AFM coupling between the ferromagnetic Cr monolayers works destructively on the magnitude of the moments under the ferromagnetic constraint along the [100] direction.

The experimental data of Brodsky *et al.* (1986) are somewhat inconclusive. The monolayer Cr sandwiches gave a paramagnetic susceptibility with a magnetic moment per atom at temperature 5 K in a field of 1 T ranging from 0.02 to $0.34\mu_B$. The two-layer Cr sandwiches had much smaller moments, which suggests AFM coupling.

VIII. TECHNICAL ANTIFERROMAGNETISM AND DOMAINS

The term "technical antiferromagnetism" was coined by Arrott (ca. 1975) by analogy with technical ferromagnetism. The latter describes the effect on a ferromagnet of structural defects and impurities in their interplay with magnetic forces so as to minimize the magnetic anisotropy and magnetoelastic energies associated with the spontaneous magnetic moment and its spatial distribution, i.e., domain-wall energies. Technical ferromagnetism has been studied intensively because of the immense importance of ferromagnets in technology. By contrast, antiferromagnets have negligible technical application, and the study of technical antiferromagnetism has thus been neglected. The absence furthermore of a spontaneous magnetic moment in an antiferromagnet makes the experimental study of AFM domain structure considerably more difficult than that of domain structure in a ferromagnet.

The magnetic phase diagram of strained Cr, discussed in Sec. VIII.A, has four distinct phases, which coexist over wide temperature intervals. An important feature of technical antiferromagnetism is the occurrence of Q domains. The methods used to obtain a single-Q sample, which is essential for the study of many physical properties of AFM Cr, are described in Sec. VIII.B. The hypothesis that interstitial nitrogen is involved in the formation of Q domains on cooling through the Néel transition is discussed and methods of observing Q domains are also described in Sec. VIII.B.

Static polarization S domains are a less well-established property of the transverse SDW AF_1 phase, which in any case would necessarily disappear at the spin-flip transition to the longitudinal SDW AF_2 phase,

TABLE XVII. Magnetic moment per atom on the surface layer of Cr(100) and epitaxial Cr/Au(100) monolayer, sandwiches, and superlattices.

	Configuration		Moment	Reference
			(μ_B)	
Theory	...Cr		2.8	a
			2.6	b
			3.0	c
			2.2	d
	...CrCrCrCrCr...	Five-layer film	2.6	e
	...CrAu	Au monolayer	3.7	f
	...AuCrCr	Cr bilayer	2.9, −2.3	f
	...AuCrAu...	Sandwich	3.1	f
	...AuCrCrAu...	Sandwich	±(<3) AFM	g
	...AuCrAuCrAuCrAuCr...	Superlattice	±3.0 AFM	g
	...AuAuAuCrAuAuAuCr...	Superlattice	3.0	g
Experiment	...Cr		2.4	h
	...Cr_n ($n=1-3$)		~5	i
	...AuCrAu...	Sandwich	Paramagnet	j
	...AuCrCrAu...	Sandwich	AFM(?)	j

[a] Allan (1978).
[b] Grempel (1981).
[c] Victora and Falicov (1985).
[d] Hasegawa (1986): −1.22, 0.95, −0.72, 0.73, and $-0.68\mu_B$ in second through sixth layers.
[e] Hirashita *et al.* (1981): second layer, $-0.9\mu_B$, center layer, $+0.6\mu_B$.
[f] Fu *et al.* (1985).
[g] Oguchi and Freeman (1986).
[h] Zajac *et al.* (1985).
[i] Hanf *et al.* (1987).
[j] Brodsky *et al.* (1986).

where the polarization flips from lying along the x or y axis to the z axis in a $\mathbf{Q}_z$ domain. The alternative "random-strain model" and the "thermal activation model" employed to describe the AF_1 phase are discussed in Sec. VIII.C. The ultrasonic attenuation and internal friction data presented in Sec. VIII.D show clearly the influence of polarization in the AF_1 phase, with some evidence for static **S** domains close to the spin-flip transition.

Finally in Sec. VIII.E we discuss the remarkable hysteresis in the pressure dependence of the wave vector **Q** and in the magnetostriction, which provide evidence for technical antiferromagnetism in the longitudinal SDW AF_2 phase.

A. Magnetic phase diagram of strained Cr

The first neutron-diffraction results of Shull and Wilkinson (1953) showed a commensurate AFM state in Cr with a Néel transition at about 200 °C. This AF_0 phase was later recognized to be associated with strain in the heavily crushed Cr powder sample. The transition from the paramagnet (P phase) to the transverse SDW (AF_1 phase) at $T_N \simeq 311$ K and then to the longitudinal SDW (AF_2 phase) at $T_{SF} \simeq 123$ K were later seen to be characteristic of a relatively unstrained Cr sample.

These three AFM structures are illustrated in Fig. 91(a); the corresponding neutron-diffraction peaks shown in Fig. 91(c) enabled Bacon and Cowlam (1969) to determine the temperature dependence of magnetic structure for several strained Cr samples, as shown in Fig. 92. Annealing a heavily crushed (coarse powder) sample progressively changed the magnetic phase diagram, as shown in Fig. 93, until behavior close to that of an ideal single crystal of Cr was obtained.

Williams and Street (1981a) used the same technique, supplemented by studies of various physical properties, to determine the magnetic phase diagram of powder samples and samples prepared by a variety of methods that might be expected to induce severe internal strains—hot-rolling and then swaging or hot-drawing. Williams and Street (1981) also showed that the increase in the temperature of the Néel transition (which was greatly broadened in these inhomogeneously strained samples) by strong tensile stress was consistent with the hydrostatic pressure dependence of the spin-flip temperature, using a model for the strain distribution associated with structural dislocations already present in the sample. Various reports of hysteresis and relaxation effects led Williams and Street (1980) to a careful study of the Néel transition, which showed, however, no hysteresis in a variety of strained and annealed samples.

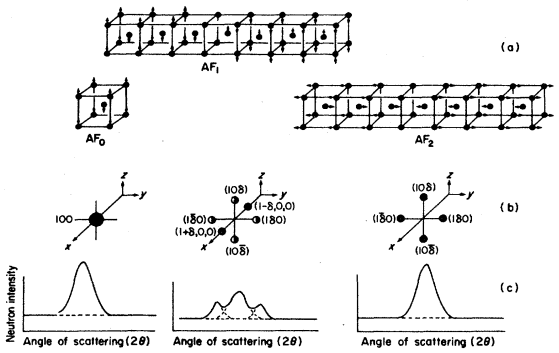

FIG. 91. Neutron diffraction peaks expected for commensurate antiferromagnetism and for the transverse and longitudinal SDW in chromium. The diagrams at (a) represent the magnetic structures AF_0, AF_1, AF_2 which occur in Cr. The arrows show the directions and approximate magnitudes of the magnetic moments. The resulting density in reciprocal space in the neighborhood of the point (100) is shown at (b) for each of the structures. The symbol ◐ indicates a peak of half the intensity of peaks marked ●, bearing in mind the available spin directions for the various domains. The curves (c) show, in each case, the shape of the peaks that would occur in the neutron-diffraction pattern, in the neighborhood of the (100) position, for a polycrystalline sample (after Bacon and Cowlam, 1969).

B. Wave-vector Q domains

We shall follow the excellent review of Street *et al.* (1968), to which little new information has been added, and where earlier references may be found:

(1) A field-cooled sample remains single-**Q**, and the distribution of **Q** domains in a poly-**Q** sample remains unchanged, for temperature cycling throughout the AF_1 and AF_2 phases.

(2) Cooling through the Néel transition with a tensile stress along [001] results in a single-$\mathbf{Q}_z$ domain. Conversely, compressive stress cooling along [001] results in a state containing $\mathbf{Q}_x$ and $\mathbf{Q}_y$ domains. These results are consistent with the spontaneous magnetostriction of a single-**Q** sample shown in Fig. 38.

(3) The application of a strong magnetic field, $\mathbf{H}\|[001]$, in the AF_2 phase of a single-$\mathbf{Q}_z$ sample results in an irreversible change to a state containing $\mathbf{Q}_x$ and $\mathbf{Q}_y$ domains. The effect is even more pronounced in a poly-**Q** sample, presumably because $\mathbf{Q}_x$ and $\mathbf{Q}_y$ domains already exist as nucleating centers before the field is applied. This experimental result is consistent with the anisotropy of the magnetic susceptibility, since $\chi_\perp^L > \chi_\parallel^L$ in the AF_2 phase, as shown in Table V. Thus the polarization **S** tends to be driven perpendicular to **H**, taking the wave vector **Q** with it, since $\mathbf{S}\|\mathbf{Q}$ in the AF_2 phase, so as to minimize the Gibbs free energy.

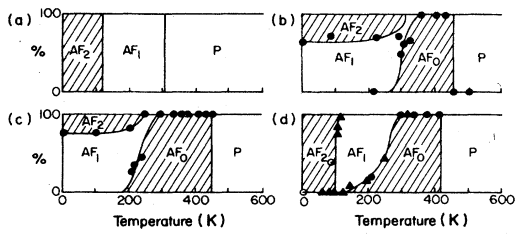

FIG. 92. Magnetic phase diagrams deduced for (a) ideal single-crystal Cr, (b) coarse powder, (c) fine powder of Cr, and (d) 99.5% Cr–0.5% Re, indicating the extent of occurrence of the magnetic structures AF_2, AF_1, AF_0, and *P* (after Bacon and Cowlam, 1969).

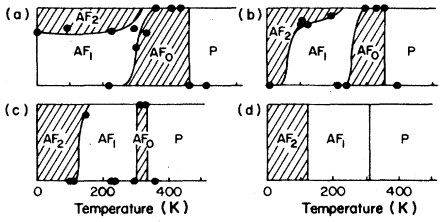

FIG. 93. The effect of annealing on the magnetic phase diagram deduced from the experimental observations for coarse powders of Cr. The initial diagram (a) is contrasted with (b), after annealing at 600 °C, and (c), after annealing at 1000 °C. Diagram (c) is approaching the behavior found in single-crystal Cr, for which the phase diagram is shown at (d) (after Bacon and Cowlam, 1969).

It should be noted that the observation of Golovkin *et al.* (1977), who found that an essentially single-$\mathbf{Q}_z$ sample may be obtained by cooling through the spin-flip transition starting from some temperature not too far below the Néel transition in a magnetic field of only about 2 T applied along [001], is completely at variance with this result. Fawcett, Holden *et al.* (1988) found that Golovkin's procedure (termed the cryomagnetic method) not only fails to produce a single-**Q** state but destroys the single-**Q** state produced by the conventional field-cooling method. They point out that this result is consistent not only with the reversal of the anisotropy at the spin-flip transition (Pepper and Street, 1966), but also with the observed depression of the transition temperature by a field **H** along **Q** and the occurrence of **Q** flipping for sufficiently large **H** (Steinitz *et al.*, 1969).

I cannot explain this serious discrepancy between the results of Golovkin *et al.* and Fawcett *et al.* It is clear, however, that the claim by Golovkin *et al.* (1977) that the cryomagnetic method is superior to conventional field cooling is seriously misleading. van Rijn and Alberts (1983) used the cryomagnetic method and, employing a field $\mathbf{H}=1.7$ T, produced a sample that was quite unsatisfactory for their study of the elastic moduli of single-**S** single-**Q** Cr. Comparison with the same study performed on a 97% single-**Q** sample (Muir *et al.*, 1987c) shows that the use of the cryomagnetic method seriously impaired the value of van Rijn and Alberts's work (Alberts, 1987).

(4) The different **Q** domains in a poly-**Q** sample may be observed by x-ray topography (Ando and Hosoya, 1971) in the AF_2 phase, where the spontaneous magnetostriction is about 20×10^{-6} (Fig. 38), or by neutron topogra-

phy in both the AF_1 and AF_2 phases (Ando and Hosoya, 1972). The domains are essentially static, apart from some motion of a domain boundary after annealing at room temperature for a few days (Ando and Hosoya, 1971), and their linear dimensions are about 1–2 mm.

Remarkable relaxation effects in the neighborhood of the Néel transition were reported in thermal expansion (Stebler and Andersson, 1969; Stebler *et al.*, 1970). This behavior and the hysteresis of the electrical resistivity in temperature sweeps at different rates through T_N were related to the diffusion of nitrogen in Cr by the observation that the temperature dependence of the relaxation time, which in an iochrome crystal varied from 9200 sec at T_N to 3200 sec at a temperature 10 K above T_N (Stebler and Andersson, 1969), corresponds to the Arrhenius plot for nitrogen in Cr determined by Klein (1967), using internal friction and elastic-aftereffect data.

Stebler and Andersson (1969) proposed that interstitial nitrogen is responsible for Q domain formation on cooling through T_N, and the hypothesis, for which there is no direct evidence, was further developed by Stebler (1970a, 1970b, 1970c). It is proposed that, on heating through T_N, the interstitial nitrogen causes persistence of some magnetic ordering in the paramagnetic phase, and lattice relaxation occurs as thermal equilibrium is achieved through diffusion.

C. Polarization S domains

Ando and Hosoya (1972, 1978) also observed static **S** domains. They found that in a [001] field-cooled sample the single-**Q** domain in the AF_2 phase, which is necessarily also single-**S** since $\mathbf{S}\|\mathbf{Q}$, breaks up into S_x and S_y domains when the temperature is raised through the spin-flip transition into the AF_1 phase. The dimensions of the **S** domains were of the same order of magnitude as those of the **Q** domains. Static domains occur in antiferromagnets with localized spins such as MnF_2 and NiO, and their properties were reviewed by Farztdinov (1964). We shall see in Sec. VIII.D that there is some evidence for static domains in the behavior of the ultrasonic attenuation close to and at the spin-flip transition.

There is a good deal of evidence, however, to support an alternative interpretation of Ando and Hosoya's apparent direct observation of static **S** domains. According to the random-strain model, the polarization direction **S**, while constrained by the magnetic anisotropy to be close to a cube axis in the plane perpendicular to the wave vector **Q**, is subject to random internal strains, which result in a continuous variation in the direction of **S** throughout the **Q** domain. The following points seem to favor the random-strain model over the static domain model.

(a) The fact that the polarization direction relaxes back with little hysteresis when the polarizing field is removed, as illustrated in Fig. 7, militates against the model of static **S** domains separated by well-defined boundaries. This near-reversible behavior is in strong contrast with the irreversible switching of the **Q** direction noted in Sec. VIII.B.3.

(b) The anomalous ultrasonic attenuation and internal friction of elastic oscillations, which occur in the AF_1 phase in the absence of a polarizing field [see Figs. 41 and 94(a)] when a longitudinal wave is propagated perpendicular to the **Q** direction, is difficult to explain in terms of static domains with relatively few boundaries, whose motion must account for the observed energy loss. On the other hand, the random-strain model quite naturally explains the entropy production as resulting from a relaxation process, as the polarization direction **S** responds to the oscillatory strain through magnetoelastic coupling.

(c) One might alternatively suppose that in a static $\mathbf{S}_x$ or $\mathbf{S}_y$ domain the direction of **S** would rotate coherently in response to the oscillatory strain. But in that case random static internal strain would also change the direction of **S**, so that this would in effect be equivalent to the random-strain model.

(d) Davidson *et al.* (1973), also using neutron topography, obtained results at variance with Ando and Hosoya (1972, 1978). They found that the polarization direction **S** varied continuously across a single-**Q** domain and that application of a polarizing field $\mathbf{H}_p = 1.6$ T along a cube axis perpendicular to **Q** resulted in an essentially uniform change in intensity of the neutron topograph by a factor of 1.72, this corresponding to the change in intensity of the Bragg peak. The random-strain model explains this behavior as resulting from essentially uniform rotation of

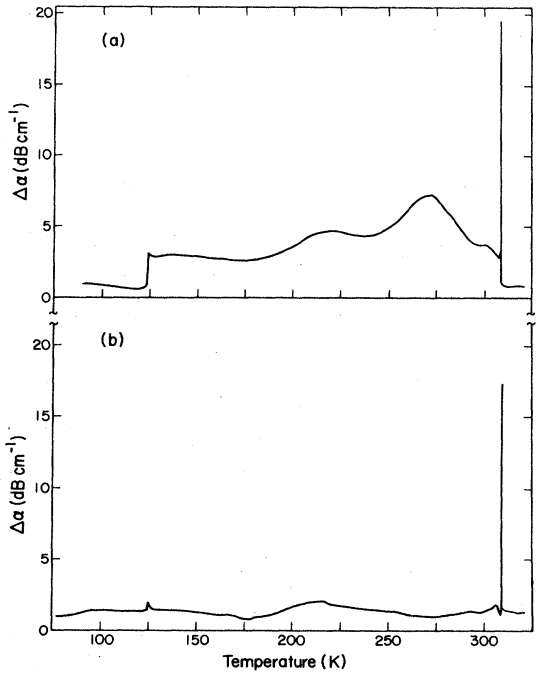

FIG. 94. Change $\Delta\alpha$ with temperature of the attenuation α of 12-MHz longitudinal sound waves with wave vector **q** along a cube axis propagating in a single-**Q** sample of Cr with (a) $\mathbf{q}\perp\mathbf{Q}$; (b) $\mathbf{q}\|\mathbf{Q}$ (after Muir, 1987).

the direction of **S** across the sample towards the cube axis perpendicular to $\mathbf{H}_p$.

Steinitz (1986) has recently reviewed the physical properties of Cr, paying particular attention to interpretation of polarization-related data in the AF_1 phase in terms of the thermal activation model. The model has achieved striking success in explaining a variety of experimental data (the field dependence of the magnetic Bragg peaks, the magnetic torque and the ultrasonic attenuation and velocity in the AF_1 phase, and the magnetic phase diagram, torque, and magnetostriction in the neighborhood of the spin-flip transition) by means of a single postulate, namely the existence of **S** domains in thermal equilibrium with each other, and a single parameter, namely the volume δV of each domain.

There are good reasons, nevertheless, for skepticism about the physical reality of the thermal activation model:

(1) The volume $\delta V \simeq 3\times 10^{-22}$ m^3 of a domain contains a number of about 10^8 atoms which is so large as to make its thermally activated "flipping" by coherent rotation difficult to envisage. On the other hand, any classical evaluation of wall energies yields a value so large as to render impossible flipping of the domains by domain-wall motion. One might remark also that δV is so large as to make negligibly small the contribution of **S** domains to the entropy, which had been suggested by Werner *et al.* (1967a), when they first introduced the thermal activation model as the driving mechanism for forming the domains.

(2) The **S** domains might be thought of as being thermally created (and not only thermally disordered) in the time during which they are reoriented. Thus the dimension $(\delta V)^{1/3}\sim 7$ μm might be thought of as the coherence length of some elementary excitation of the transverse SDW, having a characteristic energy of about 10 meV. There is, however, no evidence in the inelastic neutron scattering to support this idea. The 4- and 8-meV excitations seen in the AF_1 phase, as illustrated in Fig. 18, remained quite unaffected by a 6-T magnetic field applied transverse to the **Q** direction (Grier *et al.*, 1985), i.e., a field sufficiently strong to produce an essentially single-**S** state, and therefore to suppress any excitation associated with **S** domains.

(3) The success of the thermal activation model in employing only a single-parameter δV, whose value is essentially unchanged when optimizing the fit to various phenomena, is not too surprising, since most of the experiments were performed by Steinitz and co-workers (1986, and references therein) at the same temperature, $T\simeq 130$ K, a little above the spin-flip temperature, on the same single-crystal sample. A volume δV about five times smaller (Steinitz *et al.*, 1973) fits better the ultrasonic attenuation data of Simpson *et al.* (1971), while a volume δV about five times larger (Steinitz *et al.*, 1972) was estimated by Munday and Street (1971) from their elasticity measurements, these authors having of course used different samples.

(4) One might finally take exception to the thermal activation model, in that there is no evidence whatever that the temperature dependence of the various phenomena fits an Arrhenius plot. Being restricted to the AF_1 phase, the temperature range available for making such a fit is unfortunately restricted to only a factor less than 3. In any case there is little or no independent experimental evidence for the three parameters of the theory, namely, the anisotropy energy coefficient [C in Eq. (54)], the anisotropy of the magnetic susceptibility ($\chi_n-\chi_s$ in Fig. 36), and the domain volume δV itself.

There appears, however, to be some recent direct evidence for fluctuation of the polarization direction in the form of $1/f$ noise in the conductivity of Cr films of thickness ~ 1000 Å on silicon, sapphire, and soda-glass substrates (Israeloff *et al.*, 1987, 1988; Weissman, 1987). The conductivity noise increases rapidly with decreasing temperature at about 340 K and then decreases slowly and drops off sharply at about 140 K. The latter result may be associated with the spin-flip transition, but Weissman (1987) cautions that it may simply be due to freezing out of the fluctuations.

D. Ultrasonic attenuation and internal friction

The AF_1 phase of AFM shows ultrasonic attenuation and internal friction due to magnetoelastic coupling between the SDW and oscillatory elastic strain as discussed in Secs. III.D and VIII.C. The Néel transition and the spin-flip transition also show peaks or discontinuous steps in attenuation for different configurations of the elastic oscillations, as seen in Figs. 94 and 95.

I shall not attempt a comprehensive review of Muir's (1987) ultrasonic attenuation results for the various configurations of longitudinal, shear, and quasishear waves propagating in polydomain, single-**Q** (field-cooled in $\mathbf{H}_C=12$ T), and single-**S** single-**Q** (polarized in $\mathbf{H}_p=5$ T) states. I shall rather select a few results, with refer-

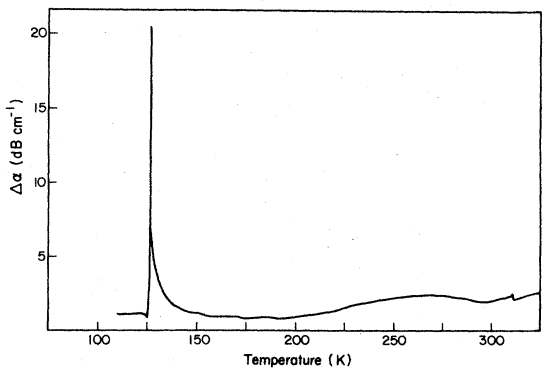

FIG. 95. Change $\Delta\alpha$ with temperature of the attenuation α of 12-MHz shear waves with wave vector **q** along a cube axis perpendicular to **Q** and displacement parallel to **Q** propagating in a single-**Q** sample of Cr (after Muir, 1987).

ence to previous work, which may help us to an understanding of the mechanisms responsible for the attenuation.

1. q⊥Q⊥H attenuation peak

This striking effect is illustrated in Fig. 96(a), and was first observed by Barak *et al.* [1981, Fig. 14; note that the peak at T_{SF} at $\mathbf{H}\simeq 1.8$ T with the same configuration in their Fig. 13 is spurious due to an error in the measuring procedure (Muir, 1987)]. The strong hysteretic peak in attenuation with $\mathbf{q}\perp\mathbf{H}$ is absent with $\mathbf{q}\parallel\mathbf{H}$ in Fig. 96(b). Muir *et al.* (1987b) argue that such an effect might be expected for static domains, but cannot be explained by the thermal activation model and is difficult to visualize for the random-strain model.

2. Comparison with MnF_2

At 4.2 K MnF_2 is a uniaxial antiferromagnet with spins polarized along the easy [001] axis. When a magnetic field is applied along [001] there is a first-order reorientation transition to the spin-flip phase at $\mathbf{H}_{SF}\simeq 9.3$ T, where the spins rotate nearly into the basal plane. King and Paquette (1973) have observed an intermediate state over an interval $\Delta\mathbf{H}\simeq 0.1$ T, between the easy-axis AFM and the spin-flip phases, which consists of alternate thin-slab domains of AFM and spin-flip material of thickness $\simeq 100\,\mu$m.

Fawcett, Muir, and Perz (1988) compared the nature of the ultrasonic attenuation anomaly at the spin-flip transition in Cr, induced by increasing temperature, with that in MnF_2, induced by increasing field, for corresponding configurations of the longitudinal or shear waves relative to the **Q** direction (Cr) or easy axis (MnF_2). The correspondence is striking, and suggests by analogy that Cr supports static domains in the transverse SDW phase near the spin-flip transition.

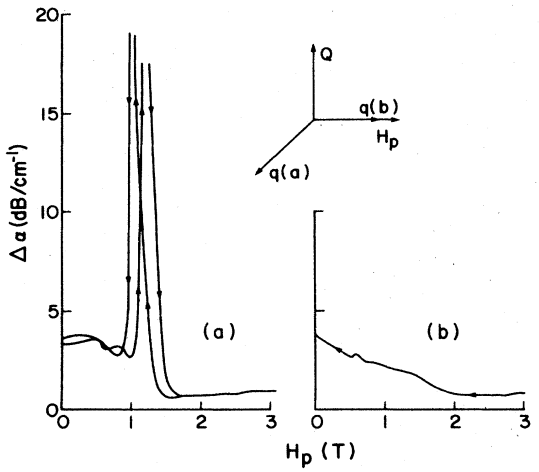

FIG. 96. Change $\Delta\alpha$ with magnetic field **H** along a cube axis perpendicular to **Q** of the attenuation α of 12-MHz longitudinal sound waves in the AF_1 phase at temperature $\simeq 146$ K and wave vector **q** also perpendicular to **Q**: (a) $\mathbf{q}\perp\mathbf{H}$; (b) $\mathbf{q}\parallel\mathbf{H}$ (after Muir *et al.*, 1987b).

3. Frequency dependence of the attenuation at T_N, in the AF_1 phase, and at T_{SF}

One might hope to learn something about the mechanisms responsible for the ultrasonic attenuation α from its dependence on the angular frequency, $\omega=2\pi f$. In the case of a relaxation mechanism having a characteristic time τ, for example, α is of the form $\omega^2\tau/(1+\omega^2\tau^2)$, passing from quadratic in ω for $\omega\tau\ll 1$ with approach to saturation for $\omega\tau\gg 1$.

Simpson *et al.* (1971) found that the peak in α at T_{SF}, for longitudinal waves propagating either parallel or perpendicular to **Q**, varies as ω^2 in the range $f=50$–100 MHz; while in the AF_1 phase, with $\mathbf{q}\perp\mathbf{Q}$, α appears to be linear in ω according to Steinitz *et al.* (1973, $f=12$–50 MHz) and Muir (1987, $f=12$–32 MHz). The attenuation of longitudinal waves at T_N is also linear in ω (O'Brien and Franklin, 1966, $f=15$–55 MHz; Fawcett, Ho, and Perz, 1975, $f=21$–273 MHz).

E. Technical antiferromagnetism in the AF_2 phase

We saw in Sec. V.B that the pressure dependence of the wave vector **Q** in the AF_2 (longitudinal SDW) phase at low temperatures varies according to the measuring conditions. Table XV shows that direct pressure gives a large volume dependence of the incommensurability parameter δ, while oscillatory magnetostriction gives $\partial\ln(\delta/a)/\partial p$ essentially zero. Since the wave vector may be written $Q=2\pi/a-2\pi(\delta/a)$, this result means that, as the lattice parameter changes with temperature, the SDW appears to be locked to the lattice periodicity.

Table XV and Fig. 74 show that either of the two different values of $\partial\ln(\delta/a)/\partial p$ may be obtained according to the history of the sample. There is an asymmetry between increasing pressure (soft mode) and decreasing pressure (hard mode), the latter corresponding to the SDW's being locked to the lattice. Littlewood and Rice (1982) calculate the change of the wave vector for a one-dimensional CDW weakly pinned by impurities when the lattice parameter is cycled, and find similar hysteretic behavior to that seen in Cr by Ruesink and Templeton (1984). Arguing by analogy, they relate the behavior to the temperature dependence of the wave vector **Q** of Cr, shown in Fig. 4, which is quite independent of temperature below the pinning temperature $T_0\simeq 80$ K. Littlewood and Rice suggest that, for $T<T_0$, the longitudinal SDW is in a metastable state pinned by impurities with $Q>Q_{equ}$, and increasing pressure overcomes the impurity pinning and drives Q towards its equilibrium value Q_{equ}. Removing the pressure then has no effect, since the system will not change spontaneously away from Q_{equ}.

Gibbs *et al.* (1987) report, however, as noted in Sec. II.B.1, that Q decreases continuously with temperature, with dQ/dT approaching zero only below 40 K, and with no evidence for a lockin transition at the supposed pinning temperature of about 80 K.

The high-pressure measurements of Venema *et al.* (1980) were performed by the helium isobaric freezing method, so that the pressure is always increased and there is no possibility of seeing hysteretic effects. The behavior should thus, as observed, correspond to the soft mode. It is not clear why the magnetostriction method should correspond to the hard mode. The magnetostriction response corresponds to maintaining thermodynamic equilibrium as the field changes, which seems to correspond neither to the hard nor to the soft mode.

Fenton (1980) suggested that domain walls, where the periodicity of the lattice changes without a corresponding change of the more rigid SDW (Fenton, 1984), could explain the hysteretic behavior. The free energy of the walls is negative, so that they can be created readily, but thermal energy is needed to destroy them. The observed increase of δ with pressure generates domain walls which, if the temperature is low enough, are retained as the pressure is decreased. Ruesink and Templeton (1984) found, however, that Fenton's prediction, that the loop width when the pressure is cycled in the hard mode [i.e., the loop (5)-(6) in Fig. 74] will depend on the sample dimensions, is not supported by their experimental data.

Hysteretic behavior in the AF_2 phase was seen by Pluzhnikov and Fawcett (1983) in the magnetostriction of Cr, whose hysteresis is strikingly similar to the pressure dependence of **Q**, as seen by comparing Fig. 97 with Fig. 74. In Fig. 97(a) one might suspect that the irreversible increase of length with increasing field is due to switching of some regions of the sample to make **Q** (and therefore in the AF_2 phase the polarization **S**) perpendicular to **H**, in accordance with the sign of the tetragonal distortion, $c/a > 1$, shown in Fig. 38. Similar hysteresis is seen, however, in Fig. 97(b), where **Q** is perpendicular to **H**.

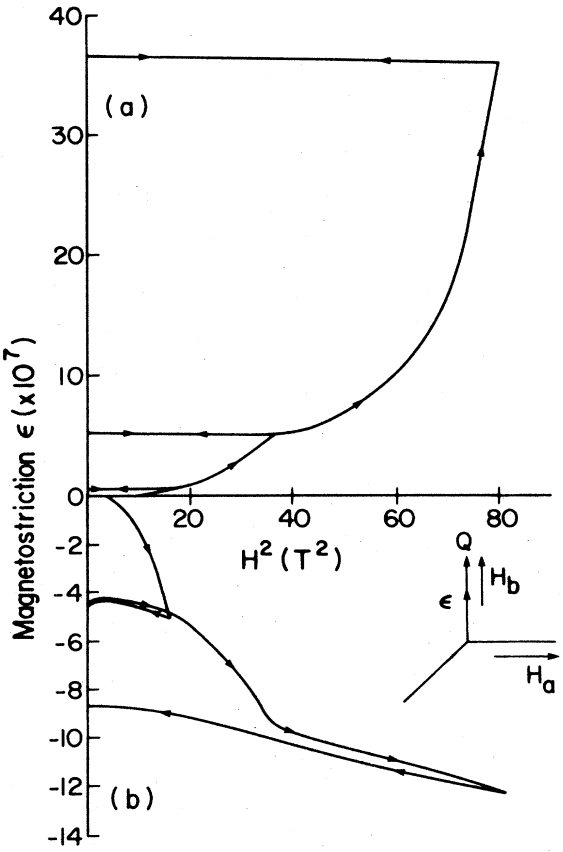

FIG. 97. Magnetostriction of single-Q Cr at temperature =4.2 K showing hysteresis: (a) strain ε, wave vector **Q**, and magnetic field **H** all parallel, $\varepsilon \| \mathbf{Q} \| \mathbf{H}$; (b) $(\varepsilon \| \mathbf{Q}) \perp \mathbf{H}$ (after Pluzhnikov and Fawcett, 1983).

IX. CONCLUSIONS

There are many unresolved problems concerning the magnetism of chromium. Perhaps the most fundamental theoretical problem is that referred to in the first paragraph—the proper introduction into the theory of chromium's being a 3*d* transition metal. We have now gone well beyond the simple picture of Fermi-surface nesting, and the recent calculation by Zhao *et al.* (1987) shows clearly a singularity in the exchange-enhanced susceptibility of Cr which is absent in the homologous 4*d* metal Mo. An examination of the matrix elements in this calculation shows how this results from the greater spatial extent of the 4*d* wave function (Fry, 1987).

The most outstanding experimental problem is the nature of the excitations in the incommensurate SDW. It is anticipated that inelastic neutron scattering in dilute Cr*V* alloys (Fawcett, Roberts *et al.*, 1986) and in commensurate AFM Cr*Mn* alloys (Werner, 1987) will shed light on this problem. Such experiments should also help us to understand the spin fluctuations in the paramagnetic state, whose nature is fundamentally different from those in an itinerant ferromagnet (Lonzarich, 1986b). It is interesting to speculate on the reason why the magnetoelastic coupling is even stronger in the paramagnetic phase than in the ordered phase of Cr (Muir *et al.*, 1987a).

Both the Néel transition and the spin-flip transition in Cr provide theoretical challenges. Experimental insight into the weak first-order Néel transition has been provided recently by the observation that the transition appears to be continuous in dilute alloys (Fawcett, Roberts *et al.*, 1986). There are a good many experimental data showing the effect of the spin-flip transition on the physical properties of Cr, but thus far no microscopic theoretical picture whatever of this phenomenon has been given.

Finally "technical antiferromagnetism" provides a wealth of interesting phenomena for experimental and theoretical study, perhaps the most puzzling of which is the hysteretic behavior of the pressure dependence of the SDW wave vector (Ruesink *et al.*, 1984).

ACKNOWLEDGMENTS

I should like to acknowledge my debt to many colleagues for their help and advice, but especially to Professor M. B. Walker for his notes on the microscopic theory and also to Professor M. O. Steinitz for his bibliography. I am grateful for the hospitality provided by the Institut Laue-Langevin, Grenoble, the CSIRO Division of Applied Physics, Sydney, and the H. C. Oersted Institute, University of Copenhagen, during the course of this work. Financial support was provided by the Natural Sciences and Engineering Research Council of Canada.

ENDORSEMENT

It is the author's wish that no agency should ever derive military benefit from the publication of this paper. Authors who cite this work in support of their own are requested to qualify similarly the availability of their results.

REFERENCES

Akhiezer, I. A., and E. A. Barannik, 1982, Ukr. Fiz. Zh. (Russ. Ed.) **27**, 598.
Akiba, C., and T. Mitsui, 1972, J. Phys. Soc. Jpn. **32**, 644.
Alberts, H. L., 1987, private communication.
Alberts, H. L., and E. S. Fisher, 1980, Phys. Status Solidi B **98**, K21.
Alberts, H. L., and J. A. Lourens, 1985, J. Phys. F **15**, 2511.
Allan, G., 1978, Surf. Sci. **74**, 79.
Allan, G., 1979, Phys. Rev. B **19**, 4774.
Allan, G., 1981, Surf. Sci. Rep. **1**, 121.
Allen, J. W., and C. Y. Young, 1975, in *Magnetism and Magnetic Materials,* AIP Conference Proceedings No. 24, edited by C. D. Graham, Jr., G. H. Lander, and J. J. Rhyne (AIP, New York), p. 410.
Allen, J. W., and C. Y. Young, 1977, Phys. Rev. B **16**, 1103.
Als-Nielsen, J., J. D. Axe, and G. Shirane, 1971, J. Appl. Phys. **12**, 1666.
Ando, M., and S. Hosoya, 1971, Phys. Rev. Lett. **26**, 321.
Ando, M., and S. Hosoya, 1972, Phys. Rev. Lett. **29**, 281.
Ando, M., and S. Hosoya, 1978, J. Appl. Phys. **49**, 6045.
Arajs, S., 1969, Can. J. Phys. **47**, 1005.
Arajs, S., K. V. Rao, H. U. Åström, and T. F. De Young, 1973, Phys. Scr. **8**, 109.
Arko, A. J., J. A. Marcus, and W. A. Reed, 1968, Phys. Rev. **176**, 671.
Arko, A. J., J. A. Marcus, and W. A. Reed, 1969, Phys. Rev. **185**, 901.
Arrott, A., 1966, "Antiferromagnetism in Metals," in *Magnetism,* edited by G. Rado and H. Suhl (Academic, New York), Vol. IIB, p. 295.
Arrott, A., ca. 1975, private communication.
Arrott, A., S. A. Werner, and H. Kendrick, 1965, Phys. Rev. Lett. **14**, 1022.
Arrott, A., S. A. Werner, and H. Kendrick, 1967, Phys. Rev. **153**, 624.
Asano, S., and J. Yamashita, 1967, J. Phys. Soc. Jpn. **23**, 714.
Asano, S., and J. Yamashita, 1971, J. Phys. Soc. Jpn. **31**, 1000.
Asdente, M., and J. Friedel, 1961, Phys. Rev. **124**, 384.
Bacon, G. E., 1961, Acta Crystallogr. **14**, 823.
Bacon, G. E., and N. Cowlam, 1969, J. Phys. C Ser. 2 **2**, 238.
Bak, P., and D. Mukamel, 1976, Phys. Rev. B **13**, 5086.
Barak, Z., E. Fawcett, D. Feder, G. Lorincz, and M. B. Walker, 1981, J. Phys. F **11**, 915.
Barak, Z., and M. B. Walker, 1981, J. Phys. F **11**, 947.
Barak, Z., and M. B. Walker, 1982, J. Phys. F **12**, 483.
Barker, A. S., and J. A. Ditzenberger, 1970, Phys. Rev. B **1**, 4378.
Barker, A. S., B. I. Halperin, and T. M. Rice, 1968, Phys. Rev. Lett. **20**, 384.
Barnes, R. G., and T. P. Graham, 1962, Phys. Rev. Lett. **8**, 248.
Bastow, T. J., and R. Street, 1966, Phys. Rev. **141**, 51.
Beaumont, R. H., H. Chihara, and J. A. Morrison, 1960, Philos. Mag. **5**, 188.
Bender, D., and J. Müller, 1970, Phys. Kondens. Mater. **10**, 342.
Benediktsson, G., and H. U. Åström, 1982, Phys. Scr. **25**, 671.
Benediktsson, G., H. U. Åström, and K. V. Rao, 1975, J. Phys. F **5**, 1966.
Benski, C., J. Berthier, G. Teisseron, and S. Choulet, 1975, Phys. Lett. A **51**, 467.
Bernhoeft, N. R., G. G. Lonzarich, P. W. Mitchell, and D. M. Paul, 1986, Physica B **136**, 443.
Bland, 1982, Z. Phys. B **48**, 233.
Bolef, D. I., and J. de Klerk, 1963, Phys. Rev. **129**, 1063.
Booth, J. G., and K. R. A. Ziebeck, 1981, J. Appl. Phys. **52**, 2107.
Booth, J. G., K. R. A. Ziebeck, and C. Escribe, 1979, J. Magn. Magn. Mater. **14**, 135.
Bos, L. W., and D. W. Lynch, 1970, Phys. Rev. B **2**, 4567.
Bridgman, P. W., 1932, Proc. Am. Acad. Arts Sci. **68**, 27.
Brodsky, M. B., P. Marikar, R. J. Friddle, L. Singer, and C. H. Sowers, 1982, Solid State Commun. **42**, 675.
Brodsky, M. B., L. R. Sill, and C. H. Sowers, 1986, J. Magn. Magn. Mater. A **54-57**, 779.
Brown, P. J., C. Wilkinson, J. B. Forsyth, and R. Nathans, 1965, Proc. Phys. Soc. London **85**, 1185.
Buker, D. W., 1982, Phys. Rev. B **25**, 991.
Burke, S. K., 1985, private communication.
Burke, S. K., and B. D. Rainford, 1978, J. Phys. F **8**, L239.
Burke, S. K., W. G. Stirling, and K. R. A. Ziebeck, 1983, Phys. Rev. Lett. **51**, 494.
Buzdin, A. I., and V. V. Tugushev, 1983a, Fiz. Tverd. Tela (Leningrad) **25**, 882 [Sov. Phys. Solid State **25**, 506 (1983)].
Buzdin, A. I., and V. V. Tugushev, 1983b, Zh. Eksp. Teor. Fiz. **85**, 735 [Sov. Phys. JETP **58**, 428 (1983)].
Bykov, V. N., V. S. Golovkin, N. V. Ageev, V. A. Levdik, and S. I. Vinogradov, 1959, Dokl. Akad. Nauk SSSR **128**, 1153 [Sov. Phys. Dokl. **128**, 1070 (1960)].
Callaway, J., A. K. Chatterjee, S. P. Singhal, and A. Ziegler, 1983, Phys. Rev. B **28**, 3818.
Castro, E. P., P. C. de Camargo, and F. R. Brotzen, 1986, Solid State Commun. **57**, 37.
Cavalheiro, R., and M. M. Shukla, 1978, Acta Phys. Acad. Sci. Hung. **45**, 75.
Colavita, E., A. Franciosi, D. W. Lynch, G. Paolucci, and R. Rosi, 1983, Phys. Rev. B **27**, 1653.
Cook, J. G., 1987, Solid State Commun., in press.
Corliss, L., N. Elliott, and J. Hastings, 1956, Phys. Rev. **104**, 924.
Corliss, L. M., J. M. Hastings, and R. J. Weiss, 1959, Phys. Rev. Lett. **3**, 211.
Cowan, W. B., 1978, J. Phys. F **8**, 423.

Cywinski, R., and T. J. Hicks, 1986, J. Magn. Magn. Mater. **54-57**, 999.
Davidson, J. B., S. A. Werner, and A. S. Arrott, 1973, in *Magnetism and Magnetic Materials,* AIP Conference Proceedings No. 18, edited by C. D. Graham, Jr., and J. J. Rhyne (AIP, New York), Part I, p. 396.
Day, R., 1968, Ph.D. thesis (Monash University).
de Camargo, P. C., and F. R. Brotzen, 1982, J. Magn. Magn. Mater. **27**, 65.
de Vries, G., 1959, J. Phys. (Paris) **10**, 438.
Dubiel, S. M., 1984, Phys. Rev. B **29**, 2816.
Dubiel, S. M., and G. Le Caër, 1987, preprint available from Department Solid State Phys., Academy of Mining and Metallurgy, PL-30-059, Krakow, Poland.
Eagan, C. F., and S. A. Werner, 1975, Solid State Commun. **16**, 1113.
Evangelou, S. N., H. Hasegawa, and D. M. Edwards, 1982, J. Phys. F **12**, 2035.
Evenson, W. E., G. S. Fleming, and S. H. Liu, 1969, Phys. Rev. **178**, 930.
Falicov, L. M., and M. J. Zuckermann, 1967, Phys. Rev. **160**, 372.
Farztdinov, M. M., 1964, Usp. Fiz. Nauk **84**, 611 [Sov. Phys. Usp. **7**, 855 (1965)].
Fawcett, E., D. Feder, W. C. Muir, and C. Vettier, 1984, J. Phys. F **14**, 1261.
Fawcett, E., R. Griessen, W. Joss, M. J. G. Lee, and J. M. Perz, 1980, "The Effect of Strain on the Fermi Surface," in *Electrons at the Fermi Surface,* edited by M. Springford (Cambridge University Press, Cambridge/New York), p. 278.
Fawcett, E., R. Griessen, and D. J. Stanley, 1976, J. Low Temp. Phys. **25**, 771.
Fawcett, E., R. Griessen, and C. Vettier, 1978, in Institute of Physics Conference Series No. 39, edited by M. J. G. Lee, J. M. Perz, and E. Fawcett, p. 592.
Fawcett, E., and D. Griffiths, 1962, J. Phys. Chem. Solids **23**, 1631.
Fawcett, E., C. S. Ho, and J. M. Perz, 1975, Phys. Lett. A **53**, 27.
Fawcett, E., T. M. Holden, W. C. Muir, and P. C. de Camargo, 1988, Zh. Eksp. Teor. Fiz., in press.
Fawcett, E., A. B. Kaiser, and G. K. White, 1986a, Phys. Rev. B **34**, 6248.
Fawcett, E., A. B. Kaiser, and G. K. White, 1986b, J. Magn. Magn. Mater. **54-57**, 1021.
Fawcett, E., W. C. Muir, and J. M. Perz, 1988, J. Phys. F, in press.
Fawcett, E., R. B. Roberts, A. Day, and G. K. White, 1986, Europhys. Lett. **1**, 473.
Fedders, P. A., and P. C. Martin, 1966, Phys. Rev. **143**, 245.
Feldman, J. L., 1970, Phys. Rev. B **1**, 448.
Fenton, E. W., 1976a, J. Phys. F **6**, 2403.
Fenton, E. W., 1976b, Solid State Commun. **20**, 115.
Fenton, E. W., 1978, J. Phys. F **8**, 689.
Fenton, E. W., 1979, Solid State Commun. **32**, 195.
Fenton, E. W., 1980, Phys. Rev. Lett. **45**, 736.
Fenton, E. W., 1984, *Superconductivity in Magnetic and Exotic Materials* (Springer, Berlin), p. 167.
Fenton, E. W., 1986, private communication.
Fenton, E. W., and C. R. Leavens, 1977, J. Phys. F **7**, 1705.
Fenton, E. W., and C. R. Leavens, 1980, J. Phys. F **10**, 1853.
Fincher, C. R., G. Shirane, and S. A. Werner, 1979, Phys. Rev. Lett. **43**, 1441.
Fincher, C. R., G. Shirane, and S. A. Werner, 1981, Phys. Rev. B **24**, 1312.
Fine, M. E., E. S. Greiner, and W. C. Ellis, 1951, J. Met. **191**, 56.
Fisher, B. E. A., 1972, J. Phys. F **2**, 806.
Fisher, M. E., and J. S. Langer, 1968, Phys. Rev. Lett. **20**, 665.
Fletcher, G. C., and C. F. Osborne, 1973, J. Phys. F **3**, 22.
Fletcher, R., 1985, Phys. Rev. B **31**, 7580.
Foord, J. S., and R. M. Lambert, 1982, Surf. Sci. **115**, 141.
Fote, A., R. Axler, H. K. Schurmann, and T. Mihalion, 1973, Phys. Rev. B **8**, 2099.
Freeman, A. J., and R. E. Watson, 1961, Acta Crystallogr. **14**, 231.
Fry, J. L., 1987, private communication.
Fu, C. L., A. J. Freeman, and T. Oguchi, 1985, Phys. Rev. Lett. **54**, 2700.
Garnier, P. R., and M. B. Salamon, 1971, Phys. Rev. Lett. **27**, 1523.
Gaspar, R., 1954, Acta Phys. Acad. Sci. Hung. **3**, 263.
Geerken, B. M., R. Griessen, G. Benediktsson, H. U. Åström, and C. van Dijk, 1982, J. Phys. F **12**, 1603.
Gibbs, Doon, K. M. Mohanty, and Jakob Bohr, 1987, Phys. Rev. B, in press.
Glötzel, D., Y. Glötzel, and O. K. Andersen, 1981, private communication to H. L. Skriver.
Goff, J. F., 1970, Phys. Rev. B **1**, 1351.
Golovkin, V. S., V. N. Bykov, V. A. Levdik, A. I. Ustinov, and I. P. Barinov, 1977, Fiz. Tverd. Tela (Leningrad) **19**, 3439 [Sov. Phys. Solid State **19**, 2010 (1977)].
Graebner, J. E., 1971, in *Proceedings of the 12th International Conference on Low Temperature Physics, Kyoto. . .1970,* edited by E. Kanda (Academic Press of Japan, Tokyo), p. 601.
Graebner, J., and J. A. Marcus, 1966, J. Appl. Phys. **37**, 1262.
Graebner, J. E., and J. A. Marcus, 1968, Phys. Rev. **175**, 659.
Grempel, D. R., 1981, Phys. Rev. B **24**, 3928.
Grier, B. H., G. Shirane, and S. A. Werner, 1985, Phys. Rev. B **31**, 2882.
Griessen, R., and E. Fawcett, 1977, J. Phys. F **7**, 2141.
Griessen, R. B., D. J. Stanley, and E. Fawcett, 1976, Solid State Commun. **19**, 1185.
Gunnarsson, O., 1976, J. Phys. F **6**, 586.
Gupta, R. P., and S. K. Sinha, 1971, Phys. Rev. B **3**, 2401.
Gutman, E. J., and L. Stanford, 1971, Phys. Rev. B **4**, 4026.
Hamaguchi, Y., E. O. Wollan, and W. C. Koehler, 1965, Phys. Rev. **138**, 737A.
Hanf, M. C., C. Pirri, J. C. Peruchetti, D. Bolmont, and G. Gewinner, 1987, Phys. Rev. B **36**, 4487.
Hasegawa, H., 1978a, J. Low Temp. Phys. **31**, 475.
Hasegawa, H., 1978b, J. Low Temp. Phys. **31**, 845.
Hasegawa, H., 1986, J. Phys. F **16**, 1555.
Hastings, J. M., 1960, Bull. Am. Phys. Soc. **5** (2), 455.
Heiniger, F., 1966, Phys. Kondens. Mater. **5**, 285.
Herring, C., 1966, *Exchange Interactions Among Itinerant Electrons,* Vol. IV of *Magnetism,* edited by G. Rado and H. Suhl (Academic, New York).
Hirashita, N., G. Yokoyama, T. Kambara, and K. K. Gondaira, 1981, J. Phys. F **11**, 2371.
Huguenin, R., G. P. Pells, and D. N. Baldock, 1971, J. Phys. F **1**, 281.
Iida, S., M. Kohno, Y. Tsunoda, and N. Kunitomi, 1981, J. Phys. Soc. Jpn. **50**, 2581.
Iida, S., Y. Tsunoda, and Y. Nakai, 1981, J. Phys. Soc. Jpn. **50**, 2587.
Israeloff, N. E., M. B. Weissman, G. A. Garfunkel, D. J. Van Haarlingen, J. H. Scofield, and A. J. Lucero, 1988, First

Mössbauer-Effect Evidence of the Third Harmonic of Spin-Density-Waves in Metallic Cr, in press.
Israeloff, N. E., M. B. Weissman, and J. H. Scofield, 1987, Bull. Am. Phys. Soc. **32**, 481.
Izuyama, T., D. J. Kim, and R. Kubo, 1963, J. Phys. Soc. Jpn. **18**, 1025.
Janak, J. F., 1977, Phys. Rev. B **16**, 255.
Johansson, L. I., L. G. Petersson, K.-F. Berggre, and J. W. Allen, 1980, Phys. Rev. B **22**, 3294.
Kaiser, A. B., G. K. White, and E. Fawcett, 1985, Phys. Rev. B **32**, 7438.
Katahara, K. W., M. Nimalendran, M. H. Manghani, and E. S. Fisher, 1979, J. Phys. F **9**, 2167.
Kimball, J. C., 1969, Phys. Rev. **183**, 533.
Kimball, J. C., and L. M. Falicov, 1968, Phys. Rev. Lett. **20**, 1164.
King, A. R., and D. Paquette, 1973, Phys. Rev. Lett. **30**, 662.
Klebanoff, L. E., S. W. Robey, G. Liu, and D. A. Shirley, 1984, Phys. Rev. B **30**, 1048.
Klebanoff, L. E., S. W. Robey, G. Liu, and D. A. Shirley, 1985, Phys. Rev. B **31**, 6379.
Klebanoff, L. E., S. W. Robey, G. Liu, and D. A. Shirley, 1986, J. Magn. Magn. Mater. **54-57**, 728.
Klebanoff, L. E., and D. A. Shirley, 1986, Phys. Rev. B **33**, 5301.
Klebanoff, L. E., R. H. Victora, L. M. Falicov, and D. A. Shirley, 1985, Phys. Rev. B **32**, 1997.
Klein, M. J., 1967, J. Appl. Phys. **38**, 819.
Köbler, U., and S. M. Dubiel, 1985, Z. Phys. B **61**, 257.
Koehler, W. C., R. M. Moon, A. L. Trego, and A. R. Mackintosh, 1966, Phys. Rev. **151**, 405.
Kohn, W., 1959, Phys. Rev. Lett. **2**, 393.
Kohn, W., and L. J. Sham, 1965, Phys. Rev. **140**, A1133.
Komura, S., Y. Hamaguchi, and N. Kunitomi, 1967, J. Phys. Soc. Jpn. **23**, 171.
Kontani, M., and Y. Masuda, 1983, J. Magn. Magn. Mater. **31-34**, 287.
Kotani, A., 1975, J. Phys. Soc. Jpn. **39**, 851.
Kotani, A., 1976, J. Phys. Soc. Jpn. **41**, 1473.
Kotani, A., 1978, J. Phys. Soc. Jpn. **44**, 1455.
Kubo, R., and Y. Obata, 1956, J. Phys. Soc. Jpn. **11**, 547.
Kübler, J., 1980, J. Magn. Magn. Mater. **20**, 277.
Kulikov, N. I., 1979, Fiz. Nizk. Temp. **5**, 363 [Sov. J. Low Temp. Phys. **5**, 173 (1979)].
Kulikov, N. I., M. Alouani, M. A. Khan, and M. V. Magnitskaya, 1987, Phys. Rev. B **36**, 929.
Kulikov, N. I., and E. T. Kulatov, 1982, J. Phys. F **12**, 2291.
Kulikov, N. I., and V. V. Tugushev, 1984, Usp. Fiz. Nauk **144**, 643 [Sov. Phys. Usp. **27**, 954 (1984)].
Landolt-Börnstein, 1986, *Numerical Data and Functional Relationships in Science and Technology,* New Series 19a: Magnetic Properties of Metals—3*d*, 4*d* and 5*d* Elements, Alloys, and Compounds, edited by H. P. J. Wijn (Springer, Berlin), p. 6.
Laurent, D. G., J. Callaway, J. L. Fry, and N. E. Brener, 1981, Phys. Rev. B **23**, 4977.
Lebech, B., and K. Mikke, 1972, J. Phys. Chem. Solids **33**, 1651.
Lee, E. W., and M. A. Asgar, 1969, Phys. Rev. Lett. **22**, 1436.
Lind, M. A., and J. Stanford, 1972, Phys. Lett. A **39**, 5.
Littlewood, P. B., and T. M. Rice, 1982, Phys. Rev. Lett. **48**, 44.
Liu, S. H., 1970, Phys. Rev. B **2**, 493.
Liu, S. H., 1981, J. Magn. Magn. Mater. **22**, 93.
Lomer, W. M., 1962, Proc. Phys. Soc. London **80**, 489.
Lomer, W. M., 1965, *Proceedings of the International Conference on Magnetism,* Nottingham 1964, edited by L. F. Bates (Institute of Physics and Physical Society, London), p. 127.
Lonzarich, G. G., 1986a, J. Magn. Magn. Mater. **54-57**, 612.
Lonzarich, G. G., 1986b, private communication.
Loucks, T. L., 1965, Phys. Rev. A **139**, 1181.
Lovesey, S. W., 1984, *Theory of Neutron Scattering from Condensed Matter* (Clarendon, Oxford), Vol. 2.
Machida, K., and M. Fujita, 1984, Phys. Rev. B **30**, 5284.
Machida, K., M. A. Lind, and J. L. Stanford, 1984, J. Phys. Soc. Jpn. **53**, 4020.
Mackintosh, A. R., and O. K. Andersen, 1980, "The Electronic Structure of Transition Metals," in *Electrons at the Fermi Surface,* edited by M. Springford (Cambridge University Press, Cambridge/New York), p. 149.
Malaspinas, A., and T. M. Rice, 1972, Phys. Kondens. Mater. **13**, 193.
Marshall W., and S. W. Lovesey, 1971, *Theory of Thermal Neutron Scattering* (Clarendon, Oxford), p. 233.
Matsuo, S., and I. Nishida, 1980, J. Phys. Soc. Jpn. **49**, 1005.
Mattheiss, L. F., 1965, Phys. Rev. **139**, 1893A.
McGuire, T. R., and C. J. Kriessman, 1952, Phys. Rev. **85**, 452.
McWhan, D. B., and T. M. Rice, 1967, Phys. Rev. Lett. **19**, 846.
Melcher, R. L., and W. D. Wallace, 1970, Solid State Commun. **8**, 1535.
Mikke, K., and J. Jankowska, 1979, J. Magn. Magn. Mater. **14**, 280.
Mitsui, T., and C. T. Tomizuka, 1965, Phys. Rev. **137**, 564A.
Møller, H. B., K. Blinowski, A. R. Mackintosh, and T. Brun, 1964, Solid State Commun. **2**, 109.
Møller, H. B., and A. R. Mackintosh, 1965, in *Inelastic Scattering of Neutrons* (IAEA, Vienna), Vol. I, p. 95.
Montalvo, R. A., and J. A. Marcus, 1964, Phys. Lett. **8**, 151.
Moon, R. M., W. C. Koehler, and A. L. Trego, 1966, J. Appl. Phys. **37**, 1036.
Moore, J. P., R. K. Wiliiams, and R. S. Graves, 1976, J. Appl. Phys. **48**, 610.
Mori, M., Y. Tsunoda, and N. Kunitomi, 1975, Bulletin of Annual Meeting of Phys. Soc. Jpn. (in Japanese).
Moriya, T., 1965, Prog. Theor. Phys. **33**, 157.
Moriya, T., and A. Kawabata, 1973, J. Phys. Soc. Jpn. **34**, 639.
Moruzzi, V. L., A. R. Williams, and J. F. Janak, 1978, *Calculated Electronic Properties of Metals* (Pergamon, New York), Chap. 5.
Moruzzi, V. L., *et al.*, 1985,
Moyer, C. A., S. Arajs, and L. Hedman, 1976, Phys. Rev. B **14**, 1233.
Moyer, C. A., S. Arajs, and A. Eroglu, 1980, Phys. Rev. B **22**, 3277.
Muheim, J., and J. Müller, 1964, Phys. Kondens, Mater. **2**, 377.
Muhlestein, L. D., E. Gürmen, and R. M. Cunningham, 1972a, in *Neutron Inelastic Scattering* (IAEA, Vienna), p. 53.
Muhlestein, L. D., E. Gürmen, and R. M. Cunningham, 1972b, in *Proceedings of the 18th Annual Conference on Magnetism and Magnetic Materials,* edited by C. D. Graham and J. J. Rhyne (AIP, New York).
Muir, W. B., and J. O. Ström-Olsen, 1971, Phys. Rev. B **4**, 988.
Muir, W. C., 1987, Ph.D. thesis (University of Toronto).
Muir, W. C., E. Fawcett, and J. M. Perz, 1987a, Phys. Rev. Lett. **59**, 335.
Muir, W. C., E. Fawcett, and J. M. Perz, 1987b, J. Magn. Magn. Mater. 69, 113.
Muir, W. C., J. M. Perz, and E. Fawcett, 1987, J. Phys. F, in press.
Munday, B. C., and R. Street, 1971, J. Phys. F **1**, 498.
Nakajima, S., and Y. Kurihara, 1975, J. Phys. Soc. Jpn. **38**, 330.

Nakanishi, K., and K. Maki, 1971, Prog. Theor. Phys. **48**, 1059.
Nakao, H., S. Ohtsuka, T. Ukai, and N. Mori, 1986, J. Magn. Magn. Mater. **54-57**, 951.
Néel, L., 1932, J. Phys. (Paris) **3**, 2035.
Néel, L., 1934, C. R. Acad. Sci. **198**, 1311.
Néel, L., 1936a, Ann. Phys. (Paris) **5**, 236.
Néel, L., 1936b, C. R. Acad. Sci. **203**, 304.
Néel, L., 1986, private communication.
O'Brien, E. J., and J. Franklin, 1966, J. Appl. Phys. **37**, 2809.
Oguchi, T., and A. J. Freeman, 1986, J. Magn. Magn. Mater. **54-57**, 797.
Oh, K. H., B. N. Harmon, S. H. Liu, and S. K. Sinha, 1976, Phys. Rev. B **14**, 1283.
Ohara, S., T. Fukama, S. Hosoya, T. Takeda, and O. Terasaki, 1974, Phys. Lett. A **49**, 337.
Overhauser, A. W., 1960, Phys. Rev. Lett. **4**, 226.
Overhauser, A. W., 1962, Phys. Rev. **128**, 1437.
Overhauser, A. W., 1971, Phys. Rev. B **3**, 3173.
Overhauser, A. W., and A. Arrott, 1960, Phys. Rev. Lett. **4**, 226.
Paakari, T., S. Manninen, and K. F. Berggren, 1975, Phys. Fenn. **10**, 207.
Palmer, S. B., and E. W. Lee, 1971, Philos. Mag. **24**, 311.
Papaconstantopoulos, D. A., 1986, *Handbook of the Band Structure of Elemental Solids* (Plenum, New York).
Papoular, R., D. Debray, and S. Arajs, 1981, J. Magn. Magn. Mater. **24**, 106.
Pattnaik, P. C., P. H. Dickinson, and J. L. Fry, 1983, Phys. Rev. B **28**, 5281.
Penn, D. R., 1966, Phys. Rev. **142**, 350.
Pepper, A. R., and R. Street, 1966, Proc. Phys. Soc. London **87**, 971.
Persson, P. E. S., and L. I. Johansson, 1986, Phys. Rev. B **33**, 8814.
Pettifor, D. G., 1980, J. Magn. Magn. Mater. **15-18**, 847.
Pindor, A. J., J. Staunton, G. M. Stocks, and H. Winter, 1983, J. Phys. F **13**, 979.
Pluzhnikov, V., and E. Fawcett, 1983, unpublished.
Polovov, V. M., 1974, Zh. Eksp. Teor. Fiz. **66**, 2164 [Sov. Phys. JETP **39**, 1065 (1974)].
Prekul, A. F., and S. V. Sudareva, 1978, Fiz. Met. Metalloved. **46**, 956 [Phys. Met. Metallogr. **5**, 46 (1979)].
Pynn, R., W. Press, S. M. Shapiro, and S. A. Werner, 1976, Phys. Rev. B **13**, 295.
Rajagopal, A. K., 1965, Phys. Rev. A **137**, 1429.
Rath, J., and J. Callaway, 1973, Phys. Rev. B **8**, 5398.
Rath, J., C. S. Wang, R. A. Tawil, and J. Callaway, 1973, Phys. Rev. B **8**, 5139.
Rau, C., and S. Eichner, 1981, Phys. Rev. Lett. **47**, 939.
Reifenberger, R., F. W. Holroyd, and E. Fawcett, 1980, J. Low Temp. Phys. **38**, 421.
Rice, T. M., 1970, Phys. Rev. B **2**, 3619.
Ruesink, D. W., J. M. Perz, and I. M. Templeton, 1980, Phys. Rev. Lett. **45**, 734.
Ruesink, D. W., and I. M. Templeton, 1984, J. Phys. F **14**, 2395.
Salamon, M. B., D. S. Simons, and P. R. Garnier, 1969, Solid State Commun. **7**, 1035.
Sato, Hirokazu, and Kazumi Maki, 1974, Int. J. Magn. **6**, 1983.
Schmidt, P. H., R. N. Castellano, H. Barz, B. T. Matthias, J. G. Huber, and W. A. Fertig, 1972, Phys. Lett. A **41**, 367.
Shaw, W. M., and L. D. Muhlestein, 1971, Phys. Rev. B **4**, 969.
Shibatani, A. (subsequently A. Kotani), 1970, J. Phys. Soc. Jpn. **29**, 93.
Shibatani, A., K. Motizuki, and T. Nagamiya, 1969, Phys. Rev. **177**, 984.
Shimizu, M., 1970, Prog. Theor. Phys. Suppl. **46**, 310.
Shimizu, M., J. Inoue, Y. Ohata, and K. Niwa, 1983, Physica B **119**, 3.
Shirane, G., and W. J. Takei, 1962, J. Phys. Soc. Jpn. **17**, Suppl. B-111, 35.
Shull, C. G., and M. K. Wilkinson, 1953, Rev. Mod. Phys. **25**, 100.
Simpson, A. M., M. Roth, and M. H. Jericho, 1971, Phys. Rev. B **4**, 3093.
Sinha, S. K., S. H. Liu, L. D. Muhlestein, and N. Wakabayashi, 1969, Phys. Rev. Lett. **23**, 311.
Sinha, S. K., G. R. Kline, C. Stassis, and N. Chesser, 1977, Phys. Rev. B **15**, 1415.
Skriver, H. L., 1981, J. Phys. F **11**, 97.
Skriver, H. L., 1985, private communication.
Slater, J. C., 1951, Phys. Rev. **81**, 385.
Snider, D. F., and R. L. Thomas, 1971, Phys. Rev. B **3**, 1091.
Sokoloff, J. B., 1969a, Phys. Rev. **185**, 770.
Sokoloff, J. B., 1969b, Phys. Rev. **185**, 783.
Sokoloff, J. B., 1969c, Phys. Rev. **187**, 584.
Sonin, E. B., 1978, Solid State Commun. **25**, 253.
Stark, R. W., and C. B. Friedberg, 1974, J. Low Temp. Phys. **14**, 111.
Stassis, C., G. R. Kline, and S. K. Sinha, 1973, Phys. Rev. Lett. **31**, 1498.
Stebler, B., 1970a, Phys. Status Solidi **40**, K9.
Stebler, B., 1970b, Phys. Scr. **2**, 53.
Stebler, B., 1970c, Phys. Scr. **2**, 57.
Stebler, B., and C.-G. Andersson, 1969, Phys. Rev. Lett. **22**, 466.
Stebler, B., C.-G. Andersson, and O. Kristensson, 1970, Phys. Scr. **1**, 281.
Steinitz, M. O., 1986, J. Magn. Magn. Mater. **60**, 137.
Steinitz, M. O., E. Fawcett, C. E. Burleson, J. A. Schaefer, L. O. Frishman, and J. A. Marcus, 1972, Phys. Rev. B **5**, 3675.
Steinitz, M. O., J. P. Kalejs, J. M. Perz, and E. Fawcett, 1973, J. Phys. F **3**, 617.
Steinitz, M. O., and D. A. Pink, 1980, J. Phys. F **10**, L247.
Steinitz, M. O., L. H. Schwartz, J. A. Marcus, E. Fawcett, and W. A. Reed, 1969, Phys. Rev. Lett. **23**, 979.
Steinitz, M. O., L. H. Schwartz, J. A. Marcus, E. Fawcett, and W. A. Reed, 1970, J. Appl. Phys. **41**, 1231.
Stirling, W. G., 1985, private communication.
Street, R., and B. Window, 1966, Proc. Phys. Soc. London **89**, 587.
Street, R., B. C. Munday, B. Window, and J. R. Williams, 1968, J. Appl. Phys. **39**, 1050.
Sully, A. H., 1954, *Chromium* (Butterworth, London/Washington, D.C.), Chap. 3.
Switendick, A. C., 1966, J. Appl. Phys. **37**, 1022.
Teisseron, G., J. Berthier, P. Peretto, C. Benski, M. Robin, and S. Choulet, 1978, J. Magn. Magn. Mater. **8**, 157.
Teraoka, Y., and J. Kanamori, 1978, Physica B **91**, 199.
Trego, A. L., and A. R. Mackintosh, 1968, Phys. Rev. **166**, 495.
Tsunoda, Y., 1985, private communication.
Tsunoda, Y., Y. Hamaguchi, and N. Kunitomi, 1972, J. Phys. Soc. Jpn. **32**, 394.
Tsunoda, Y., M. Mori, N. Kunitomi, Y. Teraoka, and J. Kanamori, 1974, Solid State Commun. **14**, 287.
Tsunoda, Y., Y. Nakai, and N. Kunitomi, 1975, Solid State Commun. **16**, 443.
Ukai, T., and N. Mori, 1982, J. Appl. Phys. **53**, 2038.
Umebayashi, H., G. Shirane, B. C. Frazer, and W. B. Daniels,

1968, J. Phys. Soc. Jpn. **24**, 368.
van Rijn, H. J., and H. L. Alberts, 1983, J. Phys. F **13**, 1559.
Venegas, R., P. Peretto. G. N. Rao, and L. Trabut, 1980, Phys. Rev. B **21**, 3851.
Venema, W. J., R. Griessen, and W. Ruesink, 1980, J. Phys. F **10**, 2841.
Victora, R. H., and L. M. Falicov, 1985, Phys. Rev. B **31**, 7335.
von Barth, U., and L. Hedin, 1972, J. Phys. C **5**, 1692.
Walker, M. B., 1976, Can. J. Phys. **54**, 1240.
Walker, M. B., 1980a, Phys. Rev. Lett. **44**, 1261.
Walker, M. B., 1980b, Phys. Rev. B **22**, 1338.
Wallace, W. D., and H. V. Bohm, 1968, J. Phys. Chem. Solids **29**, 721.
Watts, B. R., 1964, Phys. Lett. **10**, 275.
Weber, R., and R. Street, 1972, J. Phys. F **2**, 873.
Weissman, M., 1987, private communication.
Werner, S. A., 1987, private communication.
Werner, S. A., A. Arrott, and M. Atoji, 1968, J. Appl. Phys. **39**, 671.
Werner, S. A., A. Arrott, and M. Atoji, 1969, J. Appl. Phys. **40**, 1447.
Werner, S. A., A. Arrott, and H. Kendrick, 1966, J. Appl. Phys. **37**, 1260.
Werner, S. A., A. Arrott, and H. Kendrick, 1967a, Phys. Rev. **155**, 528.
Werner, S. A., A. Arrott, and H. Kendrick, 1967b, J. Appl. Phys. **38**, 1243.
West, A., G. Balzer, H. Graf, T. Moslang, and E. Recknagel, 1981, Hyperfine Interact. **8**, 543.
White, G. K., 1961, Philos. Mag. **6**, 815.
White, G. K., R. B. Roberts, and E. Fawcett, 1986, J. Phys. F **16**, 449.
Wilkinson, M. K., E. O. Wollan, W. C. Koehler, and J. W. Cable, 1962, Phys. Rev. **121**, 2080.
Williams, I. S., E. S. R. Gopal, and R. Street, 1979, J. Phys. F **3**, 431.
Williams, I. S., and R. Street, 1980, J. Phys. F **10**, 2551.
Williams, I.S., and R. Street, 1981a, Philos. Mag. **43**, 893.
Williams, I.S., and R. Street, 1981b, Philos. Mag. **43**, 955.
Window, B., 1970, J. Phys. C **2**, S210.
Windsor, C. G., 1972, J. Phys. F **2**, 742.
Windsor, C. G., 1977, Physica B **91**, 119.
Wood, J. H., 1962, Phys. Rev. **126**, 517.
Xu, Jian-hua, A. J. Freeman, T. Jarlborg, and M. B. Brodsky, 1984, Phys. Rev. B **29**, 1250.
Yakhmi, J. V., I. K. Gopalakrishnan, and R. M. Iyer, 1984, J. Phys. F **14**, 923.
Yasui, M., E. Hayashi, and M. Shimizu, 1970, J. Phys. Soc. Jpn. **29**, 1446.
Yoshimori, A., 1959, J. Phys. Soc. Jpn. **14**, 807.
Young, C. Y., and J. B. Sokoloff, 1974, J. Phys. F **4**, 1304.
Zajac, G., S. D. Bader, and R. J. Friddle, 1985, Phys. Rev. B **31**, 4947.
Zhao, Y. Z., J. L. Fry, P. C. Pattnaik, and K. Schwartzman, 1987, Phys. Rev., in press.
Zhao, Y. Z., K. Schwartzman, J. L. Fry, and P. C. Pattnaik, 1986, Bull. Am. Phys. Soc. **31**, 561.
Zhu, Xiaodong, and M. B. Walker, 1986, Phys. Rev. B **34**, 8064.
Ziebeck, K. R. A., and J. G. Booth, 1979, J. Phys. F **9**, 2433.
Ziebeck, K. R. A., J. G. Booth, P. J. Brown, H. Capellman, and J. A. C. Bland, 1982, Z. Phys. B **48**, 233.